Chuch
Duncan

DOE/ET/20255-T2(Vol.2)
(DE84002708)

Library

ergy
SOLAR

THE CROSBYTON SOLAR POWER PROJECT (PHASE I)

An Interim Technical Report of Work Accomplished from
September 1, 1976 to February 18, 1977

February 18, 1977

Work Performed Under Contract No. AC04-76ET20255

Texas Tech University
Lubbock, Texas

TECHNICAL INFORMATION CENTER
U. S. DEPARTMENT OF ENERGY

Available from the National Technical Information Service, U. S. Department of Commerce, Springfield, Virginia 22161.

Price: Printed Copy A16
Microfiche A01

Codes are used for pricing all publications. The code is determined by the number of pages in the publication. Information pertaining to the pricing codes can be found in the current issues of the following publications, which are generally available in most libraries: *Energy Research Abstracts (ERA); Government Reports Announcements* and Index (*GRA* and I); *Scientific and Technical Abstract Reports (STAR);* and publication NTIS-PR-360 available from NTIS at the above address.

DOE/ET/20255-T2(Vol.2)
(DE84002708)
Distribution Category UC-62b

THE CROSBYTON SOLAR POWER PROJECT

(PHASE I)

AN INTERIM TECHNICAL REPORT OF WORK ACCOMPLISHED

FROM

SEPTEMBER 1, 1976 TO DATE

BY

TEXAS TECH UNIVERSITY

AND

E-SYSTEMS, INC.

SUBMITTED TO

THE

UNITED STATES ENERGY RESEARCH AND DEVELOPMENT ADMINISTRATION

DIVISION OF SOLAR ENERGY

BY

TEXAS TECH UNIVERSITY

UNDER

ERDA CONTRACT NO. E(29-2)-3737

FEBRUARY 18, 1977

DR. JOHN D. REICHERT
PROJECT DIRECTOR

DR. STANLEY R. LIBERTY
PROJECT MANAGER

VOLUME II: APPENDICES A - H

The work reported here was performed by:

TEXAS TECH UNIVERSITY

Project Director: J. D. Reichert

Project Manager: S. R. Liberty

R. M. Anderson
C. A. Bell
R. M. Bethea
B. C. Brock
J. R. Burns
L. D. Clements
J. R. Dunn
W. T. Ford
D. L. Gustafson
N. Güven
D. R. Haragan
C. H. Keho
J. R. McDonald
W. M. Marcy
R. E. Peterson
M. W. Shrimplin
T. L. Simpson
J. H. Smith
M. L. Smith
J. H. Strickland
C. E. Teske
C. V. Vallabhan
W. P. Vann
D. L. Vines
F. P. Wagner
W. T. White
F. Williams

E-SYSTEMS, INC.

Program Director: Y. P. Gupta

Program Manager: R. R. Walters

* Optics, Thermodynamics, Systems

M. J. O'Neill
S. L. Hudson
D. E. Yakel
W. E. Eriksen

* Concentrator, Receiver

J. L. Perry
L. Wilson
J. Smith
B. Sheard
A. Anderson
M. Quan
D. Halsey
D. Schools
V. Goldberg
D. Muzzy
H. Poskey

* Controls

T. Gage
D. Lubin

The Project Director and Manager gratefully acknowledge our indefatigable secretarial and support staff:

Fran Dupre
Carolyn Barrier
Toni Smith
Ronda Burnett

Martha Smith	J. S. Brock
Judy Clare	G. P. Moe
Pat Turner	A. P. Kwatra
JoBeth Littlefield	H. S. Leung
Karen Dendy	D. M. Barrett
RoseMary Rodriguez	D. A. Courtney
Lucy Arandondo	R. Callicutt
Suzanne Smith	C. I. Ulmn
	N. F. Maroney
	G. M. Simmons

E-SYSTEMS

Barbara Jones
Mauricia Hawkins
Becky Harris

and express special thanks to E. C. O'Hara.

VOLUME COMPOSITION

VOLUME I (MAIN TEXT)

REPORT PERSPECTIVE AND GUIDE

I. FMDF SOLAR THERMAL ELECTRIC POWER PLANT CONCEPT
II. SITE ANALYSIS -- CONSTRAINTS FOR A RELEVANT SYSTEM
III. CROSBYTON NOMINAL SYSTEM DESCRIPTION
IV. OPTICAL-THERMAL-FLUID ANALYSIS
V. NOMINAL CONCENTRATOR SUBSYSTEM
VI. NOMINAL RECEIVER SUBSYSTEM
VII. POWER GENERATION SUBSYSTEM FOR THE NOMINAL SYSTEM
VIII. THERMAL STORAGE SYSTEM CONCEPT
IX. CONTROL SUBSYSTEMS FOR THE NOMINAL SYSTEM
X. EXPECTED PERFORMANCE OF THE NOMINAL SYSTEM
XI. EXPECTED COSTS FOR NOMINAL SYSTEM
XII. NOMINAL SYSTEM ECONOMICS
XIII. POSSIBLE IMPROVEMENTS FOR A RECOMMENDED SYSTEM
XIV. OVERALL ASSESSMENT

VOLUME II (APPENDICES A - H)

A. MONTHLY STATISTICS OF THE CROSBYTON LOAD
B. BORING LOGS FOR SOIL ANALYSIS AT CROSBYTON SITE
C. OPTICAL ANALYSIS
D. OPTICAL ANALYSIS BY E-SYSTEMS
E. DEVELOPMENT OF THE RECEIVER THERMAL-FLUID MODEL
F. E-SYSTEMS OVERALL RECEIVER THERMAL ANALYSIS
G. RECEIVER THERMAL STRESS ANALYSIS AND MATERIAL
H. OVERALL COLLECTOR ANALYSIS

VOLUME III (APPENDICES I - M)

I. CONCENTRATOR ANALYSIS
J. RECEIVER ANALYSIS
K. CONTROL AND SYSTEM MANAGEMENT
L. SYSTEMS ANALYSIS AND SIMULATION
M. PANEL DEVELOPMENT AND MIRROR REFLECTIVITY

DETAILED TABLE OF CONTENTS

FOR

VOLUME II

VOLUME COMPOSITION	II.i
BRIEF TABLE OF CONTENTS FOR VOLUME I	II.vii
BRIEF TABLE OF CONTENTS FOR VOLUME III	II.x
FIGURE LIST FOR VOLUME II	II.xii
TABLE LIST FOR VOLUME II	II.xxi

CONTENTS, VOL. II (cont.)

			Page
APPENDIX A	MONTHLY STATISTICS OF THE CROSBYTON LOAD BY HOUR FOR THE BASE YEAR (August 15, 1975 - August 13, 1976)		
APPENDIX B	BORING LOGS FOR SOIL ANALYSIS AT CROSBYTON SITE		
APPENDIX C	OPTICAL ANALYSIS		
	C-1	THE SOLAR MODEL	C-2
	C-2	BASIC EXPRESSIONS FOR OPTICAL POWER CONCENTRATIONS	C-9
	C-3	COMPUTATION METHOD FOR SPHERICAL SEGMENT REFLECTORS	C-15
	C-4	POINT SUN CONCENTRATIONS AND THE STRUCTURE RELATIONS	C-20
	C-5	FINITE SUN CONCENTRATIONS	C-31
	C-6	CONSTRAINTS ON THE INTEGRATION FOR FINITE SUN CONCENTRATION	C-38
	C-7	AN EFFECTIVE SUN SIZE METHOD TO ACCOUNT FOR MIRROR ERRORS	C-47
	C-8	OPTICAL CONCENTRATION RESULTS FOR ALIGNED CONICAL RECEIVERS	C-68
		C-8.1 Symmetric Distributions	C-70
		C-8.2 Asymmetric Distributions	C-86
		C-8.3 Pertinence of 30° and 60° Inclinations	C-107
		C-8.4 Comparison of Results	C-107
	C-9	OPTICAL CONCENTRATION ON THE MIRROR SURFACE	C-107
	C-10	RELATIONSHIP OF THE OPTICAL ANALYSIS OF E-SYSTEMS TO THE PRESENT METHOD	C-125

		Page
APPENDIX D	OPTICAL ANALYSIS BY E-SYSTEMS	
D-1	METHODOLOGY	D-3
D-2	AXISYMMETRIC OPTICAL CONCENTRATIONS ON A CONICAL RECEIVER	D-11
D-3	NON-AXISYMMETRIC OPTICAL CONCENTRATIONS ON A CONICAL RECEIVER	D-24
APPENDIX E	DEVELOPMENT OF THE RECEIVER THERMAL-FLUID MODEL	
E-1	PHYSICAL PROPERTY CORRELATIONS FOR WATER AND CALORIA HT-43	E-5
E-2	CORRELATIONS FOR THE INTERNAL HEAT TRANSFER COEFFICIENTS	E-5
E-2.1	Liquid Forced Convection	E-11
E-2.2	Fully-Developed Flow Boiling	E-13
E-2.3	Steam Superheating Region	E-14
E-3	STEAM SUPERHEATING REGION	E-15
E-4	ESTIMATION OF FLUID PRESSURE DROPS	E-18
E-5	PARAMETERS AFFECTING STEAM-GENERATING RECEIVERS	E-21
E-6	PARAMETERS AFFECTING HOT OIL RECEIVERS IN DUAL FLUID SYSTEMS	E-27
E-7	EFFECTS OF INCLUDING MULTIPLE REFLECTION COMPONENTS	E-29
APPENDIX F	E-SYSTEMS OVERALL RECEIVER THERMAL ANALYSIS	
F-1	OVERALL RECEIVER THERMAL ANALYSIS	F-1
F-2	COMPUTER CODE	F-13
F-3	WATER/STEAM RESULTS	F-16

CONTENTS, VOL. II (cont.) Page

F-4	OIL RESULTS	F-25
F-5	900 PSI NOMINAL PROTOTYPE STEAM SYSTEM RESULTS	F-27
F-6	DETAILED RECEIVER INTERNAL HEAT TRANSFER AND PRESSURE DROP STUDIES	F-31
F-7	TUBE TEMPERATURE DISTRIBUTIONS	F-34
F-8	STEADY STATE TUBE TEMPERATURES FOR A STEAM SYSTEM	F-37
F-9	TRANSIENT TUBE TEMPERATURES FOR A STEAM SYSTEM	F-52
F-10	STEADY STATE TUBE TEMPERATURES FOR AN OIL SYSTEM	F-56
F-11	INTERNAL CONVECTION AND PRESSURE DROP FOR A WATER/STEAM SYSTEM	F-59
F-12	HEATING OF THE WATER REGION	F-60
F-13	HEATING OF THE VAPOR (SUPERHEATING REGION)	F-63
F-14	BOILING IN THE TWO-PHASE FLOW REGION	F-65
F-15	SUMMARY OF PRESSURE DROPS FOR THE PROTOTYPE RECEIVER	F-70
F-16	SCALING TECHNIQUES FOR INTERNAL CONVECTION AND PRESSURE DROP FOR WATER/STEAM SYSTEMS	F-71
F-17	INTERNAL CONVECTION AND PRESSURE DROP FOR AN OIL SYSTEM	F-77
F-18	NOMINAL RECEIVER CONFIGURATION	F-79

APPENDIX G RECEIVER THERMAL STRESS ANALYSIS AND MATERIAL SELECTION

G-1	TTU ANALYSIS	G-1
G-2	E-SYSTEMS ANALYSIS	G-2

CONTENTS, VOL. II (cont.)

			Page
APPENDIX H	OVERALL COLLECTOR ANALYSIS		
	H-1	METHODOLOGY	H-1
	H-2	HOURLY AND DAILY RESULTS	H-4
	H-3	ANNUAL RESULTS	H-11

BRIEF TABLE OF CONTENTS FOR VOLUME I

		Page
REPORT PERSPECTIVE AND GUIDE		1
I.	FIXED MIRROR DISTRIBUTED FOCUS SOLAR THERMAL ELECTRIC POWER PLANT CONCEPT	
I-A	CONCENTRATOR SUBSYSTEM	I-3
I-B	RECEIVER SUBSYSTEM	I-8
I-C	POWER GENERATOR SUBSYSTEM	I-10
I-D	ENERGY STORAGE SUBSYSTEM	I-11
I-E	CONTROL SUBSYSTEM	I-11
II.	SITE ANALYSIS -- CONSTRAINTS FOR A RELEVANT SYSTEM	
II-A	OVERVIEW	II-1
II-B	THE CROSBYTON POWER SYSTEM CHARACTERISTICS	II-4
II-C	SOIL CHARACTERISTICS AT THE CROSBYTON SITE	II-11
II-D	CLIMATOLOGICAL CHARACTERISTICS of CROSBYTON	II-22
III.	CROSBYTON NOMINAL SYSTEM DESCRIPTION	
IV.	OPTICAL-THERMAL-FLUID ANALYSIS	
IV-A	OPTICAL ANALYSIS	IV-2
IV-B	RECEIVER THERMAL-FLUID ANALYSIS	IV-15
V.	NOMINAL CONCENTRATOR SUBSYSTEM	
V-A	APPROACH	V-1

BRIEF CONTENTS, VOL. I (cont.)

Page

V-B SITE RELATED FACTORS V-3

V-C NOMINAL CONCENTRATOR GEOMETRY V-4

V-D CONCENTRATOR WIND LOAD DISTRIBUTION V-7

V-E REFLECTIVE MATERIALS V-9

V-F CONCENTRATOR PANELS V-11

V-G PANEL SUPPORT STRUCTURES V-16

V-H CONCENTRATOR ERROR ANALYSIS V-24

VI. NOMINAL RECEIVER SUBSYSTEM

VI-A RECEIVER DEFINITION VI-1

VI-B THERMAL STRESS ANALYSIS OF RECEIVER TUBES VI-4

VI-C RECEIVER SUPPORT STRUCTURE VI-5

VI-D ADVANTAGES AND WEIGHT OF CANTILEVERED POLAR MOUNTED RECEIVER SUPPORT VI-12

VI-E HEAT TRANSFER FLUID LOOP VI-15

VII. POWER GENERATION SUBSYSTEM FOR THE NOMINAL SYSTEM

VII-A THERMO DYNAMIC CYCLE SELECTION SYSTEM VII-1

VII-B EQUIPMENT SELECTION -- CONVENTIONAL POWER PLANT VII-6

VIII. THERMAL STORAGE SYSTEM CONCEPT

IX. CONTROL SUBSYSTEMS FOR THE NOMINAL SYSTEM

BRIEF CONTENTS, VOL. I (cont.)

			Page
X.	EXPECTED PERFORMANCE OF THE NOMINAL SYSTEM		
	X-A	SYSTEM PERFORMANCE STUDIES	X-1
	X-B	SYSTEM PERFORMANCE RESULTS	X-4
XI.	EXPECTED COSTS FOR NOMINAL SYSTEM		
	XI-A	NOMINAL APERTURE DIAMETER SELECTION	XI-1
	XI-B	DETAILED COST ANALYSIS FOR NOMINAL COLLECTOR	XI-3
	XI-C	DETAILED COSTS FOR THE NOMINAL CONVENTIONAL POWER PLANT	XI-10
	XI-D	COSTS BY OPTION FOR NOMINAL TOTAL SOLAR POWER PLANT	XI-22
XII.	NOMINAL SYSTEM ECONOMICS		
	XII-A	METHODOLOGY	XII-1
	XII-B	ANNUALIZED SYSTEM RESULTANT COST	XII-4
	XII-C	ECONOMIC MODELING-BUSBAR ENERGY COSTS	XII-8
	XII-D	CONCLUSIONS	XII-19
XIII.	POSSIBLE IMPROVEMENTS FOR A RECOMMENDED SYSTEM		
XIV.	OVERALL ASSESSMENT		

BRIEF TABLE OF CONTENTS FOR VOLUME III

			Page
APPENDIX I	CONCENTRATOR ANALYSIS		
	I-1	INTRODUCTION	I-1
	I-2	REFLECTIVE MATERIALS	I-18
	I-3	PANELS	I-37
	I-4	PANEL SUPPORT STRUCTURE	I-59
	I-5	CONCENTRATOR ERROR ANALYSIS	I-79
APPENDIX J	RECEIVER ANALYSIS		
	J-1	INTRODUCTION	J-1
	J-2	RECEIVER SUPPORT STRUCTURE	J-9
	J-3	HEAT TRANSFER FLUID LOOP	J-65
APPENDIX K	CONTROL AND SYSTEM MANAGEMENT		
	K-1	INTRODUCTION	K-1
	K-2	COLLECTOR CONTROL SUBSYSTEM	K-9
	K-3	SOFTWARE SYSTEM	K-59
	K-4	SITE MANAGEMENT	K-79
APPENDIX L	SYSTEMS ANALYSIS AND SIMULATION		
	L-1	IDENTIFICATION OF SYSTEM CONFIGURATION	L-1
	L-2	OVERALL SYSTEM PERFORMANCE METHODOLOGY	L-12
	L-3	ANNUAL SYSTEM PERFORMANCE	L-14

BRIEF CONTENTS, VOL. III (cont.)

			Page
APPENDIX M	PROTOTYPE PANEL DEVELOPMENT, FABRICATION AND TESTING AND MIRROR REFLECTIVITY MEASUREMENTS		
	M-1	PANELS	M-1
	M-2	MIRROR REFLECTIVITY MEASUREMENTS	M-17

FIGURE LIST FOR VOLUME II

Figure		Page
C-1	Element of Area dA on Sun Illuminates Element of Area dA on the Earth	C-4
C-2	Generalized Mirror Geometry	C-11
C-3	Hemispherical Dish Multiple Reflection Geometry	C-16
C-4	Generalized Receiver Geometry and Sun Cone	C-19
C-5	Multiple Contributions to the Single Bounce Concentration	C-22
C-6	Spherical Mirror Structure Relation for n=1	C-25
C-7	Spherical Mirror Structure Relation for n=2	C-26
C-8	Spherical Mirror Structure Relation for n=3	C-27
C-9	Spherical Mirror Structure Relation for n=4	C-28
C-10	Spherical Mirror Structure Relation for n=5	C-29
C-11	Geometry Associated With Integration Over Finite Sun, Case A	C-34
C-12	Geometry Associated With Integration Over Finite Sun, Case B	C-35
C-13	Illustration of Concept of θ Constraints	C-39
C-14	Exploded β-axis Indicating Integration Ranges	C-43
C-15	Flow Chart for Application of Constraints	C-45
C-16	Reflection Error in the Ray Plane and Transverse Plane, due to Mirror Errors	C-51
C-17	Analysis of Ray Plane Error	C-53
C-18	Analysis of Transverse Plane Error	C-54
C-19	Normalized Effective Sun Size σ_n/σ for δ=0.10 (Silvered Glass)	C-63
C-20	Normalized Effective Sun Size σ_n/σ for δ=0.35	C-66

Figure		Page
C-21	Geometry of Conical Absorber	C-69
C-22	Symmetric Concentration Distribution on Receiver With $\psi_o = \sigma = 0.5^\circ$, R=1.0, $\theta_{rim}=90^\circ$	C-71
C-23	Detail of n=1 Peak	C-73
C-24	Detail of n=2 Peak	C-74
C-25	Symmetric Concentration Distribution on Receiver With $\psi_o=1.0^\circ$, $\sigma=0.5^\circ$, R=1.0, $\theta_{rim}=90^\circ$	C-76
C-26	Symmetric Concentration Distribution on Receiver With $\psi_o=1.5^\circ$, $\sigma=0.5^\circ$, R=1.0, $\theta_{rim}=90^\circ$	C-77
C-27	Symmetric Concentration Distribution on Receiver With $\psi_o = \sigma = 0.25^\circ$, R=1.0, $\theta_{rim}=90^\circ$	C-78
C-28	Symmetric Concentration Distribution on Receiver With $\psi_o = 0.5^\circ$, $\sigma = 0.25^\circ$, R=1.0, $\theta_{rim}=90^\circ$	C-79
C-29	Symmetric Concentration Distribution on Receiver With $\psi_o = 0.75^\circ$, $\sigma = 0.25^\circ$, R=1.0, $\theta_{rim}=90^\circ$	C-80
C-30	Symmetric Concentration Distribution on Receiver With $\psi_o = \sigma = 0.5^\circ$, R=0.88, $\theta_{rim}=90^\circ$	C-82
C-31	Symmetric Concentration Distribution on Receiver With $\psi_o = 0.5^\circ$, $\sigma = 0.25^\circ$, R=0.88, $\theta_{rim}=90^\circ$	C-83
C-32	Integrated Flux Distribution as Function of Position on Receiver With $\psi_o = \sigma = 0.50^\circ$, R=1.0, $\theta_{rim}=90^\circ$	C-84
C-33	Integrated Flux Distribution as Function of Position on Receiver With $\psi_o = \sigma = 0.5^\circ$, R=0.88, $\theta_{rim}=90^\circ$	C-85
C-34	Integrated Flux Distribution as Function of Position on Receiver With $\psi_o = 0.50^\circ$, $\sigma = 0.25^\circ$, R=1.0, $\theta_{rim}=90^\circ$	C-87

Figure		Page
C-35	Integrated Flux Distribution as Function of Position on Receiver with $\psi_0 = 0.50^0$, $\sigma = 0.25^0$, $R = 0.88$, $\theta_{rim}=90^0$	C-88
C-36	Concentration Distribution at $\phi_0= 0$ With $\psi_0=\sigma=0.5^\circ$, $R=1.0$, $\theta_{rim}=60^\circ$, and Solar Inclination 30°	C-89
C-37	Concentration Distribution at $\phi_0=30^\circ$ With $\psi_0=\sigma=0.5^\circ$, $R=1.0$, $\theta_{rim}=60^\circ$, and Solar Inclination $= 30^\circ$	C-90
C-38	Concentration Distribution at $\phi_0=60^\circ$ With $\psi_0=\sigma=0.5^\circ$, $R=1.0$, $\theta_{rim}=60^\circ$, and Solar Inclination $= 30^\circ$	C-91
C-39	Concentration Distribution at $\phi_0=90^\circ$ With $\psi_0=\sigma=0.5^\circ$, $R=1.0$, $\theta_{rim}=60^\circ$, and Solar Inclination $= 30^\circ$	C-92
C-40	Concentration Distribution at $\phi_0=120^\circ$ With $\psi_0=\sigma=0.5^\circ$, $R=1.0$, $\theta_{rim}=60^\circ$, and Solar Inclination $= 30^\circ$	C-93
C-41	Concentration Distribution at $\phi_0=150^\circ$ With $\psi_0=\sigma=0.5^\circ$, $R=1.0$, $\theta_{rim}=60^\circ$, and Solar Inclination $= 30^\circ$	C-94
C-42	Concentration Distribution at $\phi_0=180^\circ$ With $\psi_0=\sigma=0.5^\circ$, $R=1.0$, $\theta_{rim}=60^\circ$, and Solar Inclination $= 30^\circ$	C-95
C-43	Concentration Distribution at $\phi_0=0^\circ$ With $\psi_0=\sigma=0.5^\circ$, $R=1.0$, $\theta_{rim}=60^\circ$, and Solar Inclination $= 60^\circ$	C-97
C-44	Concentration Distribution at $\phi_0=30^\circ$ With $\psi_0=\sigma=0.5^\circ$, $R=1.0$, $\theta_{rim}=60^\circ$, and Solar Inclination $= 60^\circ$	C-98
C-45	Concentration Distribution at $\phi_0=60^\circ$ With $\psi_0=\sigma=0.5^\circ$, $R=1.0$, $\theta_{rim}=60^\circ$, and Solar Inclination $= 60^\circ$	C-99
C-46	Concentration Distribution at $\phi_0=90^\circ$ With $\psi_0=\sigma=0.5^\circ$, $R=1.0$, $\theta_{rim}=60^\circ$, and Solar Inclination $= 60^\circ$	C-100
C-47	Concentration Distribution at $\phi_0=120^\circ$ With $\psi_0=\sigma=0.5^\circ$, $R=1.0$, $\theta_{rim}=60^\circ$, and Solar Inclination $= 60^\circ$	C-101

Figure		Page
C-48	Concentration Distribution at ϕ_0=150° With $\psi_0=\sigma=0.5°$, R=1.0, θ_{rim}=60°, and Solar Inclination = 60°	C-102
C-49	Concentration Distribution at ϕ_0=180° With $\psi_0=\sigma=0.5$, R=1.0, θ_{rim}=60°, and Solar Inclination = 60°	C-103
C-50	Azimuthal Concentration Distribution for Various Values of q With $\psi_0=\sigma=0.50°$, R=1.0, θ_{rim}=60°, and Solar Inclination = 30°	C-104
C-51	Azimuthal Concentration Distribution for Various Values of q With $\psi_0=\sigma=0.50°$, R=1.0, θ_{rim}=60°, and Solar Inclination = 60°	C-105
C-52	Iso-inclination Plot for 1977	C-108
C-53	Detail of n = 1 Peak	C-109
C-54	Semispherical Collector Geometry for Determining Mirror "Hot Spot"	C-113
C-55	Concentration on Mirror Surface at ψ_0=0	C-118
C-56	Mirror "Hot Spot" Concentration for Individual Bounces for True Sun Size, σ= 0.25°	C-119
C-57	Mirror "Hot Spot" Concentration as a Function of ψ_0 for True Sun Size σ = 0.25°	C-120
C-58	Mirror "Hot Spot" Concentration for Individual Bounces for Effective Sun Size σ = 0.5°	C-121
C-59	Mirror "Hot Spot" Concentration as a Function of ψ_0 for Effective Sun Size σ = 0.5°	C-122
D-1	Mirror Hot Spot Geometry	D-4
D-2	Integration Limits for Mirror Hot Spot	D-7
D-3	Error Treatment by Cone Enlargement	D-9
D-4	FMDF Receiver Geometry	D-12

FIGURE LIST, VOL. II (cont.)

Figure		Page
D-5	Cone Intercept Geometry	D-14
D-6	Reflected Ray Cone Intercepts	D-16
D-7	Axisymmetric Flux Distribution	D-23
D-8	Non-Normal Incidence Effects	D-25
D-9	Individual Cone Intercept	D-27
D-10	Physical Limits on ϕ	D-30
D-11	Three-Dimensional Concentration Distribution (ϕ_i = 30°)	D-33
D-12	Three-Dimensional Concentration Distribution (θ_i=60°)	D-34
E-1	Schematic of TTU Thermo-Fluid Receiver Model	E-2
E-2	Schematic Flow Chart of Receiver Thermo-Fluid Analysis	E-3
E-3	Fluid Temperatures, Heat Transfer Regime, of Averaged Outside Wall Temperatures	E-12
E-4	Typical Variation of Internal Heat Transfer Coefficient Along the Receiver	E-16
E-5	Effect of Entering Fluid Temperature on Mass Flow Rate Per Tube & Total Thermal Losses	E-22
E-6	Effect of Number of Tubes on the Cumulative Pressure Drop	E-24
E-7	Development of Pressure Drop as a Function of Receiver Position & Fluid State	E-25
E-8	Effect of Number of Tubes on the Outside Averaged Wall Temperature	E-26
E-9	Effect of Flow Rate on the Inside Tube Wall Temperature Using Caloria HT-43	E-28

FIGURE LIST, VOL. II (cont.)

Figure		Page
E-10	Effect of Flow Direction on Inside Wall Temperature, Caloria HT-43	E-30
E-11	Pressure Drop in a Dual Fluid System, Caloria HT-43	E-31
E-12	Comparison of Outside Wall Temperatures for Single Bounce and Multiple Bounce Symmetric Input	E-33
E-13	Variation of Outside Wall Temperature Around the Receiver at a 30° Sun Angle (Caustic Region)	E-34
F-1	Receiver Thermal Analysis Methodology	F-2
F-2	Receiver Fluid and Surface Temperatures for 0° Concentrator Incidence Angle Versus Position on Receiver	F-18
F-3	Receiver Fluid Temperatures for 0°, 30°, and 60° Dish Incidence Angle Versus Position on Receiver	F-19
F-4	Receiver Enthalpy for 0°, 30°, and 60° Concentrator Incidence Angle Versus Position on Receiver	F-21
F-5	Receiver Fluid and Surface Temperatures for 60° Concentrator Incidence Angle Versus Position (x/R=.55 to .5) on Receiver	F-22
F-6	Receiver Net Heat Loss Per Unit Aperture Area Versus Concentrator Incidence Angle	F-23
F-7	Receiver Efficiency Versus Concentrator Incidence Angle	F-24
F-8	Receiver Fluid Temperature and Enthalpy Versus Position on Receivers (Three 100ft. Aperture Concentrators in Series)	F-26

Figure		Page
F-9	Receiver Net Heat Loss Per Unit Aperture Area Versus Oil Temperature	F-28
F-10	Receiver Fluid and Surface Temperatures for 0° Concentrator Incidence Angle Versus Position on Receiver for 900 PSI Steam	F-29
F-11	Receiver Enthalpy for 0 Concentrator Incidence Angle Versus Position on Receiver for 900 PSI Steam	F-30
F-12	Thermal Model of the Receiver Tubes	F-36
F-13	Steady State Steam Tube Temperatures (0.10 inch I.D. and h_i = 1000.0 BTU/hr. ft.^{2} °F)	F-38
F-14	Steady State Steam Tube Temperatures (0.10 inch I.D. and h_i = 500.0 BTU/hr. ft.^{2} °F)	F-39
F-15	Steady State Steam Tube Temperatures (0.10 inch I.D. and h_i = 250.0 BTU/hr. ft.^{2} °F)	F-40
F-16	Steady State Steam Tube Temperatures (0.10 inch I.D. and h_i = 100.0 BTU/hr. ft.^{2} °F)	F-41
F-17	Steady State Steam Tube Temperatures (0.25 inch I.D. and h_i = 1000.0 BTU/hr. ft.^{2} °F)	F-43
F-18	Steady State Steam Tube Temperatures (0.25 inch I.D. and h_i = 500.0 BTU/hr. ft.^{2} °F)	F-44
F-19	Steady State Steam Tube Temperatures (0.25 inch I.D. and h_i = 250 BTU/hr. ft.^{2} °F)	F-45
F-20	Steady State Steam Tube Temperatures (0.25 inch I.D. and h_i = 100.0 BTU/hr. ft.^{2} °F)	F-46

Figure		Page
F-21	Steady State Steam Tube Temperatures (0.50 inch I.D. and h_i = 1000.0 BTU/hr. ft.^{2} °F)	F-47
F-22	Steady State Steam Tube Temperatures (0.50 inch I.D. and h_i = 500.0 BTU/hr. ft.^{2} °F)	F-48
F-23	Steady State Steam Tube Temperatures (0.50 inch I.D. and h_i = 250.0 BTU/hr. ft.^{2} °F)	F-49
F-24	Steady State Steam Tube Temperatures (0.50 inch I.D. and h_i = 100.0 BTU/hr. ft.^{2} °F)	F-50
F-25	Summary of Steady State Steam Tube Temperatures	F-51
F-26	Maximum Steam Tube Surface Temperatures Under Transient Water Shut-Off Conditions	F-53
F-27	Transient Steam Tube Temperatures After 12 Seconds (0.25 inch I.D. and h_i = 1000 BTU/hr. ft.^{2} °F)	F-54
F-28	Transient Steam Tube Temperatures After 12 Seconds (0.25 inch I.D. and h_i = 250.0 BTU/hr.ft.^{2} °F)	F-55
F-29	Steady State Oil Tube Temperatures (0.50 inch I.D. and h_i = 800.0 BTU/hr. ft.^{2} °F)	F-57
F-30	Steady State Oil Tube Temperatures (0.50 inch I.D. and h_i = 500.0 BTU/hr.ft.^{2} °F)	F-58
F-31	Tube Internal Convection Coefficient Versus Position on the Prototype Receiver	F-62
F-32	Heat Transfer and Number of Tubes for Various Tube Diameters to Maintain $\Delta P_{\text{full flow superheat}}$ = 100 psi	F-73
F-33	Heat Transfer and Number of Tubes for Various Tube Diameters to Maintain $\Delta P_{\text{full flow supperheat}}$ = 50 psi	F-74

FIGURE LIST, VOL. II (cont.)

Figure		Page
F-34	Heat Transfer and Number of Tubes for Various Tube Diameters to Maintain $\Delta P_{\text{full flow superheat}} = 200$ psi	F-75
F-35	Heat Transfer and Pressure Drop for Various Tube Diameters for Single Tube on Receiver	F-76
F-36	Internal Convection Coefficients and Pressure Drops for the Prototype Oil System	F-80
F-37	Nominal Receiver for the 200-foot Concentrator	F-82
G-1	Thermal Gradient Tube Model	G-4
H-1	Hourly Performance of FMDF Solar Collector	H-6
H-2	Hourly Collection Efficiency for FMDF Collector at 15° Tilt and Steam Generation at 950°F	H-8
H-3	Heat Collection Analysis	H-12
H-4	Annual Energy Collected by FMDF Solar Collector vs. Tilt Angle	H-14

TABLE LIST FOR VOLUME II

Table		Page
A-1/A-12	Statistical Summary of Crosbyton Demand for Months 1-12 of Base Year	A-1/A-12
B-1/B-17	Boring Logs 1-17 for Soil Analysis at Crosbyton Site	B-1/B-19
C-1	Normalized Effective Sun Size $\sigma m/\sigma$ for $\delta = 0.10$	C-62
C-2	Normalized Effective Sun Size $\sigma m/\sigma$ for $\delta = 0.35$	C-65
C-3	Comparison of Selected Concentration Values for Solar Inclination of 30°	C-110
C-4	Comparison of Selected Concentration Values for Solar Inclination of 60°	C-111
E-1	Physical Property Correlations for Saturated Water Vapor	E-6
E-2	Physical Property Correlations for Saturated Liquid Water	E-8
E-3	Physical Properties of Caloria HT-43	E-10
G-1	E-Systems Thermal Stress Analysis for Receiver Tubes (Inconel 718)	G-6
H-1	Daily Average Tracking Efficiency, Absorber Thermal Loss Factor, and Whole Day Collection Efficiency for the FMDF Solar Collector	H-10

APPENDICES

A. MONTHLY STATISTICS OF THE CROSBYTON LOAD BY HOUR.

B. BORING LOGS FOR SOIL ANALYSIS

C. OPTICAL ANALYSIS

D. OPTICAL ANALYSIS BY E-SYSTEMS

E. DEVELOPMENT OF THE RECEIVER THERMAL-FLUID MODEL

F. E-SYSTEMS OVERALL RECEIVER THERMAL ANALYSIS

G. RECEIVER THERMAL STRESS ANALYSIS AND MATERIALS SELECTION

H. OVERALL COLLECTOR ANALYSIS

I. CONCENTRATOR ANALYSIS

J. RECEIVER ANALYSIS

K. CONTROL AND SYSTEM MANAGEMENT

L. SYSTEMS ANALYSIS AND SIMULATION

M. PROTOTYPE PANEL DEVELOPMENT, FABRICATION AND TESTING PROJECT AND MIRROR TEST

APPENDIX A

MONTHLY STATISTICS OF THE CROSBYTON LOAD

BY HOUR

FOR THE BASE YEAR

(AUGUST 15, 1975 - AUGUST 13, 1976)

STATISTICAL SUMMARY OF CROSBYTON DEMAND FOR
MONTH 1 OF BASE YEAR

HOUR	MEAN	STD DEV	MAX FOR HOUR	MIN FOR HOUR
1	875.61	142.02	1304	599
2	815.59	106.54	1009	578
3	794.94	106.11	1009	561
4	776.29	98.92	957	561
5	808.77	92.43	957	617
6	859.68	88.35	1028	656
7	1027.35	128.63	1244	729
8	1254.19	163.80	1499	864
9	1378.19	184.15	1685	902
10	1470.46	233.91	1810	808
11	1589.74	231.61	1897	902
12	1571.94	250.81	1651	845
13	1553.59	299.38	2205	845
14	1674.81	300.45	2049	845
15	1719.68	312.63	2099	808
16	1693.52	300.84	2035	826
17	1655.59	288.54	2035	902
18	1586.94	265.40	1996	892
19	1544.15	242.88	1939	902
20	1598.25	237.94	1996	1013
21	1494.45	240.37	1906	883
22	1270.64	198.60	1649	751
23	1041.29	144.88	1259	695
24	932.03	145.92	1237	620

STATISTICAL SUMMARY OF CROSBYTON DEMAND FOR
MONTH 2 OF BASE YEAR

HOUR	MEAN	STD DEV	MAX FOR HOUR	MIN FOR HOUR
1	674.93	76.82	941	563
2	661.97	71.25	898	579
3	645.55	71.44	907	563
4	640.67	48.37	834	581
5	690.83	61.03	932	620
6	754.20	60.58	978	621
7	989.73	116.95	1228	684
8	1097.93	104.34	1334	833
9	1138.50	153.73	1427	674
10	1202.13	177.04	1611	789
11	1250.13	167.21	1603	936
12	1193.10	176.73	1598	881
13	1257.17	217.40	1737	920
14	1267.67	235.86	1795	919
15	1281.17	252.39	1790	871
16	1287.40	259.16	1828	871
17	1241.93	235.98	1771	833
18	1201.20	213.85	1659	833
19	1331.33	187.18	1815	996
20	1297.78	187.68	1766	1017
21	1158.27	171.80	1574	876
22	993.63	159.13	1368	775
23	822.47	111.12	1092	642
24	728.83	82.45	946	600

STATISTICAL SUMMARY OF CROSBYTON DEMAND FOR
MONTH 3 OF BASE YEAR

HOUR	MEAN	STD DEV	MAX FOR HOUR	MIN FOR HOUR
1	670.45	44.07	789	601
2	654.00	31.13	722	602
3	540.58	26.42	722	603
4	638.77	29.28	683	583
5	667.39	29.78	737	610
6	732.52	51.97	852	600
7	886.61	109.11	1103	718
8	1198.90	220.07	1579	801
9	1276.90	230.77	1677	855
10	1313.71	207.11	1636	855
11	1326.42	209.75	1677	894
12	1233.48	220.02	1646	816
13	1189.65	202.95	1647	877
14	1248.06	214.58	1706	836
15	1294.10	228.09	1725	855
16	1274.97	236.17	1706	879
17	1260.58	218.47	1686	879
18	1269.35	229.77	1833	970
19	1301.94	215.62	1775	1028
20	1220.65	172.91	1736	994
21	1125.58	119.36	1563	959
22	1007.68	156.16	1602	814
23	828.03	94.67	1118	678
24	709.32	54.82	816	601

STATISTICAL SUMMARY OF CROSBYTON DEMAND FOR
MONTH 4 OF BASE YEAR

HOUR	MEAN	STD DEV	MAX FOR HOUR	MIN FOR HOUR
1	906.70	187.10	1208	661
2	861.00	196.06	1169	644
3	827.23	178.94	1139	624
4	842.90	190.41	1179	625
5	853.25	194.45	1139	623
6	944.93	209.75	1243	683
7	960.30	233.76	1286	587
8	1282.15	224.51	1791	776
9	1486.23	185.76	2010	873
10	1487.10	183.63	1786	912
11	1540.50	171.13	1737	854
12	1468.17	192.03	1754	912
13	1418.23	195.01	1695	912
14	1551.73	201.15	1620	873
15	1538.35	182.40	1601	873
16	1558.97	153.02	1601	834
17	1557.10	188.37	1620	834
18	1583.00	220.53	1930	912
19	1562.00	151.35	1756	1135
20	1455.93	177.91	1698	1147
21	1378.53	197.52	1639	1075
22	1275.10	191.85	1672	942
23	1103.77	178.99	1377	841
24	935.27	177.76	1218	722

STATISTICAL SUMMARY OF CROSBYTON DEMAND FOR
MONTH 5 OF BASE YEAR

HOUR	MEAN	STD DEV	MAX FOR HOUR	MIN FOR HOUR
1	748.98	36.38	824	684
2	714.68	35.11	827	672
3	727.55	49.70	867	644
4	717.23	40.70	788	644
5	734.29	37.82	790	672
6	787.19	39.58	886	722
7	821.01	117.92	1221	584
8	1066.55	215.46	1672	785
9	1192.01	217.45	1772	883
10	1213.58	211.32	1767	818
11	1245.07	237.55	1747	759
12	1253.81	231.75	1769	779
13	1101.27	222.47	1603	681
14	1127.33	236.71	1672	603
15	1069.05	206.33	1613	584
16	1062.13	204.75	1613	603
17	1070.08	208.20	1730	642
18	1269.74	212.78	2004	779
19	1256.23	188.77	1412	876
20	1219.45	120.56	1454	779
21	1172.58	101.22	1349	779
22	1085.51	82.84	1218	779
23	940.52	73.31	1174	829
24	812.00	51.52	951	730

STATISTICAL SUMMARY OF CROSBYTON DEMAND FOR
MONTH 6 OF BASE YEAR

HOUR	MEAN	STD DEV	MAX FOR HOUR	MIN FOR HOUR
1	708.87	46,43	781	617
2	674.05	31,27	727	617
3	673.29	42,42	748	579
4	677.74	44,73	799	611
5	681.58	47,88	780	613
6	754.71	53,42	843	611
7	850.45	61,80	1030	739
8	1078.03	125,98	1301	844
9	1167.03	120,05	1384	859
10	1191.90	105,36	1340	903
11	1215.53	114,21	1383	879
12	1206.65	111.61	1427	903
13	1125.13	103,12	1286	879
14	1112.10	112.31	1286	829
15	1059.65	108,32	1228	771
16	1042.52	112,23	1208	752
17	1049.55	99,79	1210	790
18	1138.90	115,47	1317	906
19	1242.29	73,54	1363	1093
20	1189.13	76,76	1348	1074
21	1140,39	57,69	1232	1039
22	1047.29	53.79	1154	953
23	864.52	53,67	944	751
24	745,97	42,51	826	644

STATISTICAL SUMMARY OF CROSBYTON DEMAND FOR MONTH 7 OF BASE YEAR

HOUR	MEAN	STD DEV	MAX FOR HOUR	MIN FOR HOUR
1	694.33	46.55	789	629
2	670.97	47.03	769	579
3	672.48	35.59	750	620
4	664.97	36.90	766	596
5	676.93	39.62	750	617
6	715.76	42.05	827	636
7	818.06	66.59	966	671
8	1042.24	113.34	1199	771
9	1153.21	132.48	1337	809
10	1166.10	117.99	1331	866
11	1212.41	135.17	1376	886
12	1195.24	125.19	1339	866
13	1108.75	110.56	1252	847
14	1103.75	125.27	1307	809
15	1055.63	100.29	1179	813
16	1043.72	111.39	1193	779
17	1043.52	125.72	1300	759
18	1072.79	125.42	1339	779
19	1199.34	107.72	1346	837
20	1192.62	73.63	1317	1069
21	1126.97	71.11	1252	974
22	1010.52	67.21	1114	876
23	878.62	73.03	1043	746
24	747.38	52.78	939	674

STATISTICAL SUMMARY OF CROSSYTON DEMAND FOR
MONTH 8 OF BASE YEAR

HOUR	MEAN	STD DEV	MAX FOR HOUR	MIN FOR HOUR
1	684.84	31.55	742	642
2	657.81	31.76	728	584
3	647.16	26.76	744	619
4	648.59	27.95	725	584
5	653.48	30.56	740	618
6	705.61	43.37	784	620
7	721.06	105.91	939	483
8	973.94	103.87	1125	758
9	1095.42	93.50	1252	895
10	1139.53	105.14	1272	895
11	1177.90	123.92	1356	856
12	1176.45	117.09	1377	856
13	1082.53	101.99	1300	856
14	1111.61	125.80	1336	818
15	1030.19	127.66	1336	779
16	1079.55	127.81	1338	781
17	1061.94	107.16	1358	781
18	1060.45	104.46	1474	878
19	1141.16	97.40	1435	976
20	1204.97	61.77	1289	1071
21	1134.06	54.80	1226	1036
22	1022.16	72.88	1206	779
23	860.23	54.20	972	740
24	745.61	43.97	817	642

STATISTICAL SUMMARY OF CROSBYTON DEMAND FOR
MONTH 9 OF BASE YEAR

HOUR	MEAN	STD DEV	MAX FOR HOUR	MIN FOR HOUR
1	638.37	27.55	717	584
2	628.63	28.50	684	564
3	614.53	23.99	677	575
4	612.47	24.36	648	575
5	646.40	43.50	742	575
6	665.03	80.14	805	488
7	879.67	180.56	1154	608
8	1033.40	140.42	1281	743
9	1112.53	128.82	1323	800
10	1134.57	145.59	1382	820
11	1161.77	154.07	1392	813
12	1122.15	145.82	1367	832
13	1112.23	163.24	1421	774
14	1087.67	170.35	1441	735
15	1080.57	178.43	1421	697
16	1068.77	151.08	1402	735
17	1059.37	142.97	1343	774
18	1056.03	140.35	1383	774
19	1055.50	132.65	1324	818
20	1133.30	112.18	1342	878
21	1071.10	112.90	1287	742
22	920.53	94.17	1180	781
23	794.37	94.53	1044	681
24	686.73	42.72	785	623

STATISTICAL SUMMARY OF CROSBYTON DEMAND FOR
MONTH 10 OF BASE YEAR

HOUR	MEAN	STD DEV	MAX FOR HOUR	MIN FOR HOUR
1	756.77	110.53	1038	619
2	723.45	102.98	931	581
3	695.74	98.82	942	581
4	699.65	93.41	923	581
5	739.55	96.00	961	622
6	699.03	118.31	961	505
7	930.48	113.32	1133	701
8	1125.42	195.80	1766	818
9	1209.52	210.07	1766	779
10	1302.51	209.29	1732	856
11	1386.37	227.12	1816	895
12	1343.70	241.22	1835	876
13	1380.37	260.12	1873	818
14	1406.52	265.42	1882	818
15	1431.42	298.05	1997	837
16	1447.10	286.32	2044	934
17	1429.64	302.98	2044	915
18	1372.45	276.12	1943	915
19	1313.52	258.04	1948	915
20	1363.94	232.79	2044	1035
21	1326.25	220.57	1900	974
22	1123.68	179.05	1593	779
23	927.90	158.56	1256	662
24	824.97	117.99	1058	623

STATISTICAL SUMMARY OF CROSBYTON DEMAND FOR
MONTH 11 OF BASE YEAR

HOUR	MEAN	STD DEV	MAX FOR HOUR	MIN FOR HOUR
1	932.77	124.85	1253	737
2	892.13	106.03	1063	717
3	857.37	106.69	1063	682
4	840.00	87.90	1022	696
5	870.97	85.46	1022	735
6	825.77	99.27	1041	523
7	1035.93	102.58	1313	870
8	1204.67	169.28	1561	908
9	1357.97	185.42	1793	1071
10	1471.43	212.56	1864	1071
11	1543.47	218.41	1996	1110
12	1559.17	235.44	1980	1110
13	1593.17	259.94	2028	1052
14	1641.70	261.41	2093	1013
15	1677.53	299.14	2188	993
16	1697.53	306.47	2247	1013
17	1673.50	307.54	2170	1013
18	1622.30	309.07	2123	1013
19	1555.17	276.08	2073	1062
20	1562.00	258.63	2073	1120
21	1565.93	229.76	2073	1169
22	1325.00	196.26	1929	1071
23	1119.40	145.02	1543	876
24	999.13	141.58	1446	779

STATISTICAL SUMMARY OF CROSBYTON DEMAND FOR MONTH 12 OF BASE YEAR

HOUR	MEAN	STD DEV	MAX FOR HOUR	MIN FOR HOUR
1	990.53	99.16	1197	776
2	946.13	86.07	1100	776
3	912.63	84.34	1063	737
4	906.10	81.56	1063	760
5	931.50	68.60	1061	776
6	911.93	80.05	1042	698
7	1084.77	107.00	1343	907
8	1305.13	144.34	1603	1063
9	1470.50	128.89	1696	1255
10	1595.67	159.87	1909	1352
11	1716.87	203.16	2072	1378
12	1723.90	223.49	2176	1372
13	1759.37	214.31	2096	1410
14	1830.68	232.82	2313	1455
15	1874.27	255.96	2366	1449
16	1856.67	268.92	2270	1082
17	1851.93	223.29	2173	1319
18	1794.50	240.36	2231	1184
19	1723.63	221.36	2173	1261
20	1753.63	210.39	2131	1358
21	1688.97	136.49	1905	1339
22	1447.98	150.34	1718	1142
23	1223.77	106.79	1369	990
24	1090.73	102.82	1349	834

APPENDIX B

BORING LOGS FOR SOIL ANALYSIS

AT

CROSBYTON SITE

CROSBYTON SOLAR PROJECT

CROSBYTON, TEXAS

LOG OF BORING NO. 1

DEPTH OF HOLE 30 ft

DEPTH IN FEET	DESCRIPTION OF SOIL	USC	NATURAL MOISTURE	ATTERBERG LIMITS			DEPTH OF PENETRATION VALUE	NO. OF BLOWS		REMARKS
				LL	PL	PI		1st 6"	2nd 6"	
	Dark brown sandy clay	CL	17.2	34	19	15				
	Tan sandy clay with caliche	CL	11.7	25	14	9	5	10	10	
5										
10			20.9	36	16	20	10	12	13	% passing #200 sieve = 58%
			19.0	40	18	22				
15	Light reddish sandy clay	CL					15	9	15	
20	Light green sandy clay with caliche	CL	20.4	41	23	18	20	23	27	% passing #200 sieve = 65%
25	Light green sandy clay with rock	CL	23.9	47	29	18	25	22	26	
30			17.2	37	20	17	30	25	50	% passing #200 sieve = 62%

CROSBYTON SOLAR PROJECT
CROSBYTON, TEXAS

LOG OF BORING NO. 2
DEPTH OF HOLE 30 ft

DEPTH IN FEET	DESCRIPTION OF SOIL	USC	NATURAL MOISTURE	ATTERBERG LIMITS			DEPTH OF PENETRATION VALUE	NO. OF BLOWS		REMARKS
				LL	PL	PI		1st 6"	2nd 6"	
	Dark brown sandy clay	CL	12.3							
	Brown sandy clay	CL	14.1							
5	Tan sandy clay with caliche	CL		31	14	17	5	14	19	
10	More caliche soil		7.7				10	12	14	% passing #200 sieve = 62%
15	Reddish sandy clay	CL					15	14	21	
20	Reddish sandy clay	CL		30	15	15	20	12	21	
25	Light reddish sand with rock particles						25	50*		for 2" penetration
30	Hard tan sand and caliche rock						30	50*		for 4" penetration

CROSBYTON SOLAR PROJECT
CROSBYTON, TEXAS

LOG OF BORING NO. 3
DEPTH OF HOLE 30 ft

DEPTH IN FEET	DESCRIPTION OF SOIL	USC	NATURAL MOISTURE	ATTERBERG LIMITS LL	PL	PI	DEPTH OF PENETRATION VALUE	NO. OF BLOWS 1st 6"	2nd 6"	REMARKS
	Dark brown sandy clay	CL	17.4	41	23	18				
5	Tan and reddish sandy clay with caliche	CL	13.3				5	14	16	
10	Reddish sandy clay with caliche	CL	12.6	34	12	22				
15	Light reddish sand-silt -clay	CL	8.9				15	15	17	
20	Same as above but hard			36	18	18	20	23	27	
25	Caliche rock and tan silty sandy clay						25	20	30	
30	Caliche rock and tan silt sandy clay						30	50*		for 2" penetration

CROSBYTON SOLAR PROJECT
CROSBYTON, TEXAS

LOG OF BORING NO. 4
DEPTH OF HOLE 30 ft

DEPTH IN FEET	DESCRIPTION OF SOIL	USC	NATURAL MOISTURE	ATTERBERG LIMITS			DEPTH OF PENETRATION VALUE	NO. OF BLOWS		REMARKS
				LL	PL	PI		1st 6"	2nd 6"	
	Brown sandy clay	CL	13.0	39	17	22				
5	Reddish tan sandy clay with traces of caliche	CL	15.14				5	15	18	
10	Reddish tan sandy clay with traces of caliche			34	19	15	10	9	11	
15	Light brown sandy clay with caliche	CL	17.0	40	24	16	15	23	27	
20	Reddish sandy clay	CL	18.0	42	24	18	20	23	27	
25	Hard tan sandy clay with caliche		17.0	46	29	17	25	40*		for 6" penetration
30	Hard tan sandy clay with caliche						30	50*		for 4 $\frac{1}{2}$" penetration

CROSBYTON SOLAR PROJECT
CROSBYTON, TEXAS

LOG OF BORING NO. 5
DEPTH OF HOLE 30 ft

DEPTH IN FEET	DESCRIPTION OF SOIL	USC	NATURAL MOISTURE	ATTERBERG LIMITS			DEPTH OF PENETRATION VALUE	NO. OF BLOWS		REMARKS
				LL	PL	PI		1st 6"	2nd 6"	
	Dark brown sandy clay	CL	17.2							
	Reddish tan sandy clay with caliche	CL	15.0	30	11	19				
5										
10	Tan sandy clay with caliche	CL	14.9 15.2	35	20	15	10	17	23	
15							15	19	27	
20	Tan sandy clay with caliche (hard)	CL		31	17	14	20	20	19	
25	Light brown sandy clay with caliche (very hard)	CL					25	50*		for 4" penetration
30							30	50*		for 1" penetration

CROSBYTON SOLAR PROJECT
CROSBYTON, TEXAS

LOG OF BORING NO. 6
DEPTH OF HOLE 30 ft

DEPTH IN FEET	DESCRIPTION OF SOIL	USC	NATURAL MOISTURE	ATTERBERG LIMITS			DEPTH OF PENETRATION VALUE	NO. OF BLOWS		REMARKS
				LL	PL	PI		1st 6"	2nd 6"	
	Dark brown sandy clay	CL	14.2							
				35	18	17				% passing #200 sieve = 60%
5	Reddish tan sandy silty clay with caliche	CL	11.0							
10			12.7				10	12	16	% passing #200 sieve = 77%
15							15	14	23	
				33	18	15				
20							20	16	20	
				30	17	14				
25	Caliche rock with tan silty sand	SM					25	22	28	
30							30	50*		for 1" penetration

CROSBYTON SOLAR PROJECT
CROSBYTON, TEXAS

LOG OF BORING NO. 7
DEPTH OF HOLE 30 ft

DEPTH IN FEET	DESCRIPTION OF SOIL	USC	NATURAL MOISTURE	ATTERBERG LIMITS LL	PL	PI	DEPTH OF PENETRATION VALUE	NO. OF BLOWS 1st 6"	2nd 6"	REMARKS
	Dark brown sandy clay	CL	20.1	35	20	15				
	Tan sandy clay with caliche	CL	3.7				5	18	22	
5										
				42	23	19				
10							10	15	19	% passing #200 sieve = 62%
15			13.9	42	22	20				
20	Caliche gravel with tan sandy clay	CL					20	50		
25							25	23	27	
30							30	29	27*	for 3" penetration

CROSBYTON SOLAR PROJECT
CROSBYTON, TEXAS

LOG OF BORING NO. 8
DEPTH OF HOLE 30 ft

DEPTH IN FEET	DESCRIPTION OF SOIL	USC	NATURAL MOISTURE	ATTERBERG LIMITS			DEPTH OF PENETRATION VALUE	NO. OF BLOWS		REMARKS
				LL	PL	PI		1st 6"	2nd 6"	
0	Dark brown sandy clay	CL	16.5	30	10	20				
5	Reddish tan sandy clay	CL	11.6	27	13	14				
10										
	Reddish tan sandy clay with caliche rubbles	CL		30	11	19				
15			13.5							
			14.4							
20	Greenish tan sandy clay	CL					20	14	17	
25							25	13	17	
30	Greenish sandy clay with caliche gravel	CL					30	24	26	

CROSBYTON SOLAR PROJECT
CROSBYTON, TEXAS

LOG OF BORING NO. 10
DEPTH OF HOLE 30 ft

DEPTH IN FEET	DESCRIPTION OF SOIL	USC	NATURAL MOISTURE	ATTERBERG LIMITS LL	PL	PI	DEPTH OF PENETRATION VALUE	NO. OF BLOWS 1st 6"	2nd 6"	REMARKS
	Dark brown sandy clay	CL	13.3	39	19	20				
			15.8	37	19	18				
5	Tan sandy clay with caliche pebbles	CL	17.4							
10			5.4	22	14	8	10	18	20	% passing #200 sieve = 76%
15			10.5				15	16	21	
20			13.3				20	20	30	
			2.5	23	15	8				
25	Rock and tan sandy silt	ML					25	50*		for 3" penetration % passing #200 sieve = 65%
30			4.5				30	50*		for 3" penetration

CROSBYTON SOLAR PROJECT
CROSBYTON, TEXAS

LOG OF BORING NO. 11
DEPTH OF HOLE 30 ft

DEPTH IN FEET	DESCRIPTION OF SOIL	USC	NATURAL MOISTURE	ATTERBERG LIMITS			DEPTH OF PENETRATION VALUE	NO. OF BLOWS		REMARKS
				LL	PL	PI		Ist 6"	2nd 6"	
	Dark brown sandy clay	CL	14.8	34	15	19				% passing #200 sieve = 62%
5	Tan sandy clay with caliche	CL	13.1	25	15	10				% passing #200 sieve = 68%
10			8.1	22	15	7				% passing #200 sieve = 71%
15			20.4	30	17	13				
20			13.0	31	15	16				
							20	12	15	% passing #200 sieve = 45%
25			19.0	33	17	15				
							25	17	33*	for 1" penetration
30							30	50*		for 1" penetration

CROSBYTON SOLAR PROJECT
CROSBYTON, TEXAS

LOG OF BORING NO. 12
DEPTH OF HOLE 30 ft

DEPTH IN FEET	DESCRIPTION OF SOIL	USC	NATURAL MOISTURE	ATTERBERG LIMITS LL	PL	PI	DEPTH OF PENETRATION VALUE	NO. OF BLOWS 1st 6"	2nd 6"	REMARKS
	Dark brown sandy clay	CL	22.1	39	20	19				
5	Tan sandy clay with caliche (stiff)	CL	8.8				6	16	15	
10			14.3				11	16	18	% passing #200 sieve = 70%
15			14.1	39	20	19	15	20	24	% passing #200 sieve = 42%
20	Caliche gravel & powder caliche with tan sandy silt		6.6				20	50	--	
25	Gravel with tan sandy silt	GM	2.9				25	50*		for 4" penetration
30			4.2				30	50*		for 3" penetration

CROSBYTON SOLAR PROJECT
CROSBYTON, TEXAS

LOG OF BORING NO. 13
DEPTH OF HOLE 30 ft

DEPTH IN FEET	DESCRIPTION OF SOIL	USC	NATURAL MOISTURE	ATTERBERG LIMITS			DEPTH OF PENETRATION VALUE	NO. OF BLOWS		REMARKS
				LL	PL	PI		1st 6"	2nd 6"	
	Dark brown sandy clay	CL	17.7							% passing #200 sieve = 64%
5	Reddish tan sandy clay	CL	16.6							
10			18.0							
			15.3							
15	Gray sandy clay with caliche	CL	21.4	40	18	12				
	Reddish tan sandy clay with caliche	CL	16.3							
20							20	24	26	
25	Gravel & caliche powder & sandy silt						25	30	20	for 3 $\frac{1}{2}$" penetration
30							30	50*		for $\frac{1}{2}$" penetration

CROSBYTON SOLAR PROJECT
CROSBYTON, TEXAS

LOG OF BORING NO. 14
DEPTH OF HOLE 30 ft

DEPTH IN FEET	DESCRIPTION OF SOIL	USC	NATURAL MOISTURE	ATTERBERG LIMITS LL	PL	PI	DEPTH OF PENETRATION VALUE	NO. OF BLOWS 1st 6"	2nd 6"	REMARKS
	Dark brown sandy clay	CL	15.0	35	20	15				
	Tan sandy clay with caliche			32	18	14				
5		CL	12.7	41	22	19				
10							10	16	16	% passing #200 sieve = 65.4%
			13.6							
15							15	18	21	
	Greenish tan sandy clay	CL					20	30	20	
25	Tan sandy clay with caliche	CL					25	21	29	
30							30	29	21*	for 4 $\frac{1}{2}$" penetration

CROSBYTON SOLAR PROJECT
CROSBYTON, TEXAS

LOG OF BORING NO. 15
DEPTH OF HOLE 30 ft

DEPTH IN FEET	DESCRIPTION OF SOIL	USC	NATURAL MOISTURE	ATTERBERG LIMITS LL	PL	PI	DEPTH OF PENETRATION VALUE	NO. OF BLOWS 1st 6"	2nd 6"	REMARKS
	Dark brown sandy clay	CL	16.4							
	Tan sandy clay with caliche	CL	15.7				5	15	13	
5										
			14.2	33	14	19				
10							10	16	20	
15				34	17	17	15	21	20	
	Greenish tan sandy clay	CL					20	22	23	
20										
							25	26	24*	% passing #200 sieve = 60%
25	Tan silt sandy clay with caliche	CL								*for 4" penetration
30							30	21	29	

CROSBYTON SOLAR PROJECT
CROSBYTON, TEXAS

LOG OF BORING NO. 16
DEPTH OF HOLE 30 ft

DEPTH IN FEET	DESCRIPTION OF SOIL	USC	NATURAL MOISTURE	ATTERBERG LIMITS			DEPTH OF PENETRATION VALUE	NO. OF BLOWS		REMARKS
				LL	PL	PI		1st 6"	2nd 6"	
	Dark brown sandy clay	CL	20.3	34	22	12				% passing #200 sieve = 56%
	Tan sandy clay with caliche	CL	13.2							
5							7	12		% passing #200 sieve = 62%
							8		12	
				35	18	17				
10			11.5				11	16	16	
15			16.4							
20	Tan silty sand with caliche	ML	6.7	36	21	15	19	12	24	% passing #200 sieve = 35%
25			3.4				25	50*		for $\frac{1}{2}$" penetration
30							30	21	28	

CROSBYTON SOLAR PROJECT

CROSBYTON, TEXAS

LOG OF BORING NO. 17 sh½

DEPTH OF HOLE 75 ft

DEPTH IN FEET	DESCRIPTION OF SOIL	USC	NATURAL MOISTURE	ATTERBERG LIMITS LL	PL	PI	DEPTH OF PENETRATION VALUE	NO. OF BLOWS 1st 6"	2nd 6"	REMARKS
	Dark brown sandy clay	CL								
5	Tan sandy clay with caliche	CL	13.0 14.0	38	16	22	5	11	16	
10				34	22	12	10	18	22	
15			22.0							
20			20.0				20	14	27	
25							25	25	25	
29–30	Rock layer (29–39)						30	50*		for 2" penetration
35							35	50*		for 2" penetration
39–40							40	50*		for 4" penetration

CROSBYTON SOLAR PROJECT
CROSBYTON, TEXAS

LOG OF BORING NO. 17 sh 2/2
DEPTH OF HOLE 75 ft.

DEPTH IN FEET	DESCRIPTION OF SOIL	USC	NATURAL MOISTURE	ATTERBERG LIMITS LL	PL	PI	DEPTH OF PENETRATION VALUE	NO. OF BLOWS 1st 6"	2nd 6"	REMARKS
	Tan sandy clay with caliche	CL		37	17	20				% passing #200 sieve = 65%
45							45	50*		for 4 1/2" penetration
50							50	50*		for 5 1/2" penetration
55							55	50*		for 4" penetration
60		CL		35	21	14	60	50*		for 3" penetration
							65	50		
	Red clay	CL		34	14	20				
65										
70							70	33	17*	for 2" penetration
75							75	30	20*	for 2" penetration

CROSBYTON SOLAR PROJECT
CROSBYTON, TEXAS

LOG OF BORING NO. 19 $sh^1/_2$
DEPTH OF HOLE 75 ft

DEPTH IN FEET	DESCRIPTION OF SOIL	USC	NATURAL MOISTURE	ATTERBERG LIMITS LL	PL	PI	DEPTH OF PENETRATION VALUE	NO. OF BLOWS 1st 6"	2nd 6"	REMARKS
	Dark brown sandy clay	CL	14.1	37	17	20				
	Tan sandy clay with caliche	CL	8.3				5	14	15	
5										
10							10	14	22	
15							15	13	19	
20							20	15	21	% passing #200 sieve = 41%
25							25	50*		for 3" penetration
29–39	Rock layer (samples were cored by diamond core sampler)	unconfirmed compressive strength = 20400 psf Young's Modules of Elasticity = 40,600 psi					30	50*		for 1" penetration
30										
35										
40							40	50*		for 4" penetration

CROSBYTON SOLAR PROJECT
CROSBYTON, TEXAS

LOG OF BORING NO. $19\ sh^{2}/_{2}$
DEPTH OF HOLE 75 ft

DEPTH IN FEET	DESCRIPTION OF SOIL	USC	NATURAL MOISTURE	ATTERBERG LIMITS			DEPTH OF PENETRATION VALUE	NO. OF BLOWS		REMARKS
				LL	PL	PI		1st 6"	2nd 6"	
	Tan sandy clay									
45		CL					45	50*		for 3" penetration
50							50	50*		for 3" penetration
55							55	50*		for 3" penetration
60		CL		38	17	21	60	50*		for 4" penetration
65							65	45	-	
	Red clay									
70							70	36	14*	for 2" penetration
75		CL		34	14	20	75	36	14*	% passing #200 sieve = 78% *for 1" penetration

APPENDIX C. OPTICAL ANALYSIS

In this appendix we present a powerful approach for the detailed evaluation of optical flux distributions and optical concentrations. The theory can be applied for finite sources and concentrators of arbitrary shape, specified by appropriate structure relations, but the focus of the description is upon spherical mirror segments and conical receivers. The entire approach and all of the results were developed during the present contract period.

The discussion is divided into several parts. First the irradiance per unit solid angle of a distant uniform finite source is examined and a suitable expression, (C-19), is chosen as a model for the irradiance. Then a fundamental new expression, (C-25), is derived for the optical concentration and discussed. The use of structure relations, (C-32) and (C-34) to describe the concentrator shape is explained next. Our expressions are then interpreted in terms of point sun flux distributions for spherical segment concentrators.

The range of integration for the evaluation of finite source concentrations is then considered and the role of rim effects as constraints on the integration is explained. The effective sun size approach for including averaged mirror error is examined in an attempt to determine an appropriate policy for selecting the effective sun size for multiple bounce contributions.

Various applications of our analysis are presented. We discuss the mirror hot spot first and then proceed into a presentation of our results for the input power distribution on conical receivers. The results obtained exhibit exquisite detail relevant as the limit of the assumptions our theoretical model might be approached by actual mirrors bearing real world defects and alignment errors. A comparison of some of our results with points obtained by E-Systems and by Dr. Schrenk is made, showing good agreement for single bounce radiation. Multiple bounce distributions are not treated in detail by these other approaches. The method of analysis used at E-Systems is described in the following appendix.

Finally, several ray tracing codes have been developed during the contract period but are not discussed here. Such codes are useful in certain calculations and serve as part of our backup, but can not resolve the caustic peak structure exhibited by the new method described in this appendix.

C-1 THE SOLAR MODEL

When viewed from earth, the sun appears as a disc with some distribution of light across its face. The effects of its spherical geometry can be combined into an intensity distribution over the apparent flat disc. In describing the light from the solar disc, it is useful to take advantage of some of the terminology and concepts of the disciplines of photometry and radiometry. The terms will be defined as used, however.

Consider a spherical source viewed from a point O as illustrated in Fig. C-1. The radiant exitance, M (emitted power per unit area), of the source will be considered to be uniform,

$$M = \frac{P_T}{A_T} \tag{C-1}$$

where P_T is the total power emitted from the source and A_T is the total surface area of the source. The radiance vector, $\vec{L}$ (power per unit area per steradian), is

$$\vec{L} = M\ B(\Omega,\theta_s,\phi_s)\hat{n}_s \tag{C-2}$$

where $B(\Omega,\theta_s,\phi_s)$ is the radiant brightness distribution which in general depends on the position (θ_s,ϕ_s) on the sun and the solid angle Ω. The usual radiance used in radiometry is

$$L = \vec{L}\cdot\hat{e}_{\Omega E} \tag{C-3}$$

where $\hat{e}_{\Omega E}$ is the unit vector in the direction of the observer. If the solid angle emission characteristic is uniform everywhere on the source (isotropic) then

$$L = \frac{P_T}{A_T}\ B(\Omega)\cos\alpha \quad . \tag{C-4}$$

The radiant brightness distribution, $B(\Omega)$, is normalized so that

$$1 = \iint B(\Omega)\cos\alpha d\Omega \ . \tag{C-5}$$

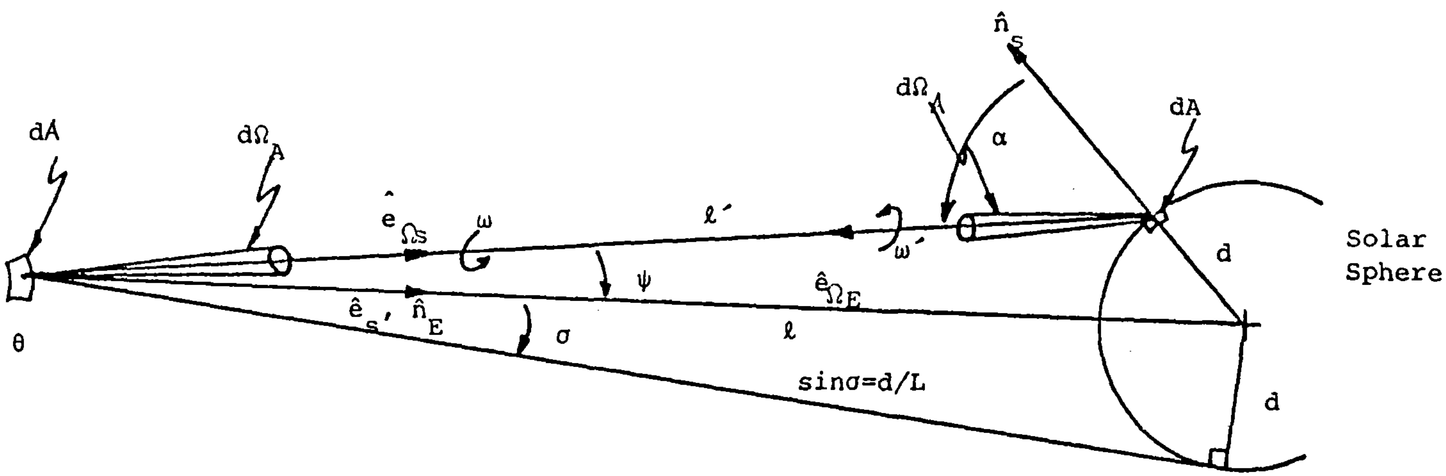

Figure C-1. Element of Area dA on Sun Illuminates Element of Area dA on the earth.

If the radiant brightness $B(\Omega)$ is constant for all Ω, then

$$B(\Omega) = 1/\pi \tag{C-6}$$

and the source is a Lambertian radiator. The radiance L is then proportional to the cosine of the angle, α, between the direction to the observer and the surface normal to the source surface. This is known as Lambert's Law (cosine law) and the source is said to have uniform brightness.

The quantity of interest is actually the power per unit area per unit solid angle (irradiance per steradian) that passes through an element of area on the earth. This element of area is oriented so that its normal lies along the direction to the sun, $\hat{e}_s$. An element of area on the sun dA illuminates an element of area dA at the earth which subtends the solid angle

$$d\Omega_A = \frac{dA}{\ell'^2}\ \hat{e}_s \cdot \hat{e}_{\Omega s} = \frac{dA}{\ell'^2} \cos\tilde{\psi} \tag{C-7}$$

when viewed from the sun along direction $\hat{e}_{\Omega E}$ as illustrated in Fig. C-1. The power received at dA is

$$\begin{aligned} dP_o &= \vec{L} \cdot \hat{e}_{\Omega E}\ d\Omega_A dA \\ &= \left(\frac{P_T}{A_T} B(\Omega)\cos\alpha\right)\left(\frac{dA}{\ell'^2} \cos\tilde{\psi}\right) dA\ . \end{aligned} \tag{C-8}$$

The area dA on the sun subtends a solid angle

$$d\Omega_A = \frac{dA}{\ell'^2}\, \hat{n}_s \cdot \hat{e}_{\Omega E}$$
$$= \frac{dA}{\ell'^2} \cos\alpha \tag{C-9}$$

when viewed from the earth. The power passing through dA becomes

$$dP_o = \left(\frac{P_T}{A_T} B(\Omega)\cos\tilde{\psi}\right)\left(\frac{dA}{\ell'^2}\cos\alpha\right)dA$$

$$= \vec{L}_E \cdot \hat{e}_s \; d\Omega_A dA \quad , \tag{C-10}$$

where

$$\vec{L}_E = (\vec{L}\cdot\hat{n}_s)\,\hat{e}_{\Omega s} \tag{C-11}$$

is the received radiance vector at the earth. The irradiance at dA from solid angle $d\Omega_A$ is

$$\frac{dP_o}{dA} = \vec{L}_E \cdot \hat{e}_s d\Omega_A \ . \tag{C-12}$$

The total irradiance from the entire sun is

$$I_o = \iint_{\Omega s} \vec{L}_E \cdot \hat{e}_s \; d\Omega_A$$
$$= \int_0^{\sigma}\int_0^{2\pi} \frac{P_T}{A_T} B(\omega,\tilde{\psi})\cos\tilde{\psi}\sin\tilde{\psi}d\omega d\tilde{\psi} \tag{C-13}$$

where $B(\omega,\tilde{\psi})$ is $B(\Omega)$ parametrized with ω and $\tilde{\psi}$.

For an isotropic Lambertian source, $B(\Omega) = 1/\pi$ and

$$I_o = \frac{P_T}{A_T}\sin^2\sigma \quad . \tag{C-14}$$

The incident radiance I (irradiance per solid angle) can be written as

$$I = \frac{I_o}{\pi \sin^2\sigma} \cos\tilde{\psi} \qquad \text{(C-15)}$$

where

$$0 \leq \tilde{\psi} \leq \sigma \quad .$$

The radiance of the source in this case is

$$L = \frac{I_o}{\pi \sin^2\sigma} \cos\alpha \ . \qquad \text{(C-16)}$$

It is interesting to note that when the source is Lambertian (follows the cosine law) it produces an incident radiance vector $\vec{L}_E$ which produces an incident radiance that follows a cosine law at the point of incidence. Emission and reception are isotropic in the same sense.

Few sources are truly Lambertian and the sun is only approximately Lambertian. At optical wavelengths, the sun appears slightly less bright at the limbs, an effect called limb-darkening. (It is interesting to note that at much longer wavelengths, this effect is reversed and limb-brightening occurs.) In such a case, the incident radiance I becomes

$$I = \frac{I_o B(\tilde{\psi}) \cos\tilde{\psi}}{2\pi \int_o^{\sigma} B(\tilde{\psi}) \cos\tilde{\psi} \sin\tilde{\psi} d\tilde{\psi}} \qquad \text{(C-17)}$$

since $B(\Omega)$ depends only on $\tilde{\psi}$ for limb-darkening effects. However, the limb-darkening effects are slight, so considering the sun to be a Lambertian source gives a useful model. Since the sun is so far away, σ is small ($\sigma = 0.267°$) so that

$$\cos\tilde{\psi} = 1 - \frac{\sin^2}{2}\tilde{\psi} \geq 1 - \frac{\sigma^2}{2} \approx 1 \; . \qquad \text{(C-18)}$$

In this case, the incident radiance can be modeled as

$$I = \frac{I_o}{\Omega_s} \qquad \text{(C-19)}$$

where

$$\begin{aligned} \Omega_s &= \int_0^{\sigma}\int_0^{2\pi} \sin\tilde{\psi}\, d\omega\, d\tilde{\psi} \\ &= 4\pi \sin^2(\sigma/2) \quad . \end{aligned} \qquad \text{(C-20)}$$

Equation (C-19) is the uniform irradiance per solid angle model for the sun.

The solar model for the radiance given by (C-19) will be used to obtain the general expression for the optical power concentration. However, the simpler model is only used for convenience and it will be shown how it can be replaced by the general model of (C-17). The results displayed below are based on the model of (C-19) simply because the limb-darkening effects are so small.

C-2 BASIC EXPRESSIONS FOR OPTICAL POWER CONCENTRATIONS

The optical power concentration, F, at a point on a receiver in a collector system is defined to be the ratio of the total optical power per unit area (irradiance) received at that point to the direct irradiance. The direct irradiance is that optical power per unit area (normal to the earth-sun line) received by the collector aperture. If an area ΔA_R at a receiver point is illuminated by the area ΔA_A in the aperture plane then the total power received at ΔA_R is

$$I_o \Delta A_A$$

where I_o is the direct irradiance in the aperture plane. The total irradiance at the receiver point is

$$I_o \, \Delta A_A / \Delta A_R \, ,$$

so that the concentration is

$$F = \frac{I_o \Delta A_A / \Delta A_R}{I_o} = \frac{\Delta A_A}{\Delta A_R} \, . \qquad \text{(C-21)}$$

The concentration is simply a ratio of areas, but ΔA_R depends not only on ΔA_A and the location of the receiver point, but also on the shape of the collector mirror. To carry this method of analysis further requires specification of the collector shape, but this approach serves to illustrate the definition of concentration.

Consider an element $\vec{d}A$ of receiver area with local "outward" surface normal, $\hat{b}$, located at $\vec{q}$ in the neighborhood of a mirror surface as indicated in Fig. C-2. Light from the sun reflected to $d\vec{A}$ through the differential of solid angle $d\vec{\Omega}$ may be considered to come from a patch of area dS in a plane tangent to the mirror. The image of the entire sun in the same tangent plane subtends the solid angle Ω_s parametrized in (C-20). The differential of irradiance at $d\vec{A}$ through $d\vec{\Omega}$, is, therefore,

$$dI = \mathcal{I} d\vec{\Omega}\cdot\hat{b} = \frac{I_o}{\Omega_s} d\vec{\Omega}\cdot\hat{b} \qquad \text{(C-22)}$$

with the requirement that $d\vec{\Omega}\cdot\hat{b} > 0$ for illumination only on the outward side of $d\vec{A}$. The differential of optical concentration at $d\vec{A}$ is the differential irradiance divided by the input solar intensity, I_o:

$$dF = \frac{\hat{b}\cdot d\vec{\Omega}}{\Omega_s} \qquad \text{(C-23)}$$

The optical concentration, then, at $d\vec{A}$ is

$$F(\vec{q},\hat{b}) = \frac{1}{\Omega_s} \iint_{\Omega_M} \hat{b}\cdot d\vec{\Omega}, \quad \text{for } \hat{b}\cdot d\vec{\Omega} > 0 \text{ only,} \qquad \text{(C-24)}$$

where Ω_M is the apparent solid angle of the entire sun as viewed in the mirror. For a concentrating mirror, one finds $\Omega_M > \Omega_s$.

Light in a <u>differential</u> of solid angle will always consider the reflector to be locally flat; i.e., will reflect repeatedly as if from the local tangent planes. Thus the expression (C-24) may be used in the presence of multiple reflections in the mirror by separating and adding the contributions from light that has reflected n times:

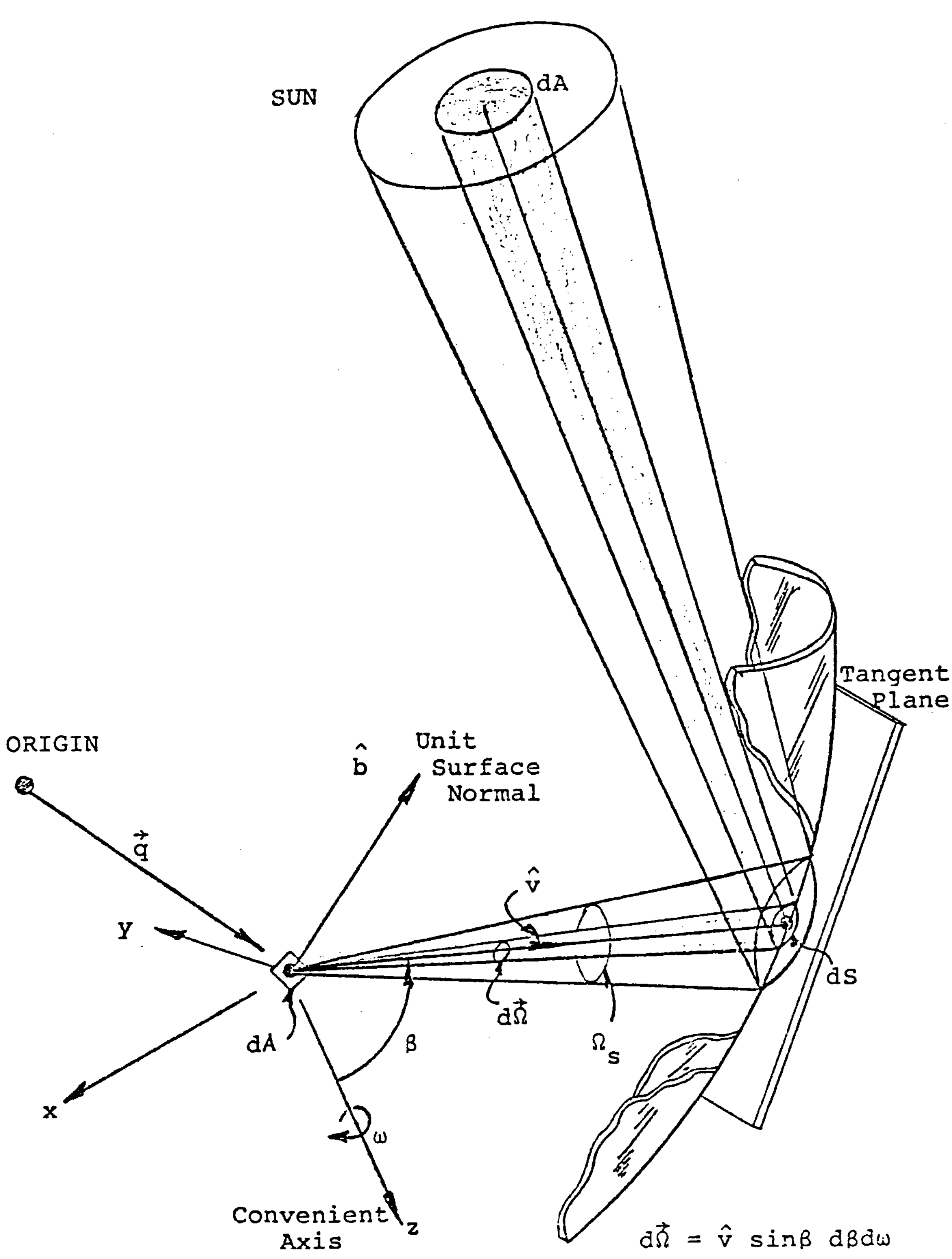

FIGURE C-2. Generalized Mirror Geometry

$$F(\vec{q},\hat{b}) = \sum_n R^n F_n(\vec{q},\hat{b}) = \frac{1}{\Omega_s} \sum_n R^n \iint_{\Omega_{Mn}} \hat{b}\cdot d\vec{\Omega}_M \tag{C-25}$$

The solid angle Ω_{Mn} is the apparent size of the sun as viewed in the mirror with radiation that has reflected n times. A reflection coefficient R has been included in (C-25) to account for reflective losses. The factor R must be kept inside the integral if one wishes to include angle of incidence effects. Similarly, if the wavelength dependence of the reflectivity is of interest, one must add an integral over $W(\lambda)d\lambda$ to the form shown in (C-25), where $W(\lambda)$ is a spectral density weight.

If one wishes to use an effective sun size σ_n that depends upon the number of reflections, then Ω_s should be expressed:

$$\Omega_{sn} \equiv 4\pi(\sin \frac{\sigma_n}{2})^2 \tag{C-26}$$

and included inside the summation shown in (C-27). Procedures for selecting σ_n are discussed in Sec. IV, Appen. D, and later in this appendix.

The ability to include limb darkening effects has apparently been sacrificed in order to provide an almost trivial derivation of (C-25). However, this feature can be recovered in a way to be described later.

As indicated in Fig. C-2 the integral in (C-25) can be parametrized using any convenient axis:

$$F_n(\vec{q},\hat{b}) = \frac{1}{\Omega_s} \iint_{\Omega_{Mn}} (\hat{b}\cdot\hat{v}) \sin\beta d\beta d\tilde{\omega}, \qquad \hat{b}\cdot\hat{v} > 0 \text{ only.} \tag{C-27}$$

If a cartesian coordinate system (x, y, z) is selected with origin at $\vec{q}$, then

$$\hat{v} = \begin{pmatrix} \sin\beta\cos\tilde{\omega} \\ \sin\beta\sin\tilde{\omega} \\ \cos\beta \end{pmatrix} \quad \text{and } \hat{b} = \begin{pmatrix} b_x \\ b_y \\ b_q \end{pmatrix} \quad \text{where } b_q \equiv b_z \tag{C-28}$$

so that

$$\begin{aligned} \hat{b}\cdot\hat{v} &= b_q \cos\beta + (b_x\cos\tilde{\omega}+b_y\sin\tilde{\omega})\sin\beta \\ &\equiv b_z\cos\beta+b_\rho\sin\beta \geq 0 \quad . \end{aligned} \tag{C-29}$$

The restriction to positive values of the dot product is the requirement that only light impinging from the "outside" is of interest at $d\vec{A}$. Thus the range of integration in (C-27) includes only that portion of Ω_{Mn} that is "above" the receiver tangent plane, $\hat{b}\cdot\hat{v} = 0$, passing through $\vec{q}$ perpendicular to $\hat{b}$. The condition (C-29) can be stated in another way:

$$\begin{gathered} \left\{ \begin{matrix} D-\frac{\pi}{2} \\ 0 \end{matrix} \right\}_{\max} \leq \beta \leq \left\{ \begin{matrix} D+\frac{\pi}{2} \\ \pi \end{matrix} \right\}_{\min} \\ \iff \beta \in [D-\tfrac{\pi}{2}, D+\tfrac{\pi}{2}] \cap [0,\pi] \end{gathered} \tag{C-30}$$

where

$$\cos D \equiv \frac{b_z}{\sqrt{b_z^2 + b_\rho^2}} \quad \text{and } \sin D \equiv \frac{b_\rho}{\sqrt{b_z^2 + b_\rho^2}}$$

Note that the range of β shown in (C-30) is not the range of integration permitted by Ω_{Mn}, but is, rather, a restriction which may reduce that range.

The results in (C-25 - C-30) are extremely general because the shape of neither the receiver nor the mirror has yet been specified. This generalization serves as a warning that the apparent simplicity is hiding difficulties somewhere. The difficulties are all in the range of integration, Ω_{Mn}. In order to actually perform the required integrals, several strategies are possible. If the mirror shape is extremely difficult to describe analytically or bears stochastic errors, then one might divide the mirror surface into cells for interrogation by a numerical integration code. Each mesh cell would be tested for the nature and amount, if any, of its contribution to the concentration. On the other hand, for simply describable surfaces such as spherical segments, cylindrical surfaces, paraboloids, and so forth, it is desirable to proceed analytically. Such an analytical procedure for spherical segment mirrors is illustrated below.

C-3 COMPUTATION METHOD FOR SPHERICAL SEGMENT REFLECTORS

As indicated above, it is difficult to describe the solid angle, Ω_{Mn} required in (C-25), the apparent solid angle at $\vec{q}$ of the entire sun as viewed in the mirror with radiation that has reflected n times. One way to describe Ω_{Mn} is to consider integration over variables other than $d\vec{\Omega}_M$.

Consider a mirror which is a segment of a sphere of radius R with center C as illustrated in Fig. C-3. (Normalized units are used so that R = 1.) Light from an element of area dA on the sun enters the dish as a plane wave front from direction $\hat{e}_s$. Such light, striking the dish at zenith θ bounces n times and comes to the field point of interest $\vec{q}$ from direction $\hat{v}$. The field point is located by spherical coordinates: q, the distance from C, and ψ, the zenith from the "sun axis," S'C. The "outward normal" $\hat{b}$ associated with an element of area $d\vec{A}$ at $\vec{q}$ may or may not lie in the plane of the figure.

For convenience, the angle β employed as a parameter in (C-27) will be measured as the zenith angle of $\hat{v}$ with respect to the axis QC, passing through the field point $\vec{q}$ from C. It is desired to obtain the geometrical connection relating β, θ, and ψ.

Using Fig. C-3, one can deduce that

$$\kappa = (\theta-\psi) - (n-1)(\pi-2\theta) \qquad \text{(C-31)}$$

and

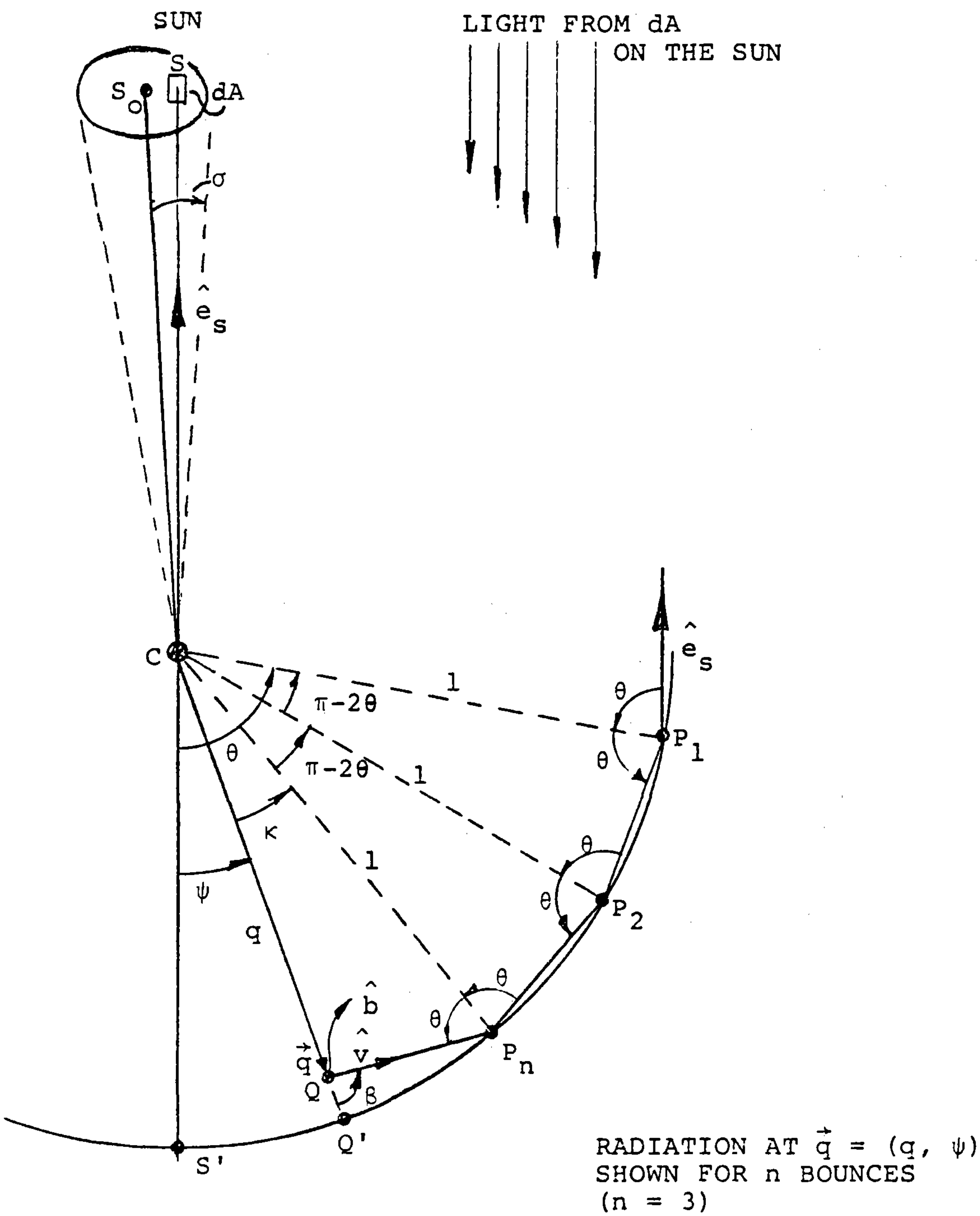

FIGURE C-3. Hemispherical dish multiple reflection geometry.

$$\beta = \kappa + \theta \quad . \tag{C-32}$$

Eliminating κ from these two expressions,

$$\beta = 2n\theta - \psi - (n-1)\pi \quad . \tag{C-33}$$

Using the Law of Sines in triangle CQP_n, one obtains

$$\sin\theta = q \sin\beta \Rightarrow \left(\frac{d\theta}{d\beta}\right)_q = q \frac{\cos\beta}{\cos\theta} . \tag{C-34}$$

The integral required in (C-27) is:

$$F_n(\vec{q},\hat{b}) = \frac{1}{\Omega s} \iint_{\Omega'_{Mn}} (\hat{b}\cdot\hat{v}) \sin\beta \quad d\beta d\tilde{\omega} \tag{C-35}$$

where Ω'_{Mn} is that portion of Ω_{Mn} that satisfies the restriction $(\hat{b}\cdot\hat{v}) \geq 0$. Now (C-33) and (C-34) may be used to accomplish a change of integration variable. Thus,

$$d\psi = \left| 2n\left(\frac{d\theta}{d\beta}\right)_q - 1 \right| d\beta = \left| \frac{2nq \cos\beta - \cos\theta}{\cos\theta} \right| d\beta . \tag{C-36}$$

Using (C-36) and (C-34) in (C-35), one obtains:

$$F_n(\vec{q},\hat{b}) = \frac{1}{\Omega_s} \iint_{\Omega'_c} (\hat{b}\ \hat{v}) \left| \frac{\cos\theta\sin\theta}{q \sin\psi[\cos\theta-2nq \cos\beta]} \right| \sin\psi \ d\psi d\omega \tag{C-37}$$

where the change of variable

$$\tilde{\omega} = \omega + \pi$$

has also been made for convenience. Now the differential $\sin\psi d\psi d\omega$ in (C-37) may be interpreted as an element of solid angle, $d\Omega_c$, measured from the center of the sphere, C. The angle ψ, the field point zenith, is measured from the S'CS line which varies inside a cone of angular radius σ as S is swept over the face of the sun. Alternatively, ψ may be interpreted as the zenith of the sun axis S'CS measured from the line Q'C passing through the field point. This second interpretation, which is conceptually easier to use, is illustrated in Fig. C-4.

If one wishes to recover the limb darkening effects, which were dismissed in order to provide a simple derivation of (C-35), he should notice that $\Omega_s^{-1}\sin\psi d\psi d\omega$ in (C-37) performs an average and then simply weight the average with the brightness distribution $B(\tilde{\psi})$ described above. However, one should also note that the angle $\tilde{\psi}$ used to parametrize $B(\tilde{\psi})$ is <u>not</u> the same angle as ψ. The angle ψ is a function of ψ, ψ_o, and ω.

The <u>principal sun axis</u> is the line $S_o'CS_o$ passing through the center of the sun disc. Specifically, the $\hat{x}$ from which $\tilde{\omega}$ and ω are measured is taken to lie in the plane containing Q, S_o', and C and is directed from Q toward the line $S_o'C$. The cone generated by S'C, shown in Fig. C-4 is called <u>the sun cone</u>.

With this interpretation, the expression for $F_n(\vec{q},\hat{b})$ in (C-37) can be simply described. One recognizes that (C-36) just requires an average to be performed over the solid angle of the sun cone. The quantity being averaged is

$$F_n(\vec{q},\hat{b}) \equiv (\hat{b}\cdot\hat{v}) \left| \frac{\cos\theta\sin\theta}{q\ \sin\psi[\cos\theta - 2nq\ \cos\beta]} \right| \qquad (C-38)$$

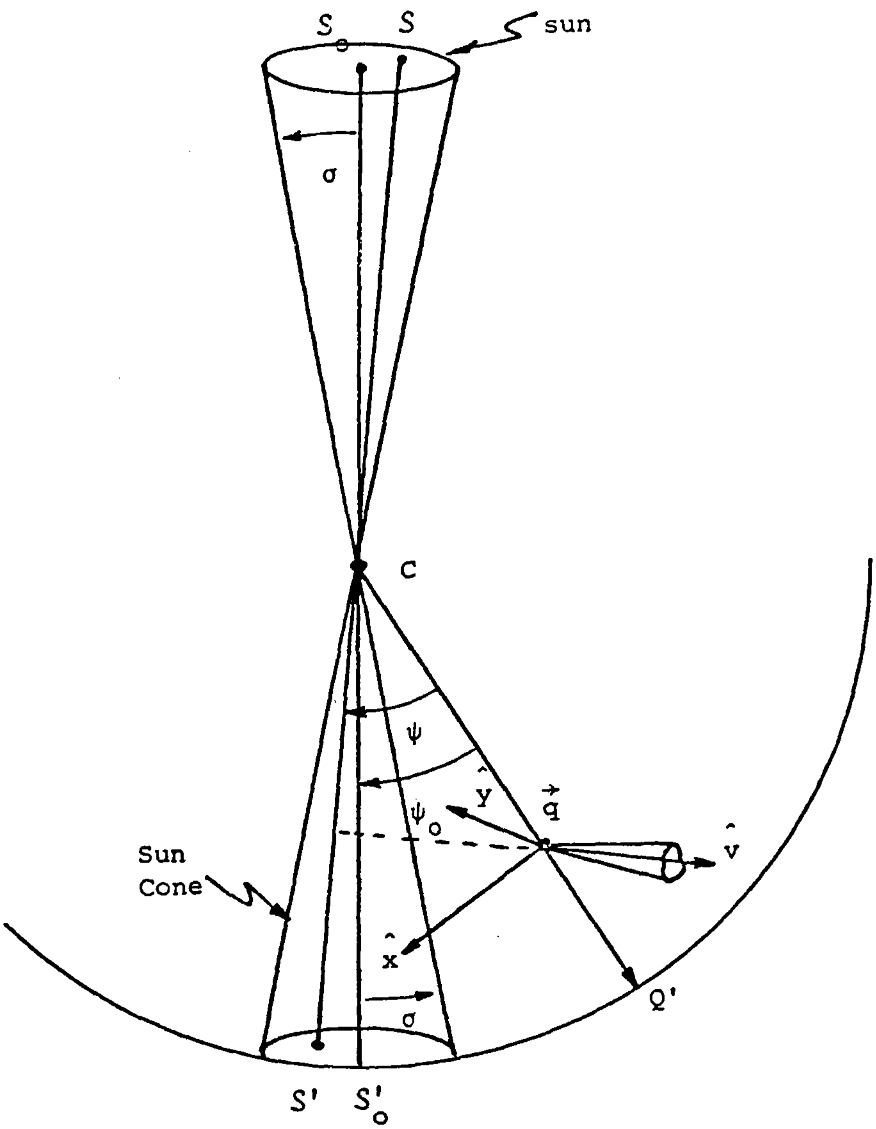

Figure C-4. Generalized Receiver Geometry and Sun Cone.

which must be the n bounce concentration produced at the field point $\vec{q}$ by a point sun at infinity. As a matter of fact, this expression is easily derived directly by starting with a point sun model and tracking the concentration of input power that passes through a differential area

$$dA_R = \sin\theta(\cos\theta\ d\theta)d\phi = \rho d\rho d\phi \quad \text{for } \rho = \sin\theta$$

lying in a reference plane, perpendicular to the earth-sun line, receiving uniform intensity I_o.

C-4 POINT SUN CONCENTRATIONS AND THE STRUCTURE RELATIONS

The point sun concentration function F_n is a useful starting point for a description of the optical concentration on a receiver. One describes the receiver shape in terms of q and ψ; e.g., for a perfectly aligned cone, $\psi = \psi_o$ = angular radius of receiver cone, $b_x = -1$, $b_y = b_z = 0$. On a conical receiver one obtains the point sun concentration distribution as a function of q by fixing ψ_o and determining β and θ as functions of q using (C-33) and (C-34). These quantities are then substituted into (C-38). Mirror rim angle, $\theta_{max}(\phi)$, and rim shadow effects may be accounted for by rejecting contributions in (C-38) from values of θ which are not available (in the mirror) at the azimuth ϕ measured in a suitable rim plane. Thus, contributions from θ should not be included if θ is greater than

$$\theta_{max}(\phi)_{effective} = \begin{Bmatrix} \theta_{max}(\phi), \text{ rim angle effects} \\ \pi - \theta_{max}(\phi), \text{ rim shadow effects} \end{Bmatrix}_{min} . \tag{C-39}$$

For fixed values of q and $\psi \equiv \psi_o$ the Eqns. (C-33) and (C-34) may allow more than one solution pair (β,θ).

The reason for multiple solution pairs (β,θ) is that the integration region used in (C-37) is folded; i.e., the integrand is multivalued. This feature was not exposed in the apparently simple step (C-36) above, but the, perhaps, unexpected use of magnitude signs was a secret warning of this complication. It should be clear that one need only determine all solutions (for available θ and for $\hat{b}\cdot\hat{v}>0$) of (C-33) and (C-34) and add their contributions in (C-38). In other words

$$F_n(\vec{q},\hat{b}) = \sum_k (\hat{b}\cdot\hat{v}_k) \left| \frac{\cos\theta_k \sin\theta_k}{q \sin\psi_o[\cos\theta_k - 2nq\cos\beta_k]} \right| \tag{C-40}$$

where the sum is over all solution pairs $\theta_k(q,\psi_o)$ and $\beta_k(q,\psi_o)$ that can contribute. This situation is illustrated in Fig. C-5 for n = 1.

As the figure indicates, for n = 1 there might be as many as three contributions to the sum in (C-40). <u>For perfectly aligned conical receivers, however, the backside contribution from P" (from $\tilde{\omega} = 0$) would violate the $\hat{b}\cdot\hat{v} > 0$ restriction</u>[+] <u>if the cone is properly sized (large enough) and should not be counted</u>. This light would be intercepted by and would

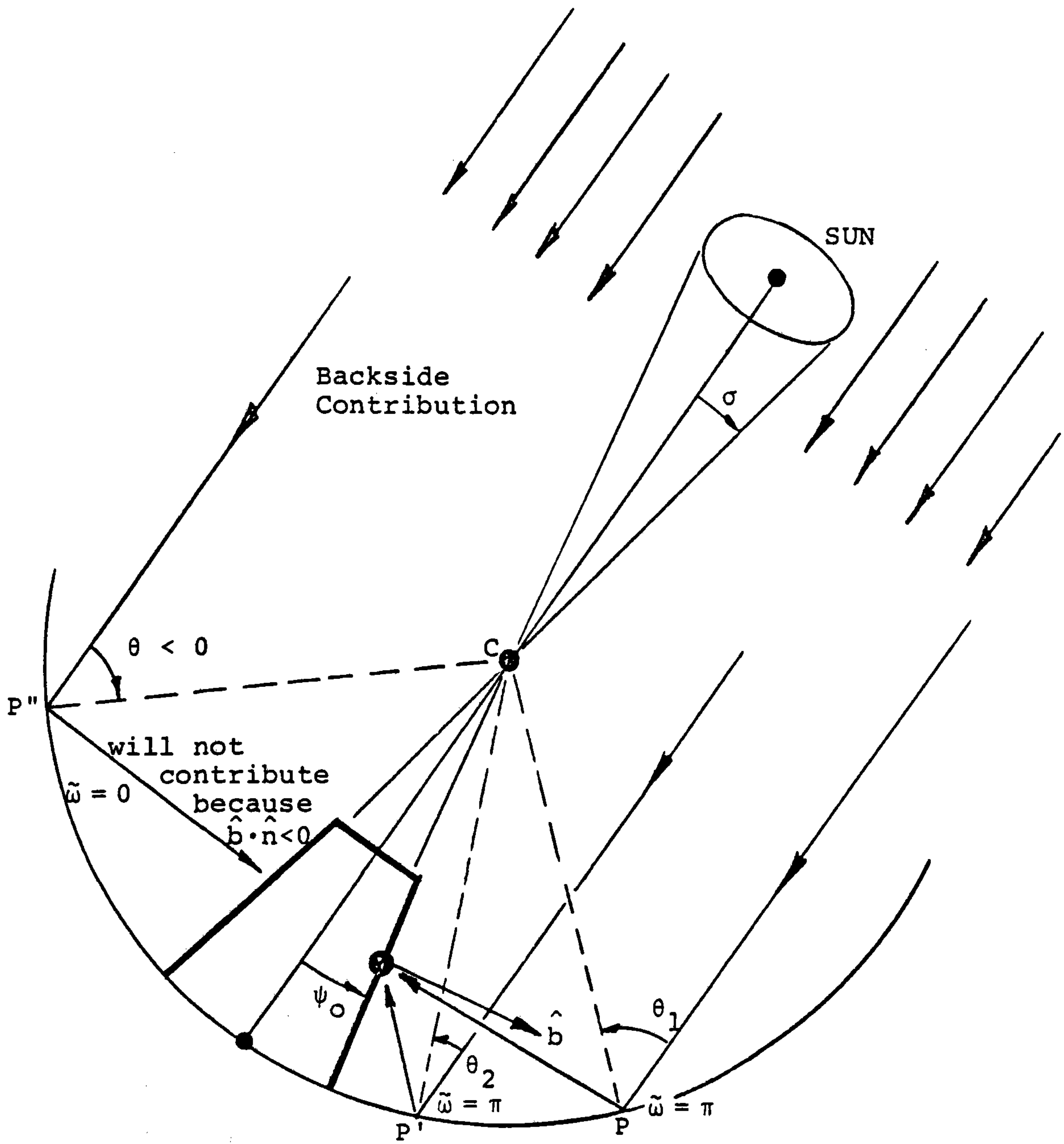

FIGURE C-5. MULTIPLE CONTRIBUTIONS TO THE SINGLE BOUNCE CONCENTRATION.

contribute to another point on the receiver surface. It can happen, however, for misaligned conical receivers, or for receivers of other shape, or for probe surfaces, that the $\tilde{\omega} = 0$ solution will contribute.

Now the derivation of (C-33) and (C-34) made use of Fig. C-3 which illustrated only the front side ($\tilde{\omega} = \pi$) contributions. A similar figure and derivation with Q' at the same location, but with P_1 located to the left of the CS' line would produce (C-34) as before, but (C-33) would be produced in the form

$$\beta = 2n\theta + \psi-(n-1)\pi \qquad \text{(C-33')}$$

One notes that the contribution of ψ enters with opposite sign. Either of two attitudes may be adopted as a device for efficiently obtaining both the $\tilde{\omega} = 0$ and $\tilde{\omega} = \pi$ contributions without dealing explicitly with (C-33')

1) One can agree to solve only (C-33) and (C-34), but to do so first for all solutions ($\beta>0,\theta>0$) for the actual $\psi(>0)$ and then to obtain all solutions ($\beta>0,\theta>0$) using $-\psi$ in (C-33),

or

2) One can agree to solve only (C-33) and (C-34), but to also include solutions for $\beta<0,\theta<0$, ex-

+Recall from Figs. C-1, C-3, and C-4 that the unit vector $\hat{v}$ opposes the direction of motion of the light.

cept that for the negative β and θ solutions the sign of the $(n-1)\pi$ term will be reversed in (C-33). One would keep $\psi>0$ in this approach. Although these two devices offer no particular advantage for evaluation of point sun concentrations, they offer enormous convenience to the specification of integration limits in the finite sun case.

The relations (C-33), (C-34), and (C-33') are called the structure relations for the system. Figures C-6 to C-10 illustrate the connections between ψ, β, and q for n=1,2,3,4, and 5. The curves show ψ plotted against β for various values of q, treated as parameter. The scale selected is not particularly useful for conical receivers with $\psi_0 \simeq \sigma \lesssim 1°$, but serves to illustrate the general features of the parameter relationships. It is the antisymmetry of these curves about the $\beta = 0$, $\psi = 0$ origin that is exploited in the devices listed above. If one wishes to use device 1), he can simply ignore the negative β axis. If he wishes to use device 2), he simply ignores the negative ψ axis. On the other hand, if neither device is of interest, then both the negative ψ and the negative β axes are ignored and the solutions of (C-33') are included and visualized by mentally folding the figure about either the ψ or the β axis.

For a perfectly aligned conical receiver of half angle ψ_0, one can locate ψ_0 on the vertical axis and imagine a

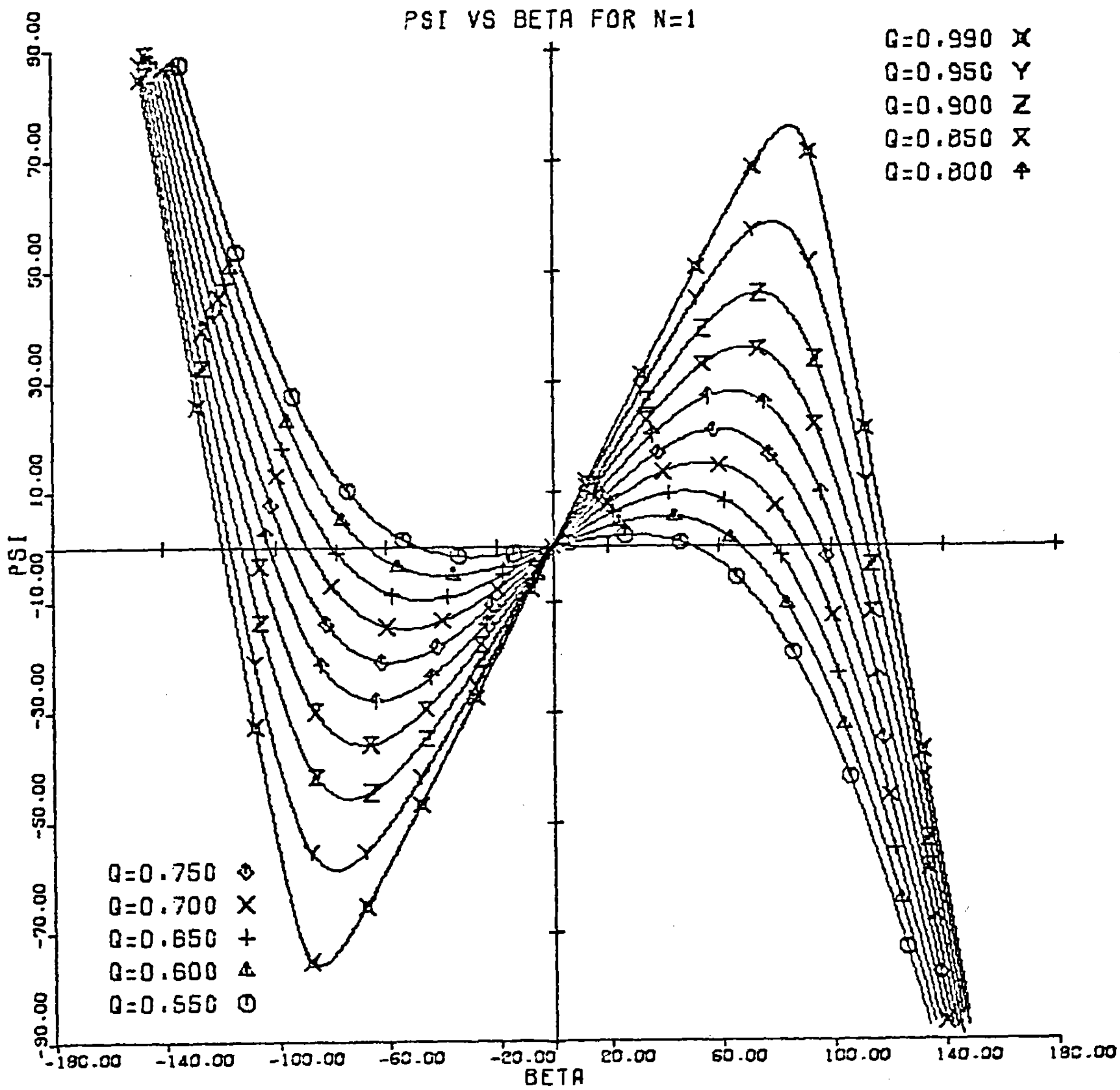

Figure C-6. Spherical Mirror Structure Relation For n=1.

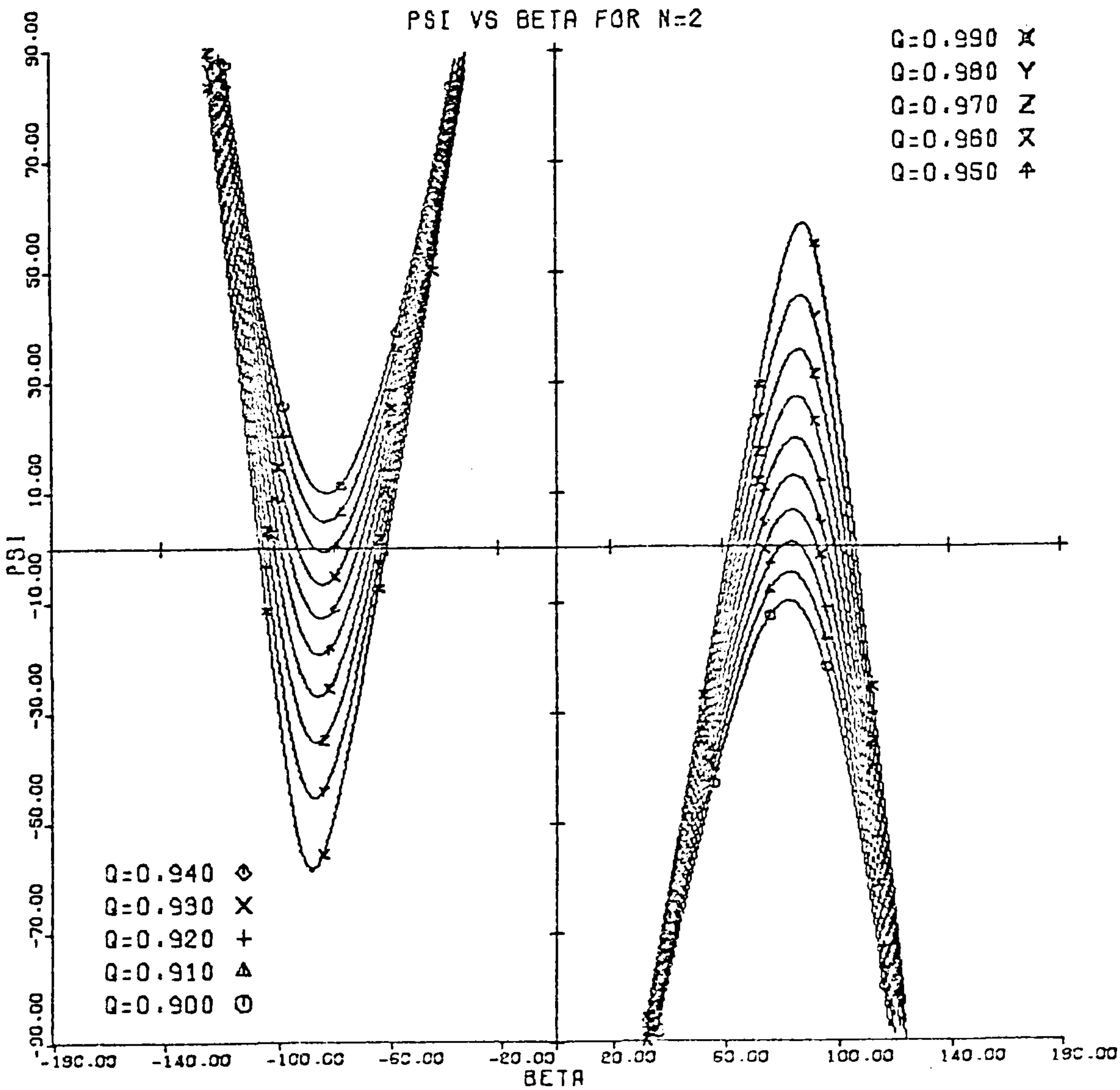

Figure C-7. Spherical Mirror Structure Relation for n=2.

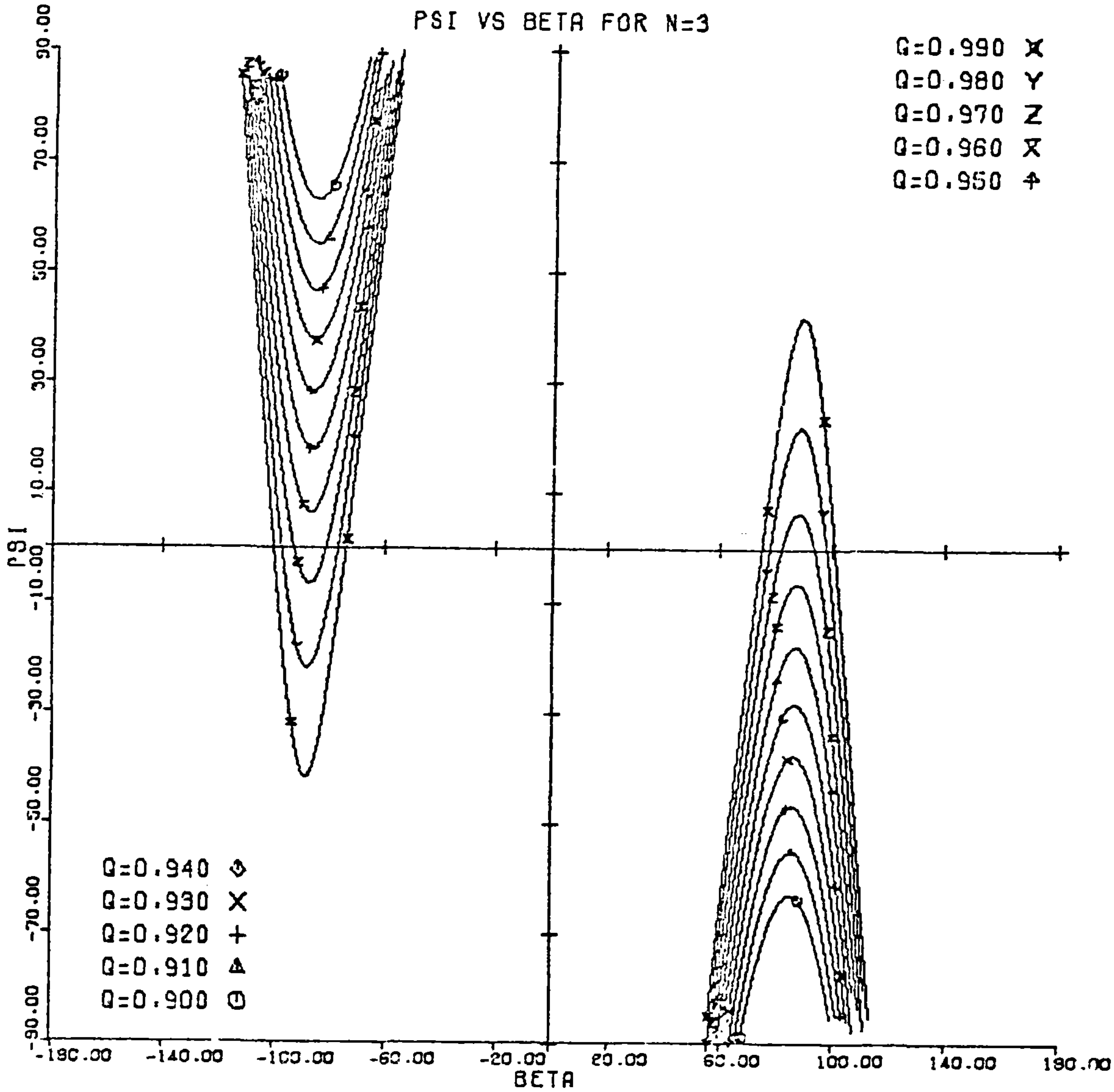

Figure C-8. Spherical Mirror Structure Relation for n=3.

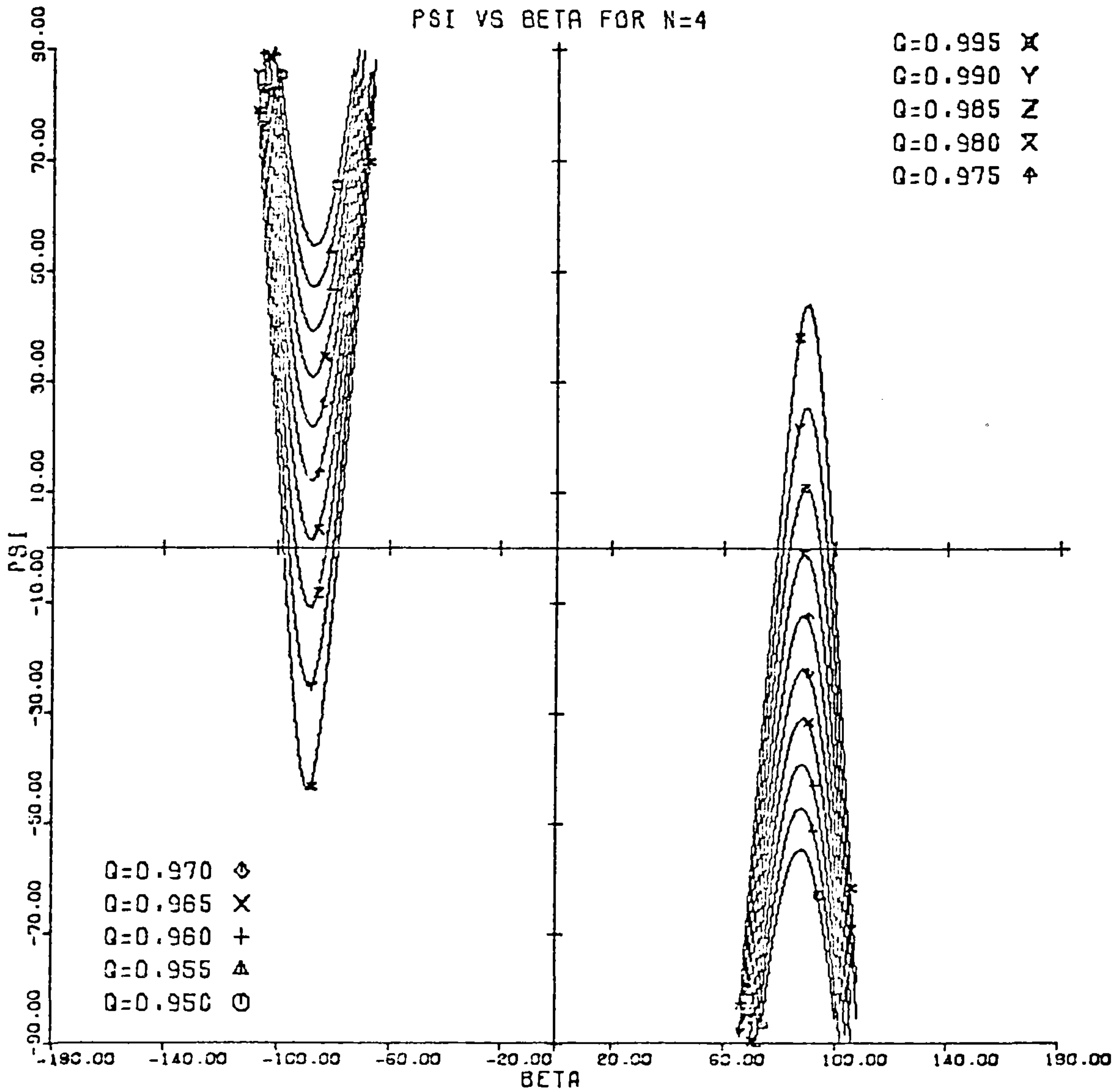

Figure C-9. Spherical Mirror Structure Relation for n=4.

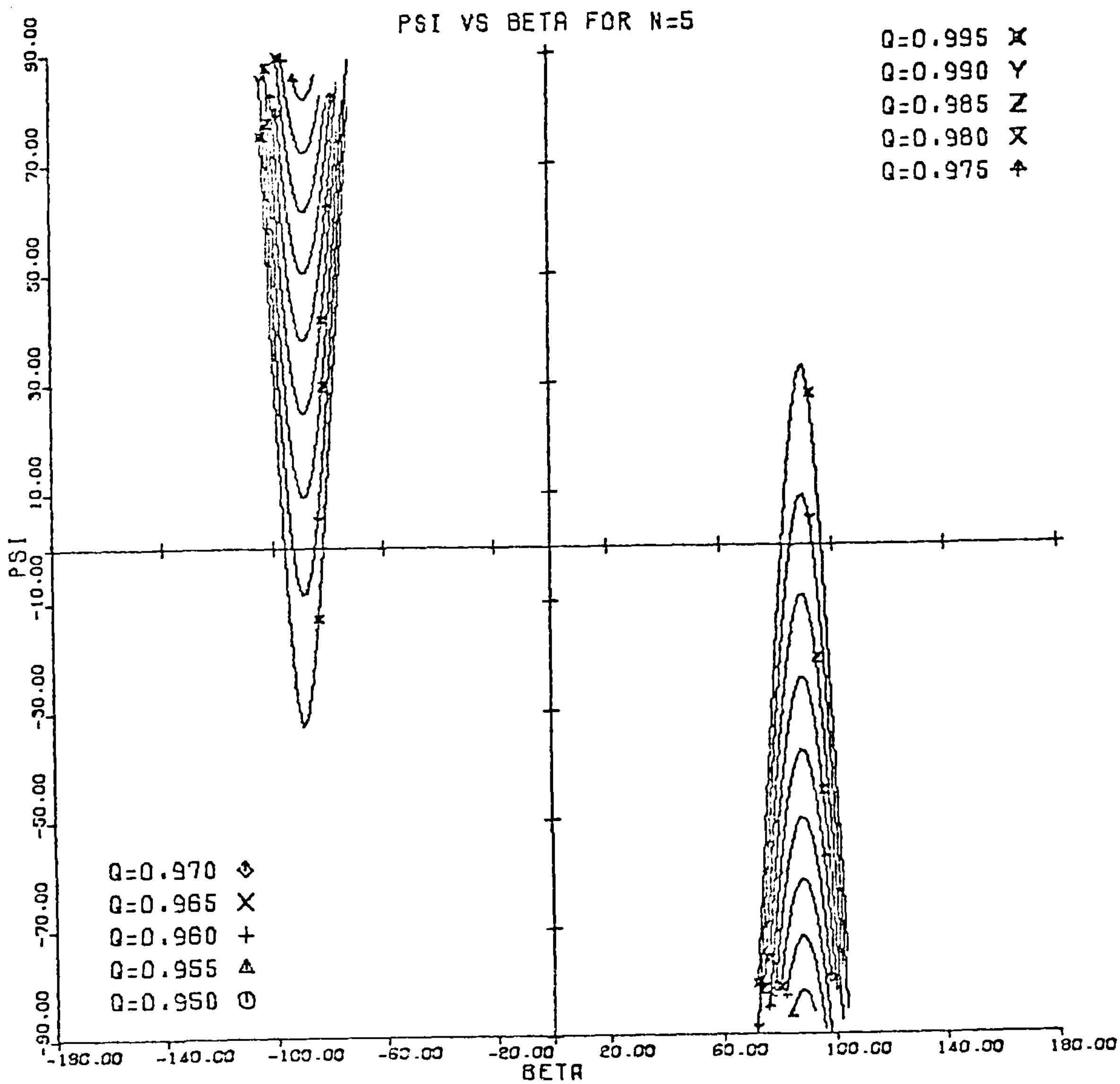

Figure C-10. Spherical Mirror Structure Relation for n=5.

horizontal line through this point. Then, for a given n and q, it is easy to find the values of β, if any, that contribute. The corresponding values of θ may then be determined from the appropriate version+ of (C-33) or (C-33'). Similar curves showing ψ as a function of θ for various q will not be presented here, but they look very similar. A noteworthy difference, however, in that for fixed q, ψ is not a single valued function of θ; the arches go out to a largest value, $\theta_{max}(q)$ and then fall back under themselves. The variable β is much more convenient than θ, particularly for $n>1$.

It is worth noting that the structure relations are significantly simpler for $n = 1$. In this case $\sin\beta$ or $\cos\beta$ can be determined, for given ψ_o and q, as the solutions of a quartic polynomial equation. Use of the algebraic root formula for a quartic gives an extremely fast method for obtaining the desired values of β.

A prominent feature of the point sun concentrations in (C-40) is the presence of singularities in $F_n(\vec{q},\hat{b})$ caused by the vanishing of the denominator factor

$$[\cos\theta_k - 2n\ q\ \cos\beta_k] = 0 \quad . \tag{C-41}$$

This feature is caused by the vanishing of the derivative $\frac{d\psi}{d\beta}$ used in (C-36). In terms of the solution of (C-33) and (C-34),

+For perfectly aligned cones, the appropriate version is (C-33) because backside contributions are impossible.

the vanishing denominator arises from multiple roots:

$$(\theta,\beta)_k \rightarrow (\theta,\beta)_{k'}, \text{ as q is varied.} \qquad \text{(C-42)}$$

These singularities in the concentration are called <u>caustics</u>. The caustic singularities in the concentration are integrable (contain finite power) and the integral of the concentration in (C-40) over the receiver

$$I_o \sum_n \iint F_n(\vec{q},b) \; (q \sin\psi_o \; d\phi dq) = \pi \sin^2\theta_{MAX} = P_{aperture} \qquad \text{(C-43)}$$

simply produces the total power entering the aperture circle of radius $(R)\sin\theta_{max}$.

The location of point sun caustics may be determined easily from Figs. C-6 to C-10. For a perfectly aligned conical receiver of half angle ψ_o, a horizontal line through ψ_o will intersect a curve of constant q either twice or not all. There is, of course, a critical value of q for which the curve is tangent to the ψ_o line. This corresponds to a multiple root as described in (C-42), so a caustic singularity occurs at this value of q. Direct evaluation of the location of point sun caustics can be achieved by solving (C-41) simultaneously with (C-43) and (C-44).

C-5 FINITE SUN CONCENTRATIONS

The contributions of the caustics are made finite by the integrations used in the averaging shown in the finite sun result of Eqn. (C-37). However, one expects and finds very sharp peaks in the distributions $F_n(\vec{q},b)$. One is also warned that numerical integration of the integral shown in (C-37) would require extreme care because of the singularities in the integrand.

How then shall the distributions $F_n(\vec{q},b)$ be evaluated? Should one deal with the simple integrand of (C-27) and the consequent complicated integration limits or should one face the unpleasant integrand of (C-37) with the convenient integration limits? An effective answer is to combine the best features of the two viewpoints. For any numerical integrations the simple, slowly varying integrand of (C-27) will be used and the limits of integration will be visualized in terms of the ranges of integration of ψ and ω in (C-37). The contact, of course, is provided by the structure relations (C-33) and (C-34):

$$\begin{aligned} \beta &= 2n\theta - \psi_{o(\mp)}(n-1)\pi \\ \sin\theta &= q \sin\beta \end{aligned} \qquad \text{(C-44)}$$

where the parenthetical sign is to be used only in association with the optional convention $\beta < 0$, $\theta < 0$ for backside radiation. It is only through the structure relations that the mirror shape ever enters the mathematics.

Except for certain complications involving the two constraints on β and $\tilde{\omega}$, which are

a) $\hat{b}\cdot\hat{v} > 0$

b) the value of θ corresponding to β must be permitted by rim angle and rim shadow constraints, (C-45)

the range of integration on ψ and ω is simply determined. Figs. C-11 and C-12 illustrate two cases:

CASE A: $\psi_o \geq \sigma_n$,

CASE B: $\psi_o \leq \sigma_n$,

and two different integration orders:

$\boxed{\text{I}}$ perform ω integral first,

$\boxed{\text{II}}$ perform ψ integral first.

The details of the algebra have been omitted in the summaries of the two integration procedures given below.

$\boxed{\text{I}}$ If <u>the ω integral is to be performed first</u>, then:

for $\psi_o \geq \sigma$, one will use:

$\boxed{\text{A}}$ $\omega\in[-\omega_m(\psi),\omega_m(\psi)]$ followed by $\psi\in[\psi_o-\sigma\ \psi_o+\sigma]$

and for $\psi_o \leq \sigma$, one will use the two ranges:

$\boxed{\text{B}}$ $\omega\in[0,2\pi]$ followed by $\psi\in[0,\sigma\ \psi_o]$ (C-46)

$\omega\in[-\omega_m(\psi),\omega_m(\psi)]$ followed by $\psi\in[\sigma-\psi_o,\sigma+\psi_o]$

where

$$\omega_{max}(\psi) \equiv \mathrm{Cos}^{-1}\left\{\frac{\cos\sigma\ \cos\psi\cos\psi_o}{\sin\psi\ \sin\psi_o}\right\} ,$$

FIGURE C-11. Geometry associated with integration over finite sun.

CASE A: $\psi_o \geq \sigma$

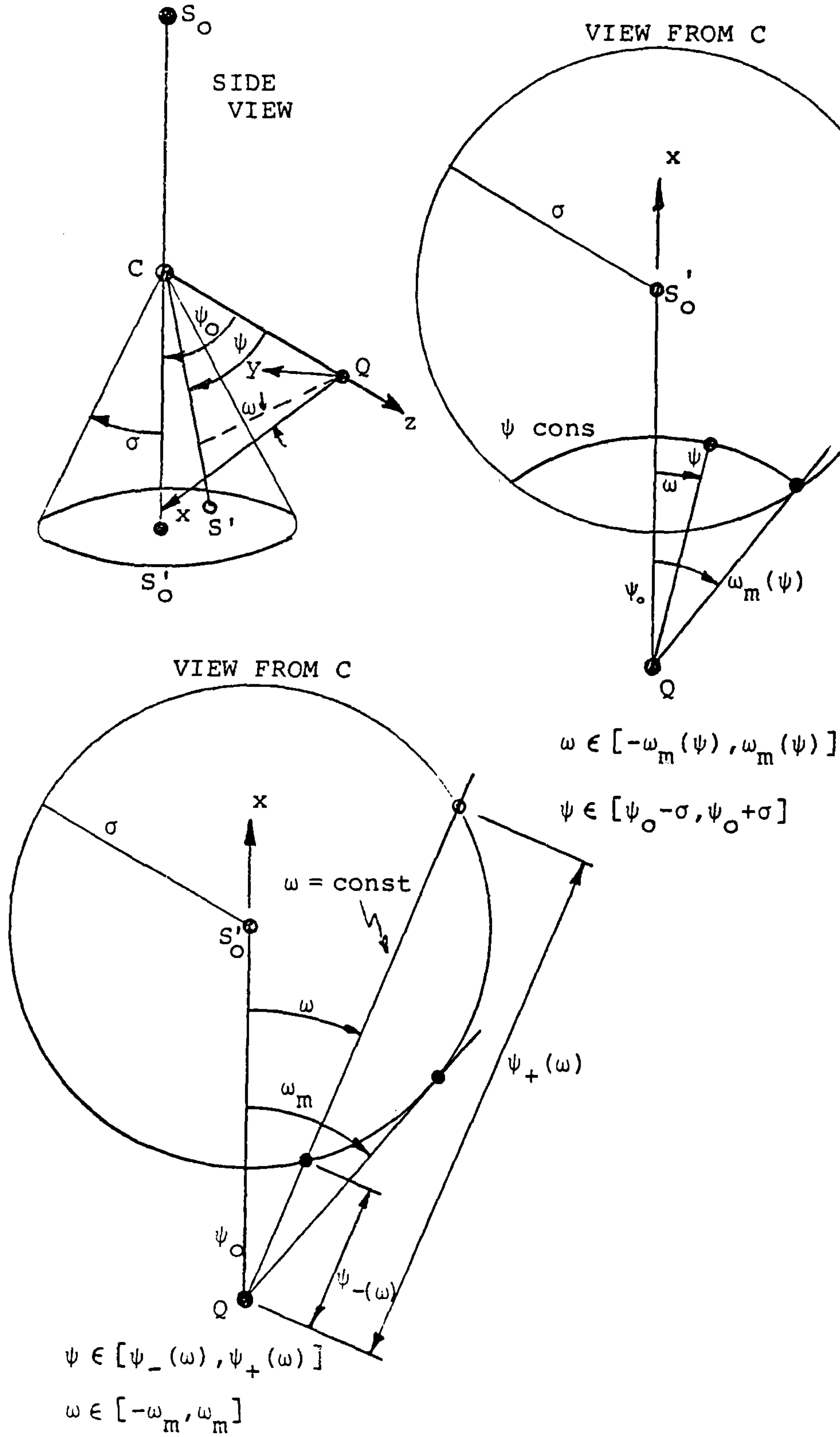

CASE B: $\psi_o \le \sigma$

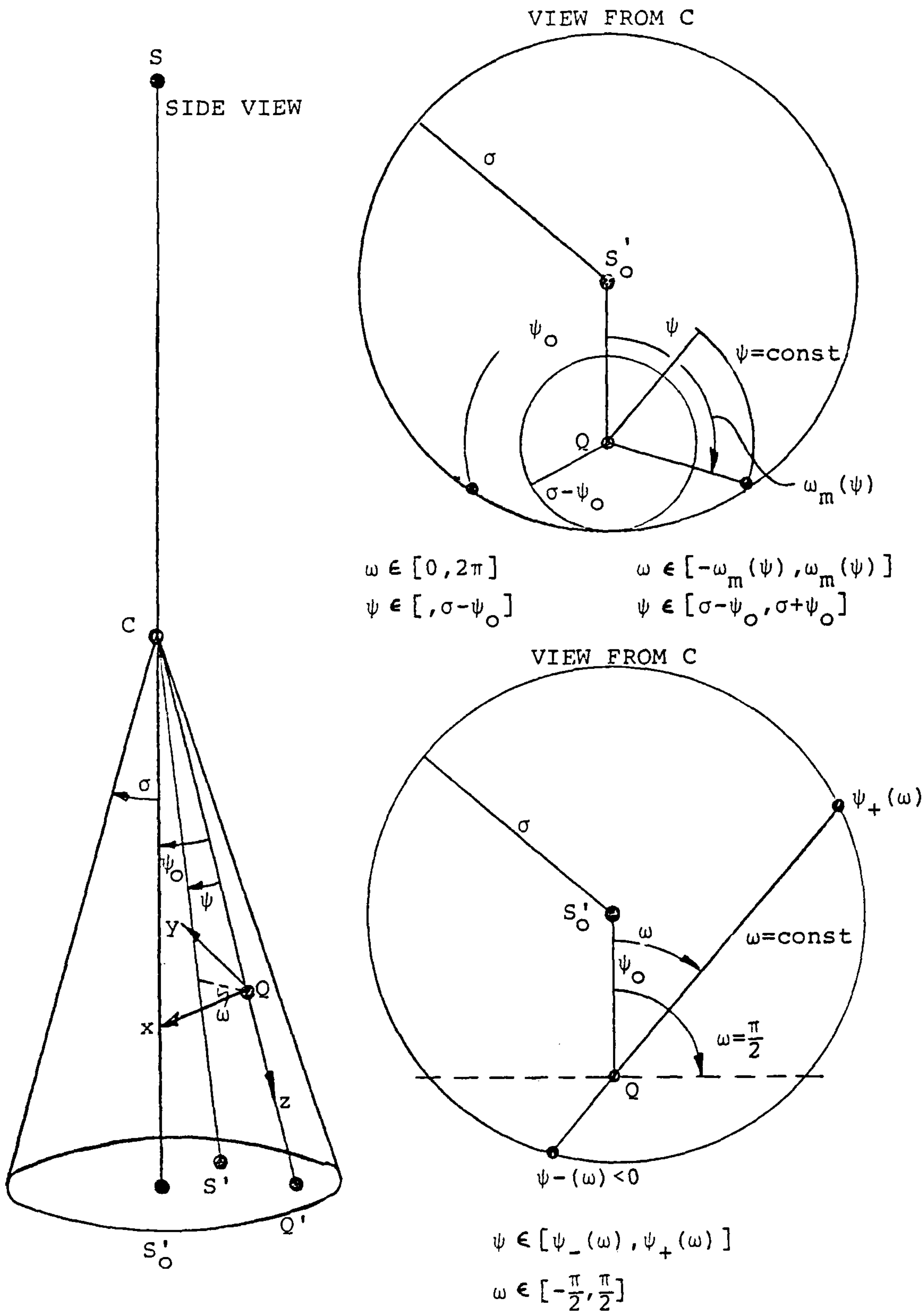

FIGURE C-12. Geometry associated with integration over finite sun.

$\boxed{\text{II}}$ On the other hand, if the ψ integral is to be performed first, then:

for $\psi_o \geq \sigma$, one will use:

$\boxed{\text{A}}$ $\psi \in [\psi_-(\omega),\ \psi_+(\omega)]$ followed by $\omega \in [-\omega_m, \omega_m]$

and for $\psi_o \leq \sigma$, one will use:

$\boxed{\text{B}}$ $\psi \in [\psi_-(\omega), \psi_+(\omega)]$ followed by $\omega \in [-\frac{\pi}{2}, \frac{\pi}{2}]$

(C-47)

where

$$\omega_m \equiv \mathrm{Cos}^{-1} \sqrt{1 - \left(\frac{\sin\sigma}{\sin\psi_o}\right)^2}$$

and

$$\psi_{\pm}(\omega) \equiv \mathrm{Sin}^{-1} \left\{ \frac{\cos\sigma \sin\psi_o \cos\omega \pm \cos\psi_o \sqrt{\sin^2\sigma - \sin^2\psi_o \sin^2\omega}}{1 - \sin^2\psi_o \sin^2\omega} \right\}.$$

The limit $\psi_-(\omega)$ will be negative for $\psi_o \leq \sigma$, consistent with device 1) for avoiding (C-33') discussed earlier.

The integrals required for (C-25) are obtained by substituting (C-29) into (C-27), using $\tilde{\omega} = \omega + \pi$:

$$F_n(\vec{q},\hat{b}) = \frac{1}{\Omega_s} \iint_{\Omega_{Mn}} [b_q \cos\beta - (b_x \cos\omega + b_y \sin\omega)\sin\beta] \sin\beta\, d\beta\, d\omega. \tag{C-48}$$

The components of $\hat{b}$ depend on $\vec{q}$ and ψ_o, the zenith of the principal sun axis from the direction $\vec{q}$. Limits of integration on ω are indicated in (C-46) or (C-47). On the other hand, limits of integration for β are not shown in (C-46) or (C-47), and must be obtained from the structure relation (C-44) using the limits of integration shown for ψ.

Figures C-6 to C-10 may be used to visualize the connection between the ψ range and the β range. The ranges for ψ shown in (C-46) or (C-47) may be located on the vertical axis in these figures and, then, a horizontal band imagined representing the ψ range. If one employs device 2) for avoiding (C-33'), then a second horizontal band is imagined using the negative of the ψ range. The intersection of the ψ band with the proper q-curve then determines (by vertical projection) the corresponding regions of integration in β. Under various conditions there may be no permitted β ranges corresponding to the ψ range.

Consider cases in which the required ψ band contains the horizontal ψ line which is tangent to the relevant q- curve. For this value of q, the β range is connected, but as q is increased the β range will divide into two unconnected intervals which rapidly spread apart from each other. As q is decreased, on the other hand, the size of the (connected) β range shrinks rapidly and finally disappears. [Expressions are easily derived from the structure relation for determination of the critical values of q for which the β range divides or disappears.] <u>From the point of view of the β integration, the caustic peaks, found in the neighborhood of the turning points q such that $\left(\frac{d\psi}{d\beta}\right)_q = 0$, are produced by the rapidly changing size of the permitted range of β integration.</u>

The general theory of this approach has now been presented and the method of calculation has been indicated. There remains, however, one very difficult matter: the implementation of the constraints in (C-45).

C-6 CONSTRAINTS ON THE INTEGRATION FOR FINITE SUN CONCENTRATION

The contraints on the integration limits will be described for integration procedure II : performing the ψ integral first. Referring to Figs. C-11 and C-13, one can see that for constant ω, the ψ integral is done in a plane as illustrated in Fig. C-3. This is very advantageous for describing the effect of the dish rim angle on the range of integration, as shown in Eqn. (C-39). Together with the requirement for positive $\hat{b}\cdot\hat{v}$, this produces the constraints of (C-45). However, the situation is somewhat more complicated than (C-45) implies.

The contraints placed by the $\hat{v}\cdot\hat{b}$ requirement are adequately stated by Eqn. (C-30). In order to evaluate the contraints placed by the rim angle, however, one is referred to Fig. C-13. A suitable collector-fixed coordinate system can be chosen for simple representation of $\theta_{rim}(\phi)$. In general $\theta_{rim}(\phi)$ is not constant, but for circular rim dishes the collector-fixed coordinate system can be chosen so that $\theta_{rim}(\phi)$ is constant.

Once $\theta_{rim}(\phi)$ is determined, then, for a given $\hat{e}_s'$

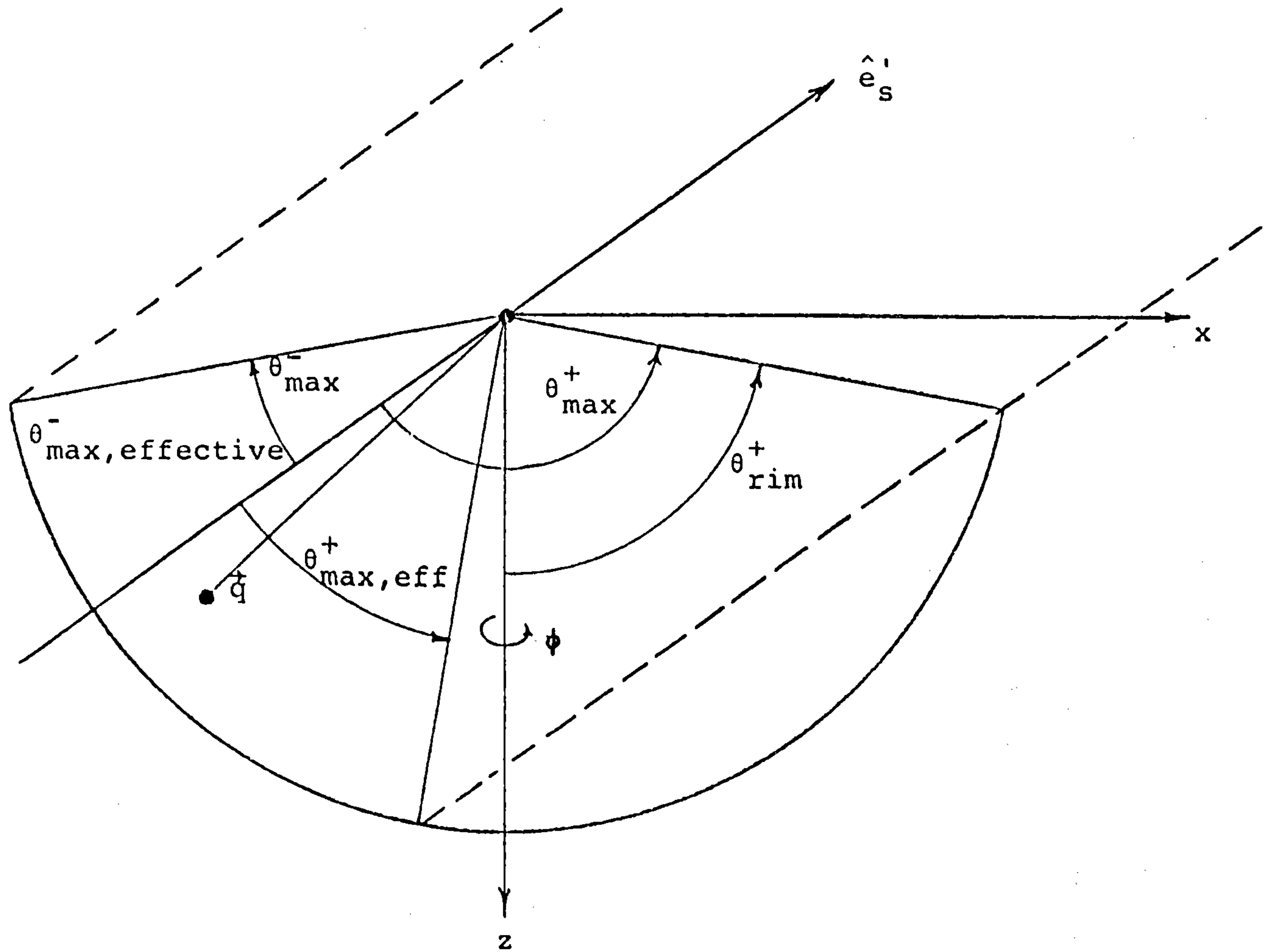

Figure C-13. Illustration of Concept of θ Constraints.

(value of ϕ), the angle θ_{max} can be obtained. [The details depend upon the choice of coordinate systems and are not included here.] The value of $\theta_{max,eff.}$ is then obtained from (C-39). For a given $\hat{e}'_s$ there are two zenith angles designated as

$$\theta^{-}_{max,\ eff.}(\phi) \qquad \text{and} \qquad \theta^{+}_{max,\ eff.}(\phi)$$

as illustrated in Fig. C-13.

The skeletal structure of the constraints has now been exposed. Since it is actually desired to integrate the optical concentration as expressed in (C-27), the integration constraints must now be expressed in terms of β.

The structure relations (C-33) and (C-34) are utilized to convert integration limits expressed in terms of ψ and θ to limits in terms of β. When the limits, $\psi_{\pm}$, defined as part of integration procedure II above, are inserted into (C-33) and (C-34), actual limits without constraints are obtained, but due to the multiplicity of the roots, there may be several $\beta_{\pm}$ pairs. All such pairs must be utilized. However, for simpler discussion, the application of the contraints will be illustrated only for a special case of interest: a perfectly aligned receiver. For an absorber whose axis is aligned along the principal sun axis, light can only reach the absorber from one side ($\tilde{\omega} \simeq \pi$), eliminating some of the $\beta_{\pm}$ pairs. The $\hat{v}\cdot\hat{b}$ constraint forces the pairs to lie in β $[0,\pi]$.

The ψ integration is over $[\psi_{-},\psi_{+}]$, which corresponds to either one or two pairs of $\beta_{\pm}$. Consider, for example, the ψ vs. β curve of Fig. C-6. If lines of constant $\psi = \psi_-$ and $\psi = \psi_+$ are drawn, one sees that each line cuts a line of constant q twice or no times (a point of tangency being a trivial limit of this statement). The integration is for constant q so only those values of β corresponding to the portion of the constant q curve that exist between the $\psi_\pm$ lines can be used. The following solutions to the structure relations are thus defined:

$$\beta_1 = \beta_< (q, \psi_-)$$

$$\beta_4 = \beta_> (q, \psi_-)$$

$$\beta_2 = \begin{cases} \beta_<(q, \psi_+) & \text{if this root exists} \\ \dfrac{\beta_1 + \beta_4}{2} & \text{otherwise} \end{cases}$$

$$\beta_3 = \begin{cases} \beta_>(q, \psi_+) & \text{if this root exists} \\ \dfrac{\beta_1 + \beta_4}{2} & \text{otherwise ,} \end{cases} \qquad \text{(C-49)}$$

and it is further required that

$$0 \leq \beta_i \leq \pi , \qquad i = 1, 2, 3, 4 \quad .$$

The <,> subscripts respectively refer to the smaller and larger solution for β in the above range. Note that in some instances β_2 and β_3 do not exist as solutions to the structure relations. By defining them as above, we can always work with two β integration ranges, which are

$$\beta \in [\beta_1, \beta_2] \tag{C-50}$$

and

$$\beta \in [\beta_3, \beta_4]$$

These are the β limits without constraints. The back rim cutoff viewed at ψ corresponds to $\theta^-_{max,\ eff.}(\psi)$, and the front rim cutoff at ψ corresponds to $\theta^+_{max.\ eff.}(\psi)$. The values of θ between these angles correspond to the illuminated portion of the dish and already include shadowing effects. The resulting constraints on the β variable are described in terms of the following definitions

$$\begin{aligned}
\beta_{5\pm} &\equiv \mathrm{Sin}^{-1}\left\{\frac{\sin[\theta^-_{max,\ eff.}(\psi_\pm)]}{q}\right\} \\
\beta_{6\pm} &\equiv \mathrm{Sin}^{-1}\left\{\frac{\sin[\theta^+_{max,\ eff.}(\psi_\pm)]}{q}\right\} \\
\beta_{7\pm} &\equiv \pi - \beta_{6\pm} \\
\beta_{8\pm} &\equiv \pi - \beta_{5\pm}
\end{aligned} \tag{C-51}$$

which satisfy structure relation (C-34).

The constraint procedure can be visualized somewhat more graphically by referring to the exploded β-axis drawing in Fig. C-14. The top arch corresponds to the β integration without constraints. The integration should be carried out in the clear window-like regions between β_1, β_2 and β_3, β_4 (except as blocked by other window shades). Although the drawing seems

FIGURE C-14. Exploded β-axis indicating integration ranges.

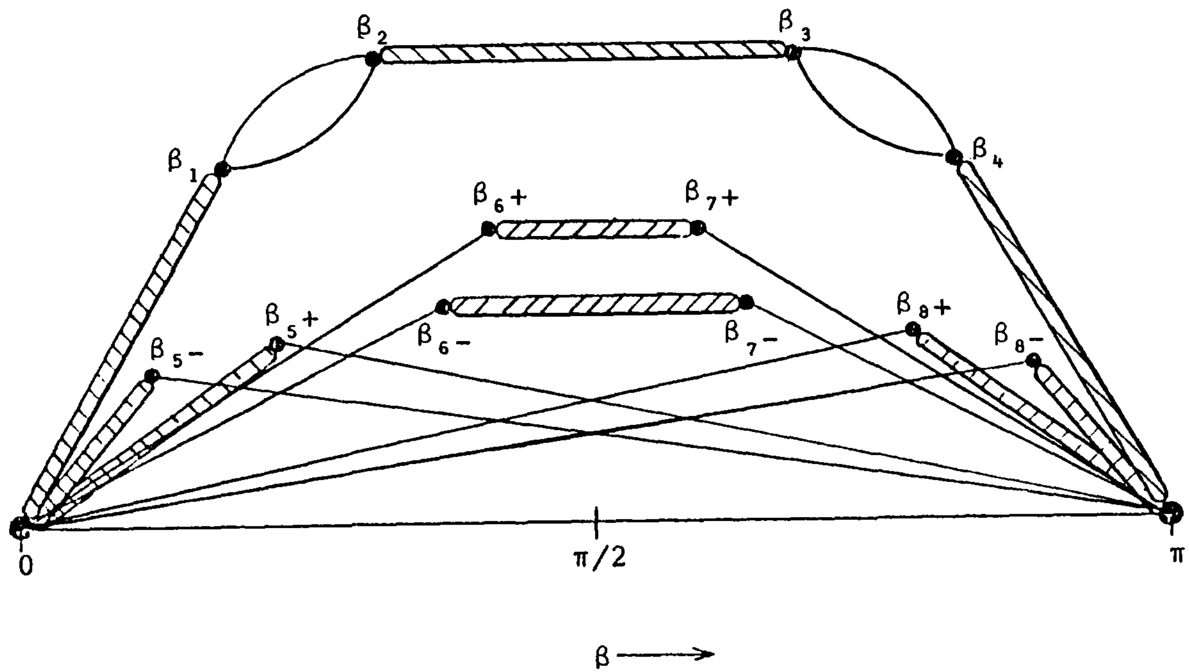

to imply $\beta_2 \neq \beta_3$, $\beta_3 > \pi/2$, and $\beta_4 > \pi/2$, these conditions may or may not exist. Only the ordering of these quantities is to be implied. Note that β_2, β_3 correspond to the intersection of the q = constant curve by ψ_+ and β_1, β_4 correspond to the ψ_- intersection.

The additional shaded regions are forbidden β regions and the integration is carried out only where the windows are not blocked by forbidden regions after the picture is put back together. The $\beta_{5\pm}$ and $\beta_{8\pm}$ correspond to limitations imposed by the backside dish rim and the $\beta_{6\pm}$ and $\beta_{7\pm}$ correspond to the frontside dish rim. In various cases the shades move and change their lengths. The only ordering implied is

$$\beta_{6\pm} \leq \pi/2 \leq \beta_{7\pm}$$

and (C-52)

$$\beta_{5\pm} \leq \pi/2 \leq \beta_{8\pm} \quad .$$

The quantities with subscript - are associated with ψ_- while the + subscripted values are associated with ψ_+. The following flow chart Fig. C-15 explains more concisely the orderly application of the constraints.

This completes the constraint procedure for the case where the absorber is perfectly aligned along the focal line, a prime case of interest. The same type of strategy must be applied in the more general case. The above proced-

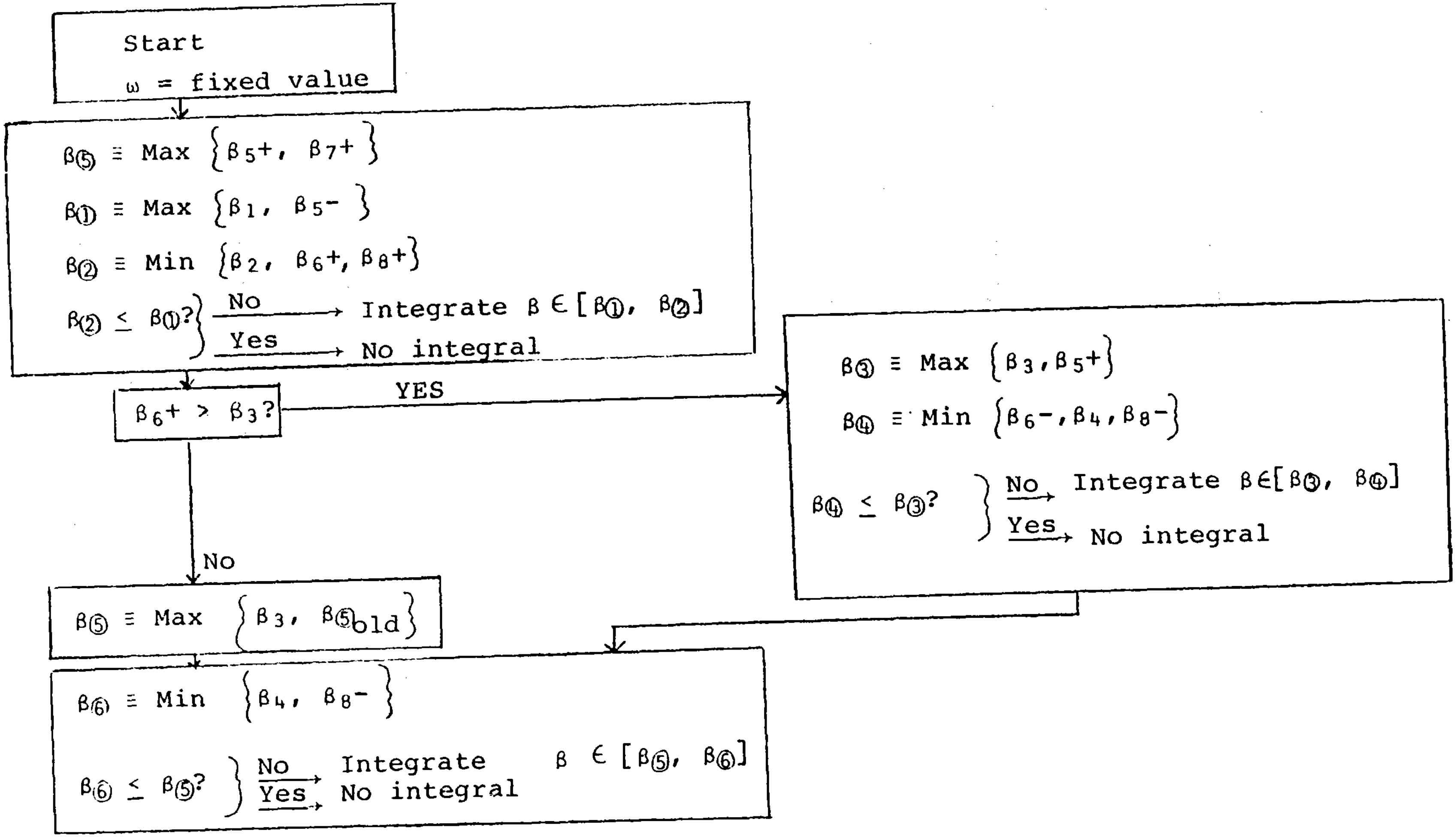

Figure C-15. Flow Chart for Application of Constraints ures have been utilized to produce the optical concentration results which are described below.

The analysis contained in this section is based on the assumption of perfect geometry for the collector. However, the notion of an effective sun size has been mentioned as a device for accounting for mirror errors. No policy has been suggested, though, for choosing the effective sun size. In the following section sources of mirror errors are discussed and a reasonable method of relating the effective sun size to measurable mirror errors is suggested.

C-7 AN EFFECTIVE SUN SIZE METHOD TO ACCOUNT FOR MIRROR ERRORS

In any practical implementation of a spherical segment mirror, there will be errors in the curvature of the mirror surface. The errors can be classed into two types; microscopic and macroscopic. The microscopic errors are due to surface defects on the order of a few wavelengths in size. These defects scatter the light slightly around the direction of spectral reflection. The result is that a perfectly collimated beam of light will diverge at some small angle after reflection. The macroscopic error is caused by defects on a scale of several hundred wavelengths and larger. It can be considered as an error in the unit normal $\hat{n}$ at each point. This error does not cause the ray to spread, but it directs the entire ray along a wrong direction.

The analysis described in C-6 assumes a perfect spherical geometry. One would like to develop a method of accounting for errors and still take advantage of the previous work. One possibility is to specify locally at each point on the mirror a normal vector $\hat{n}'$ which deviates slightly from the ideal normal $\hat{n}$. This is equivalent to expressing the structure relations not as explicit equations as in (C-33) and (C-34), but as a table of pointwise data. Besides the obvious defect of requiring an enormous number of computer operations, this method requires detailed knowledge of the error on the collector surface. This is information that is not available until a dish is constructed and any calculations based on an arbitrary assignment of errors would not be particularly useful. This latter defect could be corrected by assigning a probability distribution of the errors and then doing a Monte Carlo analysis of a number of dishes in order to obtain an expected flux distribution. This, however, requires a prohibitively large amount of computer time. A practical method that considers both microscopic and macroscopic errors is described below.

The effect of both microscopic and macroscopic errors is to spread the solar image. Since the errors make the image larger, one way to model the error is to use an effective sun size larger than the true sun size and then do the calculations with the assumption of perfect spherical geometry. In this section the relationship between sources of optical error and the effective sun size is examined. This is an effort to obtain the expectation of the image size prior to calculating the optical power concentration. The result is an expected concentration distribution from an ensemble of distributions with random errors in the geometry. Although this is not a rigorous method of obtaining an expected concentration distribution, the saving in computer time is very significant. In fact, it makes the calculation practical when it would be prohibitively expensive otherwise. The result allows a reasonable assessment of the effect of errors in the geometry.

Each time the light reflects from the mirror surface, new error accumulates and the effective sun size becomes larger. An effective sun size, σ_n, anticipated in the theoretical approach by Eqn. (C-26), will be assigned that is dependent on the number of reflections n. The macroscopic error will be treated as a random variable, but the microscopic error is deterministic. The microscopic error will be considered to be a small angular spread $\sigma\delta$ that is independent of the angle of incidence of the light. The use of such an average value for δ is reasonable. The quantity δ is a unitless number that expresses the angular spread in multiples of the true solar angular radius σ. It is not a random variable, but is a function of the material. The macroscopic error will be treated as a deviation in the ideal normal $\hat{n}$ as already mentioned,

$$\hat{n}' = \frac{\hat{n} + \vec{e}}{\sqrt{1 + e^2}} \tag{C-53}$$

where

$$\hat{n}' = \begin{pmatrix} \sin\gamma\sigma\cos\eta \\ \sin\gamma\sigma\sin\eta \\ \cos\gamma\sigma \end{pmatrix} \tag{C-54}$$

with $\gamma\sigma$ a zenith angle measured from $\hat{n}$ and η an azimuth measured from a convenient axis. Equation (C-54) expresses $\hat{n}'$ in a coordinate system that has $\hat{n}$ playing the role of the z-axis. The zenith angle is measured by the random variable

γ which is the number of the solar angular radii between $\hat{n}$ and $\hat{n}'$. The angle γ is a zero mean random variable with some probability distribution $P(\gamma)$. The azimuth η is a random variable that is uniformly distributed,

$$\eta \epsilon [0, 2\pi] \quad . \tag{C-55}$$

The random variables γ and η are assumed to be independent of each other.

The error analysis is broken into two parts. These are designated the ray plane error and the transverse plane error according to which plane the error is measured in. The total error is projected into these two planes for convenience of measurement. The ray plane is the plane containing $\hat{e}_s$ and $\vec{q}$. The transverse plane is perpendicular to $\hat{e}_s$. Figure C-16 illustrates these two errors and the planes involved. The coordinate system used for expressing $\hat{n}'$ is chosen so that the $\hat{n}$-$\hat{r}$ plane is coincident with the ray plane. The third axis, $\hat{t}$, lies always in the transverse plane. With this choice of coordinate system it can be seen that

$$\begin{aligned} \sin \epsilon\sigma &= \sin \gamma\sigma \cos\eta \Big/ \sqrt{\cos^2\gamma\sigma + \sin^2\gamma\sigma\cos^2\eta} \\ \sin \xi\sigma &= \sin \gamma\sigma \sin\eta \Big/ (\hat{n}'\cdot\hat{e}_s) \end{aligned} \tag{C-56}$$

where ϵ is the angle between the projection of $\hat{n}$ and $\hat{n}'$ in the ray plane and ξ is the angle between the projection of $\hat{n}$ and $\hat{n}'$ in the transverse plane as illustrated in Fig. C-16.

The errors will be assumed to be small so that

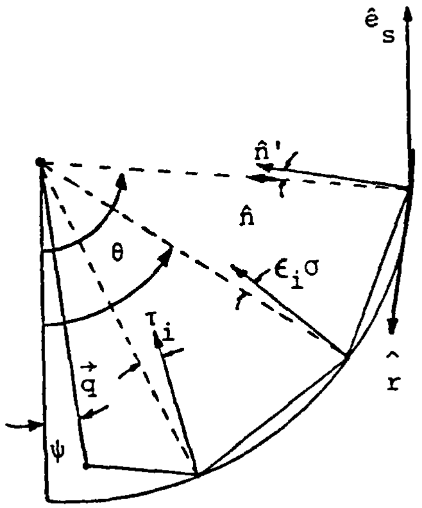

(a) Ray Plane View

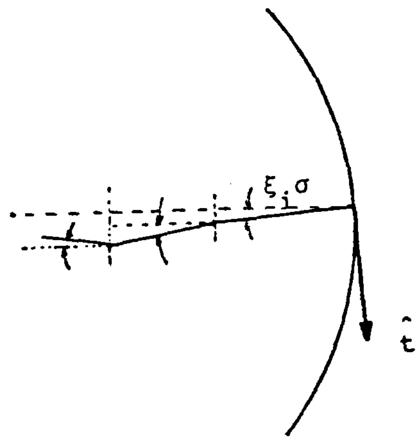

(b) Transverse Plane View

Figure C-16. Reflection Error in the Ray Plane and Transverse Plane, due to Mirror Errors.

$$\hat{n}_i' \cdot \hat{e}_s \simeq \hat{n}_i \cdot \hat{e}_s = \cos\tau_i$$

and

$$\sqrt{\cos^2\gamma\sigma + \sin^2\gamma\sigma\cos^2\eta} \simeq 1 - \frac{\gamma^2\sigma^2\sin^2\eta}{2} \simeq 1$$

Under this condition, (V-4) becomes

$$\begin{aligned} \epsilon_i &= \gamma_i \cos\eta_i \\ \xi_i &= \gamma_i \sin\eta_i / \cos\tau_i \end{aligned} \qquad \text{(C-57)}$$

Also, since the errors are small, the ray-plane analysis can be accomplished without regard to the error in the transverse plane. This allows one to think of the ray always staying in the ray plane for the purpose of measuring the angles indicated in Fig. C-17. In the transverse analysis, no significant error will be introduced by assuming the reflection angle to always be θ as indicated in Fig. C-18(a).

The ray plane error will be considered first. Referring to Fig. C-17, it is seen that

$$\kappa = \theta - \psi - \sum_{k=1}^{n-1} \Delta_k \qquad \text{(C-58)}$$

$$\Delta_k = \pi - 2\left(\theta - 2\sum_{i=1}^{k} \epsilon_i\sigma + \sum_{i=1}^{k} \delta_i\sigma\right) \qquad \text{(C-59)}$$

so that the structure relations with errors are

$$\psi = 2n\theta - \beta - (n-1)\pi - \sigma \sum_{k=1}^{n} \{[4(n-k)+2]\epsilon_k - [2(n-k)+1]\delta_k\} \qquad \text{(C-60)}$$

and

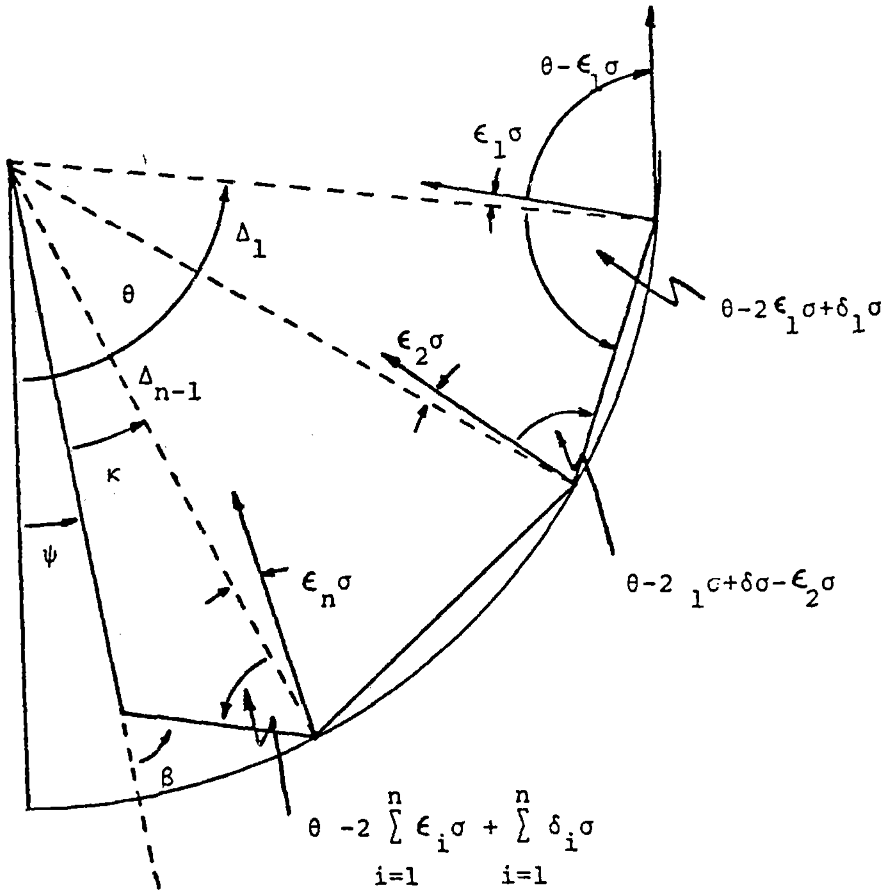

Figure C-17. Analyis of Ray Plane Error.

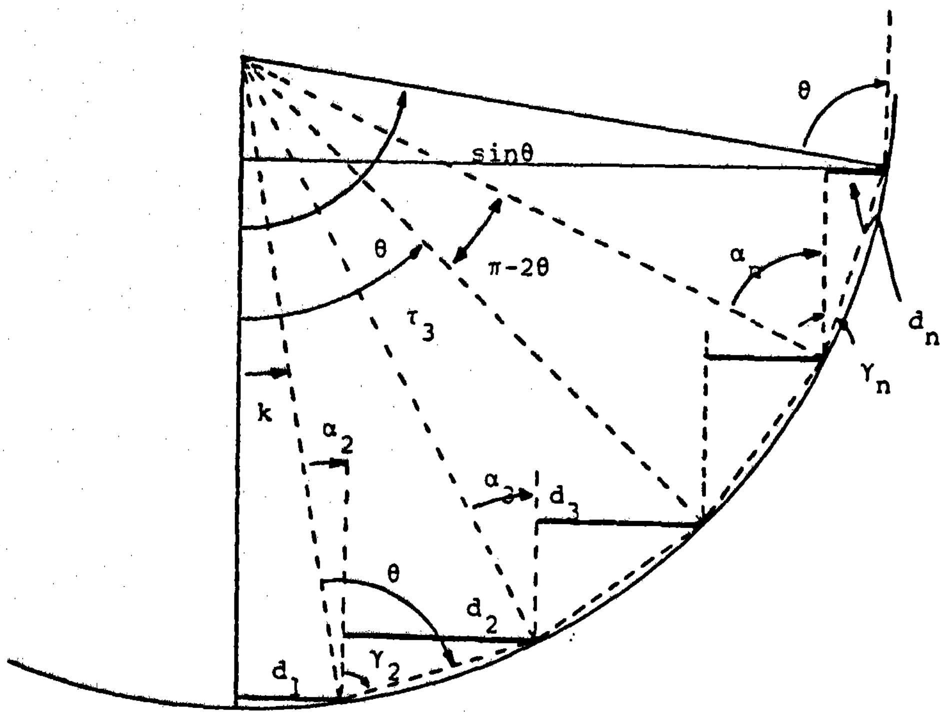

(a) Ray Plane View.

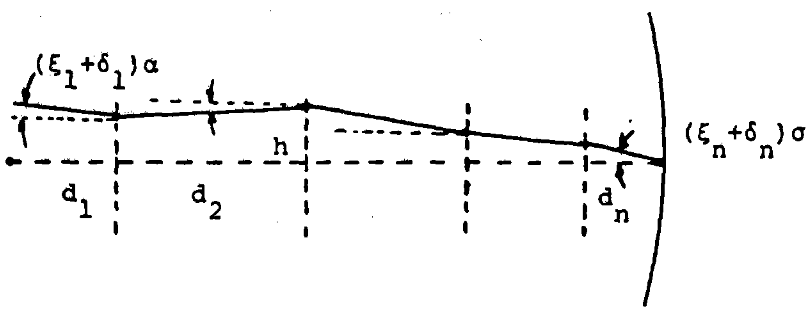

(b) Transverse Plane View

Figure C-18. Analysis of Transverse Plane Error.

$$q \sin \beta = \sin(\theta \;\; - \sigma \sum_{k=1}^{n} \; (2\epsilon_k = \delta_k)) \quad . \qquad \text{(C-61)}$$

The solar image is largest at q=1 and the light has the greatest path length to accumulate error when received at q=1. For this reason, the worst image degradation due to errors occurs when q=1. The effective sun size will be based on the worst image degradation. Therefore, with q=1, equation (C-61) produces

$$\beta = \pi - \theta + \sigma \sum_{k=1}^{n} \; (2\,\epsilon_k - \delta_k) \qquad \text{(C-62)}$$

for the worst case. Equations (C-60) and (C-62) combine to give

$$\psi = 2(n+1)\theta \;\; - n\pi \;\; - \sigma \sum_{k=1}^{n} \{4(n-k+1)\epsilon_k - 2(n-k+1)\delta_k\} \quad . \qquad \text{(C-63)}$$

Now consider the case with no errors; $\epsilon_k = \delta_k = 0$. As θ goes from θ_o to $\theta_o + \sigma$, ψ goes from ψ_o to $\psi_o + \Delta\psi$

$$\begin{aligned} \Delta\psi &= (2n+1)\sigma \\ \sigma &= \frac{\Delta\psi}{2n+1} \end{aligned} \qquad \text{(C-64)}$$

Eqn. (C-64) gives the solar angular radius in terms of $\Delta\psi$. In order to determine an effective sun size with errors, $\Delta\psi_n$ is calculated

$$\begin{aligned} \Delta\psi_n &= \psi(\theta_o + \sigma, + \text{errors}) - \psi(\theta_o, \text{no errors}) \\ &= (2n+1)\sigma \;\; - \sigma \sum_{k-1}^{n} \; (n-k+1)(4\epsilon_k - 2\,\delta_k)\} \end{aligned} \qquad \text{(C-65)}$$

An effective sun size with errors that will give the same worst case image when used with perfect geometry that the true sun size does when used with errors can be obtained from the mean square value of $\Delta\psi_n$

$$\sigma_n^2 \equiv \frac{\langle\Delta\psi_n^2\rangle}{(2n+1)^2} \quad . \tag{C-66}$$

The ϵ_k are identically distributed random variables with zero mean and are assumed independent of each other. The $\delta_k = \delta$ for all k. The mean square value of $\Delta\psi_n$ is therefore

$$\langle\Delta\psi_n^2\rangle = \sigma^2 \quad \{(2n+1)^2 + 16 \sum_{k=1}^{n} k^2 \langle\epsilon^2\rangle + 4 \sum_{k=1}^{n} k^2 \delta^2$$

$$+ 4(2n+1) \sum_{k=1}^{n} k \delta\} \quad . \tag{C-67}$$

The mean square value of ϵ is

$$\langle\epsilon^2\rangle = \int_0^\infty \int_0^{2\pi} \gamma^2 \cos^2\eta P(\gamma) d\gamma \frac{d\eta}{2\pi}$$

$$= \frac{\langle\gamma^2\rangle}{2} \tag{C-68}$$

since η is uniformly distributed. The two sums over k can be performed with the results

$$\sum_{k=1}^{n} k = \frac{n(n-1)}{2}$$

$$\sum_{k=1}^{n} k^2 = \frac{n(n+1)(2n+1)}{6} \tag{C-69}$$

The effective sun size with errors can now be obtained by combining (C-66), (C-67), (C-68), and (C-69),

$$\sigma_{nR} = \sigma \sqrt{1 + \frac{2n(n-1)}{(2n+1)}\,\delta + \frac{2}{3}\,\frac{n(n+1)}{(2n+1)}(\delta^2+2<\gamma^2>)} \qquad \text{(C-70)}$$

where the subscript R indicates that this is the effective sun size due to errors in the ray plane. The angular spread of the ray due to microscopic errors normalized by σ is δ and the mean square angular error in the surface normal normalized by σ is $<\delta^2>$.

The effective sun size due to the transverse plane errors must also be calculated. The analysis can be visualized with the aid of Fig. C-18. As shown in part (b) of the figure, any angular error contributes to a transverse error h in proportion to the distance traveled along the patch d_i,

$$\begin{aligned}\Delta h_i &= d_i \tan[(\xi_i + \delta_i)\sigma] \\ &\simeq d_i(\xi_i + \delta_i)\sigma\end{aligned} \qquad \text{(C-71)}$$

since the errors are assumed small. Note that the path length d_i is measured in the transverse plane (Fig. C-18(a)) since distance traveled perpendicular to the transverse plane cannot accumulate transverse error. Referring to Fig. C-18(a), one sees that

$$\alpha_m = \kappa + (m-1)(\pi-2\theta) \qquad \text{(C-72)}$$

where

$$\kappa = (2n-1)\theta - (n-1)\pi \quad . \tag{C-73}$$

It is also clear that

$$\gamma_m = \theta - \alpha_m \tag{C-74}$$

which when combined with (C-72) and (C-73) yields

$$\gamma_m = (n-m+1)(\pi-2\theta) \quad . \tag{C-75}$$

The parallel distance traveled after each reflection is (Fig. C-18(b))

$$d_m = 2 \cos\theta \sin\gamma_m = 2 \cos\theta \sin((n-m+1)(\pi-2\theta)). \tag{C-76}$$

The total transverse deviation h_n due to accumulated errors and the non-zero true sun size σ is

$$h_n = \sigma \sin\theta + \sum_{m=1}^{n.} (d_m)(\xi_m + \delta_m)\sigma \tag{C-77}$$

The mean squared angular spread which is just the square of the effective solar angular radius due to transverse plane errors is

$$\sigma_{nT}^2 = \frac{\langle h_n^2 \rangle}{\sin^2\theta} \tag{C-78}$$

$$= \sigma^2 [1 + \sum_{m=1}^{n} \delta \frac{d_m}{\sin\theta} + \sum_{m=1}^{n} \frac{d_m^2}{\sin^2\theta} (\langle \xi^2 \rangle + \delta^2)]$$

since the $\delta_i = \delta$ for all i.

Since the accumulated transverse error is greatest for the longest path lengths d_m, the worst effective sun size occurs when θ is the largest value possible for the given n, that is

$$\theta = \frac{n\pi}{2n+1} \quad . \tag{C-79}$$

The angle τ_i is

$$\tau_i = \theta-(n-1)(\pi-2\theta)$$

$$= \frac{i\pi}{2n+1}$$

so that the random variables ξ_i are

$$\xi_i = \frac{\gamma_i \sin\eta_i}{\cos\left(\frac{i\pi}{2n+1}\right)} \quad .$$

The mean square value of ξ_i is given by

$$\langle\xi^2\rangle_i = \int_0^\infty \int_0^{2\pi} \frac{\gamma_i^2 \sin^2\eta_i P(\gamma) d \frac{d\eta}{2\pi}}{\cos^2 i\pi/2n+1}$$

$$= \frac{\langle\gamma^2\rangle}{2\cos^2\frac{i\pi}{2n+1}} \tag{C-80}$$

Combining (C-76), (C-79), and (C-80) with (C-78) yields the square of the effective sun size due to transverse errors

$$\sigma_{nT}^2 = \sigma^2\{1 + \frac{2\delta}{\tan\left(\frac{n\pi}{2n+1}\right)} \sum_{m=1}^{n} \sin\left(\frac{m\pi}{2n+1}\right)$$

$$+ \frac{2}{\tan^2\left(\frac{n\pi}{2n+1}\right)} \sum_{m=1}^{\wedge} \sin^2\left(\frac{m\pi}{2n+1}\right) (\langle\gamma^2\rangle/[\cos^2\left(\frac{m\pi}{2n+1}\right)] + 2\delta^2)\} \quad . \tag{C-81}$$

Equation (C-81) is the square of the effective sun size due to the transverse plane errors. This needs to be combined with the effective sun size due to ray plane errors to obtain a total effective sun size.

Since σ_{nR} and σ_{nT} are not necessarily equal, they must be averaged in some logical manner. The errors in the collector tend to make the solar image elliptical when viewed from a given ray plane. However, the solar image will have circular symmetry and the optical analysis treats the sun as a circular disc. A definition of σ_n that preserves the area of the effective solar image will be used:

$$\pi\sigma_{nR}\sigma_{nT} = \pi\sigma_n^2 \quad ,$$
$$\sigma_n = \sqrt{\sigma_{nR}\sigma_{nT}} \quad . \qquad \text{(C-82)}$$

The resulting effective solar angular radius is

$$\sigma_n = \sigma\{[1 + \frac{2n}{(2n+1)}((n-1)\delta + \frac{(n+1)}{3}(\delta^2 + 2\langle\gamma^2\rangle))]$$
$$[1 + \frac{2\delta}{\tan(\frac{n\pi}{2n+1})}\sum_{m=1}^{n}\sin(\frac{m\pi}{2n+1}) \qquad \text{(C-83)}$$
$$+ \frac{2}{\tan^2(\frac{n\pi}{2n+1})}\sum_{m=1}^{n}\sin^2(\frac{m\pi}{2n+1})](\frac{\langle\gamma^2\rangle}{\cos^2(\frac{m\pi}{2n+1})} + 2\delta^2)]\}^{\frac{1}{4}}$$

where δ is the angular beam spread due to microscopic errors and $\langle\gamma^2\rangle$ is the mean square deviation of the surface normal. Both quantities are normalized by the true solar angular radius σ. Note that (C-83) preserves the true sun size when there are no errors present. When errors are present σ_n is a monotonically increasing function of either n, δ, or $\langle\gamma^2\rangle$ when the other two variables are held constant.

The microscopic beam spread for several reflector materials has been determined by Pettit [1] to produce a light distribution about the specular direction that is a Gaussian (or a sum of Gaussians, depending on the material) function of $\Delta\theta$, the deviation from the specular direction. According to Pettit, the reflectivity at $\Delta\theta$ is

$$R(\Delta\theta) = \sum_{i=1}^{k} A_i \, e^{\frac{-\Delta\theta^2}{2S_i^2}} \tag{C-84}$$

where k, A_i, and S_i are dependent on the material in question. The percent of the power that is in a cone of total angular aperture of $2\Delta\theta$ is

$$J(\Delta\theta) = \beta \int_0^{\Delta\theta} R(\Delta\theta)\sin\theta d\theta \tag{C-85}$$

where β is chosen to make $J(\pi/2) = 1$. For many materials, such as silvered glass, k = 1. If $\Delta\theta$ is small and k = 1, Eqn. (C-85) gives

$$J(\Delta\theta) = (1 - e^{\frac{-\Delta\theta^2}{2S^2}}) \quad . \tag{C-86}$$

Table C-1 and Fig. C-19 show the normalized effective sun size σ_n/σ as a function of the normalized rms deviation of the normal vector $\sqrt{\langle\gamma^2\rangle}$ for silvered glass. Pettit's data indicates that S_i = 0.15 mrad and A_1 = 0.83 for silver-

Table C-1

Normalized Effective Sun Size σ_n/σ

For δ = 0.10 (silvered glass)

rms value of γ	n=1	n=2	n=3	n=4	n=5
0	1.03	1.05	1.07	1.09	1.11
.10	1.03	1.06	1.08	1.10	1.12
.20	1.05	1.08	1.11	1.14	1.16
.30	1.09	1.12	1.16	1.19	1.22
.40	1.13	1.18	1.22	1.27	1.30
.50	1.19	1.25	1.30	1.35	1.40
.60	1.25	1.33	1.40	1.46	1.51
.70	1.32	1.41	1.50	1.57	1.63
.80	1.39	1.51	1.60	1.68	1.75
.90	1.47	1.61	1.72	1.81	1.89
1.00	1.56	1.71	1.84	1.94	2.03
1.10	1.65	1.82	1.96	2.08	2.17
1.20	1.74	1.94	2.09	2.21	2.32
1.30	1.83	2.05	2.22	2.35	2.47
1.40	1.93	2.17	2.35	2.50	2.62
1.50	2.03	2.29	2.48	2.64	2.78
1.60	2.13	2.41	2.62	2.79	2.93
1.70	2.23	2.53	2.76	2.94	3.09
1.80	2.33	2.66	2.90	3.09	3.25
1.90	2.43	2.78	3.04	3.24	3.41
2.00	2.54	2.91	3.18	3.39	3.57

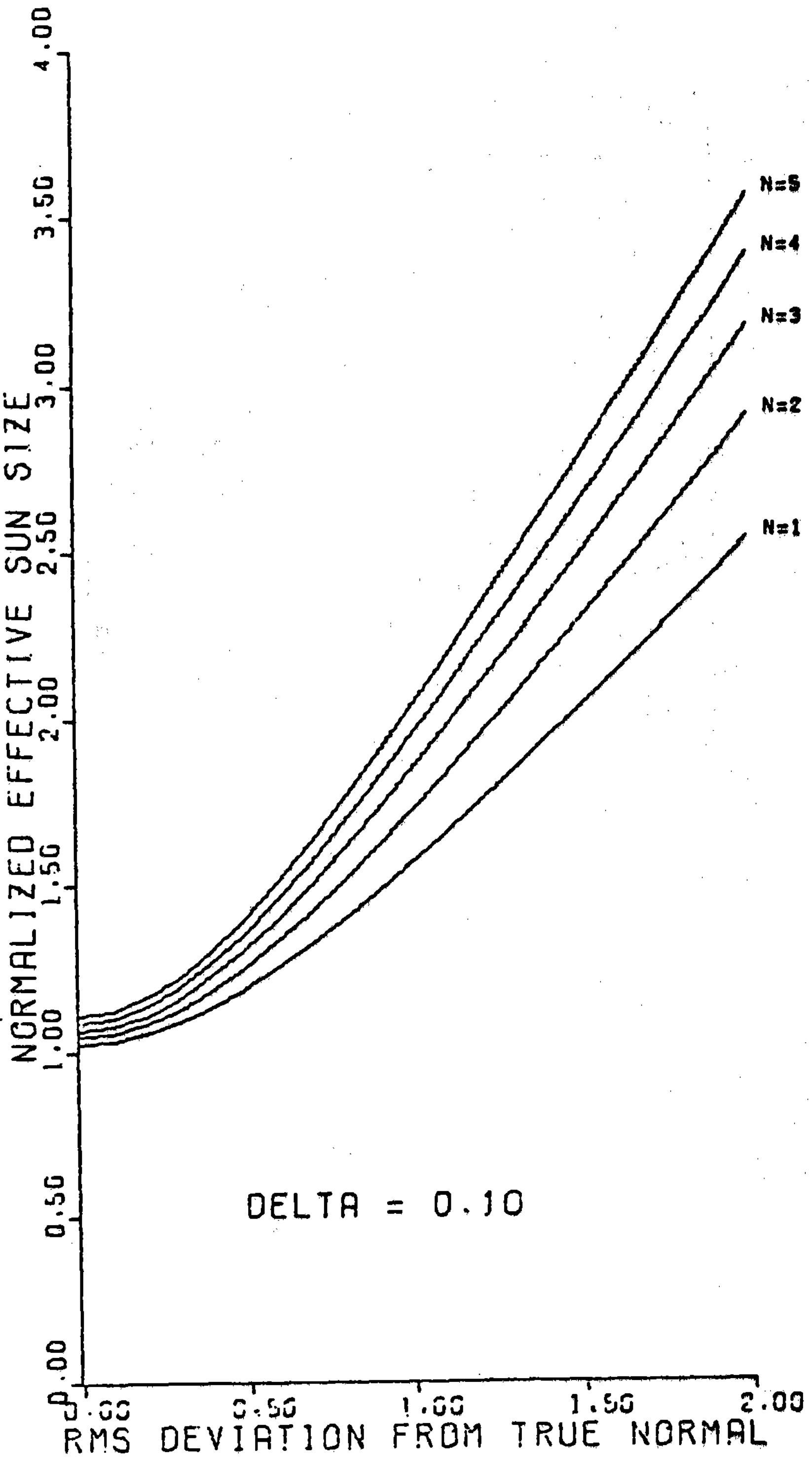

Figure C-19. Normalized Effective Sun Size σ_n/σ for $\delta = 0.10$ (silvered glass).

ed glass. For a value of $\delta = 0.1$ ($\sigma = 0.267°$, true sun size) the scattered beam will contain over 99% of the light. This is the value of δ used in Table C-1 and Fig. C-19. Curves and data are shown for up to 5 reflections.

The data in Table C-2 and Fig. C-20 are for a similar material, with k=1, but $S_1 = 0.5$ mrad which makes it a much poorer specular reflector than silvered glass. A value of $\delta = 0.35$ ($\sigma = 0.267°$) puts more than 99% of the light into the spread beam. This is the value of δ used in Table C-2 and Figure C-20. Data are shown for one to five reflections.

The effective sun size data σ_n/σ are shown for a range of the normalized rms deviation of the normal ($\sqrt{\langle\gamma^2\rangle}$) from 0 to 2. A structural analysis based on practical construction methods indicates that a reasonable value under moderate wind loading is (see Appen. D).

$$\sigma\sqrt{\langle\gamma^2\rangle} = 0.226° \quad .$$

This corresponds to $\sqrt{\langle\gamma^2\rangle} \simeq 0.85$. Referring to Fig. C-19, one sees that σ_n/σ is bounded by 1.85 under these conditions when the collector is silvered glass. The ratio σ_n/σ gets correspondingly worse when the rms deviation of the normal increases

The method for relating the effective sun size to actual mirror errors presented in this section is not rigorous. However, it does provide a useful estimate of the effect of errors on the solar image. The policy adopted in the following section is to use an upper limit for the effective sun size

Table C-2

Normalized Effective Sun Size σ_n/σ

For δ = 0.35

rms value of γ	n=1	n=2	n=3	n=4	n=5
0	1.12	1.18	1.25	1.31	1.36
.10	1.12	1.19	1.26	1.32	1.37
.20	1.14	1.21	1.28	1.35	1.40
.30	1.17	1.25	1.33	1.39	1.45
.40	1.21	1.30	1.38	1.46	1.52
.50	1.26	1.36	1.46	1.53	1.60
.60	1.32	1.44	1.54	1.62	1.70
.70	1.38	1.52	1.63	1.72	1.81
.80	1.45	1.61	1.73	1.83	1.92
.90	1.53	1.70	1.84	1.95	2.05
1.00	1.61	1.80	1.95	2.07	2.18
1.10	1.70	1.90	2.07	2.20	2.31
1.20	1.79	2.01	2.19	2.33	2.45
1.30	1.88	2.12	2.31	2.46	2.59
1.40	1.97	2.24	2.44	2.60	2.74
1.50	2.07	2.35	2.57	2.74	2.89
1.60	2.16	2.47	2.70	2.88	3.04
1.70	2.26	2.59	2.83	3.03	3.19
1.80	2.37	2.71	2.97	3.17	3.34
1.90	2.47	2.84	3.10	3.32	3.50
2.00	2.57	2.96	3.24	3.47	3.66

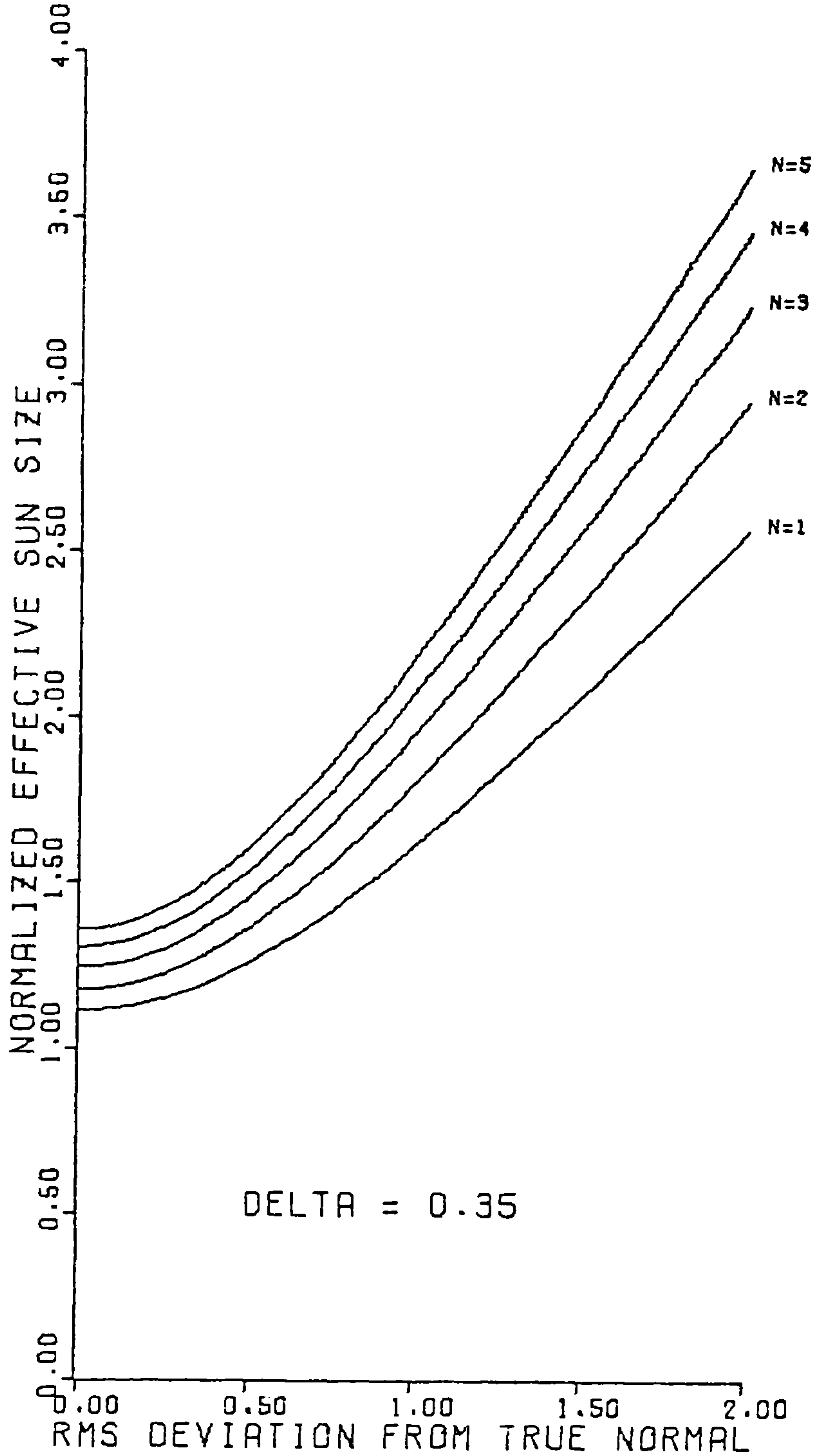

Figure C-20. Normalized Effective Sun Size σ_n/σ for δ = 0.35.

which is independent of the bounce number n. This will under emphasize the single bounce concentration with respect to the multiple bounce concentration, if this upper limit is based on the maximum bounce number. The nominal upper limit, $\sigma_n = 0.50°$, corresponds to $\sigma_n/\sigma = 1.87$. This is a reasonable value for a collector surface of silvered glass with structural errors similar to those determined in Appen. D.

C-8 OPTICAL CONCENTRATION RESULTS FOR ALIGNED CONICAL RECEIVERS

The calculation procedures described above have been implemented with computer codes and numerous optical concentration distributions have been calculated for a perfectly aligned conical receiver. The following collection of results offers a study of several relevant parameters and demonstrates the capability of the computer codes. High resolution multiple bounce (multiple reflection) distributions are included. Such detail has never before been available.

The geometry of a conical receiver is shown in Fig. C-21. A point on the surface of the absorber is located by a length q and an angle ϕ_o. The top of the absorber is q=0.50 while the foot is q=1.00. The length q is measured along the cone surface and is the usual spherical radial coordinate of the field point measured from the center of curvature of the dish, normalized to the dish radius. The angle ϕ_o is the cylindrical azimuth angle measured around the cone axis, with $\phi_o=0$ taken on the side of the receiver facing the sun. The center of the sun lies in the $\phi_o=0$ plane. The half apex angle of the cone is ψ_o.

The optical concentration distributions are plotted for a spherical segment with θ_{RIM}= constant (Fig. C-13). The sun is located by I, the angle of incidence, measured from the upward normal to the aperture plane. Normal incidence (sun

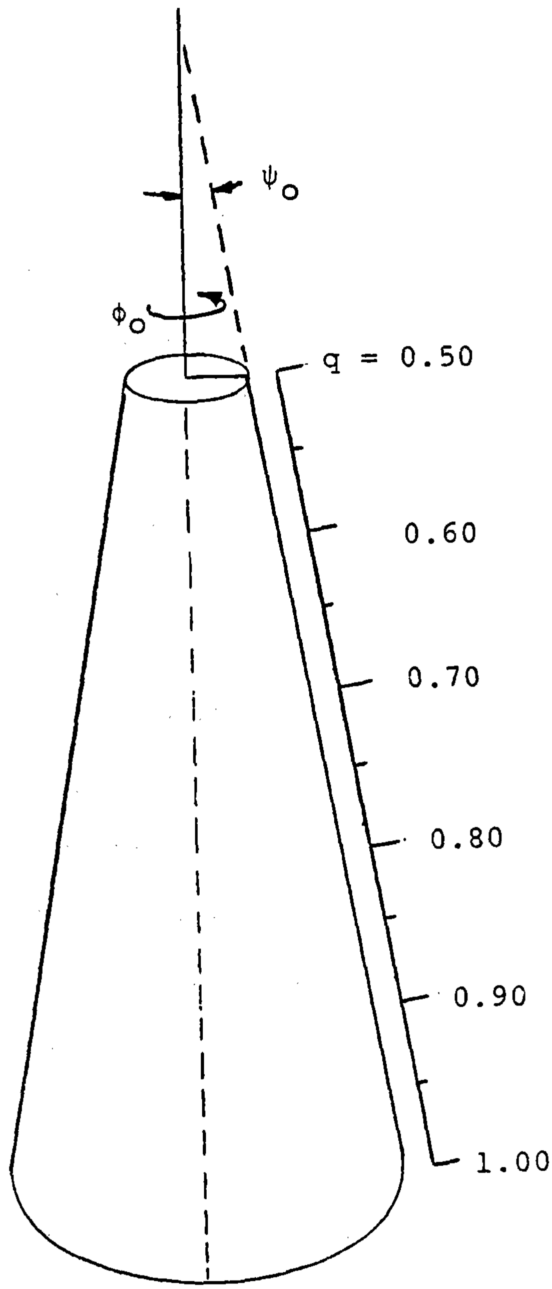

Figure C-21. Geometry of Conical Absorber directly over the dish symmetry axis) corresponds to $I=0°$. The $I=0°$ case is called the symmetric case because there is no ϕ_o variation in the optical concentration.

In the results presented here, the multiple bounce contribution is evaluated with $\sigma_n=\sigma_1$. This allows for the nominal mirror error but not for error accumulation.

C-8.1 Symmetric Distributions

The symmetric case for $\psi_o = \sigma_n = 0.50°$, $\theta_{RIM}=90°$ (five bounce limit), and reflection coefficient R = 1.0 is shown in Fig. C-22. The concentration goes to zero at q = 0.500 (paraxial focus) as a result of the non-zero cone radius. The cone intercepts the rays that would go to the paraxial focus along its entire length. The single bounce peak is thus shifted toward the foot of the cone and occurs at $q \approx 0.529$. At this point, the concentration reaches about 572 suns. The concentration then falls away smoothly as q is increased, until the multiple bounce contributions begin to be seen for q larger than about 0.92. The dotted curve in this region represents only single bounce radiation. The peaks for n > 1 (n is the bounce number) are very narrow, rising extremely rapidly with a somewhat slower rate of fall-off after the peak is reached. In this regard, they resemble the n = 1 peak but are so narrow that they contain much less power even though, for example, the n = 2 peak exceeds 800 suns in height.

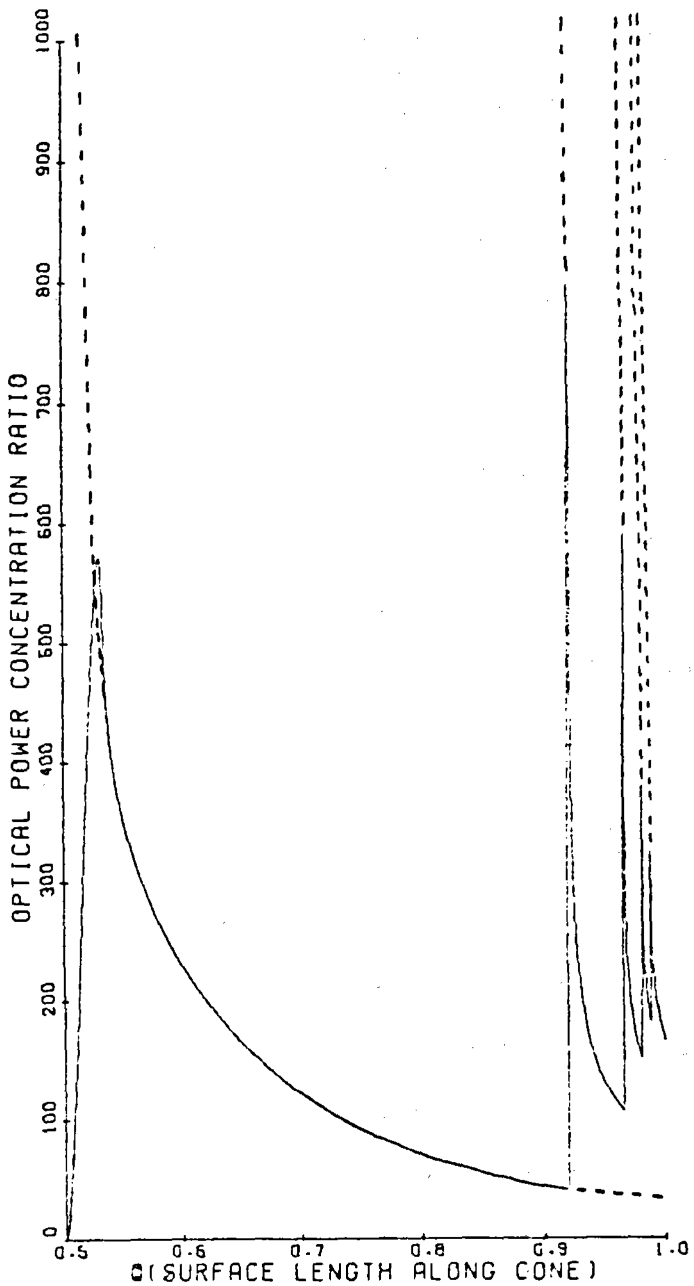

Figure C-22. Symmetric Concentration Distribution on Receiver With $\psi_o = \sigma = 0.5°$, R=1.0, $\theta_{rim} \approx 90°$.

The peaks for $n > 2$ are extremely narrow and, since they contain so little energy in the narrow region, it has not been considered useful to probe those peaks in great detail to determine their exact height. However, such detailed probing has been done for the $n = 1$ peak and $n = 2$ peak which are illustrated in Fig. C-23 and C-24, respectively. These two curves are greatly expanded plots of the appropriate portions of Fig. C-22. The results shown in these two curves were determined with exquisite accuracy, hundreds of points having been probed. In Fig. C-23 ($n = 1$), note that the curve rises smoothly from zero and rolls over smoothly at the peak. There are no cusps or discontinuities. The $n = 2$ case in Fig. C-24 has the same smoothness properties showing a smoothly rounded peak, but it is much more narrow. The rise starting at $q \approx .9182$ is very rapid but the slope is finite. (The rise was documented at numerous probe points.) Obviously, the major energy contribution from the $n = 2$ light is not under the narrow peak, but is in the slowly falling tail. As stated previously, the peaks for $n > 2$ are even more narrow, and since most of the energy is contained in the more easily resolved portions of the contribution, the exact peak height has not been probed in ultimate detail. It is important to note that there are no singularities in the peaks and that they <u>can</u> be probed to any desired level of detail.

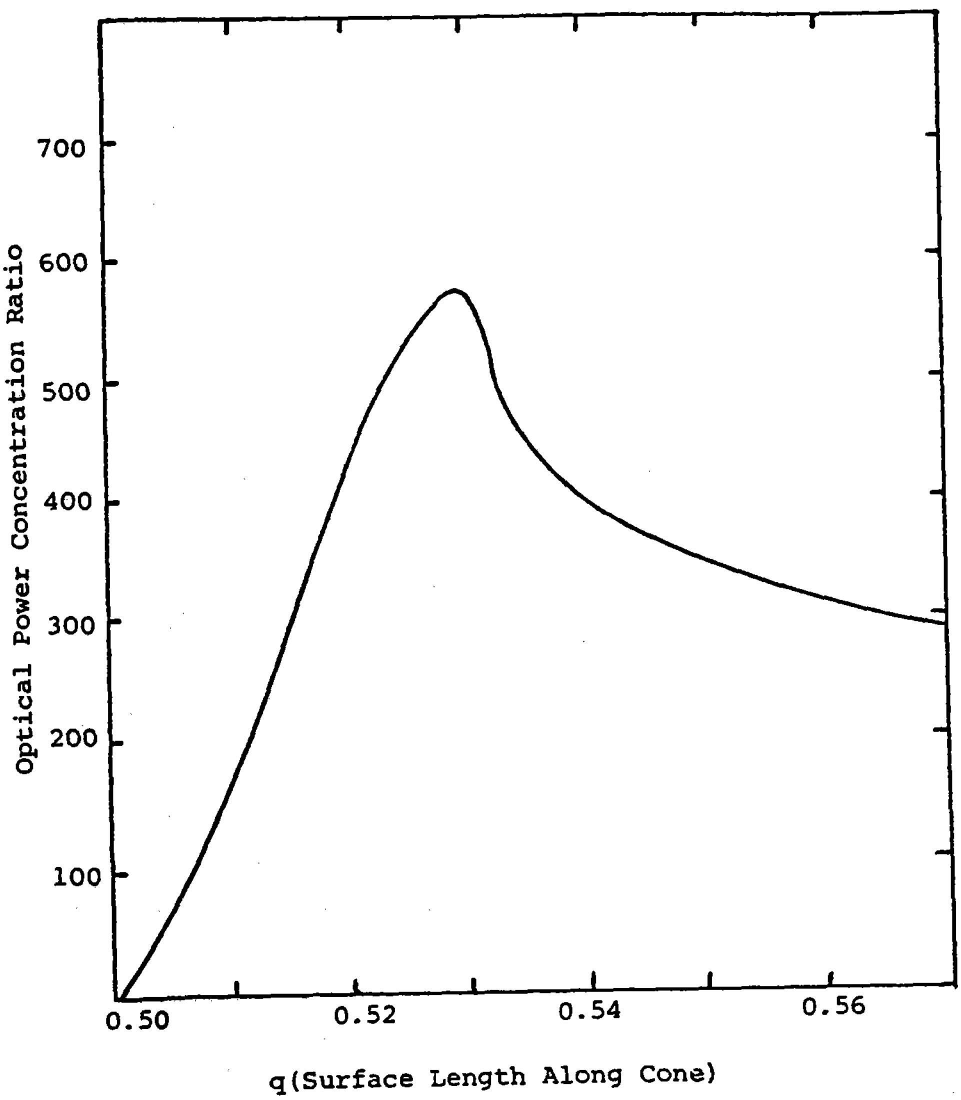

Figure C-23. Detail of n=1 Peak.

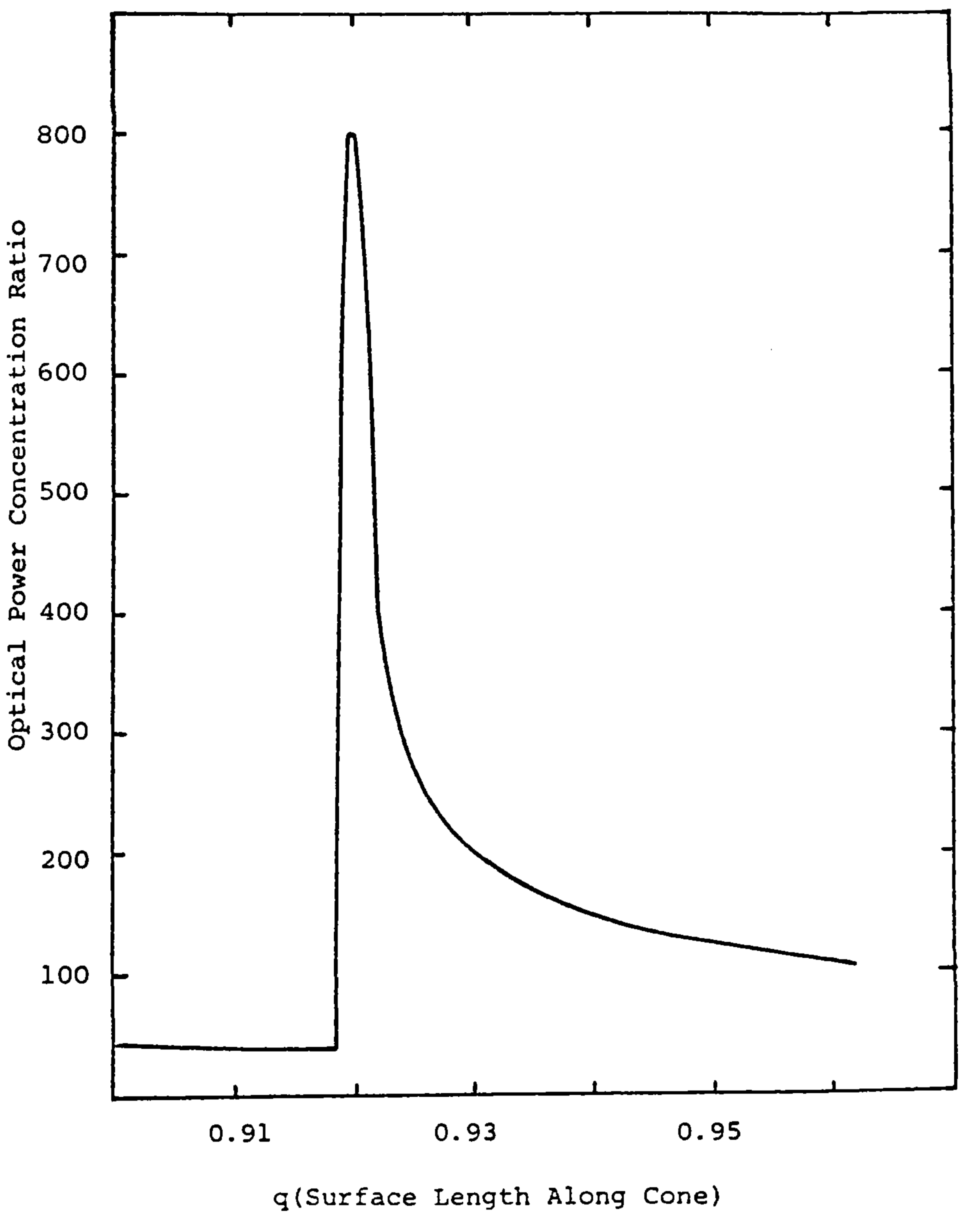

Figure C-24. Detail of n=2 Peak.

The effects of changing ψ_o and σ are illustrated in Figs. C-25 to C-29. The dotted curves in Fig. C-22 and Fig. C-27 at the peaks are for the point sun limit, σ_n=0, which does exhibit singularities. The point sun limit and the finite sun case agree away from the caustics. Figs. C-25 and C-26 maintain the condition that σ=0.50°, but the cone angle is increased, ψ_o=1.0° in C-25 and ψ_o=1.5° in C-26. As expected, the concentration is lower for larger ψ_o since the receiver area has increased. Note that, since the receiver cone does not match the sun cone in angular size, there is a dark region near q = 0.50. Also, as the absorber size increases, the n = 1 peak moves slightly toward the receiver foot. The n > 2 peaks show very little change in position.

Figures C-27 to C-29 document symmetric distributions in which the sun size has been reduced to approximately actual size, σ = 0.25°. This corresponds to perfect optics (no errors). The matched receiver ψ_o = 0.25° in Fig. C-27 shows much higher concentration than in the presence of errors (Fig. C-22). The n = 1 peak reaches over 1200 suns while the n = 2 peak exceeds 2000 suns. The n = 1 peak occurs for a slightly smaller q value, also. As ψ_o is increased to 0.50° and 0.75°, respectively, in Figs. C-28 and C-29, the effects described previously for Figs. C-26, C-27 again occur. Note that for perfect optics (σ=0.25°) and the nominal sized absorber (ψ_o = 0.50°, Fig. C-28) the concentration peaks are somewhat higher than in the nominal

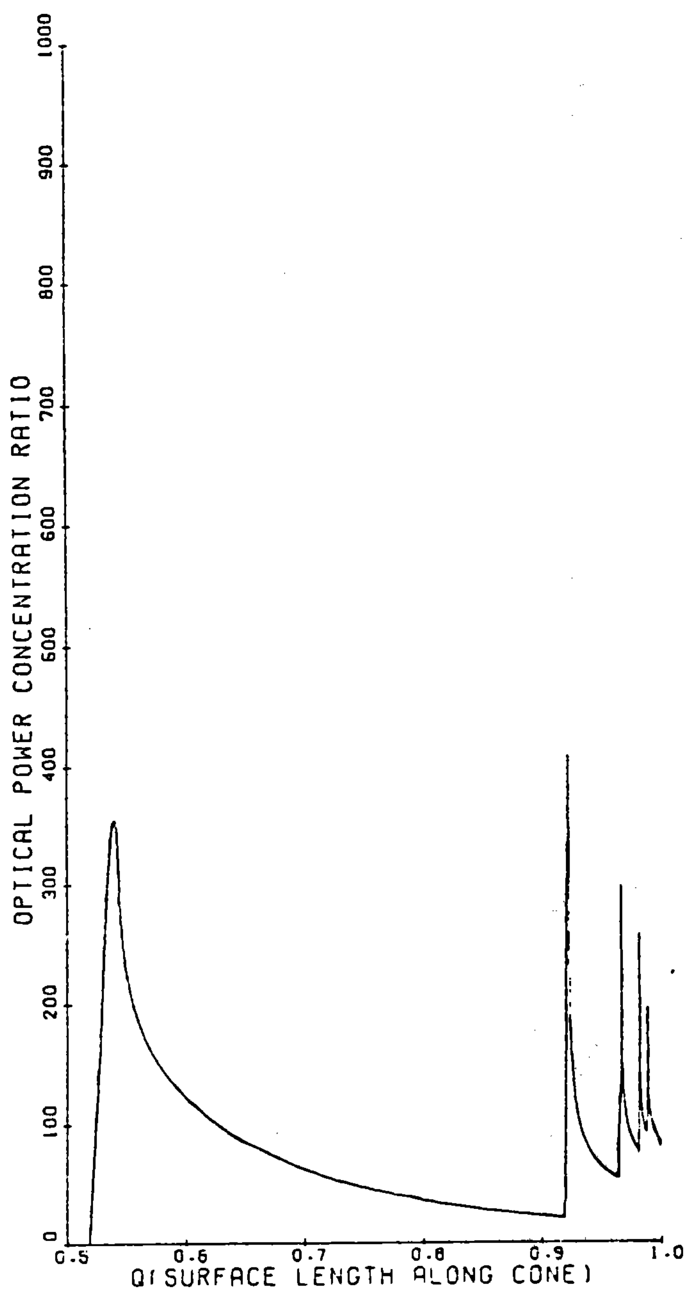

Figure C-25. Symmetric Concentration Distribution on Receiver With ψ_0=1.0°, σ=0.5°, R=1.0, θ_{rim}=90°.

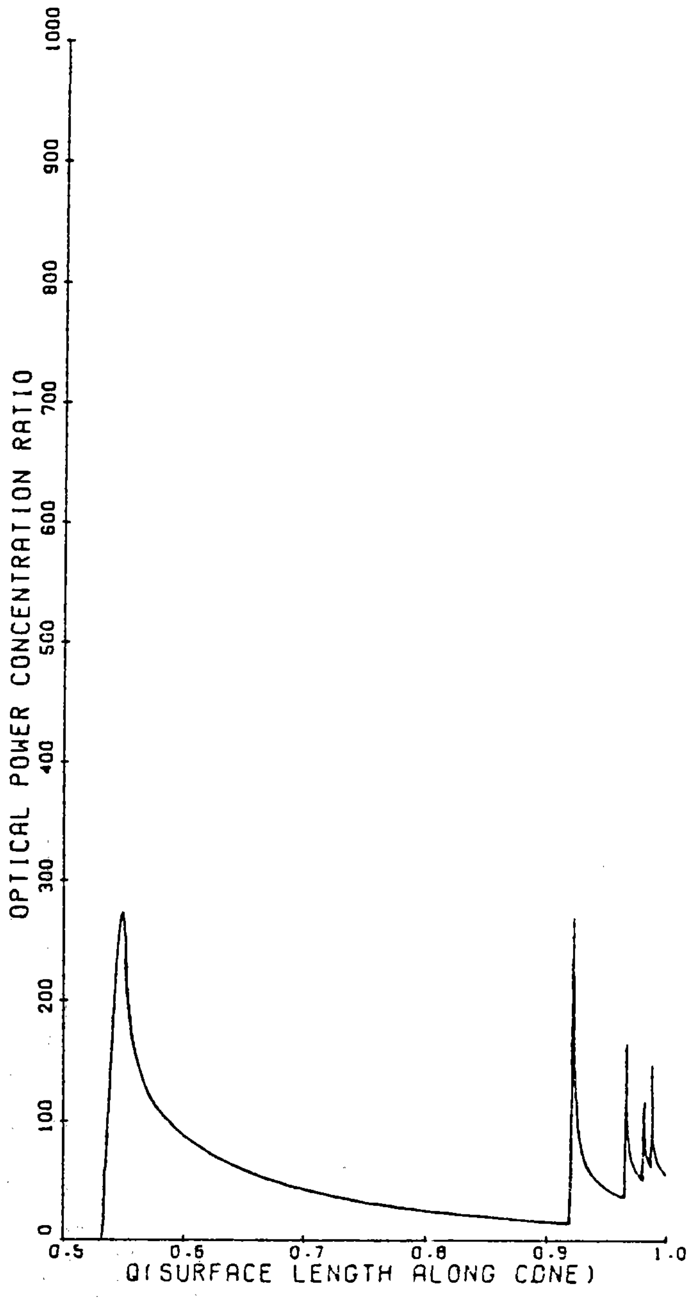

Figure C-26. Symmetric Concentration Distribution on Receiver With ψ_o=1.5°, σ=0.5°, R=1.0, θ_{rim}=90°.

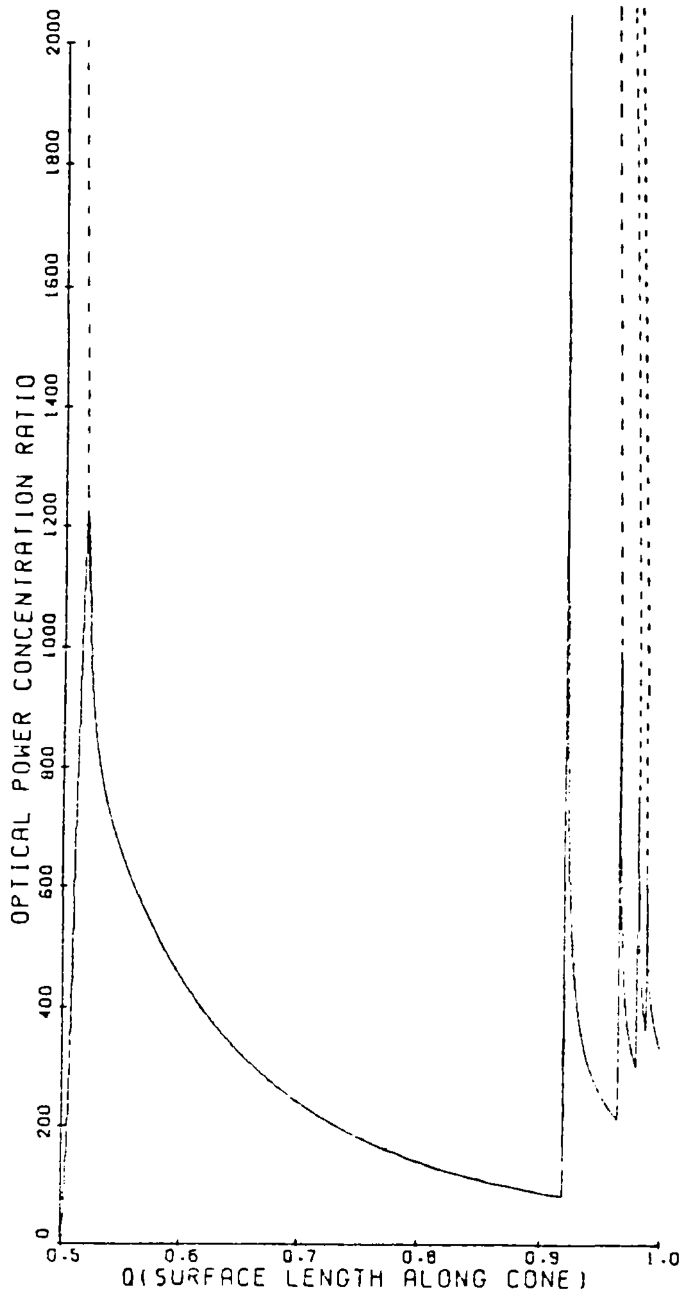

Figure C-27. Symmetric Concentration Distribution on Receiver With $\psi_o = \sigma = 0.25°$, R=1.0, $\theta_{rim} \approx 90°$.

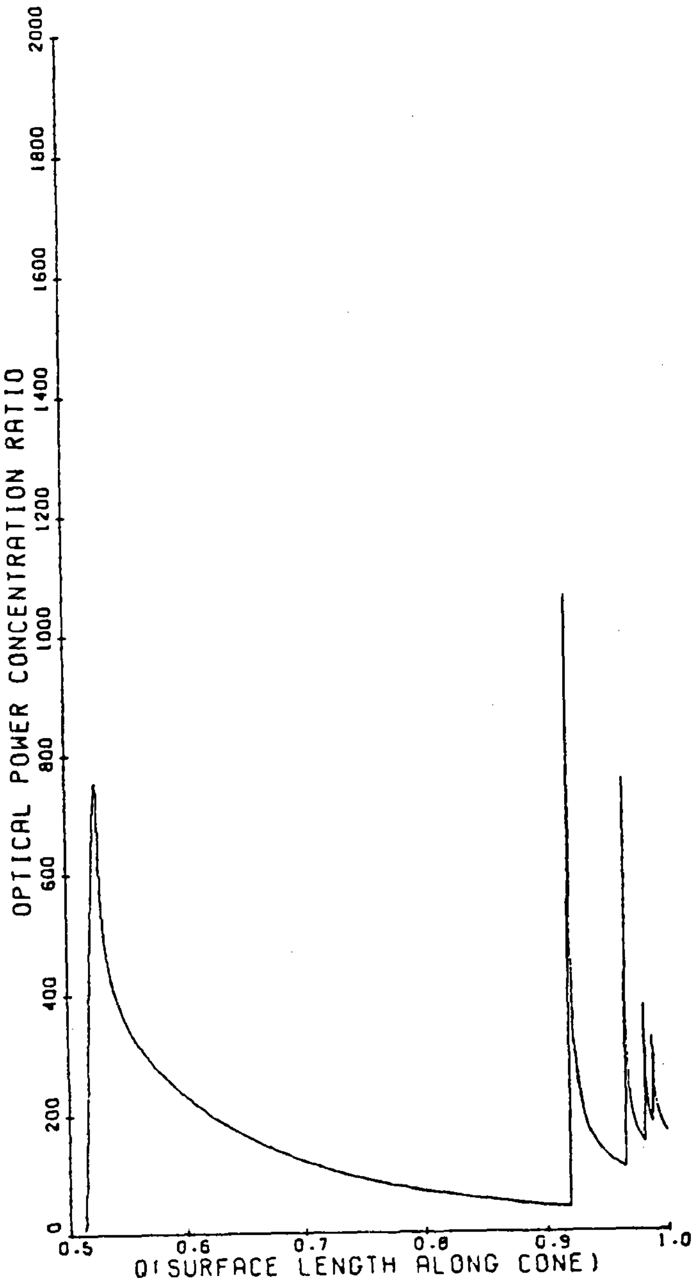

Figure C-28. Symmetric Concentration Distribution on Reciever With $\psi_o = 0.5°$, $\sigma = 0.25°$, R=1.0, $\theta_{rim} \approx 90°$.

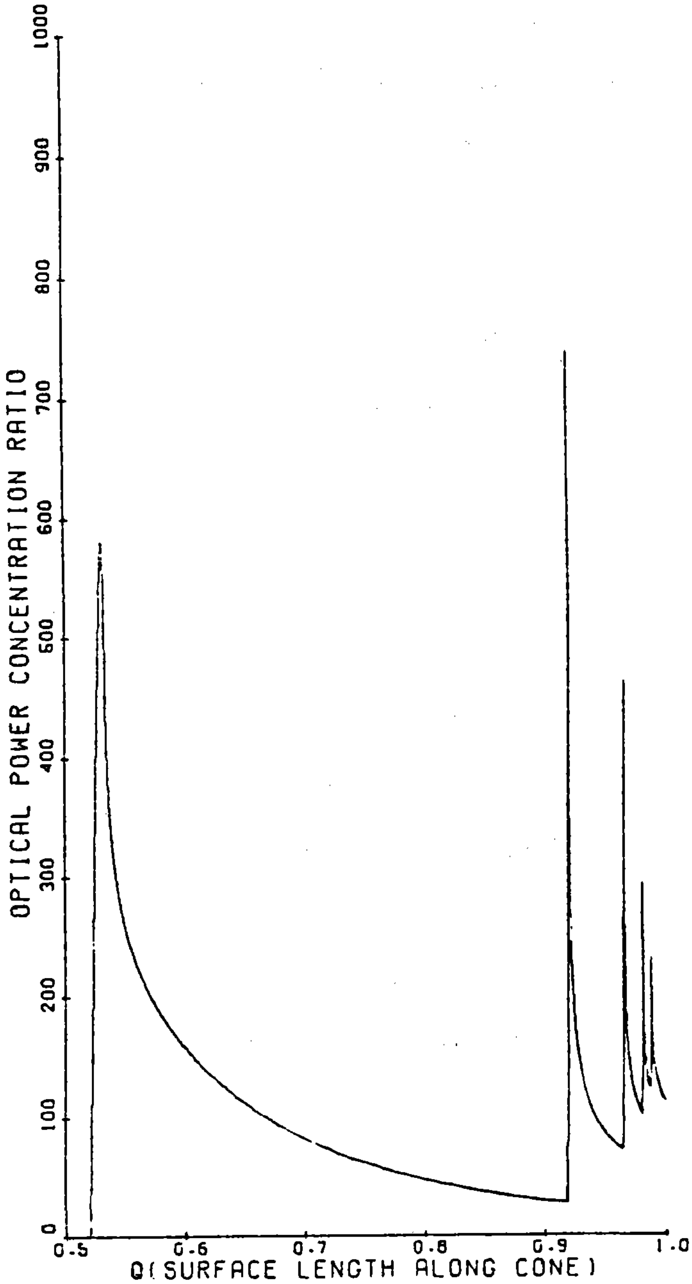

Figure C-29. Symmetric Concentration Distribution on Reciever With $\psi_o = 0.75^o$, $\sigma = 0.25°$, R=1.0, $\theta_{rim} \simeq 90°$.

case (ψ_o = σ = 0.50°, Fig. C-22). Situations in which the absorber is undersized (ψ_o < σ) will be presented later.

In all distributions presented at this point, the reflectivity, R, of the mirror has been taken as unity. Figs. C-30 and C-31 show the ψ_o = σ = 0.50° and ψ_o = 0.50°, σ = 0.25° symmetric cases respectively for R = 0.88. Since the concentration is weighted by R^n, the distributions for each n are separately scaled versions of their R = 1.0 counterparts in Figs. C-22 and C-28. The importance of the multiple bounce radiation is thus reduced with respect to single bounce radiation.

The symmetric distributions have been integrated and plotted to show the fraction of total power received between 0.50 and q. Fig. C-32 shows the integrated flux distribution for ψ_o=σ=0.50 and R = 1.0. Note that, although the n > 2 region has very high, sharp peaks, they contain only about 30% of the total power found in the symmetric case. The reflectivity has been decreased to 0.88 for the same ψ_o, σ in Fig. C-33. The primary differences are that the curve rises more rapidly in the n = 1 region and that the n > 2 region represents approximately 25% of the total power. [It should be noted that "n > 2 region" is used here somewhat loosely in that some n = 1 radiation reaches the absorber in this region and is also included.] Also, although both of the curves in Figs. C-32, C-33 are normalized to reach 1.0 at q=1.0, it should be remem-

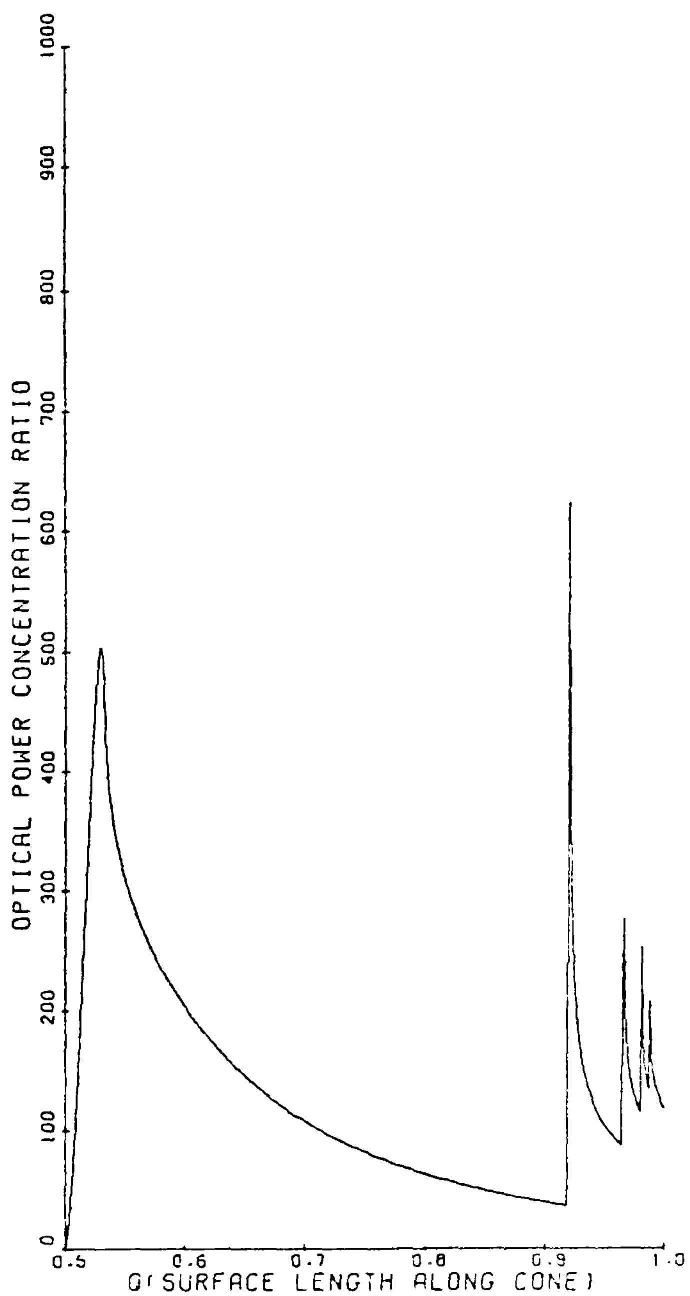

Figure C-30. Symmetric Concentration Distribution on Receiver With $\psi_c = \sigma = 0.5°$, R=0.88, $\theta_{rim} \approx 90°$.

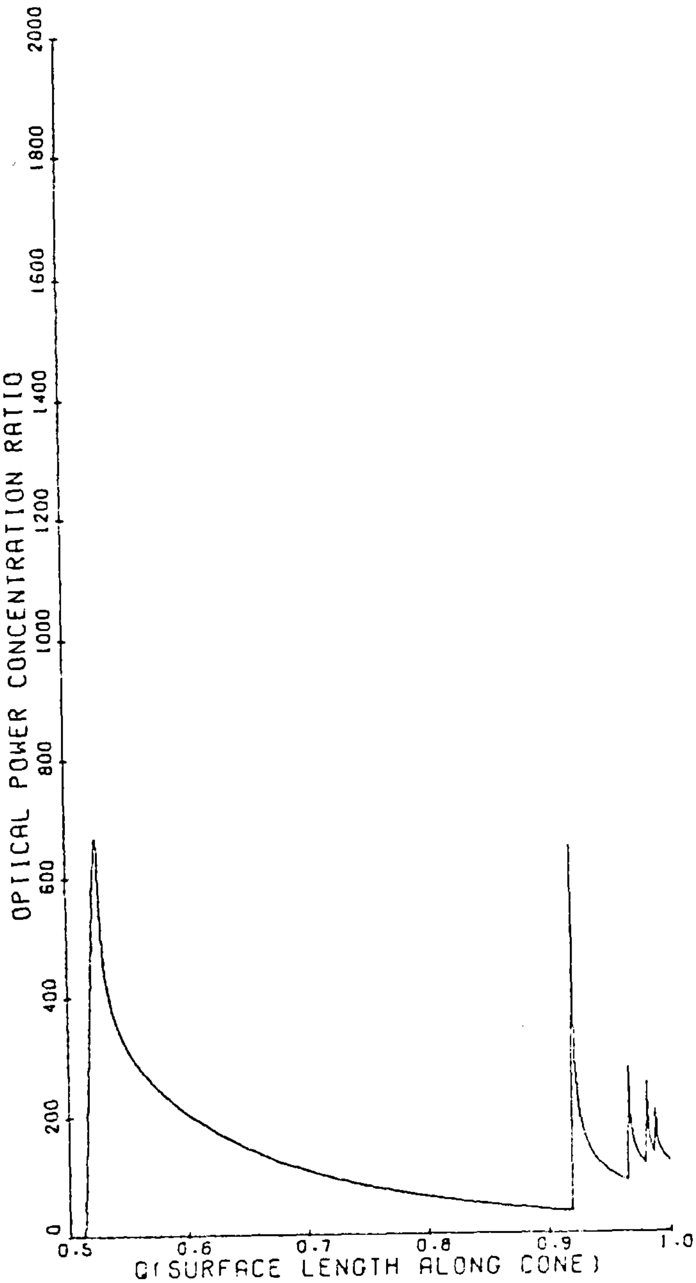

Figure C-31. Symmetric Concentration Distribution on Receiver With $\psi_o = 0.5°$, $\sigma = 0.25°$, R=0.88, $\theta_{rim} = 90°$.

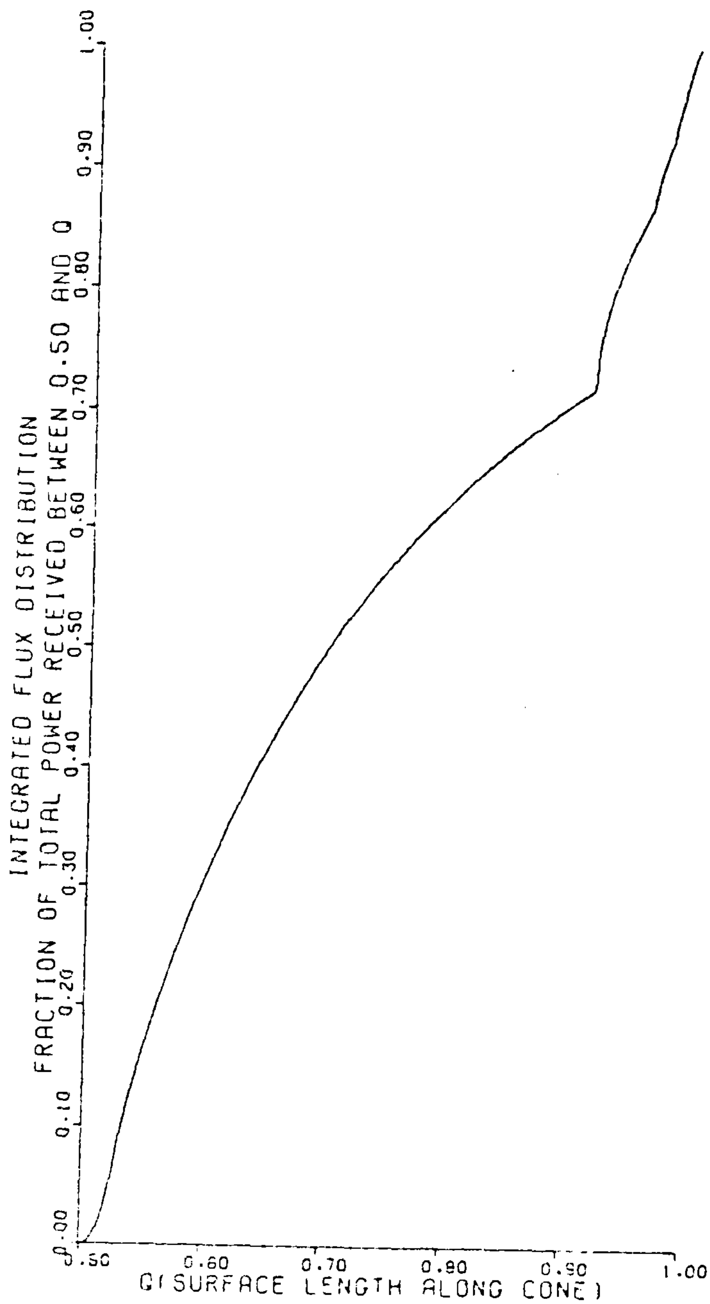

Figure C-32. Integrated Flux Distribution as Function of Position on Receiver With $\psi_o = \sigma = 0.50°$, R=1.0, θ_{rim}=90°.

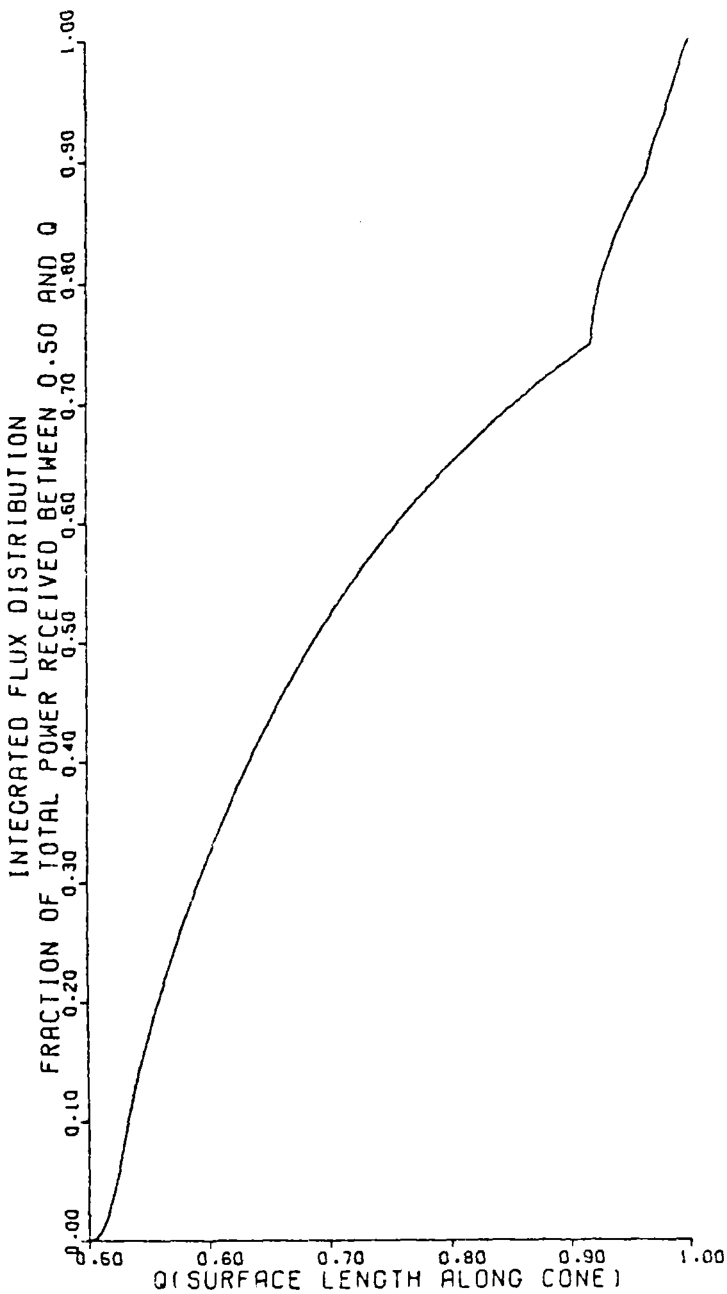

Figure C-33. Integrated Flux Distribution as Function of Position on Receiver With $\psi_o = \sigma = 0.5°$, R=0.88, θ_{rim}=90°.

bered that they do not represent the same total collected power since non-unity reflectivity causes a collection loss. The same information for $\psi_o = 0.50°$ and $\sigma = 0.25°$ (no errors) is shown in Figs. C-34 and C-35. The integration of the symmetric distributions provide an interesting test for the calculation procedure. The point by point calculation procedure was never required specifically to conserve total power. However, the R=1.0 results do conserve energy, as expected. This check on the numberically integrated distributions showed agreement to better than one fortieth of one per cent.

C-8.2 Asymmetric Distributions

The nominal collector-receiver combination is $\psi_o = \sigma = 0.50°$ and $\theta_{RIM} = 60°$. This case has been studied for two relevant values of solar inclination, I, with R = 1.0. Figs. C-36 to C-42 show a family of curves for $I = 30°$. Each curve is for a different value of ϕ_o, the receiver aximuth. In Fig. C-36, $\phi_o = 0$ and ϕ_o increases by 30° in each succeeding figure, ending with $\phi_o = 180°$ in Fig. C-42. [The distributions are symmetric about the $\phi_o = 0$, $\phi_o = 180°$ plane.]

At $\phi_o = 0$, the receiver sees a large portion of the collector with a $\theta_{RIM,\ eff.}$ near 90°. This produces the strong multiple bounce contributions indicated in Fig. C-36. As ϕ_o is increased, the multiple bounce region is affected first. This effect can be seen at $\phi_o = 30°$ in Fig. C-37. The n=1 region is affected as ϕ_o is further increased. At $\phi_o = 60°$

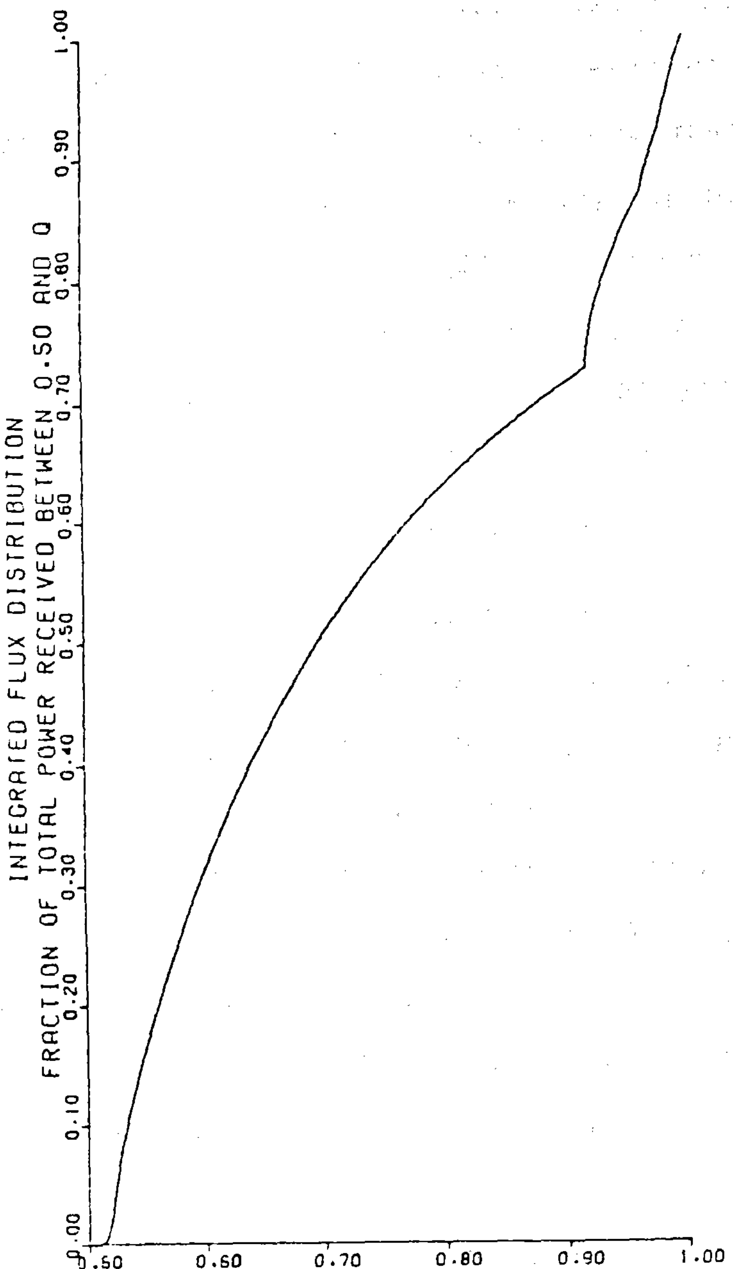

Figure C-34. Integrated Flux Distribution as Function of Position on Receiver With ψ_o = 0.50°, σ = 0.25°, R=1.0, θ_{rim}≈90°.

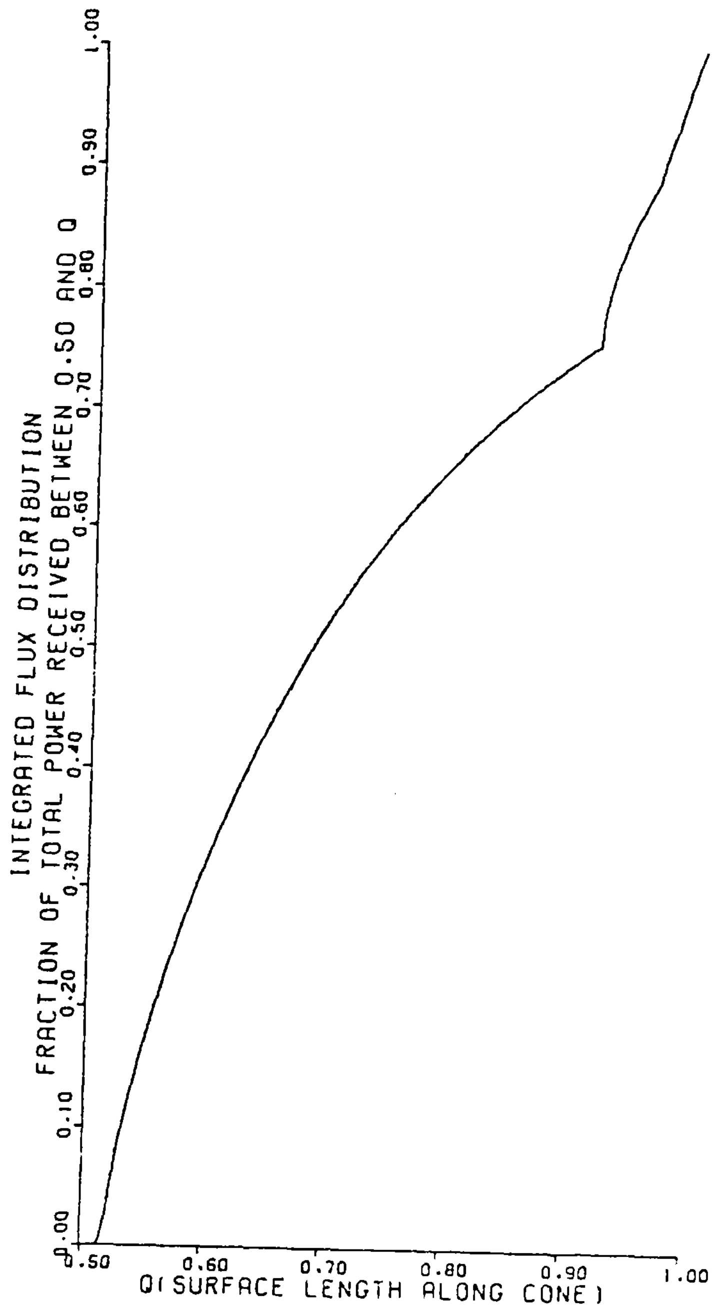

Figure C-35. Integrated Flux Distribution as Function of Position on Receiver With ψ_o =0.50°, σ = 0.25°, R=0.88, θ_{rim}=90°.

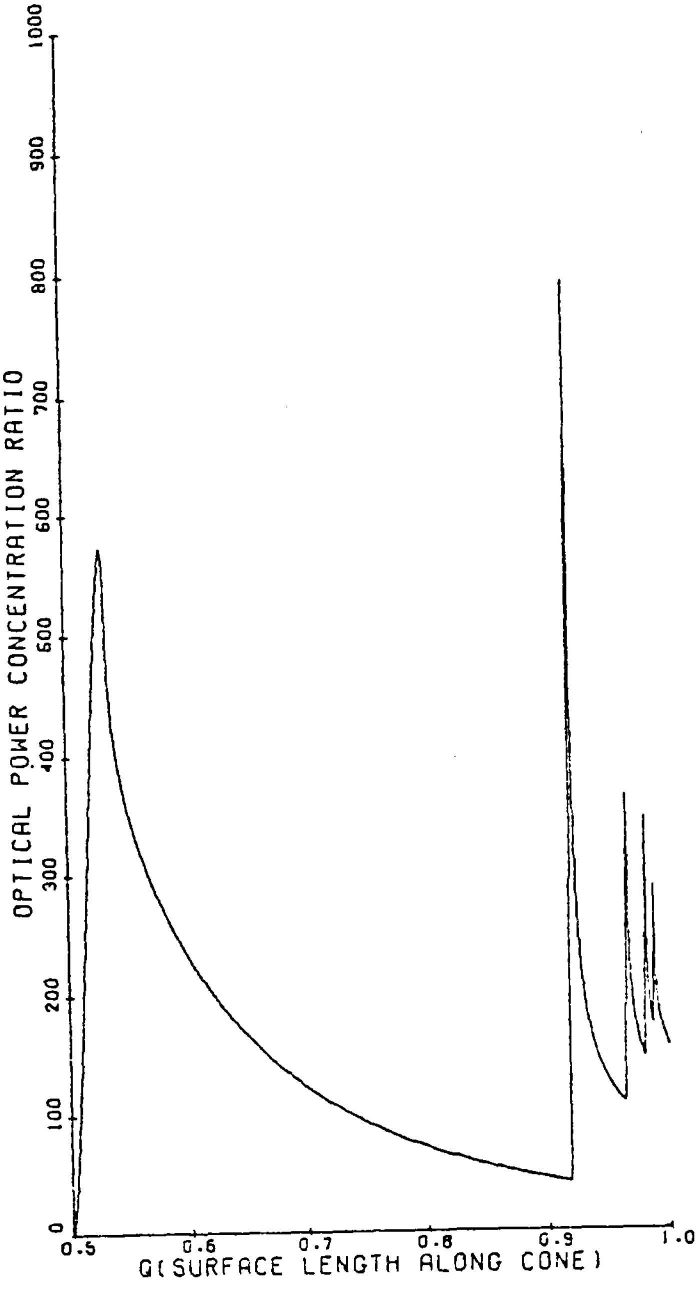

Figure C-36. Concentration Distribution at ϕ_0=0 With ψ_0=σ=0.5°, R=1.0, θ_{rim}=60°, and Solar Inclination 30°.

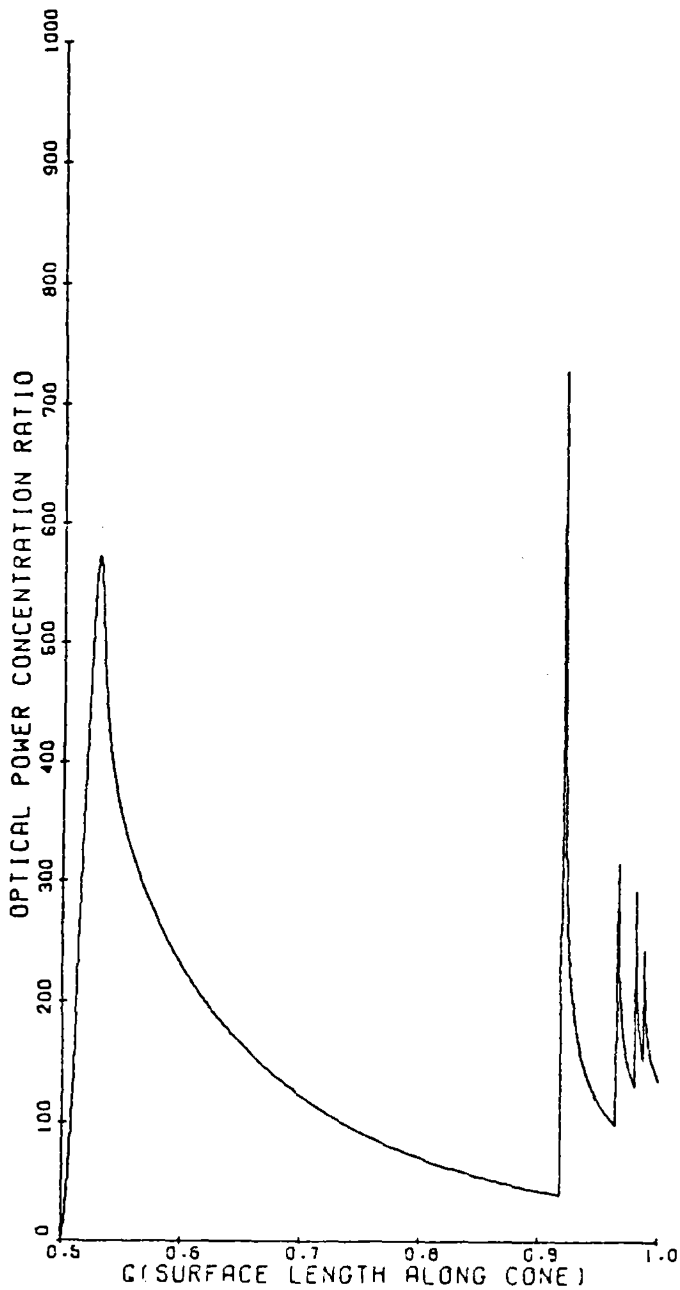

Figure C-37. Concentration Distribution at ϕ_o=30° With ψ_o=σ=0.5°, R=1.0, θ_{rim}=60°, and Solar Inclination = 30°.

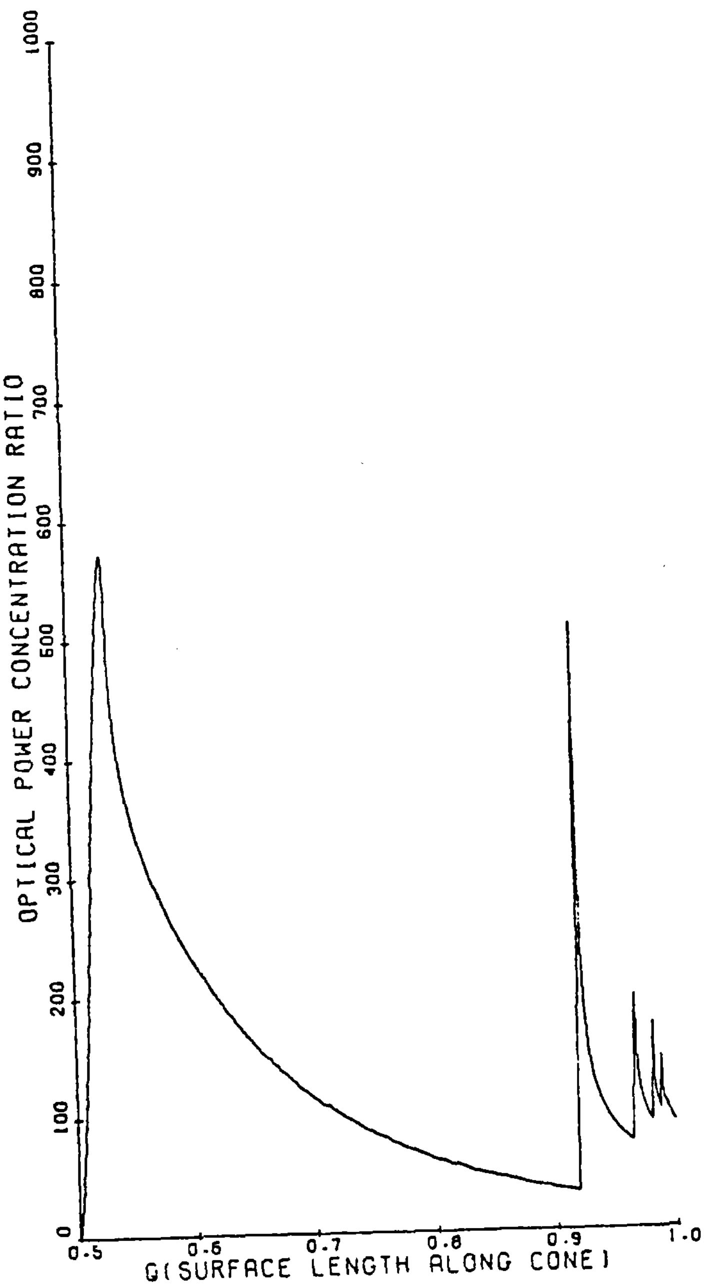

Figure C-38. Concentration Distribution at ϕ_o=60° With ψ_o=σ=0.5°, R=1.0, θ_{rim}=60°, and Solar Inclination = 30°.

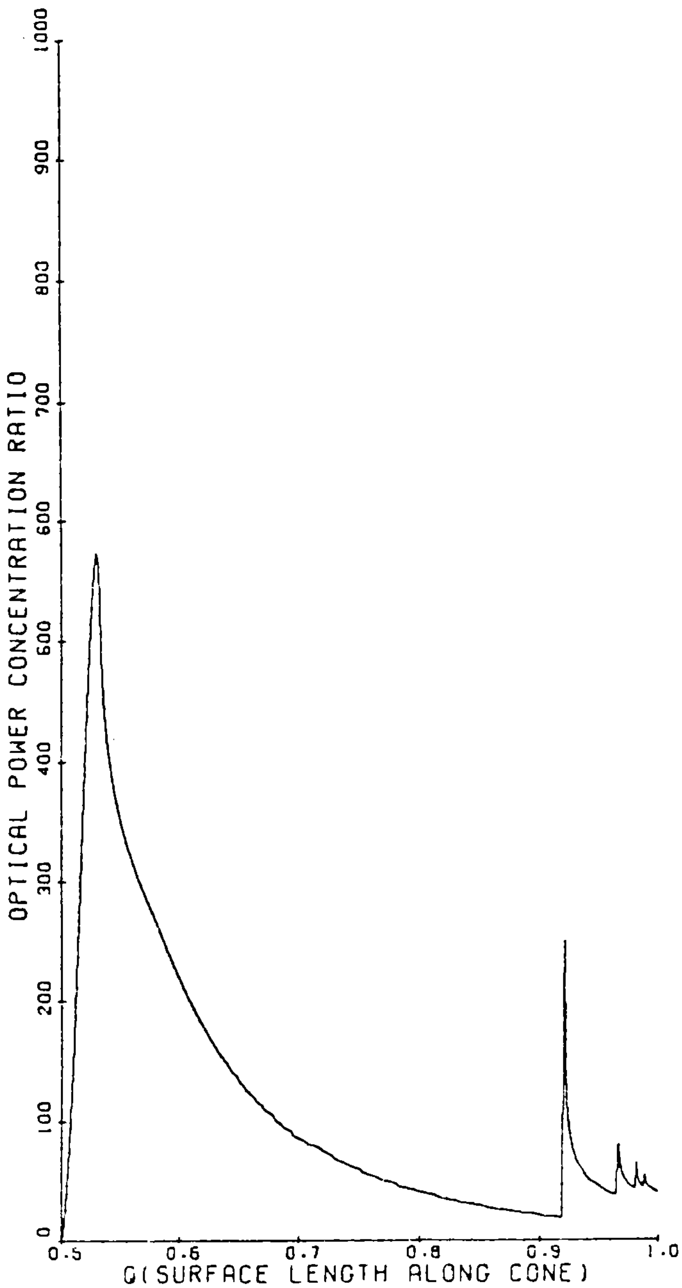

Figure C-39. Concentration Distribution at ϕ_0=90° With ψ_0=σ=0.5°, R=1.0, θ_{rim}=60°, and Solar Inclination = 30°.

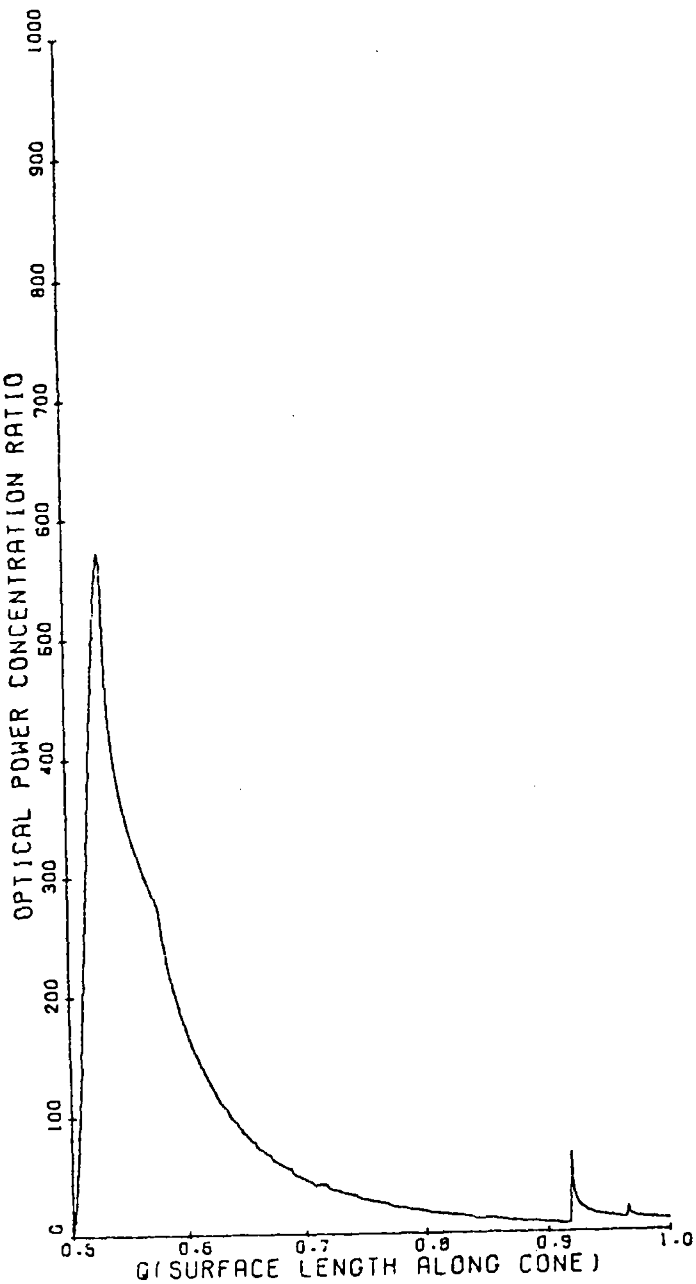

Figure C-40. Concentration Distribution at ϕ_o=120° with ψ_o=σ=0.5°, R=1.0, θ_{rim}=60°, and Solar Inclination = 30°.

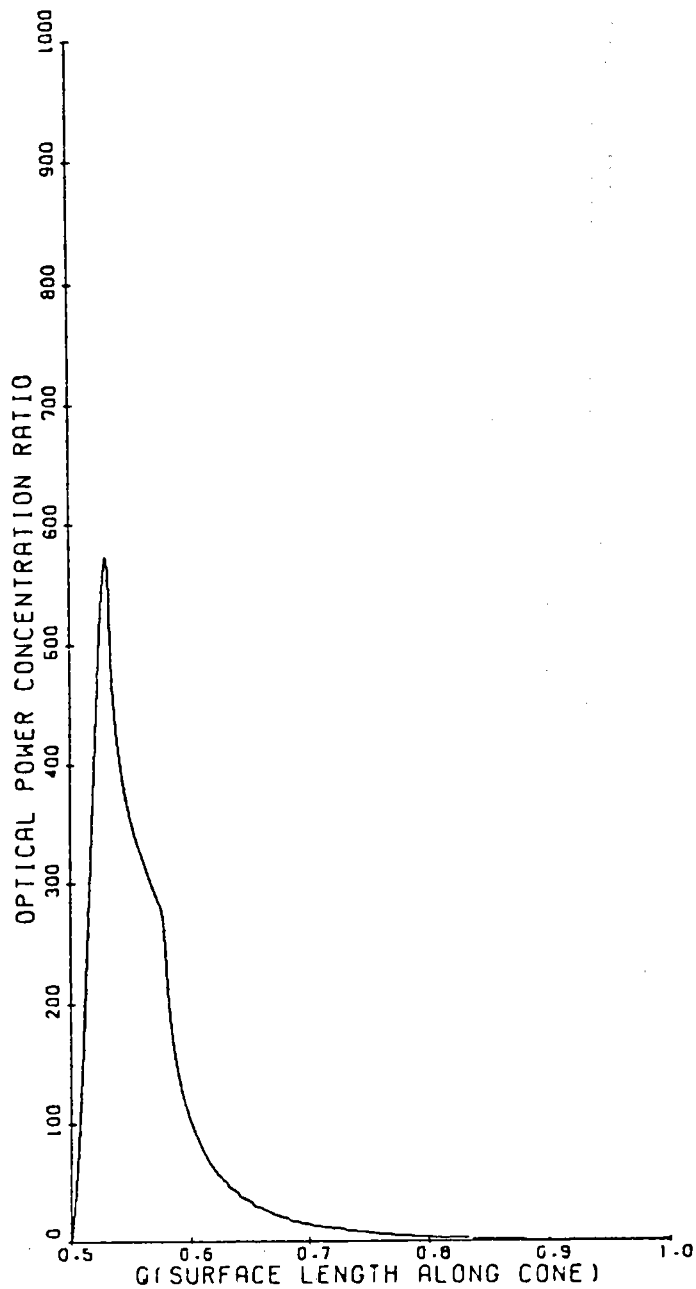

Figure C-41. Concentration Distribution at ϕ_o=150° With ψ_o=σ=0.5°, R=1.0, θ_{rim}=60°, and Solar Inclination = 30°.

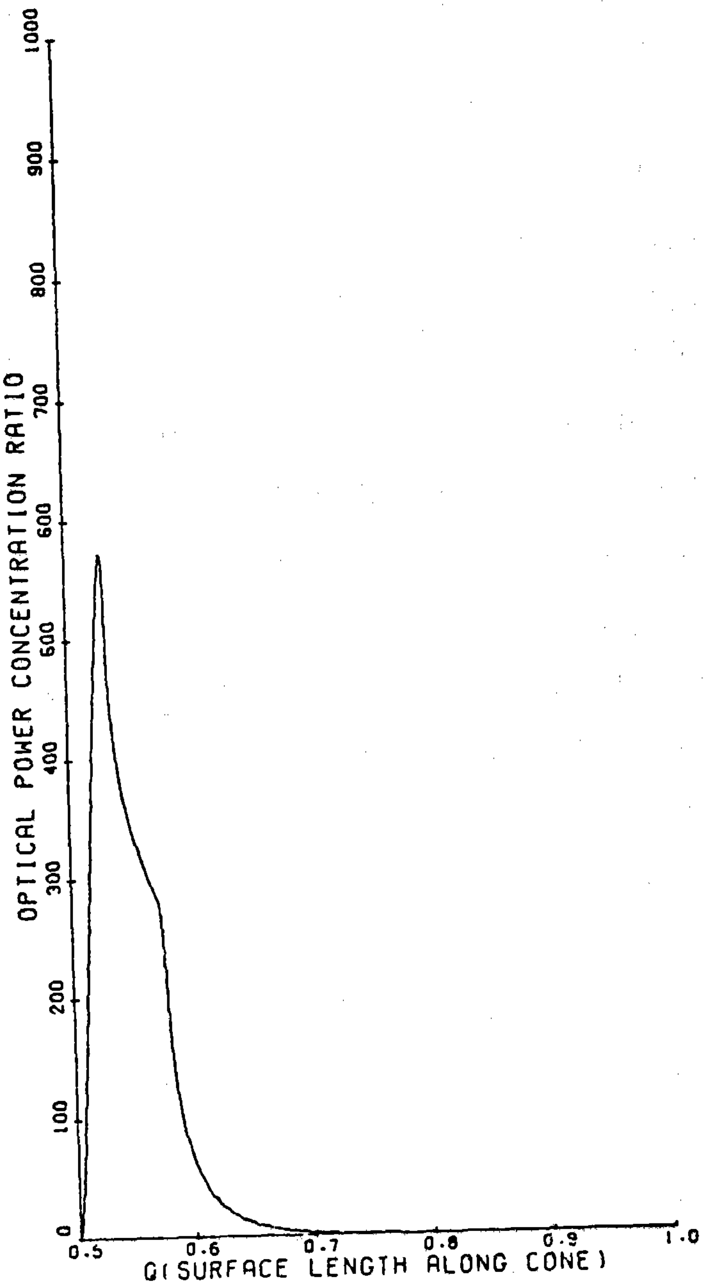

Figure C-42. Concentration Distribution at ϕ_o=180° With ψ_o=σ=0.5°, R=1.0, θ_{rim}=60°, and Solar Inclination =30°.

(Fig. C-38), the n=1 curve begins to dip somewhat in the neighborhood of $q \simeq .60$ as less mirror surface is available. These effects are more pronounced as ϕ_o is increased further as shown in Figs. C-39 to C-42. The multiple bounce radiation can still contribute past $\phi_o = 120°$ (Fig. C-40), but the n = 1 region is beginning to suffer considerably. The final two curves $\phi_o = 150°$ and $\phi_o = 180°$ show no multiple bounce contribution and the single bounce region has been drastically cut away. It should be noted, however, that the n=1 peak is not reduced at this inclination.

Figures C-43 to C-49 present the same type of results for the nominal collector-receiver combination with solar inclination I=60°. At $\phi_o = 0$ in Fig. C-43 the receiver sees less multiple bounce radiation and in the region near q=.90, the single bounce contribution is slightly lower, than in the $I = 30°$ case. As ϕ_o is increased, the n=1 region (including the peak) begins to immediately show some degradation and, while the multiple bounce contributions are also reduced; they are still present at $\phi_o = 120°$ in Fig. C-47. At these large values of ϕ_o, the concentration curve has suffered drastically because very little illuminated collector can be seen. In fact, for $\phi_o = 180°$, Fig. C-49, the receiver is dark since the entire collector lies below this receiver line and no light from the mirror surface can reach this region.

The data presented in Figs. C-36 to C-49 are presented in another form in Figs. C-50 and C-51. Here,

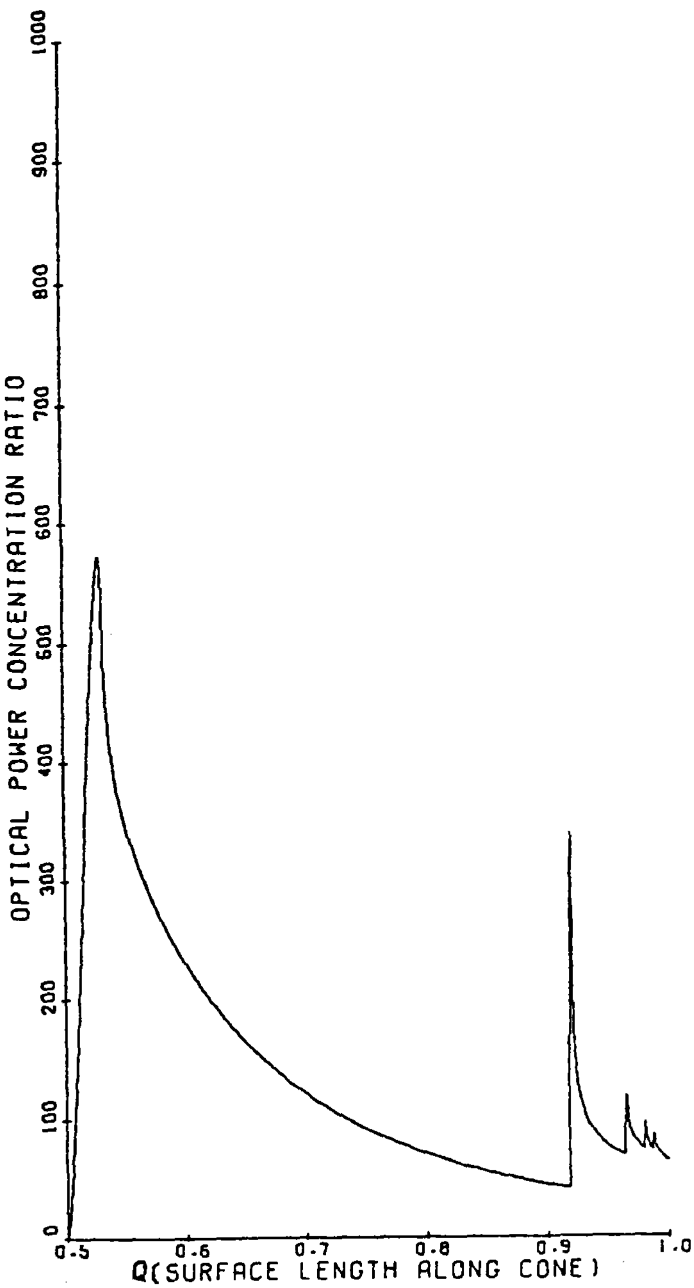

Figure C-43. Concentration Distribution at ϕ_o=0° With ψ_o=σ=0.5°, R=1.0, θ_{rim}=60°, and Solar Inclination =60°.

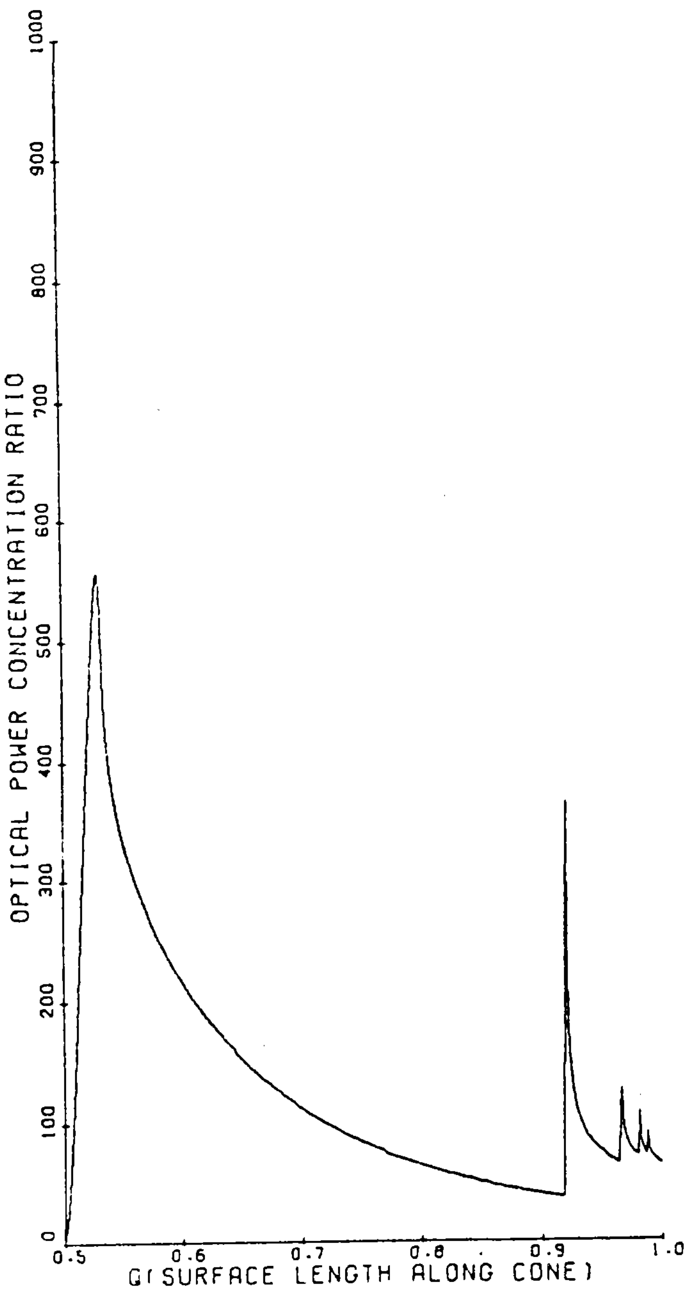

Figure C-44. Concentration Distribution at ϕ_0=30° with ψ_0=σ=0.5°, R=1.0, θ_{rim}=60°, and Solar Inclination = 60°.

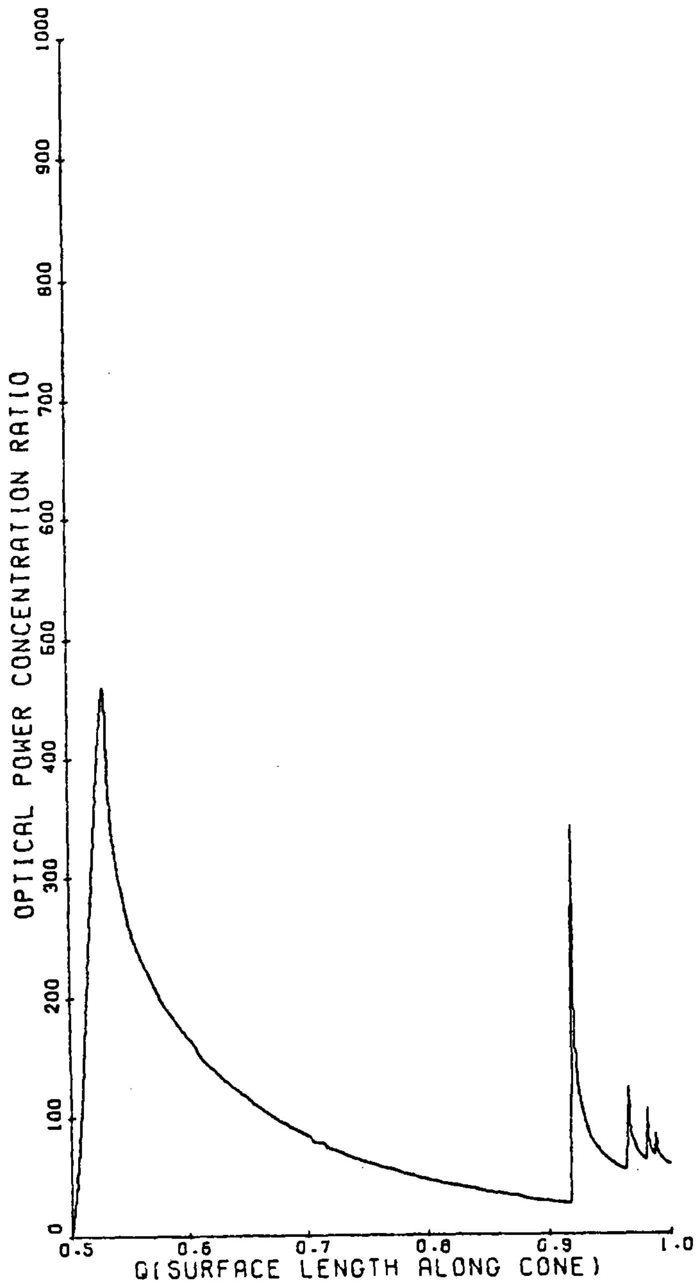

Figure C-45. Concentration Distribution at ϕ_o=60° with ψ_o=σ=0.5°, R=1.0, θ_{rim}=60°, and Solar Inclination =60°.

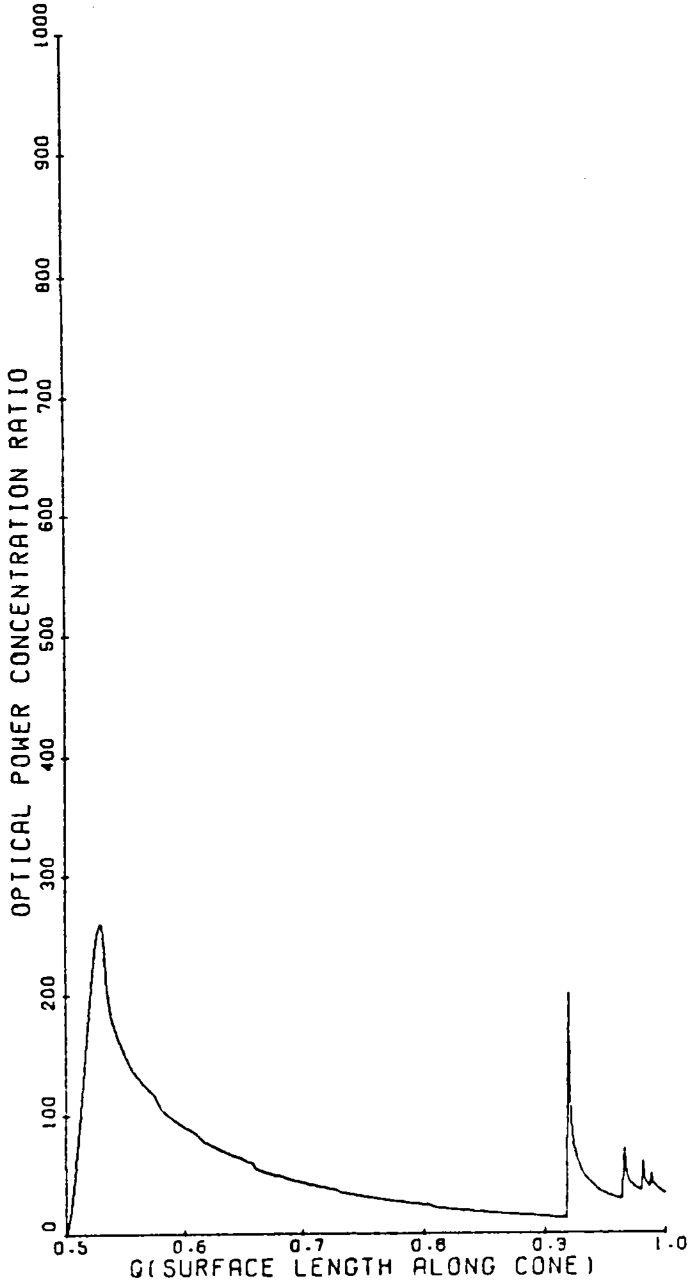

Figure C-46. Concentration Distribution at ϕ_o=90° With ψ_o=σ=0.5°, R=1.0, θ_{rim}=60°, and Solar Inclination =60°.

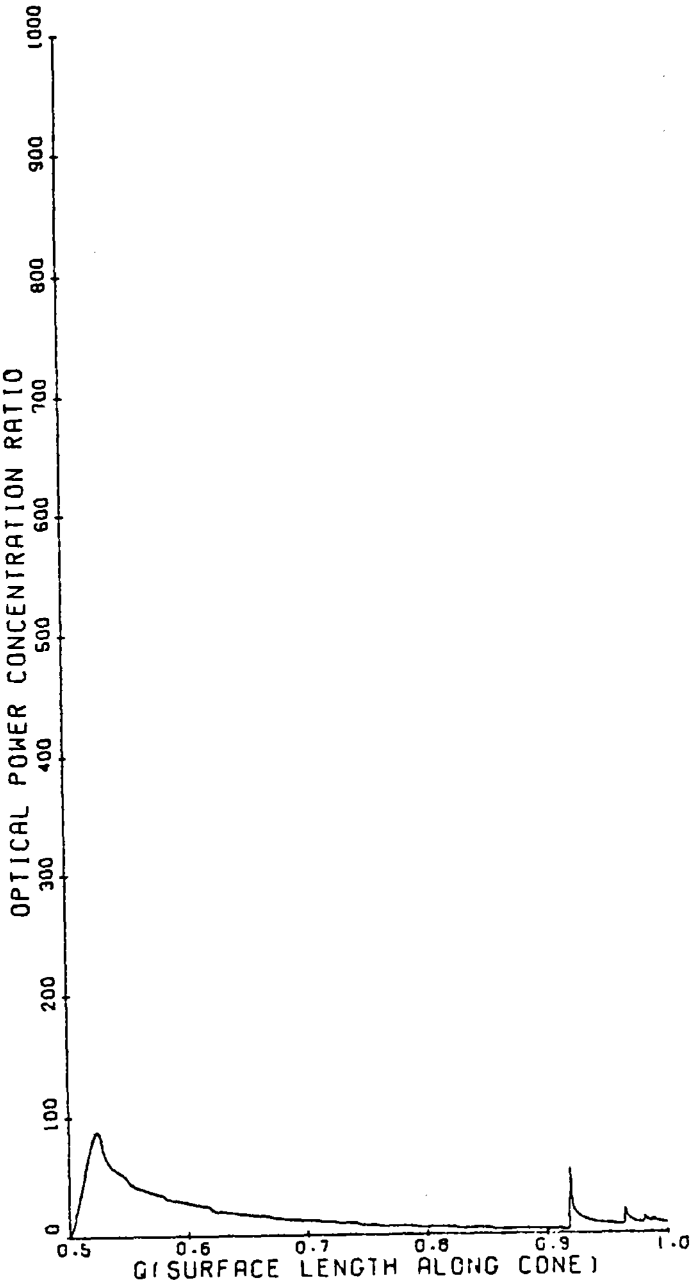

Figure C-47. Concentration Distribution at ϕ_o=120° With ψ_o=σ=0.5°, R=1.0, θ_{rim}=60°, and Solar Inclination =60°.

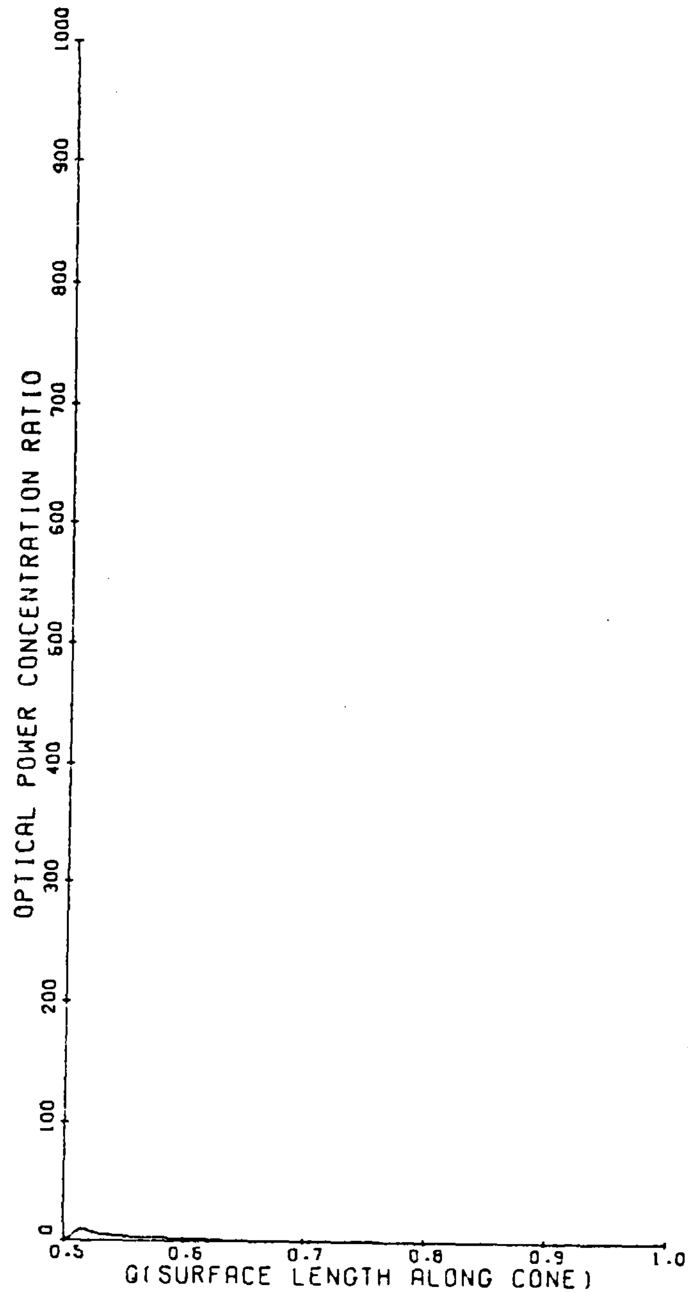

Figure C-48. Concentration Distribution at ϕ_o=150° With ψ_o=σ=0.5°, R=1.0, θ_{rim}=60°, and Solar Inclination = 60°.

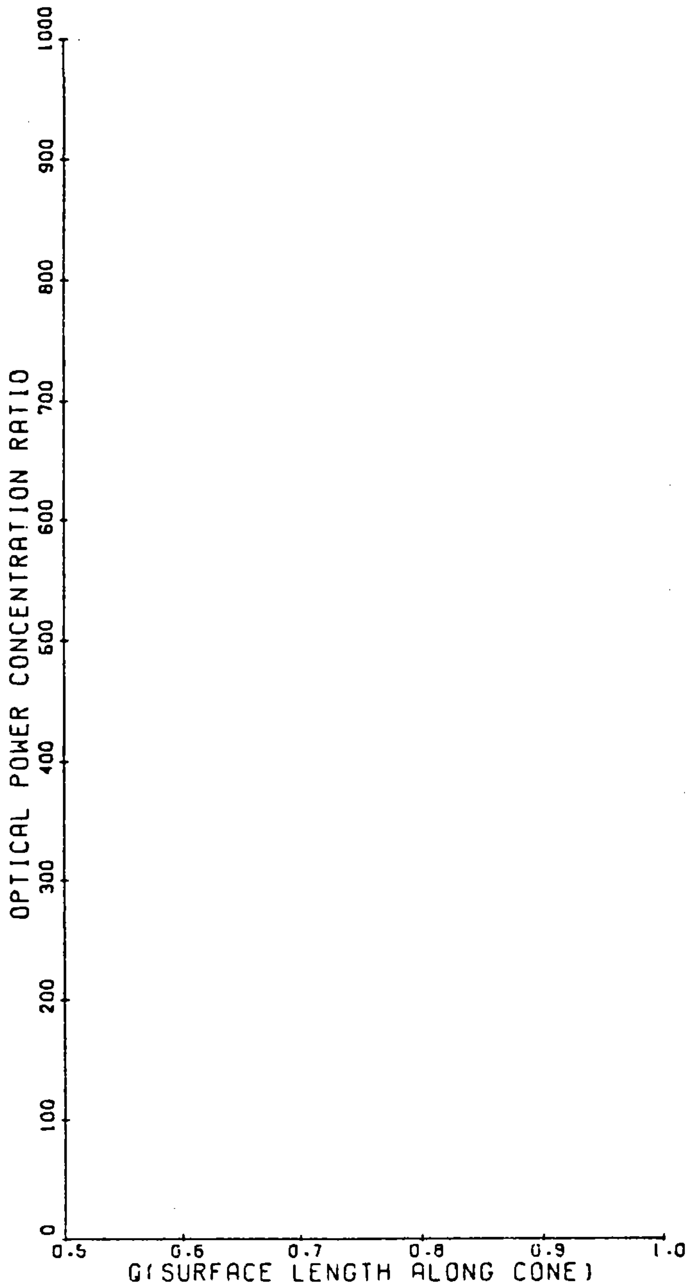

Figure C-49. Concentration Distribution at ϕ_o=180° With ψ_o=σ=0.5°, R=1.0, θ_{rim}=60°, and Solar Inclination =60°.

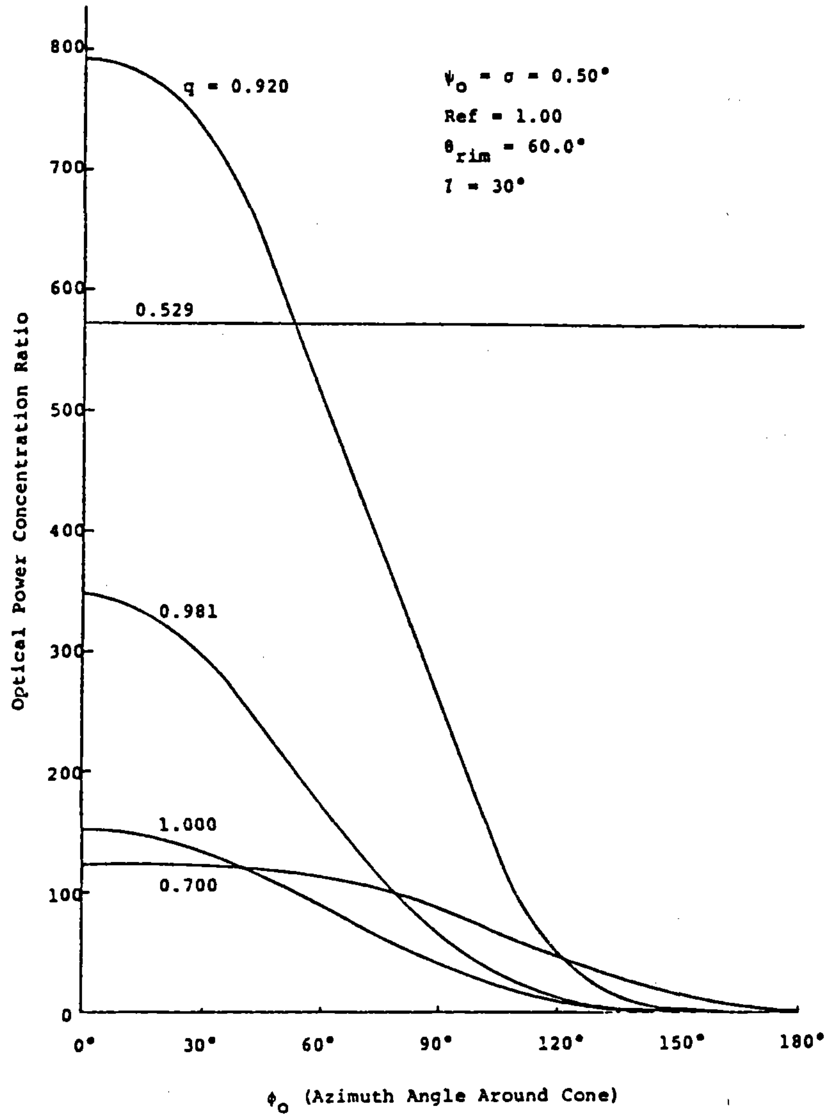

Figure C-50. Azimuthal Concentration Distribution for Various Values of q With ψ_o=σ=0.50°, R=1.0, θ_{rim}=60°, and Solar Inclination = 30°.

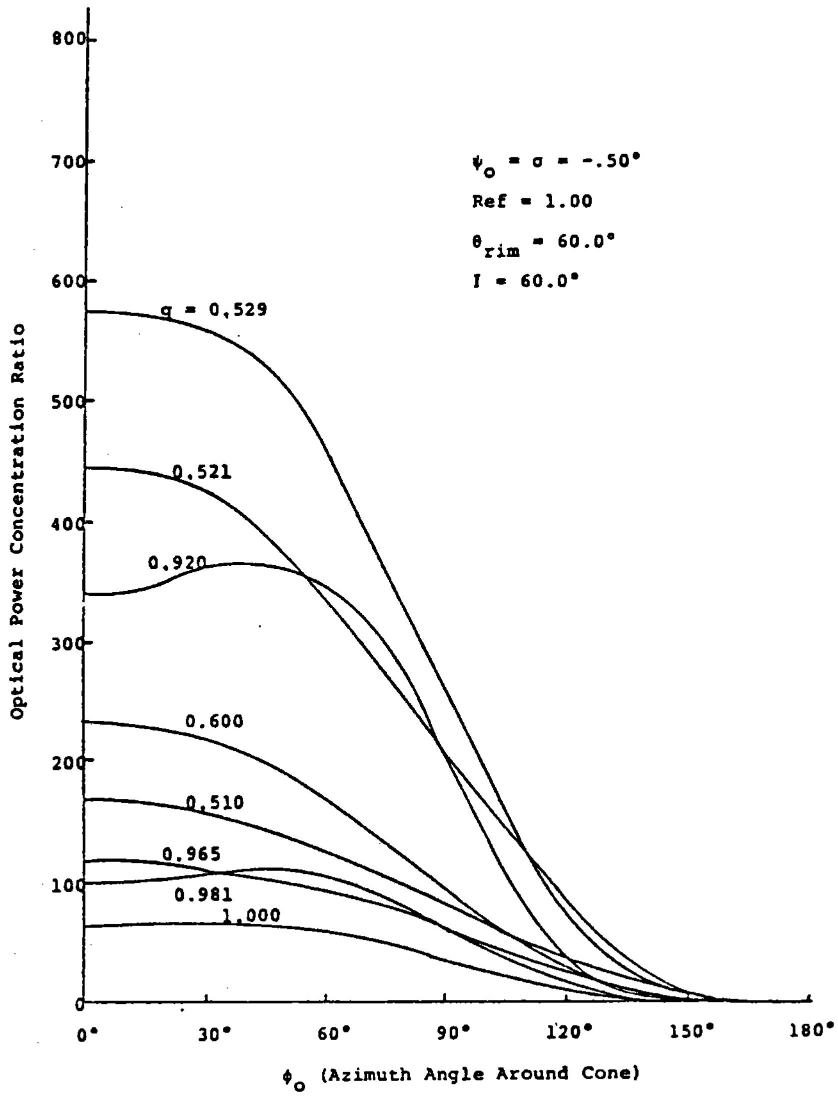

Figure C-51. Azimuthal Concentration Distribution for Various Values of q With $\psi_o = \sigma = 0.50°$, R=1.0, $\theta_{rim} = 60°$, and Solar Inclination = 60°.

concentration is plotted as a function of ϕ_o for various values of parameter q. The inclination angle is 30° for Fig. C-50 and 60° for Fig. C-51. It is interesting to note that for I=60°, there are some q values where the concentration increases and then decreases as ϕ_o is increased, even though the total power over a selected cone area is decreasing for increasing ϕ_o. [This effect arises because the finite sun can get light to a point from planes with larger effective rim angle than the rim angle used by the center of the sun.]

Numerous effects can be studied using the figures presented in this section. The ones emphasized in the present discussion serve to indicate the primary features obtained by varying some of the parameters. Many other curves can be obtained easily by employing the codes developed at Texas Tech in conjunction with proper computers and plotting hardware. At this point, however, attention will be directed to another type of concentration distribution, the concentration on the reflector surface itself. This matter is discussed in Section C-9.

C-8.3 <u>Pertinence of 30° and 60° Inclinations</u>

An iso-inclination plot for 1977 is given in Fig. C-52. By following the curves for I=30° and I=60°, one can determine local solar time when the above distributions are valid. The iso-inclination data is for a dish tilted so that the symmetry axis is 15° from the local normal and points toward the south. The dish is located at latitude 33.65° which corresponds to the location of Crosbyton, Texas. This is considered as the nominal dish position for this study.

C-8.4 <u>Comparison of Results</u>

The optical flux concentrations for n=1 have also been calculated with the streamlined approximation methods of E-Systems and with the generalized cone optics codes of Shrenk. [See references in Appendix D] Fig. C-53 shows detail of the n=1 peak of the nominal case with I=30°. The point data shows the results of E-Systems. Selected data points from the three calculation methods are listed in Tables C-3 and C-4. The agreement is seen to be quite good and illustrates that the streamlined approximation method of E-Systems (described in Appendix D) is justified system analysis. This is confirmed by the fluid behavior as described in Appendix E.

C-9 OPTICAL CONCENTRATION ON THE MIRROR SURFACE

As another example of a concentration calculation using this method, consider the "mirror hot spot" on a hemis-

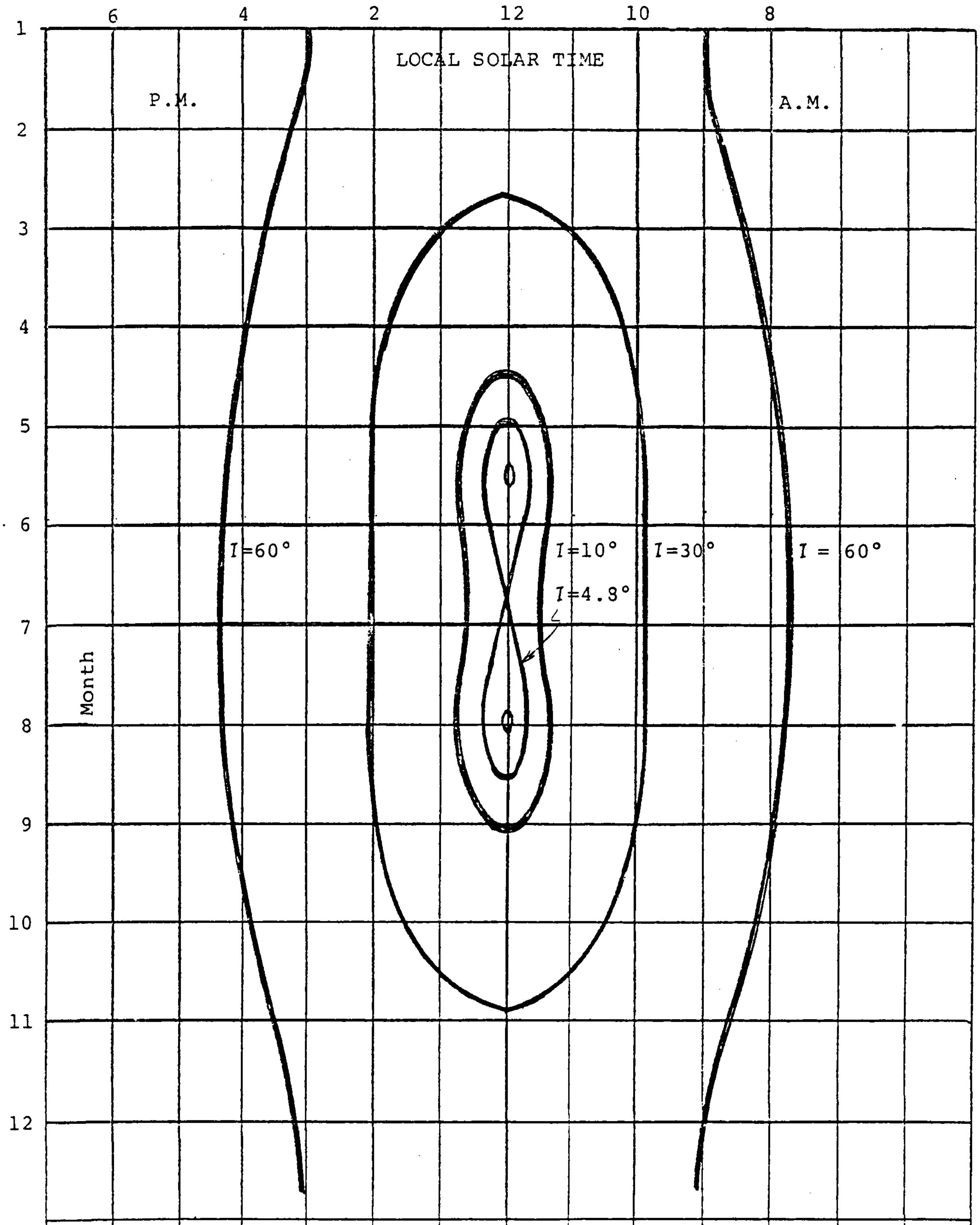

FIGURE C-52. Iso-inclination Plot for 1977.

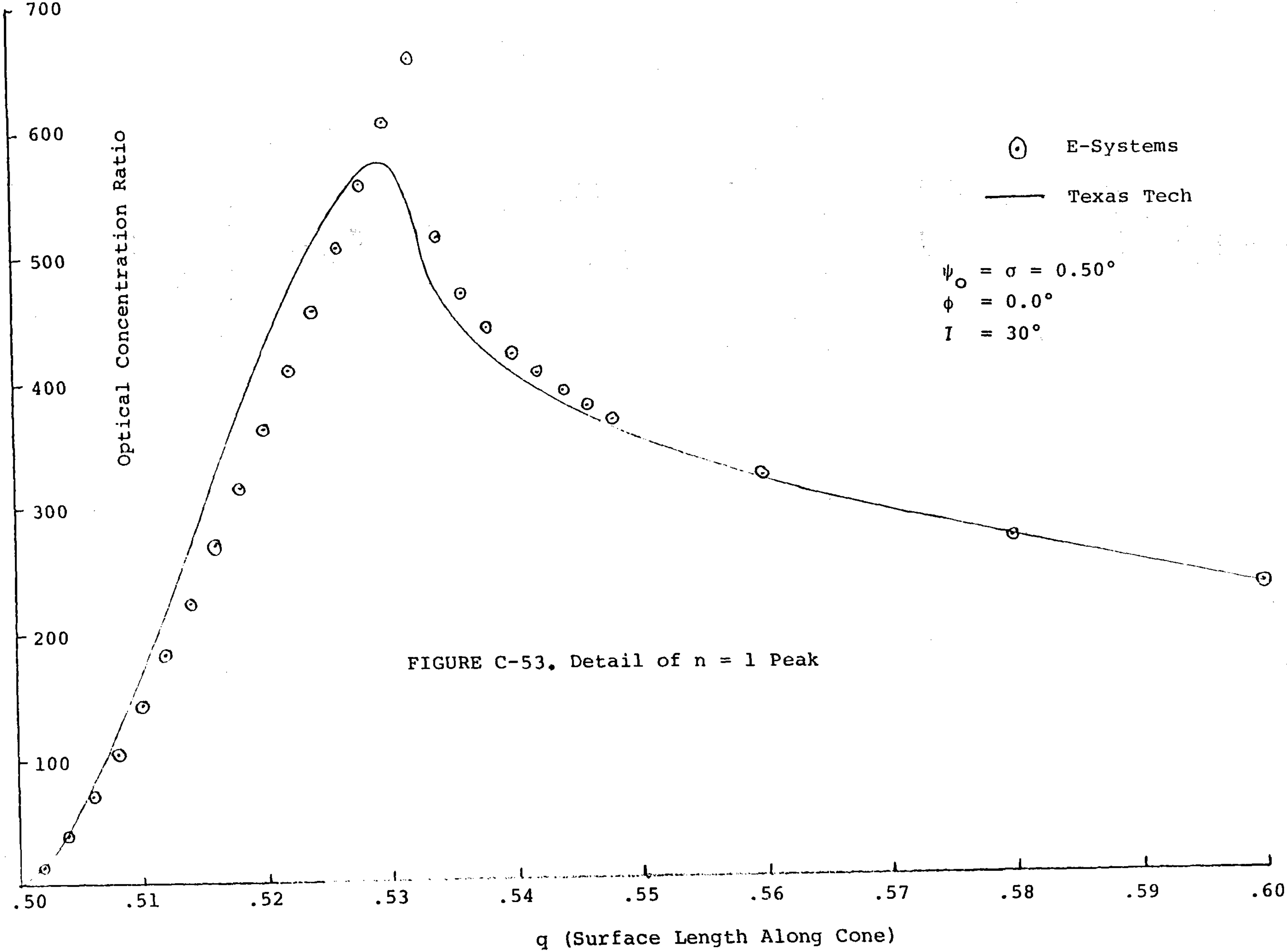

FIGURE C-53. Detail of n = 1 Peak

TABLE C- 3

COMPARISON OF SELECTED CONCENTRATION VALUES FOR SOLAR INCLINATION OF 30°

q	ϕ_o	Texas Tech	Schrenk	E-Systems
.52	0°	420.91	418	361
.53	0°	571.08	570	607
.54	0°	403.53	396	420
.55	0°	350.56	350	357
.6	0°	229.92	225	230
.7	0°	121.35	116	121
.85	0°	55.3	57	54.9
1.0	0°	28.7	33	28.4
.6	90°	218.7	218	220
.7	120°	45.6	48	46.9
.85	120°	11.66	11	11.3
1.0	120°	3.67	3.8	3.8
.7	150°	14.58	18	14.5
.6	180°	62.8	64	73.9

TABLE C-4

COMPARISON OF SELECTED CONCENTRATION VALUES

FOR SOLAR INCLINATION OF 60°

q	ϕ_o	Texas Tech	Schrenk	E-Systems
.52	0°	420.9	420	361
.525	0°	528.1	532	482
.53	0°	571.0	575	607
.535	0°	453.5	458	487
.54	0°	403.5	404	420
.7	0°	120.7	121	120
.9	0°	43.4	44	43.0
.52	120°	80.4	76	60.6
.53	120°	68.13	67	97.8
.54	120°	54.76	55	63.3
.7	120°	11.8	12.2	11.7
.9	120°	3.4	3.2	3.26

pherical collector. A hot spot on the collector surface results when the absorber is removed from the focus during maintenance or failure conditions. It is also important to know the distribution of light on the surface of the collector due to multiple bounce radiation under normal operating conditions. Because the collector is a concentrating reflector, this multiple bounce light may reach large concentration ratios on the reflector surface, near the foot of the absorber. The situation is illustrated in Fig. C-54.

In this illustration, a point on the hemispherical collector at angle ψ_o from the $\hat{e}_s$ vector pointing to the sun is illuminated by two single bounce (n=1) rays. The θ_1 ray is an obvious contributor, but since the θ_2 ray is usually blocked by the absorber, its presence may seem surprising at first glance. However, for each n (bounce number), there are two contributing rays, assuming the absence of the receiver. If the receiver is present along the focus and if it extends to the collector surface, then only θ_1 type rays need be considered. The details of the calculation follow using the formalism discussed above.

The general result of Eqn. (C-27) gives the correct integral for the optical concentration, but it must be applied to this specific case. The geometry of Fig. C-2 is relevant to parametrize the vectors $\hat{b}$ and $\hat{v}$. As before

$$\hat{v} = \begin{pmatrix} \sin\beta \sin\tilde{\omega} \\ \sin\beta \cos\tilde{\omega} \\ \cos\beta \end{pmatrix}, \qquad \text{(C-87)}$$

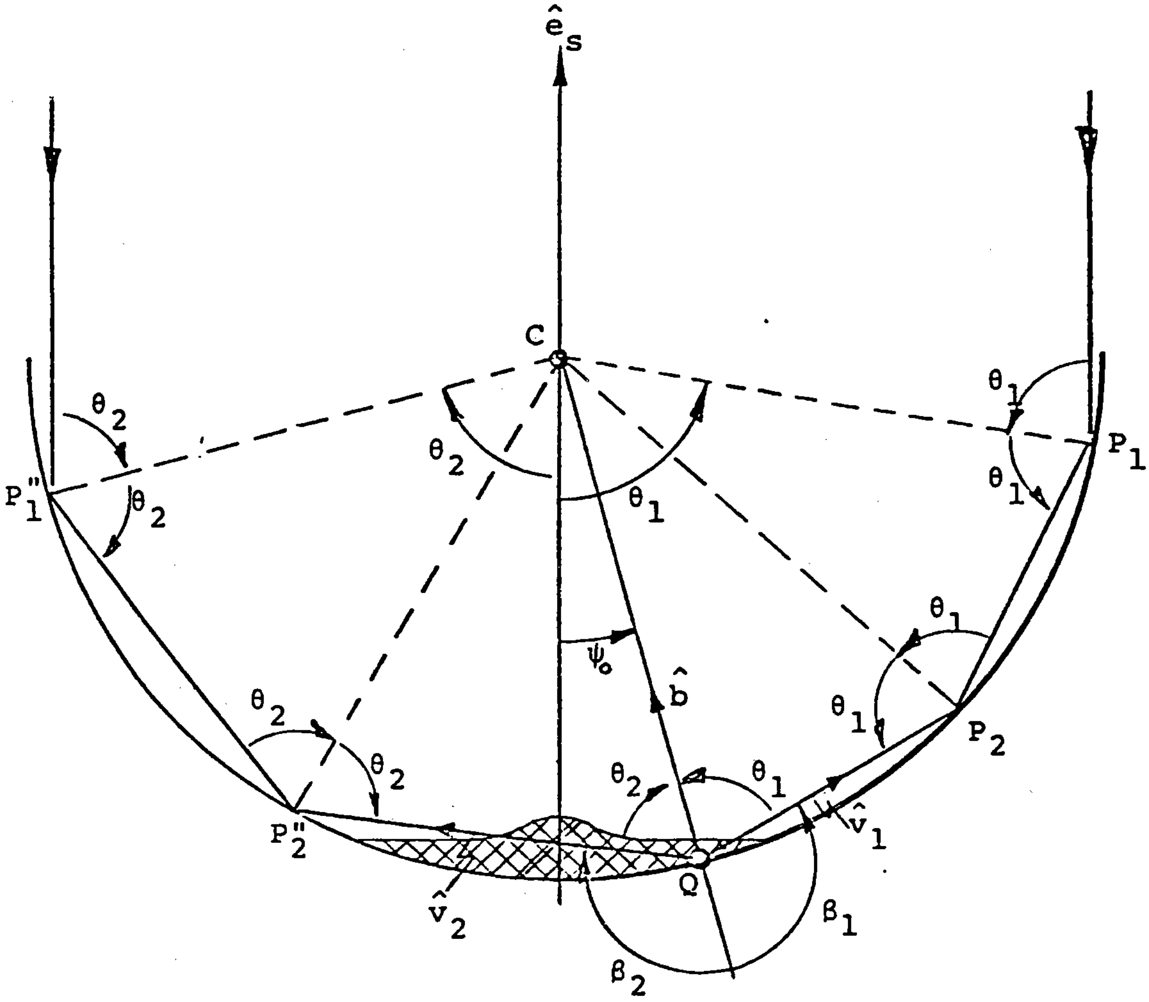

Figure C-54. Semispherical Collector Geometry for Determining Mirror "Hot Spot".

but for this case

$$\hat{b} = \begin{pmatrix} 0 \\ 0 \\ -1 \end{pmatrix} \tag{C-88}$$

so that

$$\hat{b} \cdot \hat{v} = -\cos\beta \quad . \tag{C-89}$$

The requirement that

$$\hat{b} \cdot \hat{v} \geq 0 \tag{C-90}$$

indicates that

$$\pi/2 \leq \beta \leq 3\pi/2 \quad . \tag{C-91}$$

It is emphasized that the above range is not a set of limits for β in the integral of Eqn. (C-27), but the limits must lie in this range. The optical concentration can now be written as

$$F_{dish}\,(\psi_o) = \frac{1}{\Omega_s} \int\!\!\int_{\Omega_m} (-\cos\beta)\sin\beta \; d\beta d\tilde{\omega} \tag{C-92}$$

Although Ω_m could be described in terms of β and $\tilde{\omega}$ and the integral evaluated, it is much more convenient to make a change of variables before doing the integral. Use is made of the structure relations (C-33) and (C-34), remembering, of course, that q = 1 for this calculation. The structure relation (C-34) gives

$$\theta = \pi-\beta$$

as can be seen directly in Fig. C-54. Using this expression to eliminate β from the structure relation (C-33), one obtains the following expression for θ

$$\theta = \frac{\psi + n\pi}{2n + 1} \qquad \text{(C-93)}$$

where n represents the number of bounces of the light prior to striking the dish at ψ. Also from (C-34),

$$\cos\beta = \cos\theta \frac{d\theta}{d\beta}$$

and from (C-93),

$$d\theta = \frac{d\psi}{2n+1}$$

so that

$$F_{dish,n}(\psi_o) = \frac{1}{2(2n+1)\Omega_{s,n}} \int_\psi \int_\omega \sin\left(\frac{\psi + n\pi}{n + 1/2}\right) d\psi d\omega \ . \qquad \text{(C-94)}$$

The above expression for the optical concentration is now ready to integrate according to procedures outlined previously, but careful attention must be paid to the limits. Recall that contributions occur for both θ_1 and θ_2 in Fig. C-54.

The θ_2 contribution is blocked when a receiver is in place. The dish optical concentration is called $F_{D1,n}(\psi_o)$ when the absorber is in place along the focus, and $F_{D2,n}(\psi_o)$ when the absorber is removed. Using device (1) as described previously, one can write

$$\theta_1 = \frac{n\pi \quad +\psi}{2n + 1} \qquad \text{(C-95)}$$

and

$$\theta_2 = \frac{n\pi - \psi}{2n + 1} \quad . \tag{C-96}$$

Calculations are made now for $F_{D1,n}(\psi_o)$ using only θ_1 and for $F_{D2,n}(\psi_o)$ using both θ_1 and θ_2. Thus, by performing the ψ integral first, the following expressions are obtained,

$$F_{D1,n}(\psi_o) = \frac{1}{2(2n+1)\Omega_{s,n}} \int_{-\omega_M}^{\omega_M} \int_{\psi_-(\omega)}^{\psi_+(\omega)} \sin\left(\frac{n\pi + \psi}{n + 1/2}\right) d\psi d\omega \tag{C-97}$$

$$F_{D2,n}(\psi_o) = \frac{1}{2(2n+1)\Omega_{s,n}} \int_{-\omega_M}^{\omega_M} \int_{\psi_-(\omega)}^{\psi_+(\omega)} \left[\sin\left(\frac{n\pi + \psi}{n + 1/2}\right) + \right.$$
$$\left. + \sin\left(\frac{n\pi - \psi}{n + 1/2}\right)\right] d\psi d\omega \tag{C-98}$$

where

$$\omega_m = \begin{cases} \mathrm{Cos}^{-1} \sqrt{1 - \left(\frac{\sin\sigma}{\sin\psi_o}\right)^2} & , \ \psi_o \geq \sigma \\ \pi/2 & , \ \psi_o < \sigma \end{cases} \tag{C-99}$$

and

$$\omega_\pm(\omega) = \mathrm{Sin}^{-1} \left\{ \frac{\cos\sigma\sin\psi_o\cos\omega \pm \cos\psi_o \sqrt{\sin^2\sigma - \sin^2\psi_o \sin^2\omega}}{1 - \sin^2\psi_o \sin^2\omega} \right\} \tag{C-100}$$

It should be noted that the constraints on ω and ψ due to dish rim cutoff must still be imposed, but the restriction on $\hat{b}\cdot\hat{v}$ is already built into the results and is automatically satisfied. A special case of interest is the hot point $\psi_o=0$ when the absorber is removed (symmetrical case):

$$F_{D2,n}(0) = \frac{\sin\left(\frac{n\pi}{n + 1/2}\right)\sin\left(\frac{\sigma_n}{n + 1/2}\right)}{4\sin^2(\sigma_n/2)} \ , \tag{C-101}$$

where σ_n is the apparent solar semidiameter due to error accumulation for the n^{th} bounce. For a rim angle of 90° there are contributions for all n=0,1,2,... . For a rim angle of 60°, the range of n depends on the sun elevation and receiver aximuth. Figure C-55 illustrates $F_{D2,n}(0)$ and $\sum_n F_{D2,n}(0)$ as a function of n with the parameter σ. For each curve $\sigma_n = \sigma$ is used for all n. The subscript n on the above quantities is a reminder that one must sum over all bounces, weighting the result by the mirror reflection coefficient and using the appropriate Ω_{sn} for mirror error accumulation. Therefore

$$F_{Di}(\psi_o) = \sum_n R^n F_{Di,n}(\psi_o), \qquad i = 1,2 \qquad \text{(C-102)}$$

and R is the mirror reflection coefficient. The F_{D2}'s are plotted for σ=0.25° and σ=0.50° in Figs. C-56 to C-59 with R=1 and R=0.88 with five bounces. The individual bounce contributions are shown in Figs. C-56 and C-58 while the five bounce sums are displayed in Figs. C-57 and C-59. One sees the rapid fall off of the curves in the neighborhood of $\psi_o \simeq \sigma$, but the concentration is still equivalent to several suns for ψ_o equal to several multiplies of σ.

An interesting situation to consider is the hypothetical case of a perfectly reflecting full hemispherical collector. The light reflects infinitely many times in this case. If the receiver is not in place, the hot spot at $\psi_o=0$ becomes

Figure C-55. Concentration on Mirror Surface at $\psi_o = 0$.

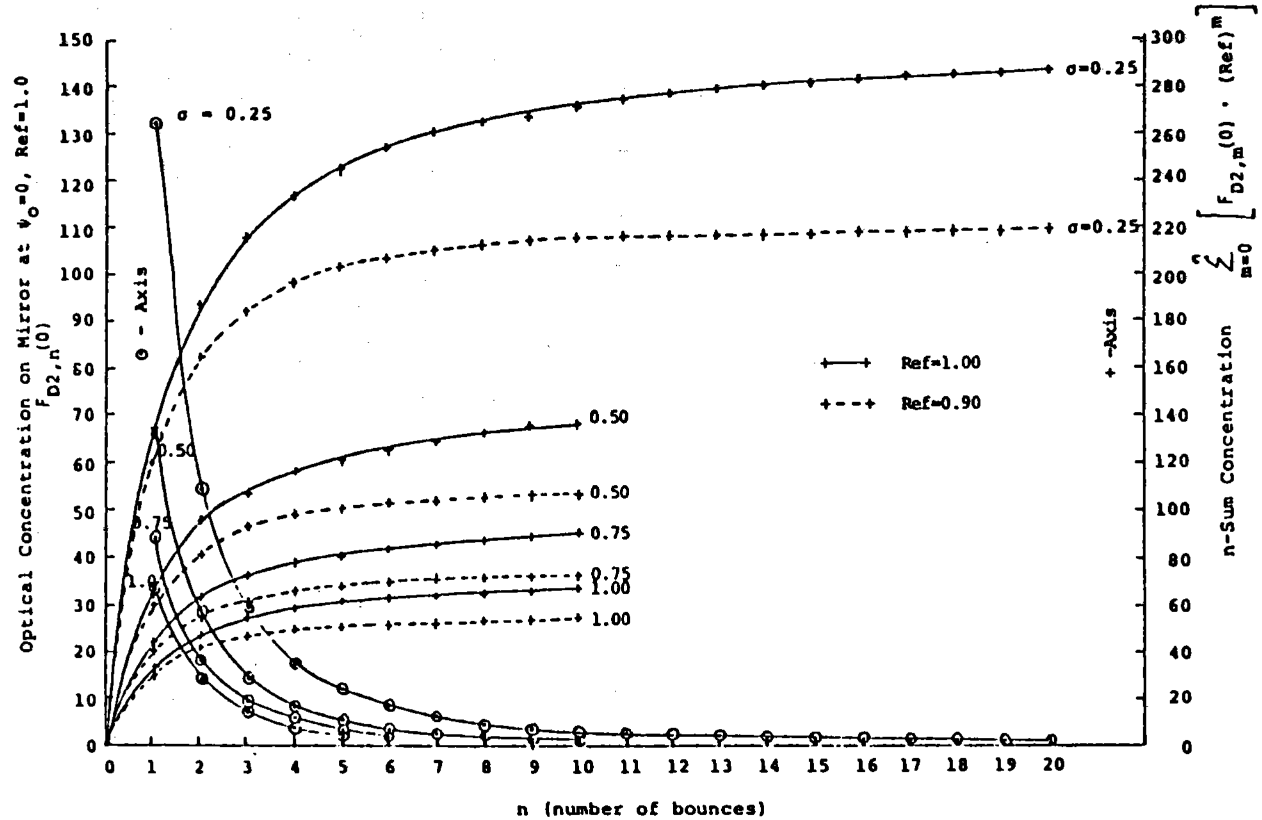

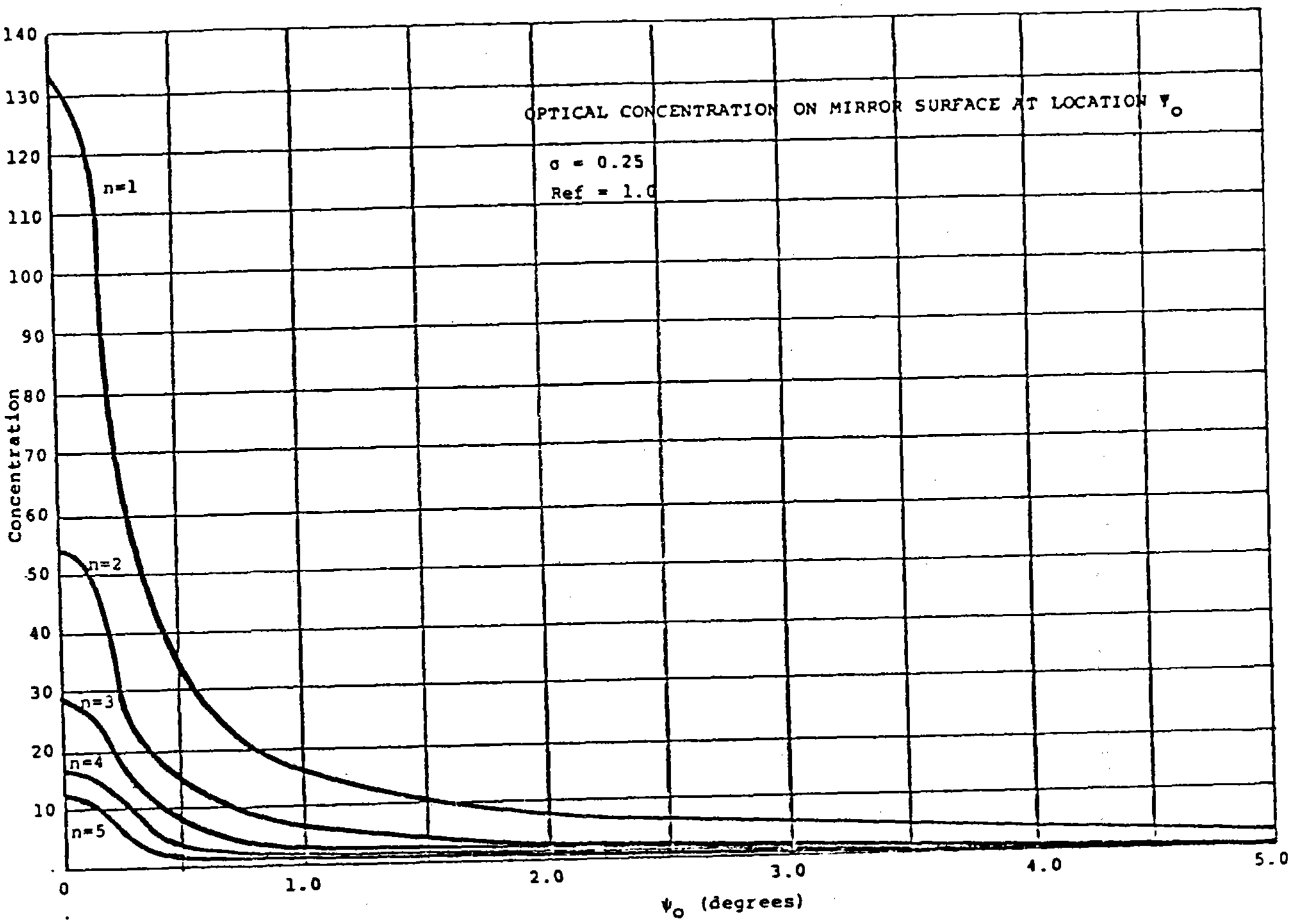

Figure C-56. Mirror "Hot Spot" Concentration for Individual Bounces for True Sun Size, $\sigma = 0.25^0$

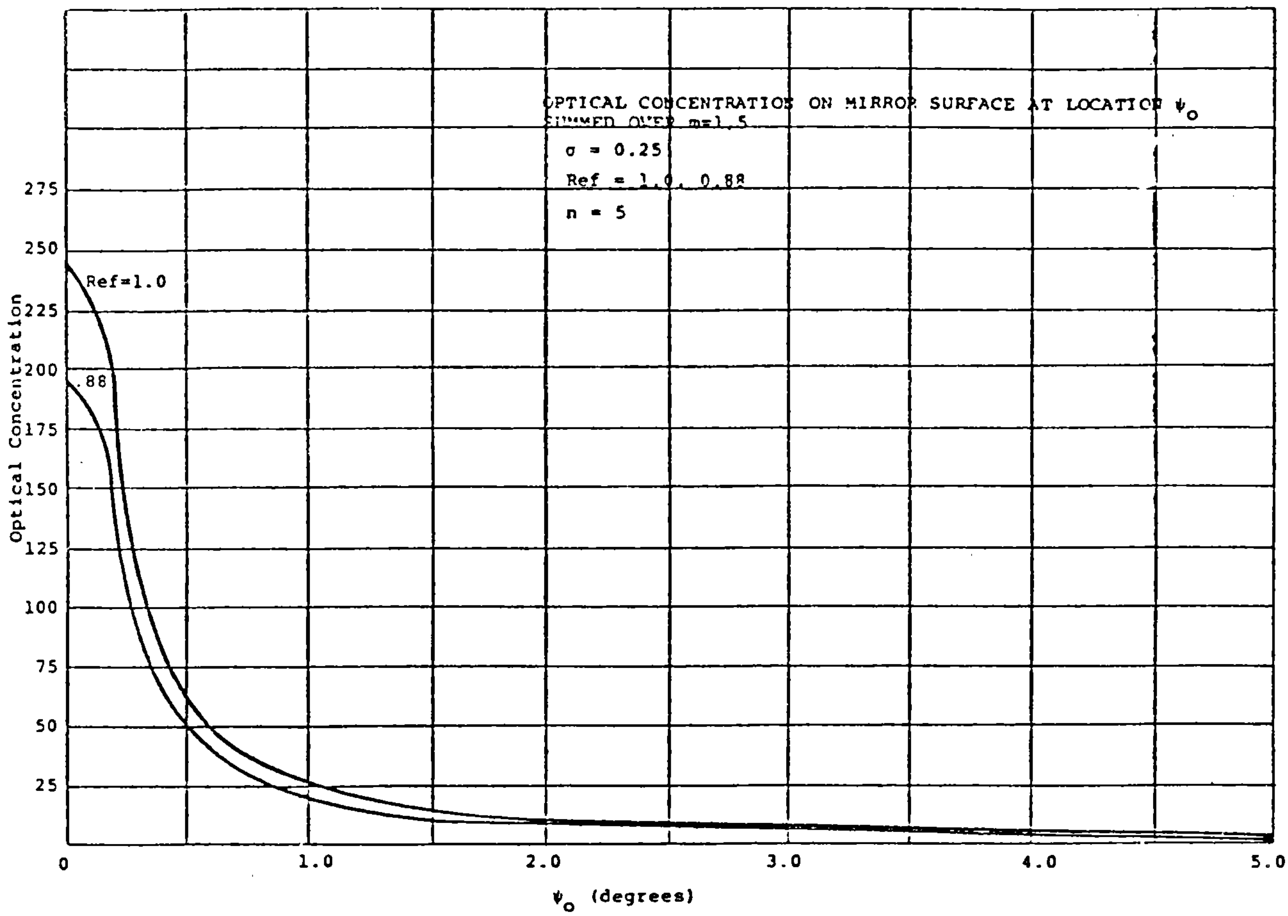

Figure C-57. Mirror "Hot Spot" Concentration as a Function of ψ_0 for True Sun Size $\sigma = 0.25^0$

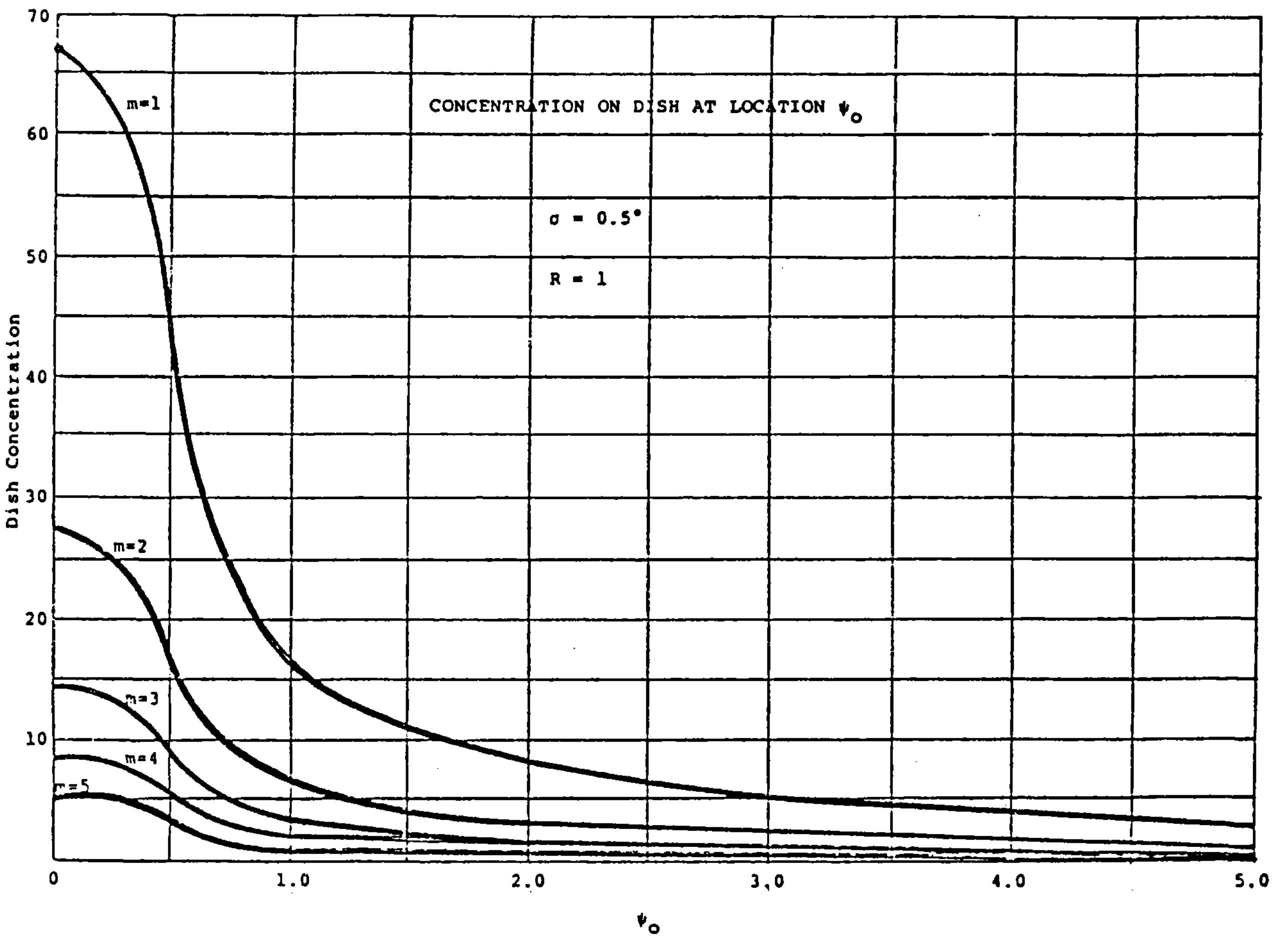

Figure C-58. Mirror "Hot Spot" Concentration for Individual Bounces for Effective Sun Size $\sigma = 0.5^0$

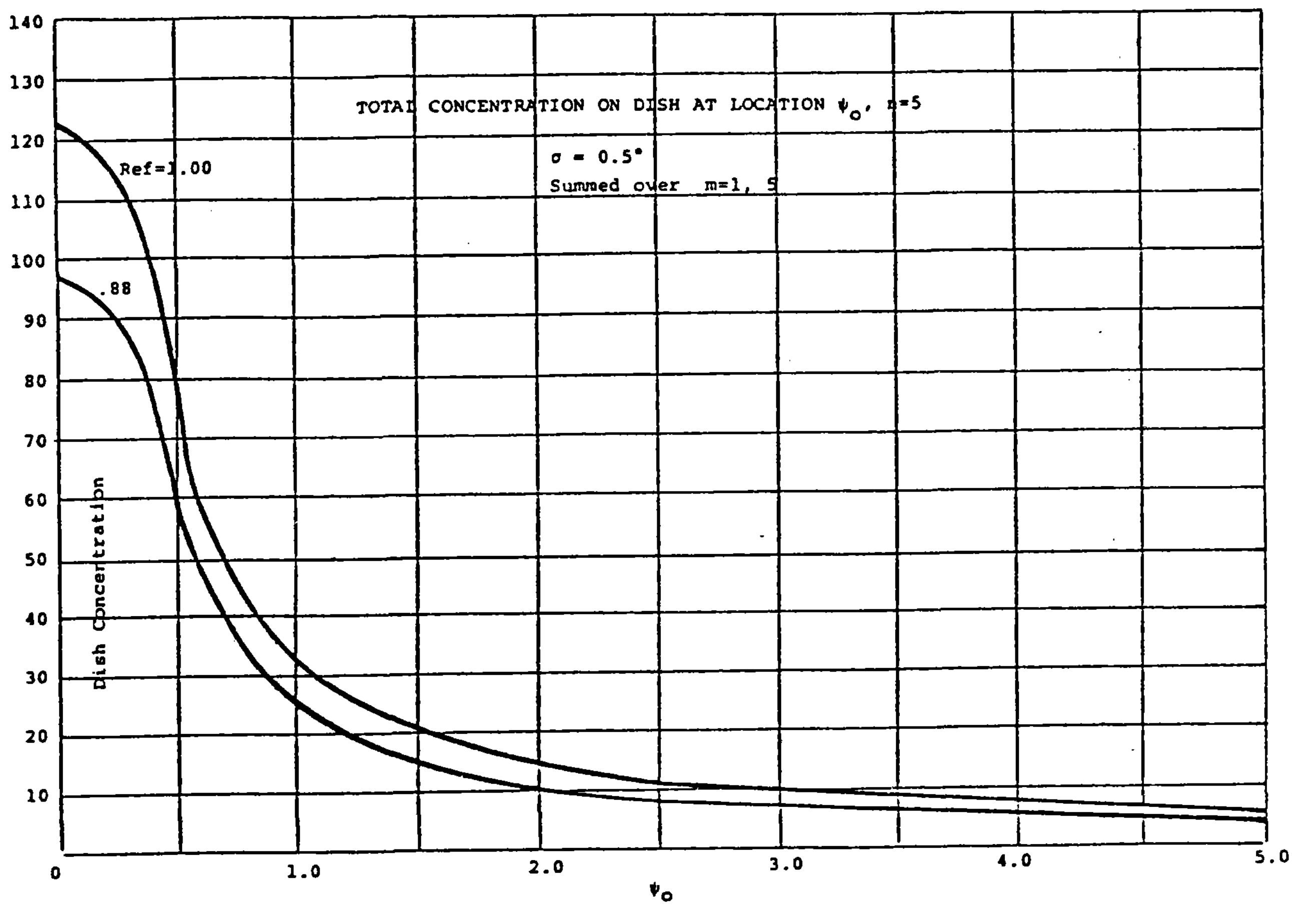

Figure C-59. Mirror "Hot Spot" Concentration as a Function ψ_0 for Effective Sun Size $\sigma = 0.5^0$

$$F_{D2}(0) = \sum_{n=1}^{\infty} \frac{\sin(\frac{n\pi}{n+1/2})\sin(\frac{\sigma}{n+1/2})}{4\sin^2(\sigma/2)} . \qquad \text{(C-103)}$$

Here, perfect optics are assumed so that $\sigma_n = \sigma$. The sum converges rather slowly. In fact, it almost has a logarithmic type singularity. A good approximation is needed that requires fewer terms. Noting that

$$\sin\frac{n\pi}{n+1/2} = \sin\frac{\pi}{2n+1} ,$$

and for large n,

$$\sin\frac{\pi}{2n+1} \simeq \frac{\pi}{2n+1} ,$$

one can approximate the series as follows

$$F_{D2}(0) \simeq \frac{1}{4\sin^2(\sigma/2)} \sum_{n=1}^{N} [\sin(\frac{\pi}{2n+1})\sin(\frac{2\sigma}{2n+1}) - \frac{2\sigma\pi}{(2n+1)^2}]$$

$$+ 2\sigma\pi \sum_{n=1}^{\infty} \frac{1}{(2n+1)^2} , \qquad \text{(C-104)}$$

where N is large enough to allow the above approximation to be reasonable. The infinite sum in (C-104) can be evaluated as

$$\sum_{n=1}^{\infty} \frac{1}{(2n+1)^2} = \frac{3}{4}\xi(2) - 1 \qquad \text{(C-105)}$$

where $\xi(n)$ is the Reiman Zeta function and

$$\xi(2) = \pi^2/6 .$$

The resulting sum is

$$F_{D2}(0) \simeq \frac{1}{4\sin^2(\sigma/2)} \sum_{n=1}^{N} \left[\sin\left(\frac{\pi}{2n+1}\right)\sin\left(\frac{2\sigma}{2n+1}\right) - \frac{2\sigma\pi}{(2n+1)^2}\right] +$$

$$+ 2\sigma\pi\left(\frac{\pi^2}{8} - 1\right) \qquad \text{(C-106)}$$

which becomes exact in the limit as N becomes infinite. For N=1, and $\sigma=0.5°$ ($\simeq$ twice the true sun size), the above sum gives

$$F_{D2}(0) \simeq 154.42$$

which is too high. For N=10, the sum has converged to five significant figures:

$$F_{D2}(0) \simeq 151.72 \qquad (\sigma = 0.5°)$$

For $\sigma=0.25°$ ($\simeq$ true sun size), the sum converges to five significant figures at N=12:

$$F_{D2}(0) \simeq 303.43 \qquad (\sigma=0.25°) \quad .$$

This sum requires far fewer terms than the original sum which requires over 850 terms for similar accuracy. These concentration ratios are useful because they represent the worst peak optical power concentration ratio on the collector surface.

The $F_{D2,n}(\psi_o=0)$ are plotted as a function of n in Fig. C-55 for various σ values. The circled data points are these data and the left hand axis is the appropriate scale. The + data points are the $\sum_{i=0}^{n} [F_{D2,i}(0) \cdot R^i]$. The solid curves are for R=1.0 and the dotted curves for R=0.90. The appropriate scale for these data is the righthand axis. The almost logarithmic nature of the sum shows quite clearly. It must be noted that these are discrete valued curves, even though smooth curves are drawn between the points. A policy using $\sigma_n \neq \sigma$ (to account for errors) would reduce the predicted concentrations considerably as one may estimate from the results shown in the figures.

The "mirror hot spot" is a real concept that must be taken into consideration. For practical mirror surfaces ($R \neq 1.0$), energy will be absorbed by the collector. The results of this section indicate that the resulting heating of the collector surface can be significant.

C-10 RELATIONSHIP OF THE OPTICAL ANALYSIS OF E-SYSTEMS TO THE PRESENT METHOD

The remarkable closed form expression used by E-Systems has a nice interpretation. Eqns. (D-21) and (D-33) of the following appendix are reproduced below in the notation of this appendix (note that θ and ϕ have their meanings interchanged in the notations of Appen. C and Appen. D.)

$$F_{1S}(q,\psi_o) = \int_{\theta_a}^{\theta_b} F_1'(\theta)\,d\theta \qquad \text{(C-107)}$$

$$F_{1NS}(q,\psi_o,\phi_o) = \int_{\phi_o - \frac{\pi}{2}}^{\phi_o + \frac{\pi}{2}} \frac{2}{\pi}\cos^2(\phi - \phi_o)\left[\int_{\theta_a}^{\theta_b} F_{1S}(q,\theta)\,d\theta\right] d\phi \qquad \text{(C-108)}$$

where the subscripts S and NS refer to the azimuthally symmetric configuration for a given rim angle and to the non-azimuthally symmetric configuration for the same angle. These formulas apply to perfectly aligned conical receivers and the subscript, 1, indicates single bounce radiation. The integrand $F_{1S}(\theta)$ is the same function as the $F_{1S}(q,\psi_o)$ except that structure relation (C-33) and (C-34) are to be used to properly parametrize the function as a function of ψ_o in one case and as a function of θ in the other.

The form in (C-108) is particularly elegant, offering the nice interpretation explained in the next appendix.

The normalized azimuthal weight function chosen:

$$\frac{2}{\pi} \cos^2 (\phi-\phi_o) \tag{C-109}$$

is extremely effective as the detailed comparisons with our method shows. The exact weight chosen is not crucial. The weight chosen is an extremely simple function with essentially all of the right properties. One simply requires a normalized function, peaked at ϕ_o which falls smoothly to small positive values as ϕ approaches $\phi_o \pm \frac{\pi}{2}$. One is strongly reminded of saddle point approximation procedures.

The integrand in (C-108) has an interesting interpretation from our point of view. When the integration variables of (C-27) are converted to employ the differential $\sin\theta d\theta$, the resulting integrand is <u>not</u> the same as $F_1'(\theta)$ even though the limits of integration are, to within the approximation used, exactly the same. The striking difference is that our integrand is the exact point sun distribution function bearing the caustic singularities, whereas $F_1'(\theta)$ has no singularities. Here is a way to explain the difference.

There is a way of performing integrals known as <u>integrand averaging or the local mean value method</u>. In order to evaluate an integral, one may write:

$$\int_{\alpha}^{\beta} K(x)f(x)dx \simeq \int_{\alpha}^{\beta} K(x)\bar{f}(x)dx \qquad \text{(C-110)}$$

where

$$\bar{f}(x) = \int_{x^-}^{x^+} \rho(x,y)f(y)dy \qquad \text{(C-111)}$$

The weight function $\rho(x,y)$ is normalized

$$\int_{x^-}^{x^+} \rho(x,y)dy \equiv 1 \text{ and } \rho(x,y) > o \qquad \text{(C-112)}$$

so that $\bar{f}(x)$ is actually an average value of $f(x)$ over the inteval. Notice, in particular that exact equality pertains if $p(x,y) = \delta(x-y)$. Such approximations can be extremely good for small ε and are a useful device for removing singularities from integrands to facilitate machine integration.

The integrand, $F_1(\theta)$, may be considered to be an averaged representation of the point sun distribution function, averaged over an interval of length $2\sigma \equiv \Delta\psi$. Since σ is very small for the cases considered, one should not be surprised to find that Eqns. (C-107) and (C-108) are accurate. Thus, one finds that the procedure used by E-Systems is very powerful and fast.

APPENDIX C REFERENCES

[1] Pettit, Richard B., "Specular Reflectance Properties of Mirror Materials," Proceedings of the Joint Conference of the American Section of the International Solar Energy Society of Canada. August 15-20, 1976, Winnipeg, Canada, pp. 331-338.

APPENDIX D. OPTICAL ANALYSIS BY E-SYSTEMS

Until recently, the optical properties of a large aperture hemispherical solar concentrator had not been subjected to detailed analytical treatment. Recent papers by Kreider (Ref. D-1), Steward and Kreith (Ref. D-2), McKenney (Ref. D-3), and Clausing (Ref. D-4) present optical analyses of hemispherical concentrators. In Reference D-1 and D-2, the concentration distribution over the linear receiver of a hemispherical concentrator is presented for a point-source sun and for perpendicular illumination of the aperture. Point sun distributions produce troublesome infinite solar concentration at the caustic hot spot on the receiver near the paraxial focus. Reference D-3 presents a numerical methodology for defining the solar concentration distribution over the linear receiver for perpendicular illumination of the aperture and for a three-point model of the sun. Although no results were presented in Ref. D-3, the three-point model of the sun virtually eliminates the possibility of attaining realistic flux* levels near the caustic hot spot, and the receiver shape considered was cylindrical rather than the more efficient conical shape matched to the optics. Ref. D-4 presents a simplified optical approach defining the <u>average</u> concentration over the

---

* In this appendix, "flux" is used synonymously with "areal power density", i.e., input energy per unit area per unit time.

receiver, which is then analyzed for thermal performance. Since there is actually a variation in local concentration level by a factor of 20 from one end of the receiver to the other, the approach of Ref. D-4 yields highly pessimistic performance levels compared to a more realistic treatment of the optics. Since none of the published optical approaches were found to be acceptable for accurately defining the optical behavior of a hemispherical solar concentrator, O'Neill (Ref. D-5) formulated a cone optics approach to the problem at E-Systems in 1975, which provides accurate three-dimensional solar concentration distributions over the conical receiver for all operating conditions, as verified by a point-by-point comparison with the numerical calculations of Schrenk (Ref. D-6) and the work by Texas Tech.[+] The methodology and results of this solution are presented in the following subsections.

+ The notation of this section differs from that of the previous Appendix. For convenience, the reader may note the following correspondences.

$$2\alpha = \Delta\psi, q\cos\psi_o = \frac{x}{R}, C = F, 2\gamma\sigma = \Delta\psi_{error}$$

D-1 METHODOLOGY

As chronicled by Schrenk (Ref. D-6), the method of tracing cones to treat the finite extent of the solar disc has been successfully employed in the analysis of solar concentrators for more than two decades (e.g., Ref. D-7). The basic method is best explained by an illustrative example. For this example, let us consider the mirror hot spot (i.e., the high concentration point on the mirror surface which is formed when the receiver is not present due to shut down, (malfunction or the like), since the geometry is much simpler for the mirror hot spot than for the receiver concentration distribution which will be considered later. Fig. D-1 shows the problem geometry. The mirror hot spot of interest (under perpendicular illumination of the aperture) occurs at the point of intersection of the optical axis with the spherical reflector. If a differential area of aperture is investigated (as shown in Fig.D-1), the incident and reflected solar radiation is contained within solid cones of total included angle $\Delta\psi$, the angular diameter of the sun. The reflected cone illuminates a quasi-elliptical area of mirror near the hot spot, as shown. From basic geometry, the area of an ellipse is

$$A_{ellipse} \approx \frac{\pi}{4} (\ell \tan\Delta\phi) \frac{(\ell \tan \Delta\psi)}{\cos\phi} \qquad \text{(D-1)}$$

$$= \pi \tan^2\Delta\psi \, R^2 \cos\phi.$$

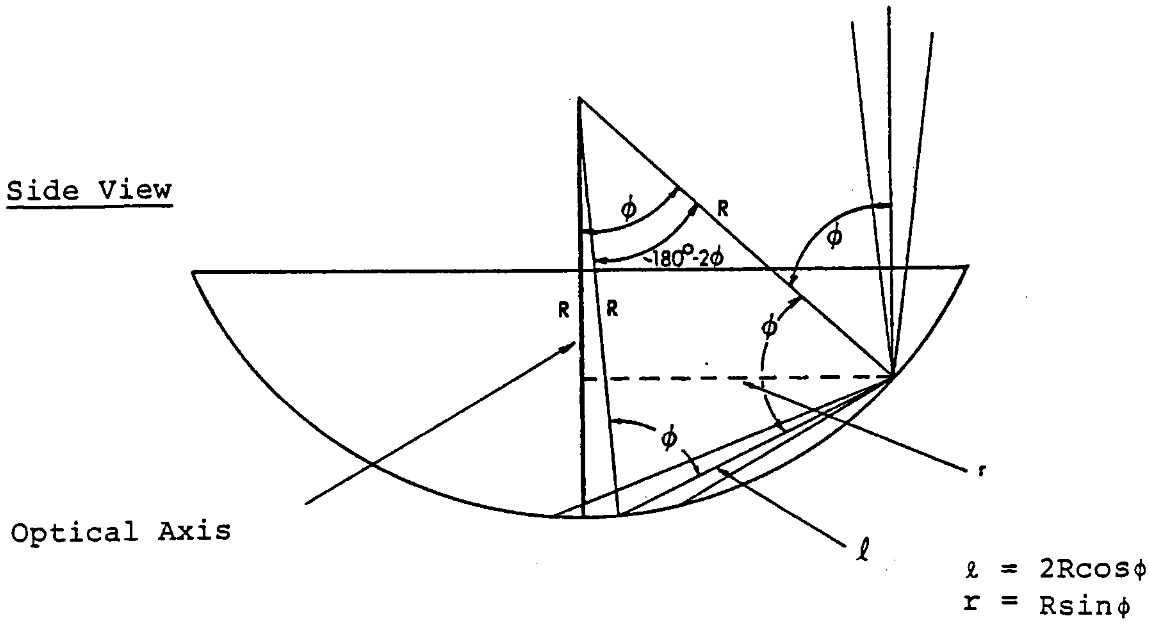

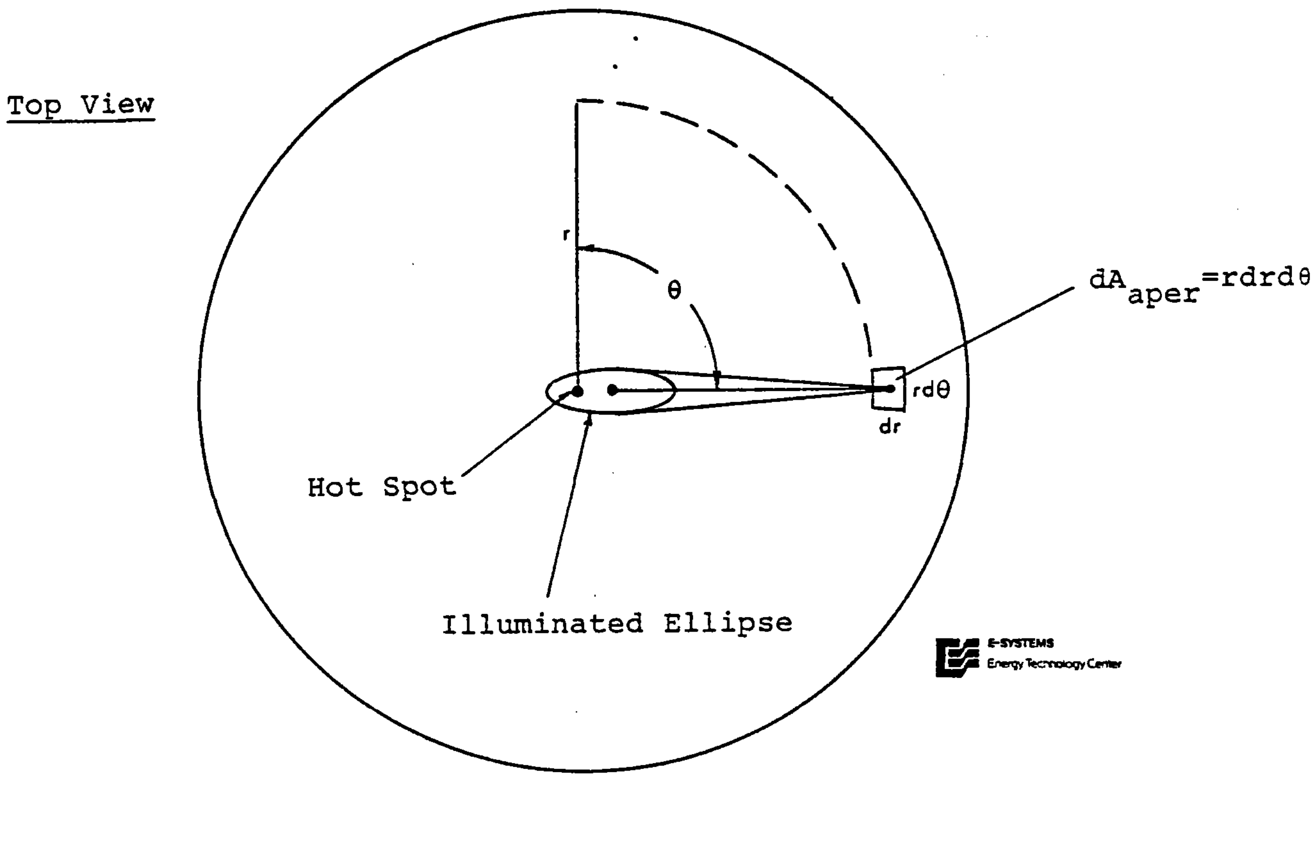

Figure D-1. Mirror Hot Spot Geometry

The energy contained within the incident cone is proportional to the differential aperture area intercepting the incoming light:

$$\begin{aligned} d\dot{Q} &= I_{dn}\, dA_{aper} \\ &= I_{dn}\, r\, dr d\theta \qquad \text{(D-2)} \\ &= I_{dn}\, R^2 \sin\phi \cos\phi \; d\phi \; d\theta \; . \end{aligned}$$

Thus, assuming a mirror reflectivity of 1.00 the areal power density within the elliptical image is:

$$\begin{aligned} d\dot{q} &= \frac{d\dot{Q}}{A_{ellipse}} \approx \frac{I_{dn} R^2 \sin\phi \cos\phi \; d\phi \; d\theta}{\pi \tan^2 \Delta\psi \; R^2 \cos\phi} \qquad \text{(D-3)} \\ &= \frac{I_{dn} \sin\phi \; d\phi \; d\theta}{\pi \tan^2 \Delta\psi} \; . \end{aligned}$$

Now, to determine the total flux at the hot spot, we must integrate over all ϕ and θ values which correspond to ellipses which overlap the hot spot. Because of axial symmetry, we can immediately integrate about θ:

$$\dot{q} = \frac{I_{dn}}{\pi \tan^2 \Delta\psi} \int_{\phi_1}^{\phi_2} \int_0^{2\pi} d\theta \sin\phi \, d\phi$$

$$\dot{q} = \frac{2I_{dn}}{\tan^2 \Delta\psi} \int_{\phi_1}^{\phi_2} \sin\phi \, d\phi. \qquad \text{(D-4)}$$

To complete the integration, we must determine the values of ϕ_1 and ϕ_2. These limits occur when the extremities of the major axis of the ellipse overlap the hotspot. Fig. D-2 shows the applicable geometry for each limit. Thus

$$\phi_1 = 60° - \Delta\psi/3 \qquad \text{(D-5)}$$

$$\phi_2 = 60° + \Delta\psi/3.$$

Performing the ϕ- integration and making the limit substitutions yields:

$$\dot{q} = \frac{2I_{dn}}{\tan^2 \Delta\psi} \left[\cos\left(60° - \frac{\Delta\psi}{3}\right) - \cos\left(60° + \frac{\Delta\psi}{3}\right) \right]$$

$$\dot{q} = \frac{4I_{dn}}{\tan^2 \Delta\psi} \sin 60° \sin\frac{\Delta\psi}{3} \qquad \text{(D-6)}$$

$$= \frac{(3.464)I_{dn}}{\tan^2 \Delta\psi} \sin\frac{\Delta\psi}{3} \quad .$$

Since $\Delta\psi$ is small,

$$\dot{q} = \frac{(1.155)I_{dn}}{\Delta\psi} \quad . \qquad \text{(D-7)}$$

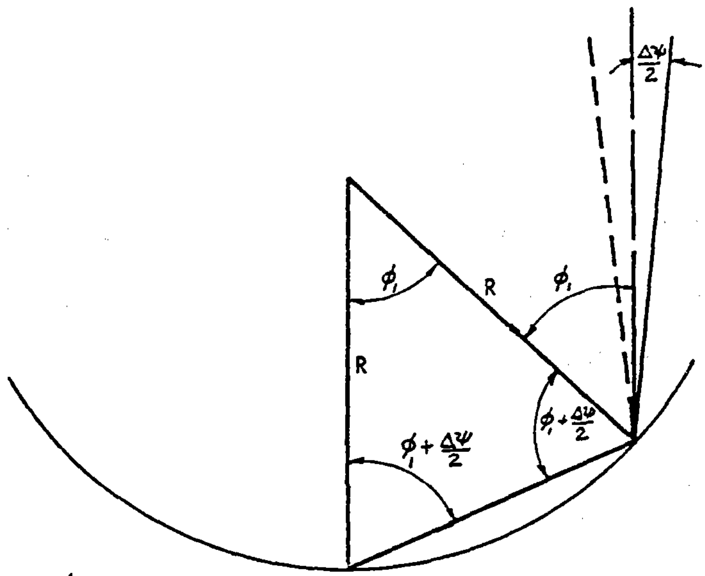

$$\phi_1 + \left(\phi_1 + \frac{\Delta\psi}{2}\right) \div \left(\phi_1 + \frac{\Delta\psi}{2}\right) = 180°$$

$$\phi_1 = \frac{180° - \Delta\psi}{3}$$

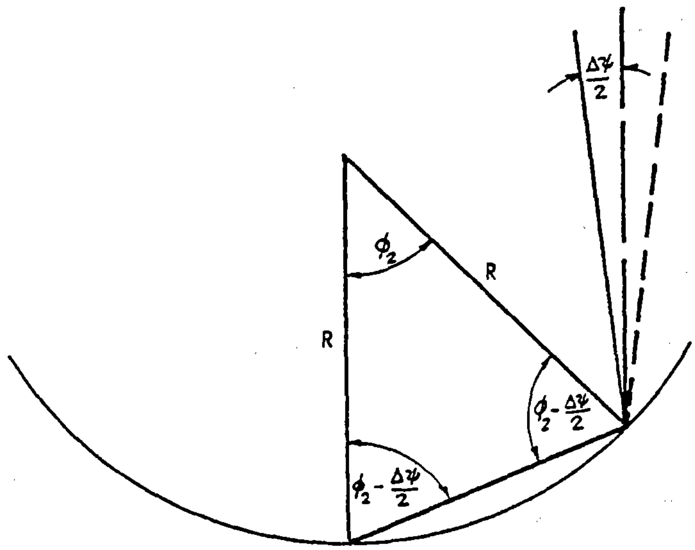

$$\phi_2 + \left(\phi_2 - \frac{\Delta\psi}{2}\right) + \left(\phi_2 - \frac{\Delta\psi}{2}\right) = 180°$$

$$\phi_2 = \frac{180° + \Delta\psi}{3}$$

E-SYSTEMS
Energy Technology Center

Figure D-2. Integration Limits for Mirror Hot Spot

By the definition of concentration (C):

$$C = \frac{\dot{q}}{I_{dn}} = \frac{1.155}{\Delta\psi} . \quad \text{(D-8)}$$

Now the annual average value of $\Delta\psi = 0.533^\circ = 0.0093$ radians.

$$\text{Thus:} \quad C = \frac{1.155}{0.0093} = 124. \quad \text{(D-9)}$$

The value of C above assumes a perfect mirror geometry with no slope errors. Since finite errors will always be present in an actual concentrator, we must treat their effect on the concentration level. One method of treating such errors in an approximate yet physically meaningful manner is shown in Fig.D-3. If mirror inaccuracies are characterized by an angular error ($\Delta\psi_{error}$) in surface normal direction, and if this error is equally likely to be in any direction, then it is easily shown that the reflected radiation will be bounded by and contained within a cone of included angle ($\Delta\psi_{sun} + 4\ \Delta\psi_{error}$). The factor 4 arises from the possibility of either a positive or negative error in slope (yielding a factor of 2), and from the fact that an error in surface normal of $\Delta\psi_{error}$ causes an error of $2\Delta\psi_{error}$ in reflected ray direction since the error is present in both incidence angle and reflection angle (another factor of 2). Based upon the assumption that the reflected radiation is equally likely to be anywhere within the enlarged reflected ray cone, we can further assume that the radiation is uniformly distributed within the reflected ray cone for a first-order

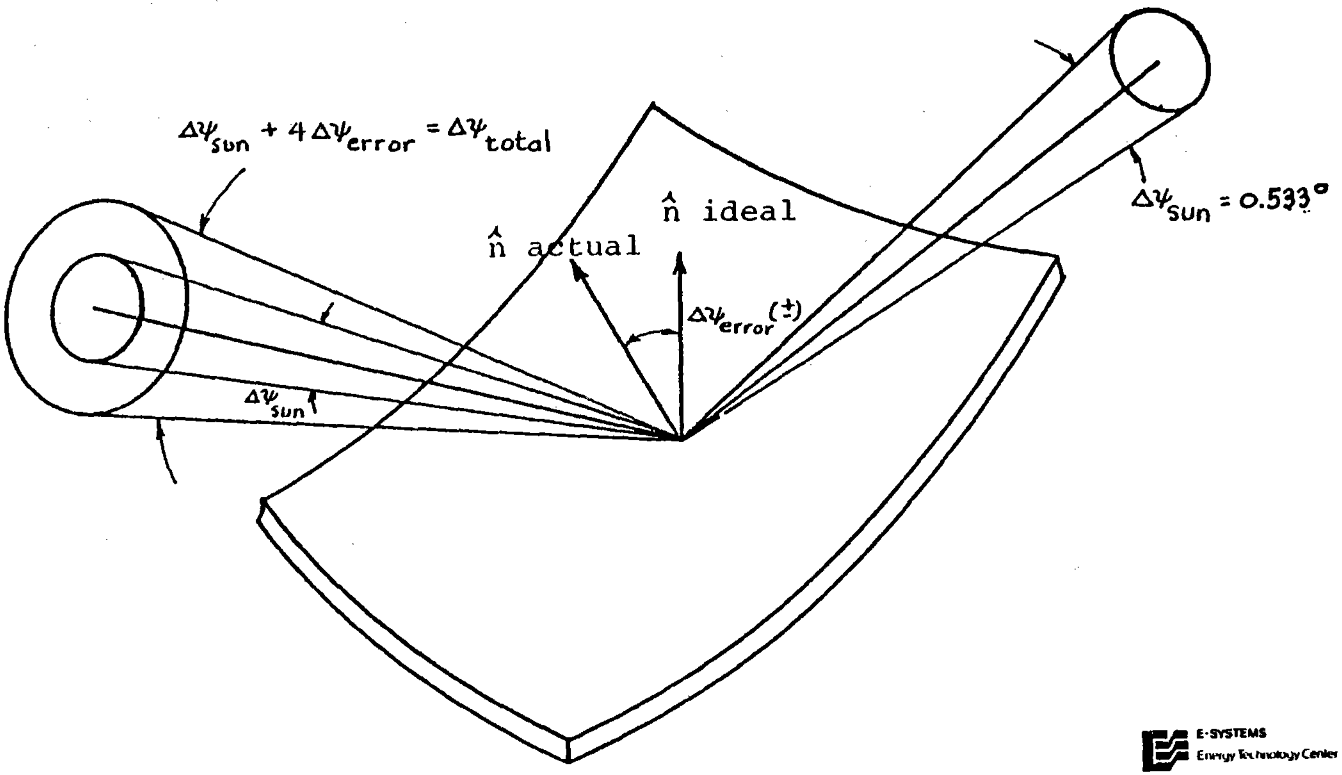

E-SYSTEMS
Energy Technology Center

Figure D-3. Error Treatment by Cone Enlargement analytical treatment of the errors. This method will allow us to properly size the receiver to intercept the reflected radiation, and will provide a reasonable indication of the effects of cone spreading due to mirror surface inaccuracies. A more sophisticated statistical treatment of errors has been presented by Schrenk (Ref. D-6), and this method is planned for use in later phases of this study, but is not part of the current investigations. As discussed in Section IV of the text, a value of $\Delta\psi_{total} = 1.0°$ has been selected as a nominal, practically achievable reflected ray cone angle, including errors. Using this value, the mirror hot spot concentration level including the effect of errors will be about:

$$C_{\substack{\text{Mirror}\\\text{Hot}\\\text{Spot}}} = \frac{1.155}{\Delta\psi_{total}} = \frac{1.155}{0.01745} = 66. \qquad \text{(D-10)}$$

The above discussion (and example calculation) has presented the basic cone optics methodology and error treatment technique. We will now proceed to describe the use of this analytical formulation to define concentrations on the receiver of the FMDF collector.

D-2 AXISYMMETRIC OPTICAL CONCENTRATIONS ON A CONICAL RECEIVER

Consider the schematic of Fig. D-4, which shows the FMDF collector under axisymmetric illumination. A reflected ray cone at location ϕ is shown proceeding toward a receiver.

The reflected ray path length is seen to equal x, the same distance as that measured to the point of interception with the optical axis from the center of curvature. In order to intercept all the reflected energy within the reflected cone, the receiver diameter must equal at least $x \tan \Delta\psi$, from the sectional drawings in Fig. D-4. This simple observation defines the optimal (minimum exposed area) receiver, namely:

$$d_{abs} = x \tan \Delta\psi. \qquad \text{(D-11)}$$

This shape is a cone with vertex at the center of curvature and total included angle $\Delta\psi$. Simple trigonometry further yields the following relation between x and ϕ.

$$x = \frac{R}{2 \cos \phi} . \qquad \text{(D-12)}$$

Thus at $\phi = 0$ (the paraxial ray),

$$x = \frac{R}{2} .$$

At $\phi = 60°$,

$$x = R.$$

(For $\phi > 60°$, reflected rays will reintercept the mirror prior to intercepting the receiver. (These multiply reflected rays

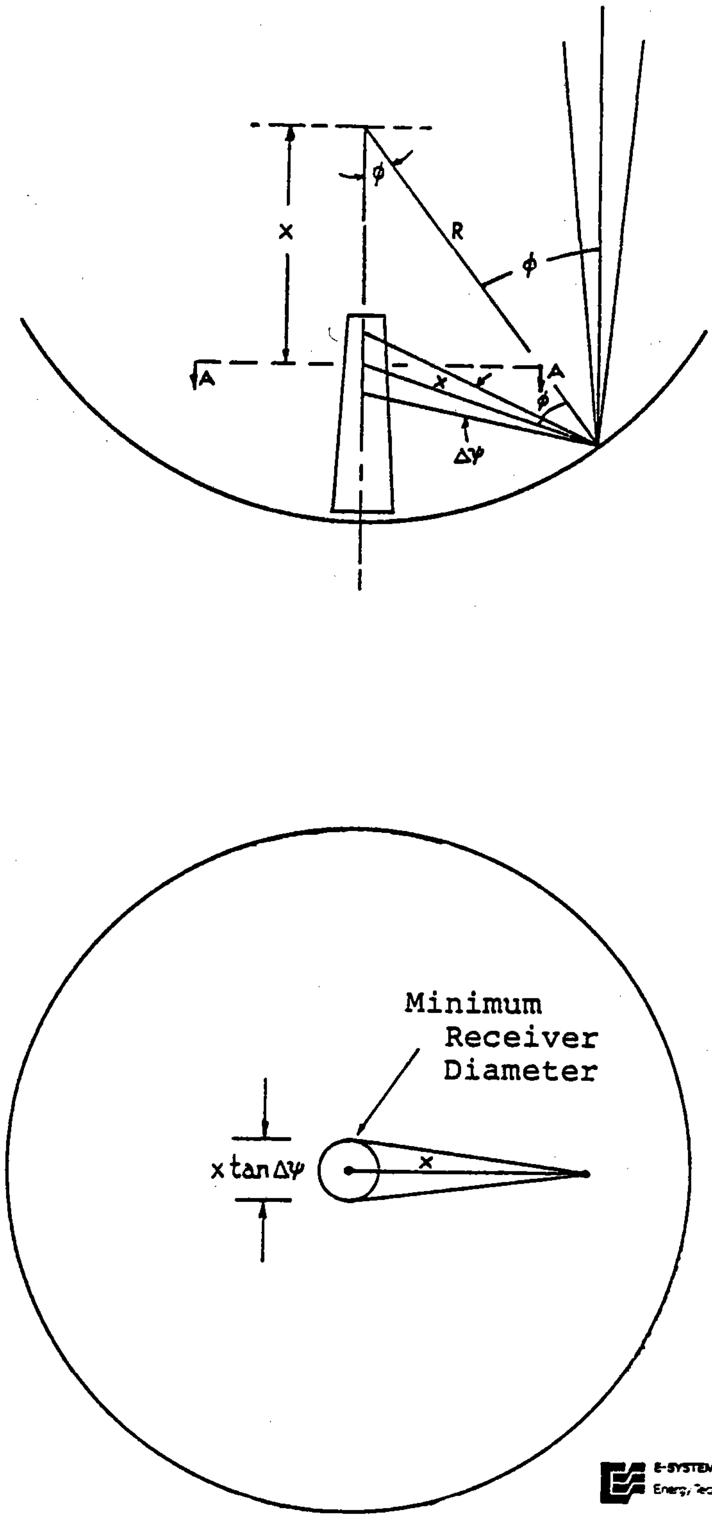

E-SYSTEMS
Energy Technology Center

Section A-A

Figure D-4. FMDF Receiver Geometry

will be discussed later.)

Thus, all rays entering the aperture from $\phi = 0°$ to $\phi = 60°$ will intercept a truncated cone extending from $\frac{R}{2} \leq x \leq R$. This fully defines the preferred receiver geometry, namely a truncated cone of length R/2 and diameter x tan $\Delta\psi$. Any other receiver shape will either have a larger exposed surface area (higher heat losses to the surroundings), or will not intercept all reflected radiation (higher optical losses).

Knowing the receiver geometry, we can proceed to calculate the concentration distribution over the receiver. First, we will consider the axisymmetric case, i.e., perpendicular illumination of the aperture. Fig. D-5 shows the cone intercept geometry for a finite conical receiver. The illuminated region on the receiver will be an axisymmetric band extending from x_{min} to x_{max}. Trigonometry easily yields the following intercept formulae:

$$\frac{x_{min}}{R} = \frac{\cos\frac{\Delta\psi}{2}\,\sin(\phi - \frac{\Delta\psi}{2})}{\sin(2\phi - \Delta\psi)} \quad ,$$

$$\frac{x_{max}}{R} = \frac{\cos\frac{\Delta\psi}{2}\,\sin(\phi + \frac{\Delta\psi}{2})}{\sin 2\phi} \quad . \qquad \text{(D-13)}$$

These intercept equations have been plotted in Fig. D-6 for the nominal case, i.e., $\Delta\psi = 1.0°$. Note that the x_{max} - curve is U-shaped and therefore has two ϕ - values for each x value. Thus each point on the receiver

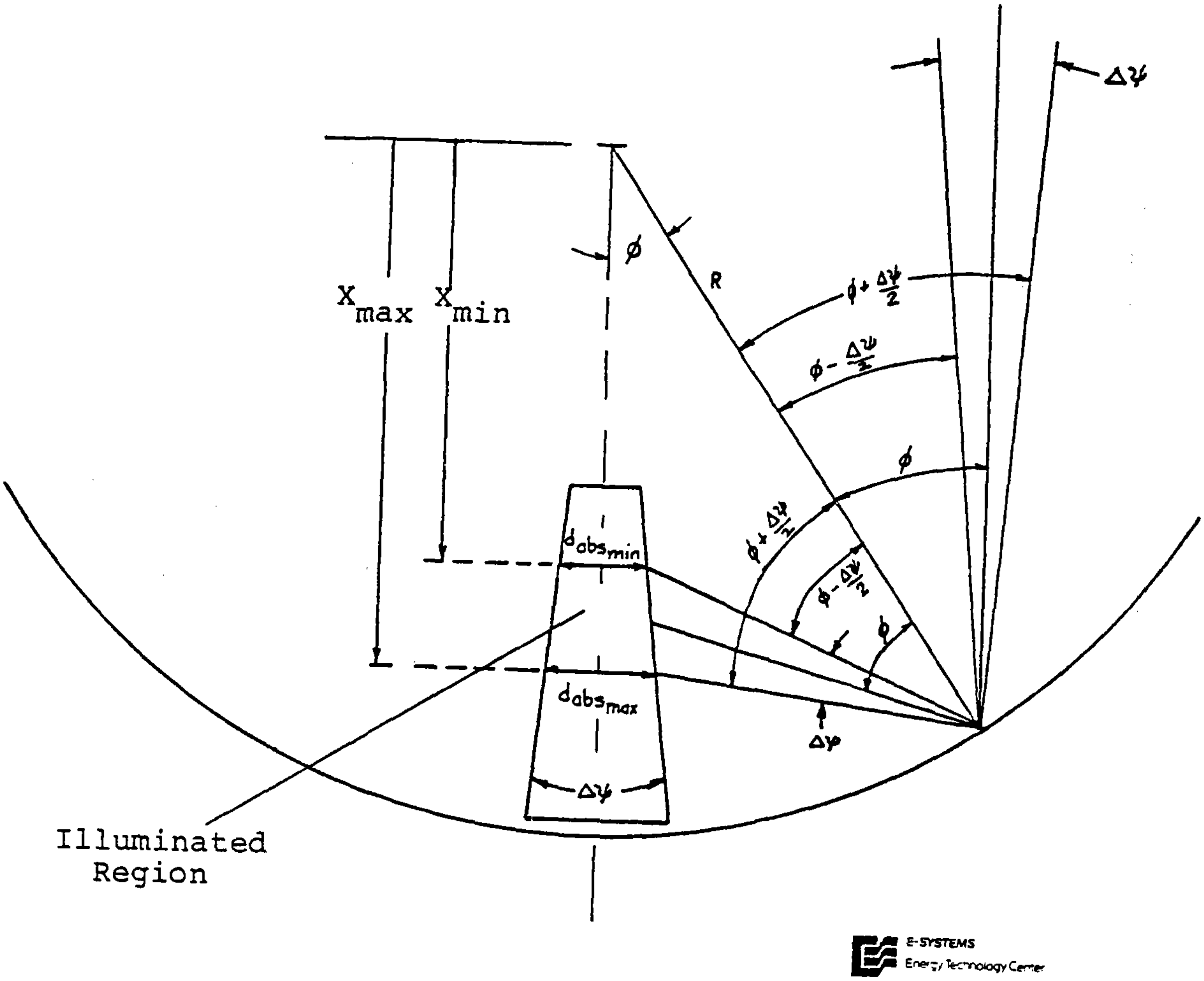

Figure D-5. Cone Intercept Geometry

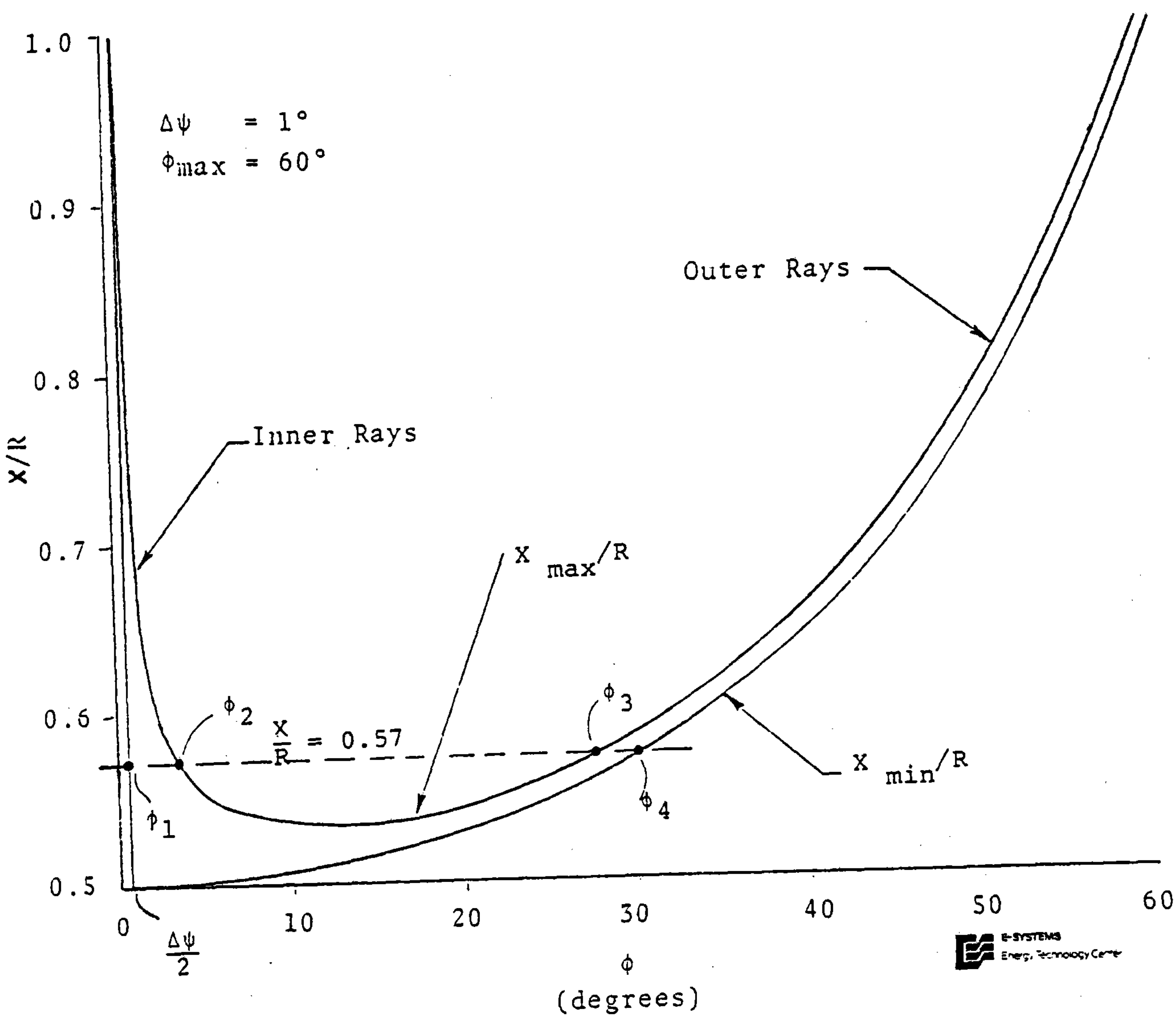

Figure D-6. Reflected Ray Cone Intercepts has concentration contributions coming from two distinct regions of the mirror concentrator. These are labeled inner and outer rays in Fig. D-6. However, the two regions merge into a single region for $x/R < 0.53208$, the minimum point on the x_{max} curve.

Knowing the cone intercept formulae, we can proceed to calculate the differential flux contributed by any differential area of aperture to the illuminated area on the receiver. Using the same coordinate system as shown in Fig. D-1 the differential energy transfer rate from any (ϕ,θ) location is again equal to:

$$d\dot{Q} = I_{dn}\, dA_{aper} = I_{dn}\, R^2 \sin\phi \cos\phi\, d\phi\, d\theta. \tag{D-14}$$

Since we are considering the axisymmetric case, we can immediately integrate about θ to obtain the differential energy transfer rate from a differential ring of aperture:

$$\begin{aligned} d\dot{Q} &= 2\pi R^2\, I_{dn} \sin\phi \cos\phi\, d\phi \\ &= \pi R^2 I_{dn} \sin 2\phi\, d\phi\, . \end{aligned} \tag{D-15}$$

This power is distributed inside the illuminated region of receiver shown in Fig. D-5, the area of which is

$$\begin{aligned} A_{illum.} = A_i &= \frac{\pi (d_{abs_{max}} + d_{abs_{min}})(x_{max} - x_{min})}{2 \cos \frac{\Delta\psi}{2}} \\ &= \frac{\pi (x_{max} \tan \Delta\psi + x_{min} \tan\Delta\psi)(x_{max} - x_{min})}{2 \cos \frac{\Delta\psi}{2}} \\ &= \frac{\pi \tan\Delta\psi}{2 \cos\Delta\psi/2} (x_{max}{}^2 - x_{min}{}^2). \end{aligned} \tag{D-16}$$

If we assume a mirror reflectivity of 1.00 and that the differential power is uniformly distributed over the illuminated area on the receiver, the differential flux is easily defined:

$$d\dot{q} = \frac{d\dot{Q}}{A_i} = \frac{2\pi R^2 I_{dn} \cos\frac{\Delta\psi}{2} \sin 2\phi \, d\phi}{\pi \tan\Delta\psi \, (x_{max}^2 - x_{min}^2)}$$

$$= \left[\frac{2I_{dn}\cos\frac{\Delta\psi}{2}}{\tan\Delta\psi}\right] \left[\frac{\sin 2\phi d\phi}{\left(\frac{x_{max}}{R}\right)^2 - \left(\frac{x_{min}}{R}\right)^2}\right] \tag{D-17}$$

Substituting for $\frac{x_{max}}{R}$ and $\frac{x_{min}}{R}$ yields:

$$d\dot{q} = \left(\frac{2I_{dn}\cos\frac{\Delta\psi}{2}}{\tan\Delta\psi}\right) \bullet$$

$$\bullet \left[\frac{\sin 2\phi d\phi}{\left(\frac{\cos\frac{\Delta\psi}{2}\sin(\phi+\frac{\Delta\psi}{2})}{\sin 2\phi}\right)^2 - \left(\frac{\cos\frac{\Delta\psi}{2}\sin(\phi-\frac{\Delta\psi}{2})}{\sin(2\phi-\Delta\psi)}\right)^2}\right] \tag{D-18}$$

$$\equiv F(\phi)d\phi.$$

wherein $F(\phi)$ represents the messy function of ϕ which must be integrated to yield $\dot{q}$.

By the definition of concentration,

$$dC = \frac{F(\phi)}{I_{dn}} d\phi \equiv F'(\phi)d\phi. \tag{D-19}$$

Next we must determine the range of integration over which $F'(\phi)$ should be integrated to yield the local concentration C for a particular x/R location. Referring to Fig.

D-6, suppose we wish to determine the concentration at $\frac{x}{R}$ = 0.57, the dashed line in the figure. From the figure, we can see that concentration contributions occur over two ranges of ϕ, namely

$$\phi_1 \leq \phi \leq \phi_2, \text{ and}$$
$$\phi_3 \leq \phi \leq \phi_4.$$

Therefore the concentration is given by

$$C = \int_{\phi_1}^{\phi_2} F'(\phi)d\phi + \int_{\phi_3}^{\phi_4} F'(\phi)d\phi \qquad \text{(D-20)}$$

This equation applies for all $\frac{x}{R}$ values above the minimum value of $\frac{x_{max}}{R}$ = 0.53208 for the stated conditions. Below this value, the two regions of integration merge into a single region, namely:

$$\phi_1 \leq \phi \leq \phi_4.$$

The limits ϕ_1, ϕ_2, ϕ_3 and ϕ_4 must now be determined as functions of x/R. Obviously, $\phi_1 = \Delta\psi/2$ from Fig. D-6. Also, ϕ_2 and ϕ_3 are the positive real roots of the x_{max}/R intercept formula, while ϕ_4 is the positive real root of the x_{min}/R intercept formula. These roots can be expressed in exact, explicit form by algebraic manipulation of the intercept formulae to yield quartic equations which may be solved by formula. Knowing now the range of integration and the integrand, $F'(\phi)$, we can numerically integrate to obtain the concentration versus x/R. However, as discussed in Appendix F several thousand such integrations are required for each thermal analysis case considered; therefore, it is highly desirable to reduce the complicated integral to a form which can be closed-form integrated. Also, it is desirable to provide a simpler method of evaluating ϕ_2, ϕ_3 and ϕ_4, since quartic roots require some effort to evaluate. If one carefully applies order-of-magnitude analysis to the various terms in the integrand and the intercept formulae, after a great deal of algebra it can be shown that the following simplified equations accurately represent the integral and limits.

$$\boxed{C \approx \frac{1}{\tan^2 \Delta\psi} \int_{\phi_a}^{\phi_b} \sin 2\phi \, \sin\left(2\phi - \frac{\Delta\psi}{2}\right)\left[1+\cos\left(2\phi - \frac{\Delta\psi}{2}\right)\right] d(2\phi)} \quad \text{(D-21)}$$

For $\frac{x}{R} > \left(\frac{x_{max}}{R}\right)_{min}$, the limits are:

$[\phi_1 \leq \phi \leq \phi_2$ and $\phi_3 \leq \phi \leq \phi_4]$.

(D-22)

For $\frac{x}{R} \leq \left(\frac{x_{max}}{R}\right)_{min}$, the limits are:

$[\phi_1 \leq \phi \leq \phi_4]$.

These limits can be adequately calculated using:

$$\phi_1 = \Delta\psi/2$$

$$\phi_2 = \sin^{-1}\left[\frac{\sin\ \Delta\psi/2}{3(x/R)} + 2\sqrt{\frac{1}{3} - \frac{R^2}{12x^2}}\right.$$

$$\left.\cos\left[240° + \frac{1}{3}\cos^{-1}\left\{\frac{\frac{-\sin\ \Delta\psi/2}{2(x/R)}\left(\frac{R^2}{4x^2} + 2\right)}{\sqrt{\frac{\left(1 - \frac{R^2}{4x^2}\right)^3}{3}}}\right\}\right]\right]$$

$$\phi_3 = \sin^{-1}\left[\frac{\sin\Delta\psi/2}{3(x/R)} + 2\sqrt{\frac{1}{3} - \frac{R^2}{12x^2}}\right. \cdot \tag{D-23}$$

$$\left.\cos\left[\frac{1}{3}\cos^{-1}\left\{\frac{\frac{-\sin\ \Delta\psi/2}{2(x/R)}\left(\frac{R^2}{4x^2} + 2\right)}{\sqrt{\frac{\left(1 - \frac{R^2}{4x^2}\right)^3}{3}}}\right\}\right]\right]$$

$$\phi_4 = \frac{\Delta\psi}{2} + \cos^{-1}\left[\frac{1}{2(x/R)}\right]$$

The above integral can be integrated closed-form to yield slightly <u>low</u> values of C if we alter the first term slightly:

$$\sin(2\phi) \rightarrow \sin(2\phi - \frac{\Delta\psi}{2}).$$

This approximation yields:

$$C_{low} = \frac{1}{\tan^2 \Delta\psi} \left[\phi - \frac{\sin(4\phi - \Delta\psi)}{4} + \frac{\sin^3(2\phi - \frac{\Delta\psi}{2})}{3} \right]_{\phi_a}^{\phi_b} \qquad \text{(D-24)}$$

wherein ϕ_a and ϕ_b represent the proper limits of integration for the x/R value of interest, as discussed previously.

The above integral can be integrated closed-form to yield slightly <u>high</u> values if we alter the second and fourth terms slightly:

$$\sin(2\phi - \frac{\Delta\psi}{2}) \rightarrow \sin 2\phi$$

$$\cos(2\phi - \frac{\Delta\psi}{2}) \rightarrow \cos 2\phi.$$

This approximation yields:

$$C_{high} = \frac{1}{\tan^2 \Delta\psi} \left[\phi - \frac{\sin 4\phi}{4} + \frac{\sin^3 2\phi}{3} \right]_{\phi_a}^{\phi_b} . \qquad \text{(D-25)}$$

Comparison of the results of C_{high} and C_{low} with numerical integration of (Eq. D-21) has shown that:

$$C = \frac{C_{low} + C_{high}}{2} \qquad \text{(D-26)}$$

agrees with the integral to within a fraction of a percent.

Thus we finally have achieved a <u>fully closed-form representation of C as a function of (x/R)</u> for the nominal case, these results are shown in Fig. D-7.

To validate the results of this closed-form method, Dr. George Schrenk utilized a numerical, finite-area-element computer program (described in Reference D-6) to calculate several points for comparison. These points are superimposed on Fig. D-7 . In spite of totally different analytical methods, the correlation of results is seen to be excellent. The important point to emphasize here is the extreme relative speed of a closed form expression.

The following section describes the extrapolation of the above-described method to define non-axisymmetric, three-dimensional concentrations on the receiver for the general case of non-normal illumination of the aperture.

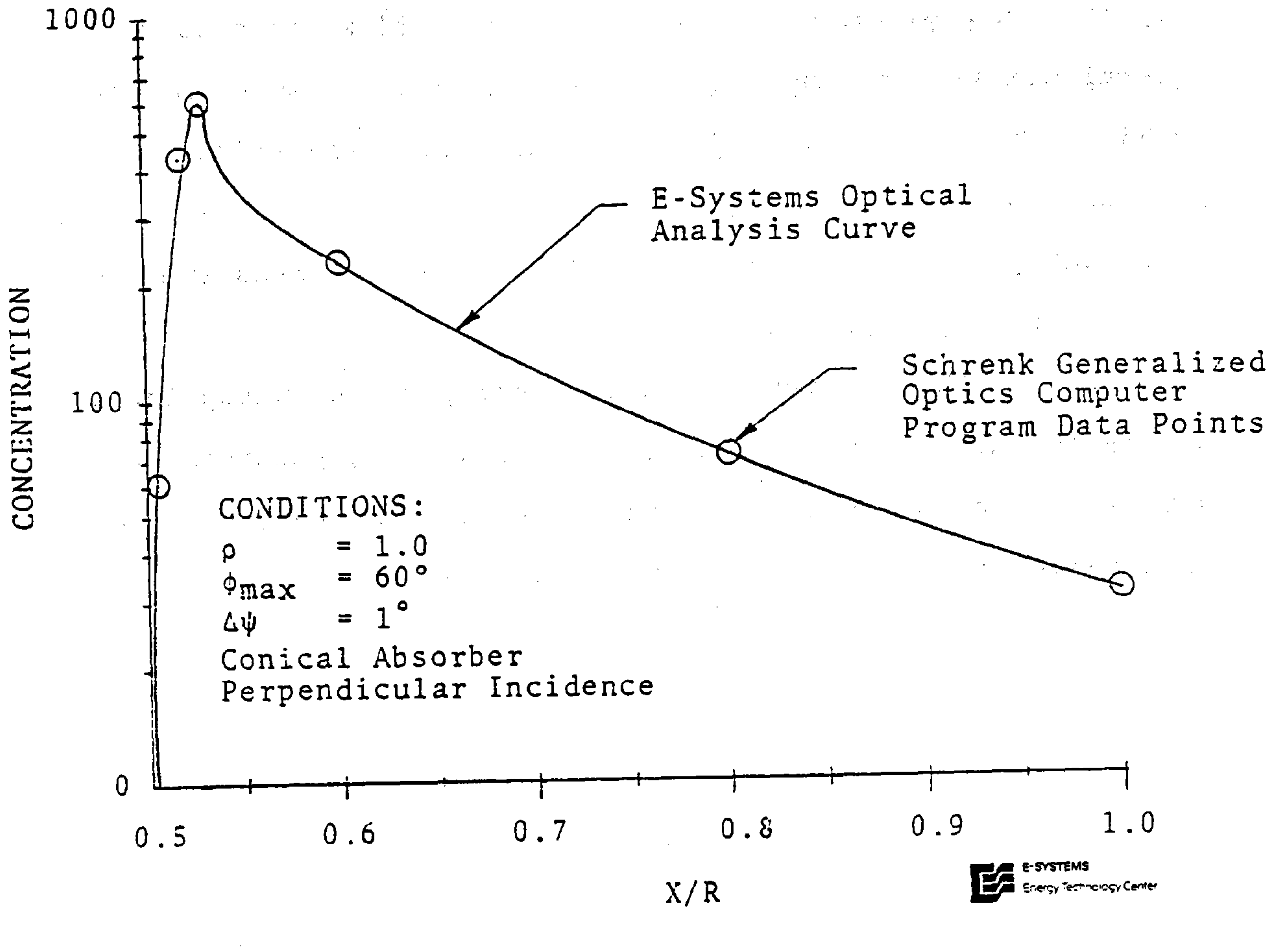

Figure D-7. Axisymmetric Flux Distribution

D-3 NON-AXISYMMETRIC OPTICAL CONCENTRATIONS ON A CONICAL RECEIVER

For the general condition of non-normal incidence insolation, i.e., the solar rays form a non-zero angle θ_i with the aperture normal vector, we can no longer automatically integrate about the circumferential variable θ (Fig. D-1), since azimuthal symmetry will no longer prevail. This effect is shown schematically in Fig. D-8 . As discussed previously, singly reflected rays will intercept the receiver for $0° \leq \phi \leq 60°$. For $\phi > 60°$, rays will require multiple reflections to reach the receiver. Thus the shaded area of Fig. D-8 corresponds to the multiple reflection region of aperture. The remainder of the projected aperture corresponds to single reflections. For the current discussion, we will limit our interest to these single reflections. Our coordinate system will be fixed to the receiver, with α defining the circumferential location of a point on the receiver, and θ defining the circumferential location of a point on the concentrator. The other coordinates ($\frac{x}{R}$ and ϕ) remain identical with their previously defined meanings.

The axisymmetric solution of Section D-2 will still define the axial variation in concentration if it is corrected to account for two effects:

(1) For each reflected cone containing a differential quantity of energy, we must define how this energy is mapped circumferentially around the

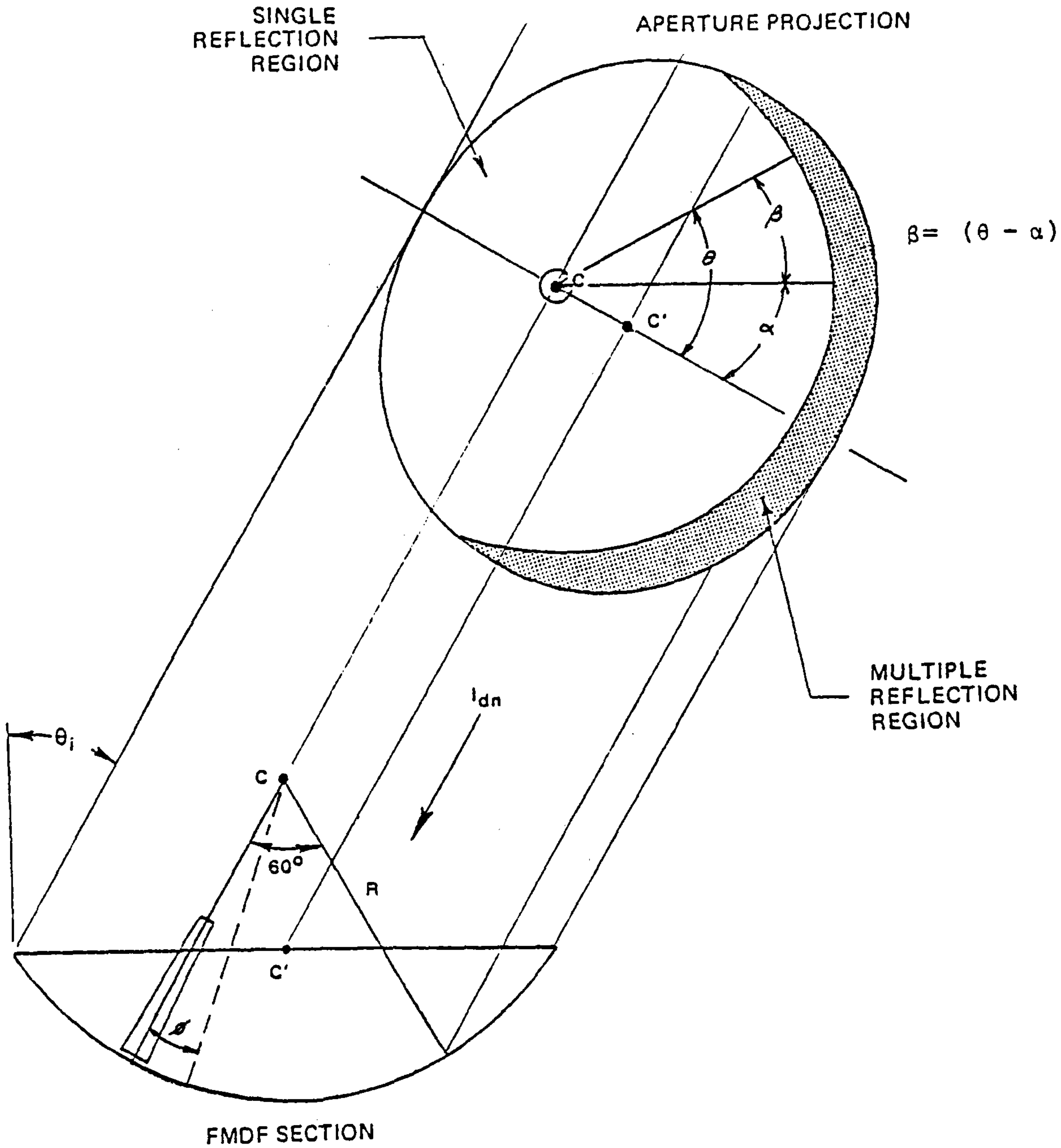

Figure D-8. Non-Normal Incidence Effects receiver.

(2) Since ϕ is now subjected to physical limits corresponding to the rim of the concentrator, the integration limits (ϕ_1, ϕ_2, ϕ_3, ϕ_4) must be checked against these physical limits, and the integration carried out only over ϕ-regions common to both.

Let us consider the first effect, as represented in Fig.D-9 . The intercept of a singly reflected ray cone is shown, forming a quasi-elliptical image on the receiver surface. If we unwrap the receiver surface as shown in the lower sketch of Fig. D-9 , the illuminated spot will cover half of the receiver perimeter, e.g., $-90° \leq \beta \leq 90°$, if the receiver is sized according to the discussion of Section D-1. Also, the circumferential variation in illuminated area is a continually decreasing function from a maximum at $\beta = 0°$ to a zero-value at $\beta = \pm 90°$. Therefore, a reasonable (though not exact) weighting function for this distribution is:

$$dA_i = k_1 \cos\beta \, d\beta \ , \qquad \text{(D-27)}$$

where k_1 is a constant.

Now the energy intercepted by this differential area is proportional to the projected area ($dA_i \cos\beta$) of this differential strip, i.e.:

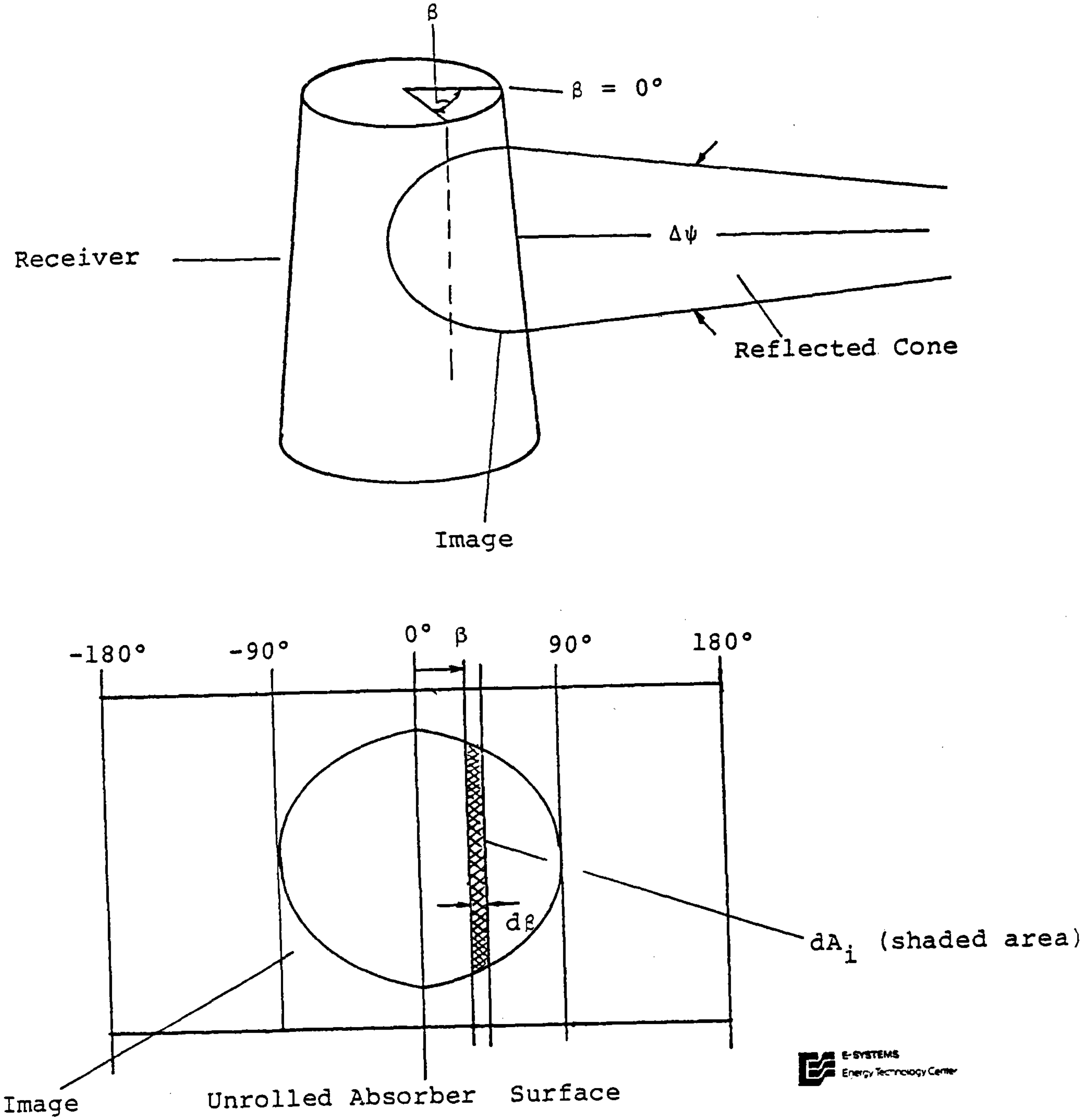

Figure D-9. Individual Cone Intercept

$$\dot{dQ}_\beta = k_2 dA_i \cos\beta$$

$$= k_2 \, k_1 \cos^2\beta \, d\beta \qquad \text{(D-28)}$$

$$= k \cos^2\beta \, d\beta$$

where k_2 and k are also proportionality constants, and $\dot{dQ}_\beta$ is the power intercepted by the strip at location β. Now if we integrate $\dot{dQ}_\beta$ over $-90° \leq \beta \leq 90°$, we must obtain $\dot{dQ}$, the total energy within the reflected ray cone. Thus:

$$\dot{dQ} = \int_{-90°}^{90°} \dot{dQ}_\beta$$

$$= 2\,k \int_{0}^{90°} \cos^2\beta d\beta \qquad \text{(D-29)}$$

$$= 2k\left(\frac{\pi}{4}\right) = \frac{\pi}{2}k \,.$$

Thus: $k = \frac{2}{\pi}\dot{dQ}$, yielding:

$$\dot{dQ}_\beta = \frac{2\dot{dQ}}{\pi} \cos^2\beta d\beta. \qquad \text{(D-30)}$$

This cosine-squared circumferential variation should approximately represent the actual intensity variation around the receiver. This approximation will be shown to yield results in excellent agreement with numerical calculations by Schrenk (Ref. D-6) later in this section.

The second effect noted above concerning physical limits on ϕ is a straightforward analytical geometry problem. There are two possible conditions to be analyzed, as shown in Fig. D-10, corresponding respectively to the receiver tip ($\frac{x}{R} = 1.0$) being in or out of the concentrator dish. For the first case, for any θ - value, there is a maximum physical limit on ϕ corresponding to point P_1. This limit is easily shown to be (for the nominal case with rim angle = 60°):

$$\phi_{P_1} = \mathrm{Sin}^{-1}\left\{\frac{\sin\theta_i\cos\theta + \cos\theta_i\sqrt{3-4\sin^2\theta\sin^2\theta_i}}{2-2\sin^2\theta\sin^2\theta_i}\right\}. \quad \text{(D-31)}$$

For the second case, an additional lower limit on ϕ due to point P_2 exists. It is easily shown that this limit is:

$$\phi_{P_2} = \mathrm{Sin}^{-1}\left\{\frac{\sin\theta_i\cos\theta - \cos\theta_i\sqrt{3-4\sin^2\theta\sin^2\theta_i}}{2-2\sin^2\theta\sin^2\theta_i}\right\}. \quad \text{(D-32)}$$

Both of the expressions above would produce complex angles for planes of constant θ which have no intersections P_1 or P_2. For such cases, there are no contributing portions of mirror located at such θ values.

Now that both types of complications found with three-dimensional effects have been overcome, we can write the concentration integral:

Case 1

Receiver Tip In Dish

Case 2

Receiver Tip Out of Dish

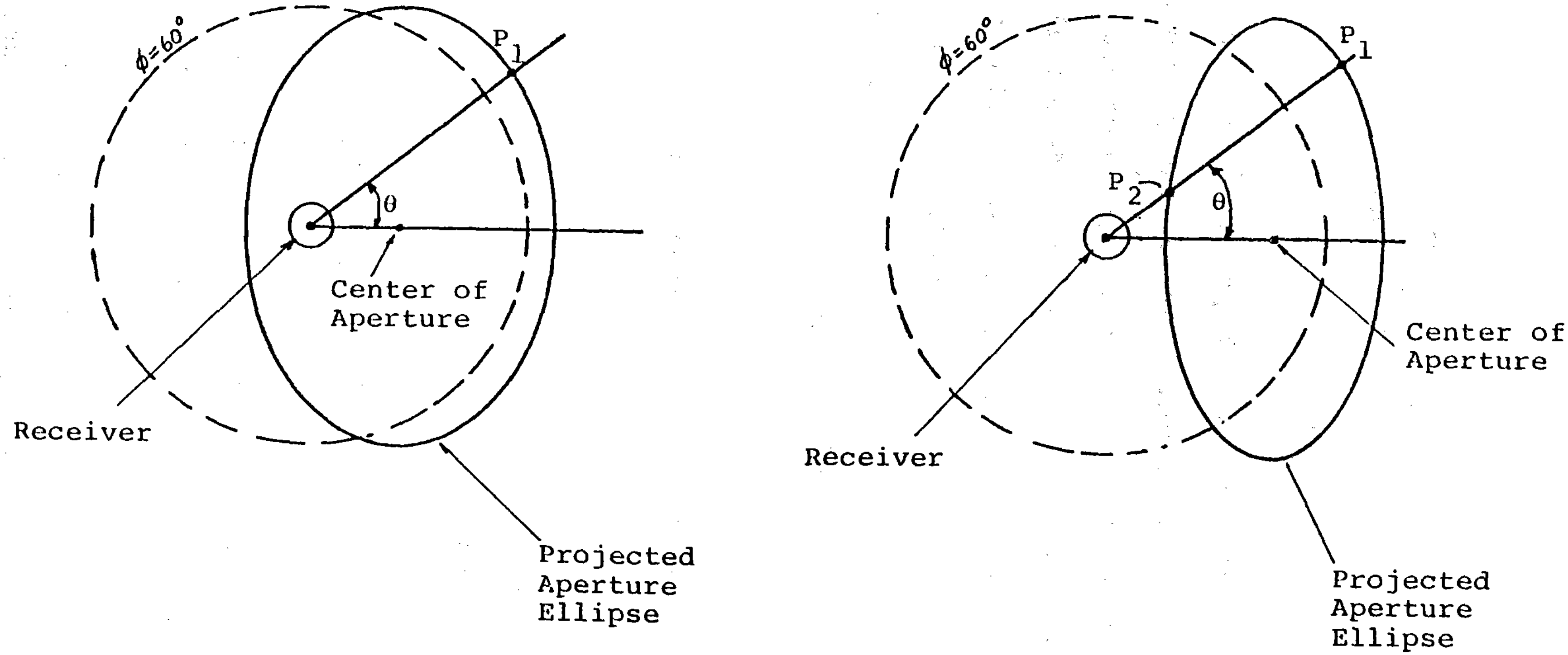

Figure D-10. Physical Limits on ϕ

$$C = \int_{\alpha - 90°}^{\alpha + 90°} \frac{2}{\pi} \cos^2(\theta-\alpha) \left[\int_{\phi_a}^{\phi_b} F'(\phi)d\phi \right] d\theta \ , \tag{D-33}$$

wherein C is the local concentration at a point ($\frac{x}{R}$,α) on the receiver, F' (ϕ) is the same integrand as for the previously discussed axisymmetric case, (θ - α) is the angle β of Fig. D-8 which is the argument of the cosine-squared circumferential flux variation, and (ϕ_a, ϕ_b) are the integration limits over variable ϕ . These limits are now subject to the physical limits (ϕ_{P_1}, ϕ_{P_2}) as well as the analytical limits (ϕ_1,ϕ_2,ϕ_3, ϕ_4) previously discussed. The proper range of integration can be written as follows.

For $\frac{x}{R} \leq \left(\frac{x_{max}}{R}\right)_{min}$ (0.53208 for the nominal), use

$$(\phi_1 \leq \phi \leq \phi_4) \cap (\phi_{P_2} \leq \phi \leq \phi_{P_1}) \ ; \tag{D-34}$$

For $\frac{x}{R} > \left(\frac{x_{max}}{R}\right)_{min}$, use

$$(\phi_1 \leq \phi \leq \phi_2 \text{ and } \phi_3 \leq \phi \leq \phi_4) \cap (\phi_{P_2} \leq \phi \leq \phi_{P_1})$$

wherein $\cap$ represents the intersection of the ϕ-sets, i.e., those ranges of ϕ within both the analytical and physical limits.

While the above concentration integral can be integrated approximately in closed-form fashion, for selected

(x/R, α) points, the multiple checks required on the ϕ-limits make a numerical integration over θ more practical, with the closed-form solution for the ϕ-integration reapplied at each step in the $\Delta\theta$ integration. Since the θ-variation of the integrand is smooth and well-behaved (simple $\cos^2 \theta$ functionality), large steps in $\Delta\theta$ can be used with high accuracy (e.g., $\Delta\theta = 5°$). Thus, the computer time required per concentration point is trivial, a complete three-dimensional distribution with adequate resolution for the thermal analysis requiring less than a minute of computer time (CDC 6600 or IBM 370).

Typical three-dimensional concentration distributions are presented in Figs. D-11 and D-12. These are for the nominal collector at incidence angles of 30° and 60° respectively. For comparison, comparative numerical calculations conducted by Schrenk (Ref. D-6) are overlayed on the curves of both figures. Note the excellent correlation of the two results.

Concerning multiple reflections which occur for ϕ-values greater than 60°, as analyzed in Ref. D-8, these rays represent less than 14% of the annual energy entering the aperture of the nominal collector (60° rim angle, 15° tilt angle). Furthermore, since errors will accumulate at each reflection and since some absorption will occur with each reflection, the collectability of these multiply reflected rays is questionable. Therefore, to be conservative

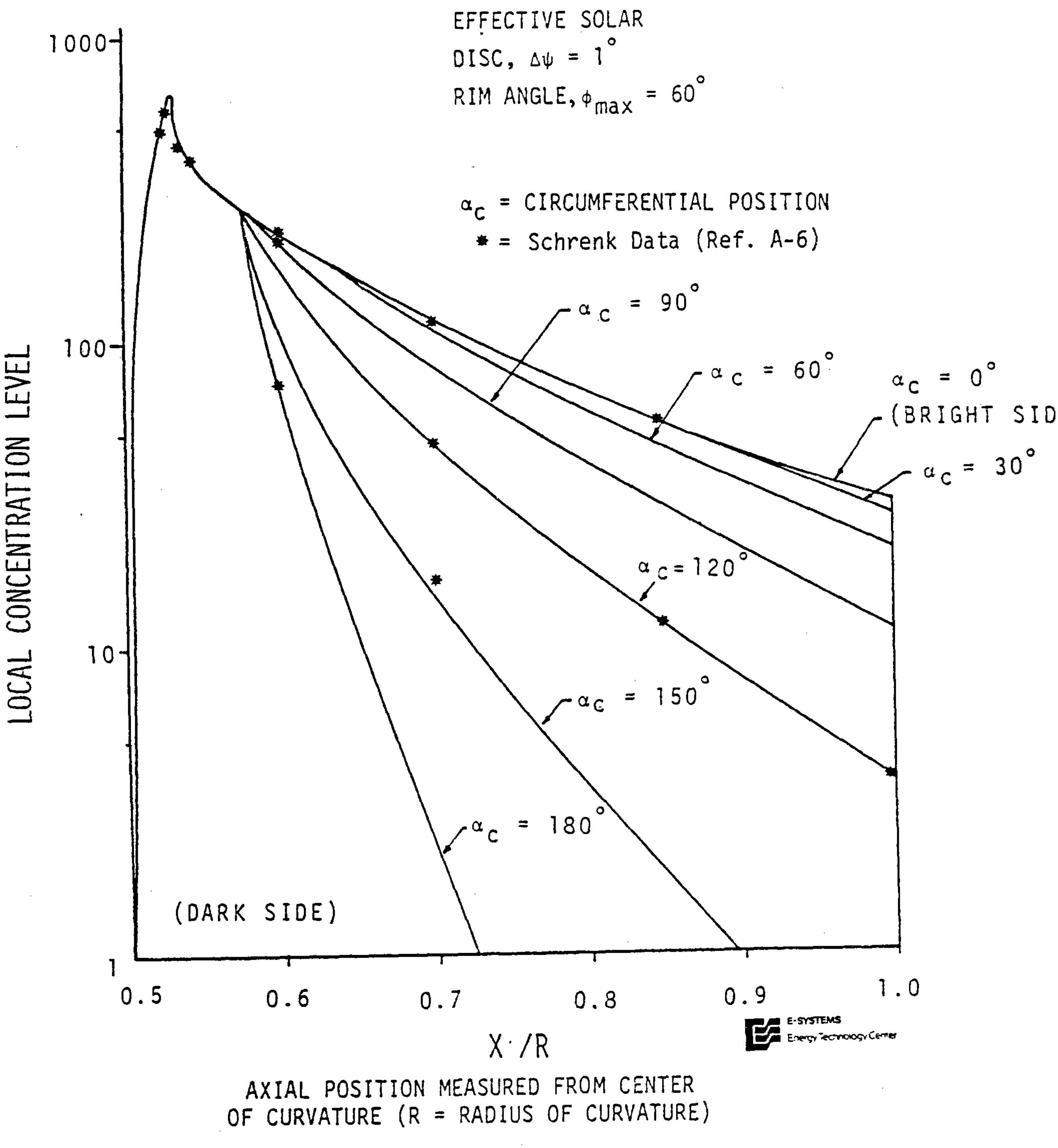

Figure D-11. Three-Dimensional Concentration Distribution (θ_i = 30°)

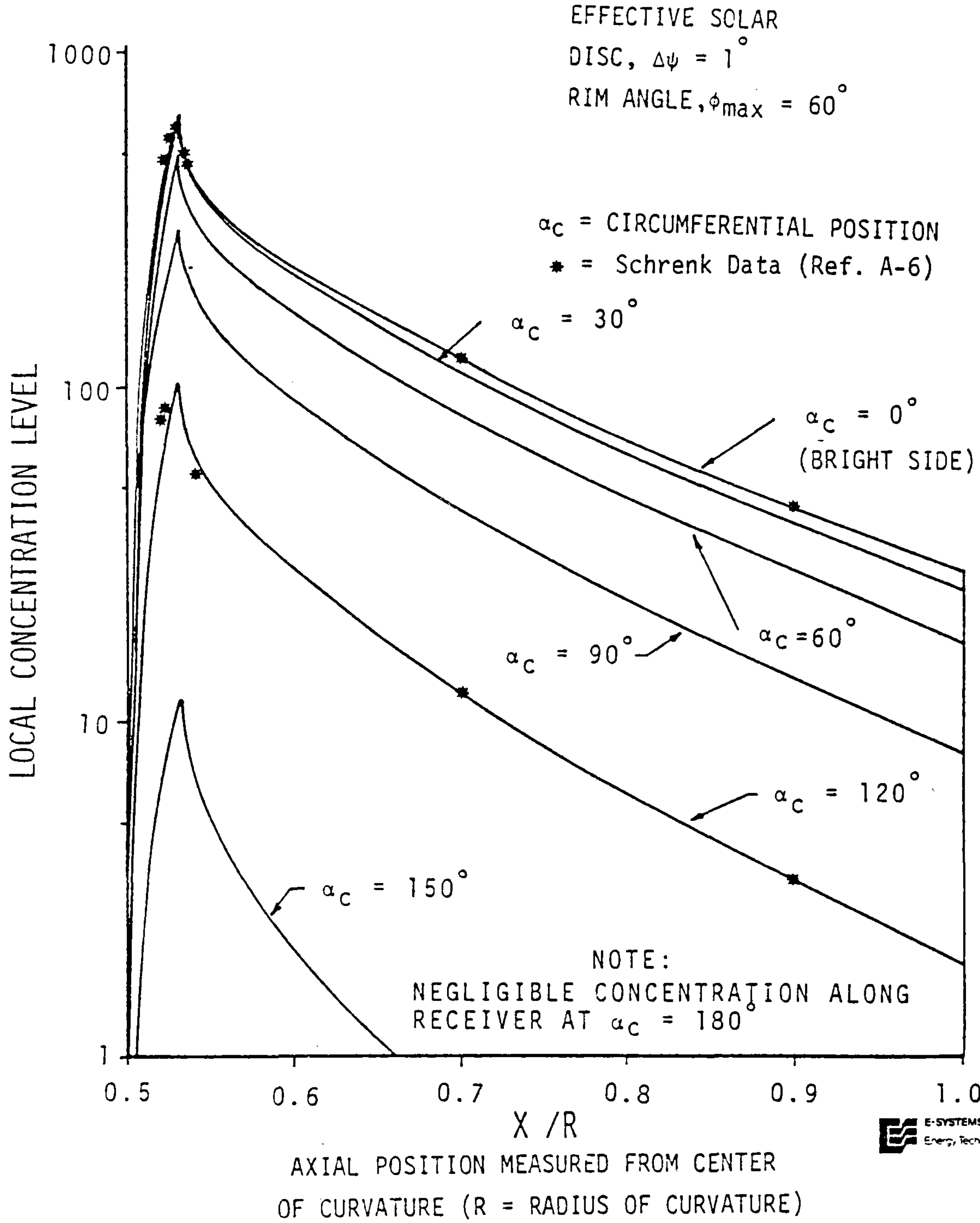

E-SYSTEMS
Energy Technology Center

Figure D-12. Three-Dimensional Concentration Distribution (θ_i =60°)

no collection of these rays has been considered in the current study.

Appendix F describes how the optical solution was incorporated into a total receiver thermal analysis model, and presents the results of these thermal studies.

<u>APPENDIX D REFERENCES</u>

D-1 Kreider, Jan F., "The Stationary Reflector/Tracking Absorber Solar Concentrator," Environmental Consulting Services, Inc., Boulder, Colorado, 1974.

D-2 Steward, W. G. and F. Kreith, "Stationary Concentrating Reflector cum Tracking Absorber Solar Energy Collector: Optical Design Characteristics," <u>Applied Optics</u>, Vol. 14, No. 7, p. 1509, July 1975.

D-3 McKenney, D. B., "Focal Characteristics of Large-Aperture Spherical Reflectors," Helio Associates, Inc., Tucson, Arizona, 1975.

D-4 Clausing, A.M., "The Performance of a Stationary Reflector/Tracking Absorber Solar Concentrator," ISES'76, Volume 2, p. 304, Winnepeg, Canada, August 1976.

D-5 O'Neill, Mark J., "Optical Analysis of the Fixed Mirror/ Distributed Focus (FMDF) Solar Energy Collector," Report No. 9-19100/TR75-02, E-Systems, Inc., Dallas, Texas, December 1975 (Revised April 1976).

D-6 Schrenk, George L., "Solar Collection Limitation for Dynamic Converters - Simulation of Solar-Thermal Energy Conversion Systems," Proc. of AGARD Conference, Cannes, France, March 1964. (and personal communications with Dr. Schrenk from 1975-1977).

D-7 Cabannes, F. and Le Phat Vinh, A. "Calcul De La Repartition De L'energie Solaire Reflechie Par Un Miroir Parabolique," <u>Le Journal De Physique Et Le Radium</u>, 15 (December 1954) p. 817.

D-8 O'Neill, Mark J., "Thermo-Optical Performance Analysis of the Fixed Mirror/Distributed Focus Solar Thermal Electrical Power System (FMDF-STEPS)," Report No. 9-19100/TR76-04, E-Systems, Inc., Dallas, Texas, May 1976.

APPENDIX E. DEVELOPMENT OF THE RECEIVER THERMAL-FLUID MODEL

The thermal-fluid model developed to describe the receiver for the FMDF system is a very general, but detailed, analysis of the heat transfer and fluid mechanical behavior of flow in a long pipe with an external heat source.

This model conceptually divides the receiver into a number of equal width, cylindrical elements of varying diameters such as indicated in Fig. E-1. The width of each element is equal to the number of parallel tubes in a bundle times the outside diameter of a single tube. In the case of asymmetric solar concentration patterns, each element is further divided into 12 arc sections of 30° included angle each.

For any element the analysis begins with the entering fluid temperature. A calculational flow sheet is shown in Fig. E-2. The average heat flux into the element is calculated by interpolation from concentration distribution data which are converted into a heat flux per unit area by

$$\frac{q}{A_i} = C\left(\frac{x}{R}\right)_i I_o \alpha \beta \tag{E-1}$$

where $C(x/R)_i$ is the concentration factor at position $(x/R)_i$, I_o is the solar insolation. This varies with time of day, but is approximately 300 Btu/ft^{2}hr at solar noon). The absorptivity of the receiver is α (constant at 0.9), and β is the reflectivity of the collector (constant at 0.88).

FIGURE E-1. Schematic of TTU Thermo-Fluid Receiver Model

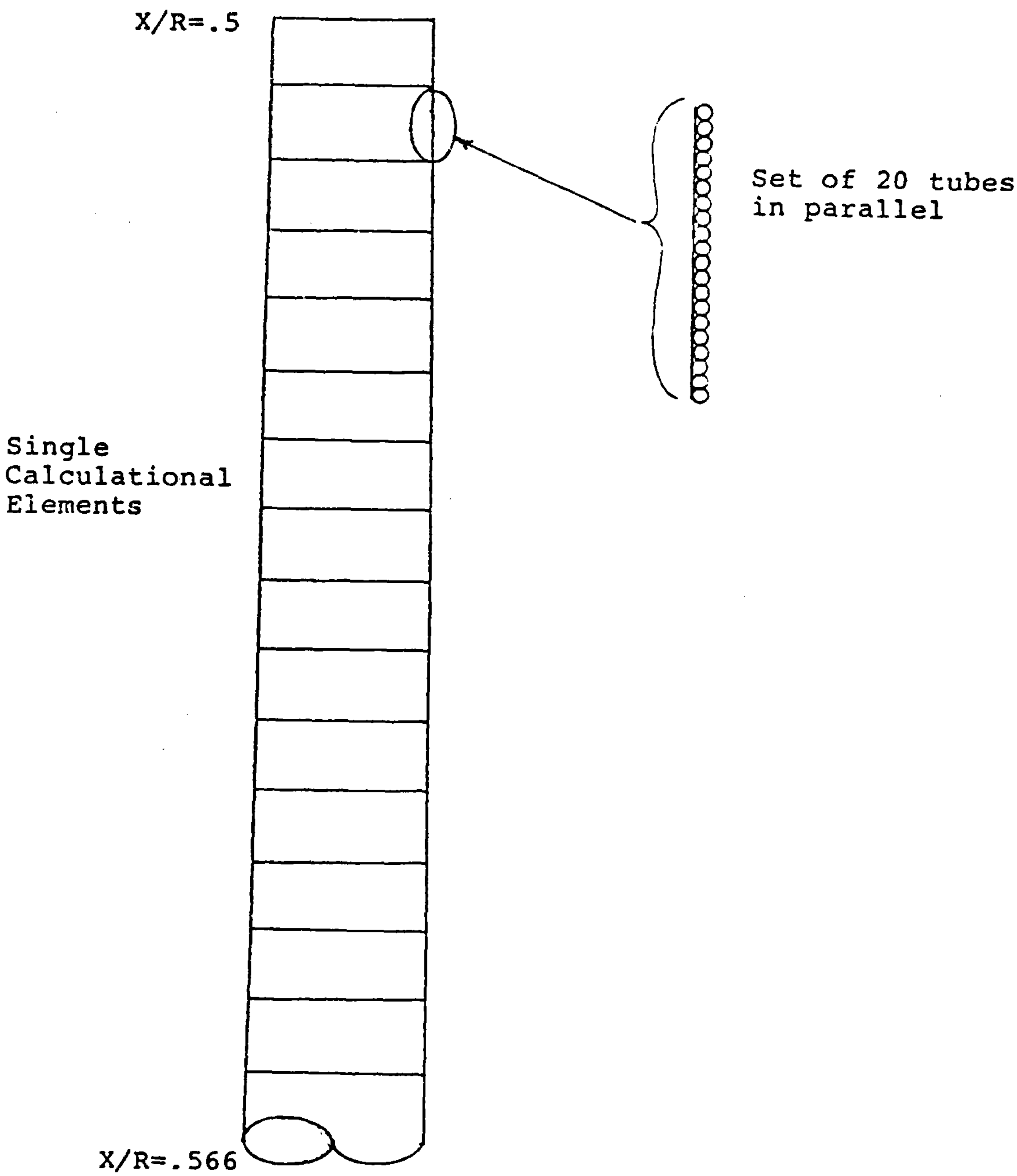

Drawn to Scale

Note: This figure denotes a set of 20 tubes, ¼"ID X 0.030" wall, in parallel.

FIGURE E-2. Schematic Flow Chart of

Receiver Thermo-Fluid Analysis

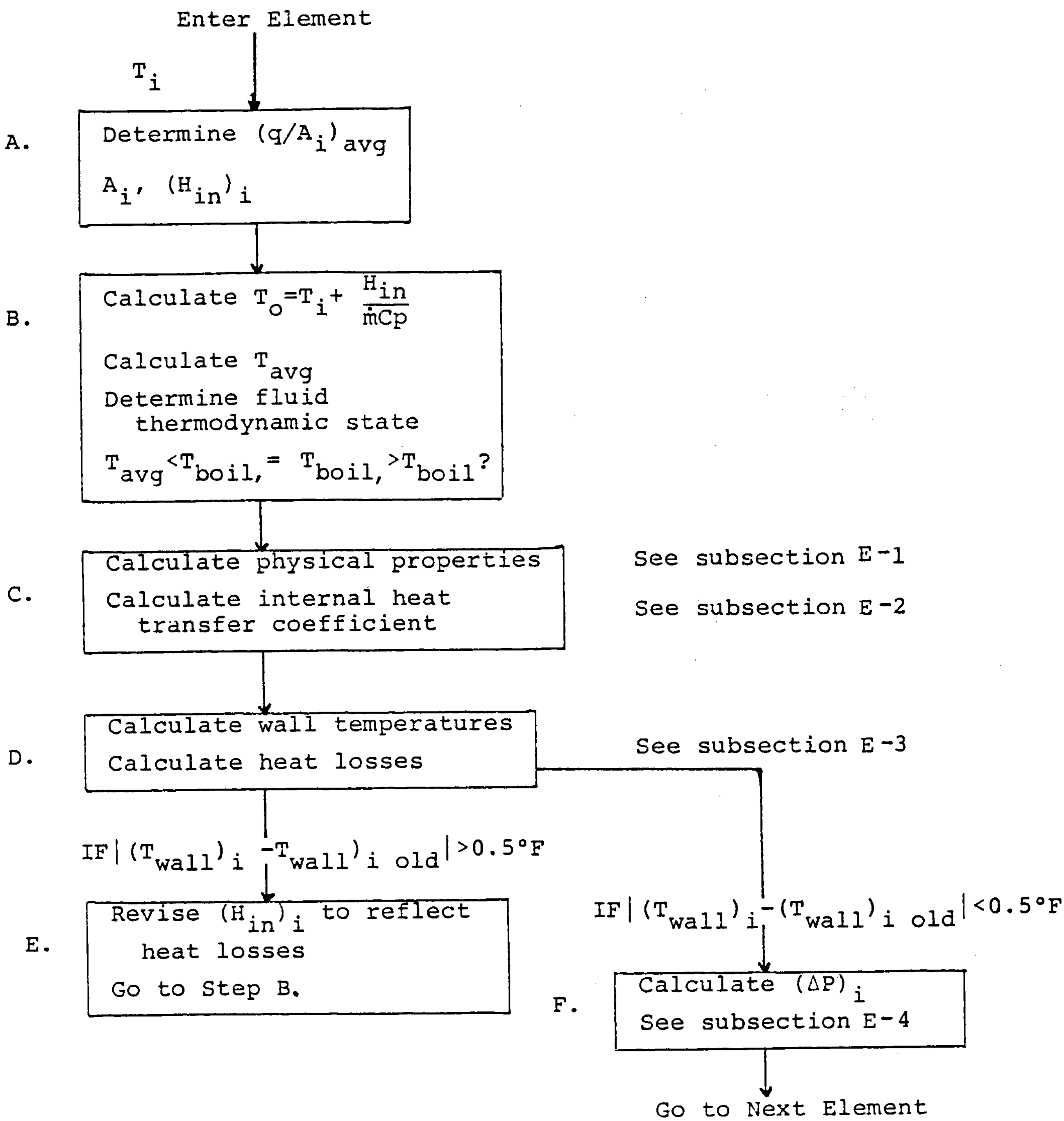

The computer code then calculates a fluid outlet temperature for the element and an average temperature within the element. The thermodynamic state of the fluid within the element is determined and physical properties evaluated.

Then the code determines the internal heat transfer coefficient for the element, based upon the fluid's thermodynamic state, and calculates inside and outside wall tempertures. The outside wall temperature is combined with the external wind speed and ambient temperature to predict convective and radiative heat losses. The input heat is adjusted for losses and the process is repeated until successive wall temperatures agree within 0.5°F. Finally a pressure drop for the fluid flowing through the element is determined and the program proceeds to the next flow element.

The internal heat transfer coefficients and the fluid pressure drops are calculated using the best available correlations from the literature. Similarly, the physical property data are temperature dependent, and where appropriate, pressure dependent fits of literature experimental data. The subsections which follow are keyed to Fig. E-2 to describe in detail the techniques and correlations used in this model.

E-1 PHYSICAL PROPERTY CORRELATIONS FOR WATER AND CALORIA HT-43^R

Water physical property data are incorporated into the thermo-fluid model as empirical correlations for saturated liquid and the saturated vapor state. With the exception of the superheated vapor density, only data at saturation are used and pressure effects are neglected. The liquid water physical property correlations are summarized in Table E-1 and the vapor correlations in Table E-2. In both cases either the source of the correlation or the source of the data is indicated. Superheated vapor densities are found by using curve fits of density as a function of temperature at constant pressure and then interpolating between pressures as needed. The superheated vapor correlations are not shown, but the source of the data is <u>Thermodynamic Properties of Steam</u>, J. H. Keenan and F. G. Keyes, John Wiley and Sons, New York, 1936.

All of the Caloria HT-43^R correlations are least squares fits of curves supplied by the manufacturer. These correlations are shown in Table E-3.

E-2 CORRELATIONS FOR THE INTERNAL HEAT TRANSFER COEFFICIENTS

The thermo-fluid receiver model uses a sequence of correlations to predict the tube wall-to-fluid internal heat transfer coefficient. The choice of correlation used is dictated by the temperature of the fluid and, where appropriate,

TABLE E-1

Physical Property Correlations for Saturated Water Vapor

Density[1]: $\ln(1/\rho)[lb_m/ft^3]=5.48664-0.012174T \quad T<425°F$

$\ln(1/\rho)[lb_m/Ft^3]=4.68087-0.010202T \quad T>425°F$

Heat Capacity[2]: $c_p[Btu/lb_m°F]= 1.9448-0.89253\times10^{-2}T + 0.17883\times10^{-4}T^2-0.118442\times10^{-7}T^3$

$273<T<535°k$

$c_p[Btu/lb_m°F]= 0.443222-0.285391\times10^{-4}T + 0.198477\times10^{-6}T^2-0.663724\times10^{-10}T^3$

$T>535°k$

Viscosity[3]: $\mu[poise]=\mu_o+10^{-4}[\tau(6.36-2.31)(10^{1340\tau})p + 3.89\times10^{-2}(10^{-5.476\times10^{-3}T})p^2]$

where

$\mu_o=1.501\times10^{-5}(T)^{1/2}/(1+446.8\tau)$

$\tau=1/T, T, °k$ and $p, kg/cm^2$

Thermal Conductivity[4]: $k[mW/cm°k]=0.00084T-0.07133$

$273<T<450°k$

$k[mW/cm°k]=0.001065T-0.17424 \quad T>450°k$

References:

1. Keenan, J. H. and Keyes, F. G., Thermodynamic Properties of Steam, pp. 34-39, John Wiley and Sons, New York, 1936. (Data)

2. Touloukian, Y. S., ed., Thermophysical Properties of Matter, Vol. 6, pp. 105-111, Plenum Press, New York, 1970. (Correlation)

3. Keenan, J. H. and Keyes, F. G., Thermodynamic Properties of Steam, pp. 23-24, John Wiley and Sons, New York, 1936 (Correlation).

4. Touloukian, Y. S., ed., Thermophysical Properties of Matter, Vol. 3, pp. 125-128, Plenum Press, New York, 1970. (Data)

TABLE E-2

Physical Property Correlations for Saturated Liquid Water

Density[1]: $$\rho\,[g/cm^3] = \frac{[1+d(t_c-t)^{1/3}+e(t_c-t)]}{v_c+a(t_c-t)^{1/3}+b(t_c-t)+c(t_c-t)^4}$$

where

$v_c = 3.1975\ cm^3/g$

t_c = critical temperature = 374.11°C

t = temperature, °C

$a = -0.3151548$

$b = -1.203374 \times 10^{-3}$

$c = 7.48908 \times 10^{-13}$

$d = 0.1342489$

$e = 3.946263 \times 10^{-3}$

Heat Capacity[2]: $$c_p[Btu/lb_m°F] = 2.13974-0.968137\times10^{-2}T + 0.268536\times10^{-4}T^2-0.242139\times10^{-7}T^3$$

for $273<T<410°K$

$$c_p(Btu/lb_m°F)=-11.1558+0.0796443T -0.174799\times10^{-3}T^2+0.129156\times10^{-6}T^3$$

$410<T<590°K$

Viscosity[3]: $\ln\mu[cp] = -.52009 + 1477.31/T$ $\quad 273<T<473°K$

$\ln\mu[cp] = -4.3437 + 1120.93/T$ $\quad T>473°K$

(Table E-2, cont'd.)

Thermal Conductivity[4]:

$$10^6 k[\mathrm{mW/cm°k}] = -1390.53 + 15.1937T - 0.0190398T^2$$

$$273<T<413°k$$

$$10^6 k[\mathrm{mW/cm°k}] = -339.838 + 9.86669T - 0.0123045T^2$$

$$T>413°k$$

References:

1. Keenan, J. H. and F. G. Keyes, Thermodynamic Properties of Steam, p. 21, John Wiley and Sons, New York, 1936 (Correlation).

2. Touloukian, Y. S., ed., Thermophysical Properties of Matter, Vol. 6, p. 102-104, Plenum Press, New York, 1970 (Correlation).

3. Eisenberg, D., and W. Kauzmann, The Structure and Properties of Liquid Water, Oxford Univeristy Press, New York, 1969 (Data).

4. Touloukian, Y. S., ed., Thermophysical Properties of Matter, Vol. 3, p. 120-124, Plenum Press, New York, 1970 (Correlation).

TABLE E-3

Physical Properties of Caloria HT-43[R]

Density: $\rho[lb_m/ft^3]=55.322-0.022945\ T[°F]$

Heat Capacity: $c_p[btu/lb_m°F]=0.4742+0.00038T \quad T<200°F$

$c_p[Btu/lbm°F]=0.4525+0.000495T \quad T>200°F$

Viscosity: $\ell n\mu[lb_m/fthr]=-4.5971+4844.51T\ [°R]$

Thermal Conductivity: $k\cdot[Btu/fthr°F]=0.0791-0.000022T\ [°F]$

the boiling regime. As seen in Fig. E-3, the fluid undergoes a very repeatable sequence of heat transfer events as it progresses through the receiver. The heat transfer correlations and qualifying assumptions used with each are outlined below.

E-2.1 Liquid Forced Convection

In the region where the liquid is below its saturation temperature, all heat transfer is from a hot tube wall to a turbulent fluid. The laminar flow regime has been excluded because of unfavorable heat transfer rates. No entrance region is considered. The correlation used to estimate the internal heat transfer coefficient in this regime is the Seider-Tate equation [1] modified for hot wall effects.

$$h_i[\mathrm{Btu/ft hr\,^\circ F}]=0.027(k_\ell/D_i)\left[\frac{GD_i}{\mu_\ell}\right]^{0.8}\left[\frac{\mu_\ell c_{p\ell}}{k_\ell}\right]^{0.33}\left[\frac{\mu_\ell}{\mu_\omega}\right]^{0.14} \qquad \text{(E-2)}$$

Since there can be some extremely high heat fluxes encountered due to multiple bounce reflections at the lower end of the receiver, at each element in the subcooled liquid region there is a check for the occurrence of a subcooled critical heat flux excursion. The Macbeth correlation [2]

$$q_{1c}[\mathrm{Btu/ft^2hr}]=10^6\cdot\frac{[10^{-6}G(\lambda+\Delta H_{sub})]}{158D_i^{0.1}\ 10^{-6}G^{\ 0.49}+4L/D_i} \qquad \text{(E-3)}$$

is used for this. The $4L/D_i$ term, however is set at zero in the subcooled region, because of the extremely large L/D_i ratios encountered before any boiling even begins. Once the fluid

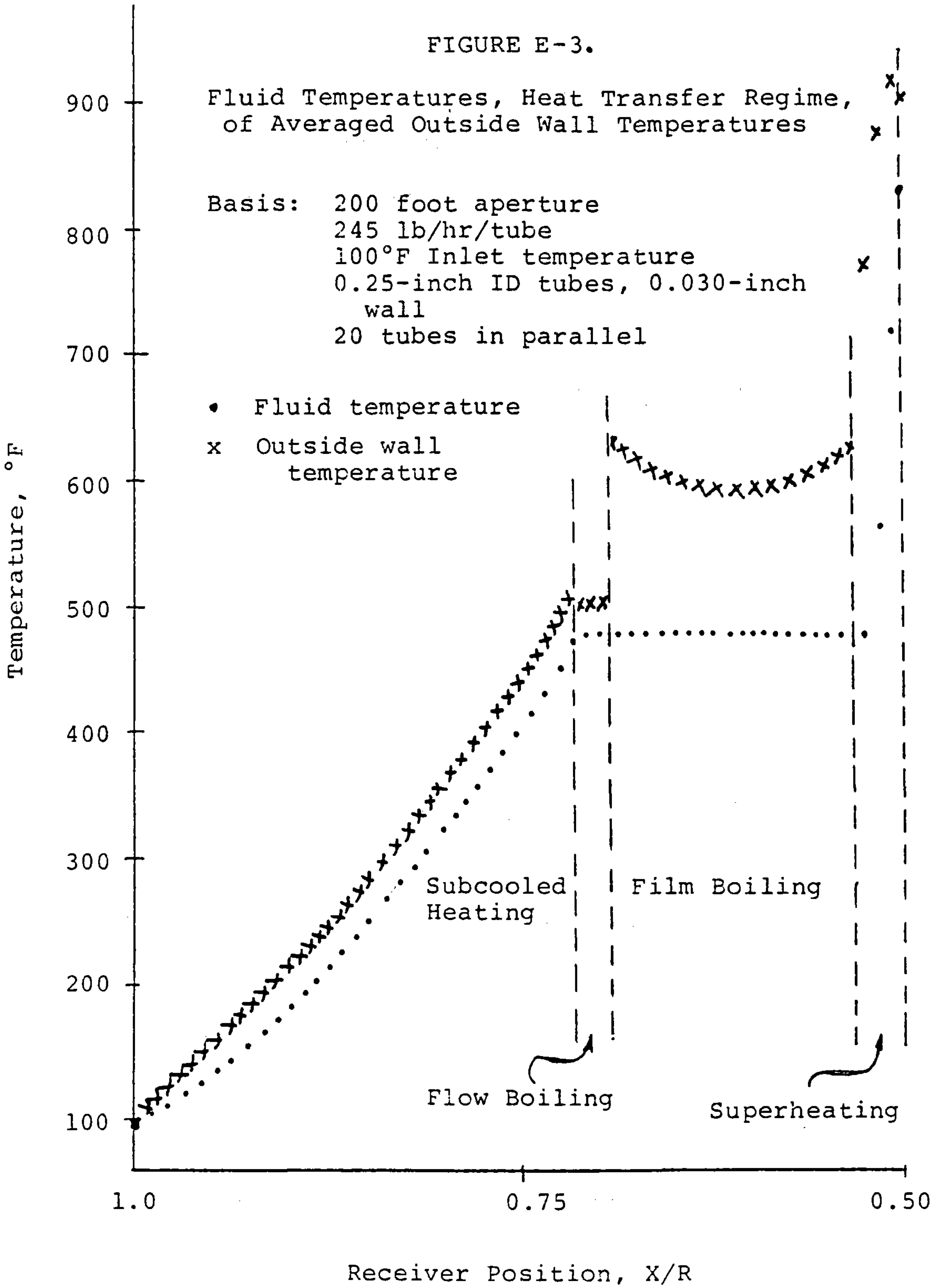
FIGURE E-3.
Fluid Temperatures, Heat Transfer Regime, of Averaged Outside Wall Temperatures
Basis: 200 foot aperture
245 lb/hr/tube
100°F Inlet temperature
0.25-inch ID tubes, 0.030-inch wall
20 tubes in parallel
• Fluid temperature
x Outside wall temperature
900
800
700
600
500
400
300
200
100
Temperature, °F
Subcooled Heating
Film Boiling
Flow Boiling
Superheating
1.0
0.75
0.50
Receiver Position, X/R

has reached the saturation temperature, the L/D_i effect is included in the critical heat flux estimation.

If there is sufficient heat flux in an element to cause a critical excursion in the subcooled liquid, then the subcooled boiling heat transfer coefficient is represented by the Jens-Lottes expression [3]

$$h_i \,[\mathrm{Btu/ft^2hr^\circ F}] = 0.772 e^{p/225} \frac{[T_w - T_{sat}]^4}{T_w - T_{fluid}} \qquad \text{(E-4)}$$

The only circumstances we have encountered where subcooled boiling crises occur have been when considering some multiple bounce reflections. In actual operation it is doubtful if this regime would actually exist.

E-2.2 Fully-Developed Flow Boiling

The incipient boiling transition which occurs as the fluid temperature approaches the saturation temperature in this model and all boiling is considered to be fully developed. The Dengler-Addoms [4] correlation is used to describe fully developed flow boiling

$$(h_i)_{conv}[\mathrm{Btu/ft^2hr^\circ F}] = 0.023(k_\ell/D_i)\left[\frac{D_i G(1-X)}{\mu_\ell}\right]^{0.8}\left[\frac{\mu_\ell c_{p\ell}}{k_\ell}\right]^{0.4}$$

$$\chi_{tt} = \left[\frac{x}{1-x}\right]^{0.9}\left[\frac{\rho_\ell}{\rho_v}\right]^{0.5}\left[\frac{\mu_v}{\mu_\ell}\right]^{0.1} \qquad \text{(E-5)}$$

$$(h_i)_{flow\ boiling}[\mathrm{Btu/ft^2hr^\circ F}] = 3.5\,(h_i)_{conv}\left(\frac{1}{\chi_{tt}}\right)^{0.5}$$

The critical heat flux in fully developed flow boiling is estimated using the Macbeth correlation described above, with the L/D_i term included. Once the boiling crisis has occurred, film boiling is assumed to exist until all of the liquid is vaporized. For convenience, equilibrium is assumed to exist in the film boiling regime, with the fluid stream maintaining the saturation temperature until vaporization is complete. Effects of the inaccuracy of this assumption on the heat transfer coefficient are expected to be balanced by the enhancing effect of the helical flow geometry. The Rohsenow and Federovich[5] correlation is used for film boiling

$$h_i[\mathrm{Btu/ft^2hr^\circ F}]=0.023(k_\ell/D_i)\left(\frac{GD_i}{\mu_\omega}\right)^{0.8}\left(\frac{\mu_\omega c_{p\omega}}{k_\omega}\right)^{0.8}A^{0.8}B$$

$$A = x + \frac{\rho_\nu}{\rho_\ell}(1-\chi)$$

$$B = 1+0.1\left(\frac{\rho_\ell}{\rho_\nu}-1\right)^{0.4}(1-x)^{0.4} \qquad \text{(E-6)}$$

E-2.3 Steam Superheating Region

In the steam superheating region, the internal heat transfer coefficient is estimated using the Seider-Tate equation in the vapor phase.

In the entire heat transfer analysis, the effects of the helical flow geometry have been neglected. This measure should cause the estimated coefficients to be somewhat conservative. The effect of the considerable flux tilt on the heat transfer is neglected, as are the effects of the highly asymmetric local fluxes around a single tube. The Macbeth correlation is assumed valid even though it was developed from data measured in once-through experiments with dryout occuring at the tube exit, instead of well back from the tube exit as it occurs here. With these assumptions and the correlations noted above, a typical pattern of values for the internal heat transfer coefficient is shown in Fig.E-4. It is evident from this figure that the E-Systems constant internal heat transfer coefficient of 1000 Btu/ft^{2}hr ^{o}F is reasonably good.

E-3 STEAM SUPERHEATING REGION

For a given heat flux entering an individual tube element, once the average fluid temperature and the internal heat transfer coefficient has been determined, the inside and outside wall temperatures are fixed by the relations

$$\left(T_w\right)_{inside} = \left(T_{fluid}\right)_{avg} + \left(Q_{element_{avg}}\right) \Big/ \left(h_{i_{element}}\right) \quad (E\text{-}7)$$

and

$$\left(T_w\right)_{outside} = \left(T_{wall}\right)_{inside} + \frac{\left(Q_{element}\right)_{avg} r_o \ln(r_o/r_i)}{k_{wall}} \quad (E\text{-}8)$$

The log mean wall thickness is used instead of the true wall thickness to account for the fact that each individual absorbing element is a tube instead of a flat plate. This is in contrast to the E-Systems flat plate assumption. The net effect of using a log mean wall thickness is a slightly higher predicted outside wall temperature.

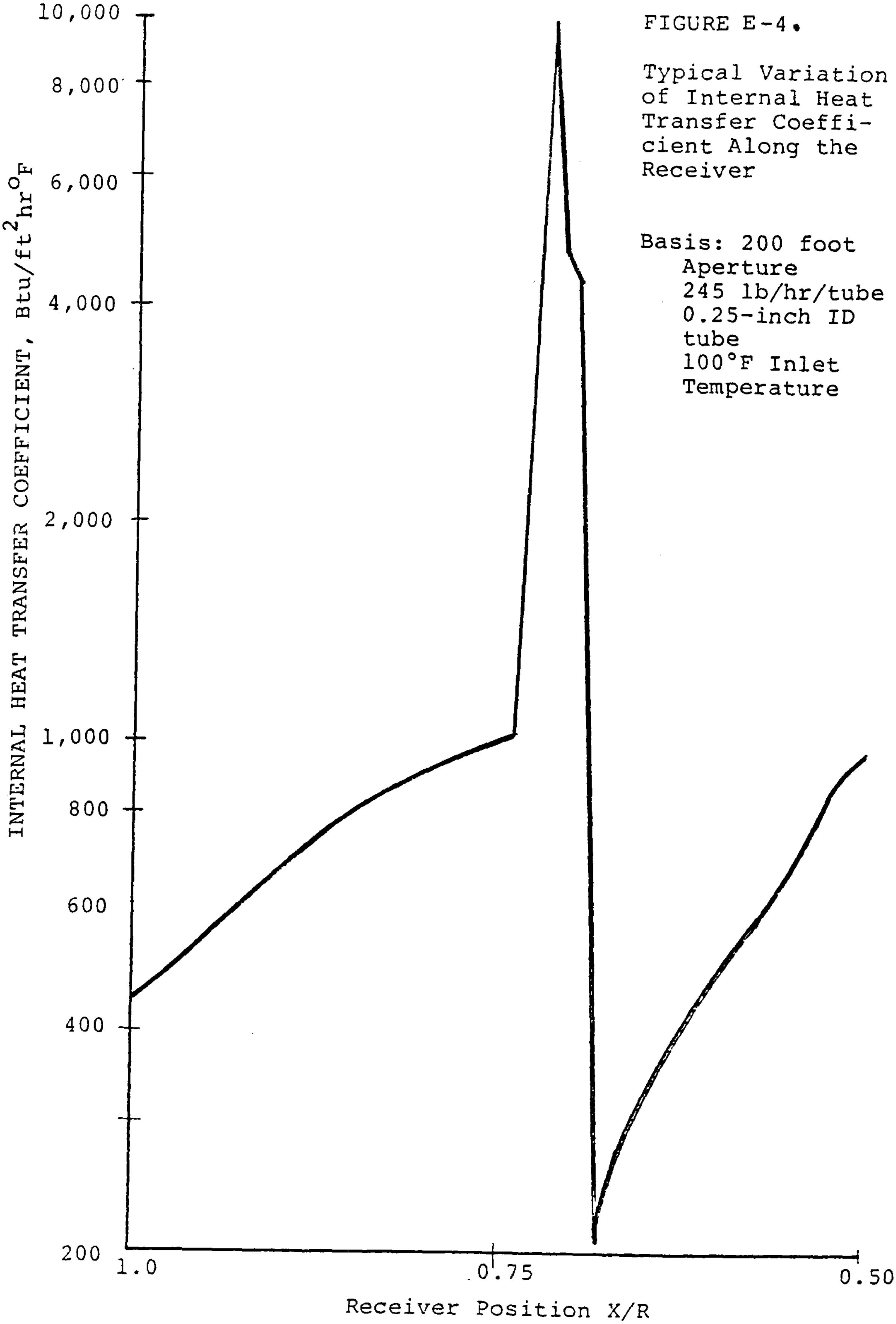

FIGURE E-4. Typical Variation of Internal Heat Transfer Coefficient Along the Receiver

Basis: 200 foot Aperture
245 lb/hr/tube
0.25-inch ID tube
100°F Inlet Temperature

The $(Q_{element})_{avg}$ used in Eqs. (E-7) and (E-8) depends, in turn on the outside wall temperature because the rate of heat loss is a direct function of $(T_W)_{outside}$. This is handled in the model by initially assuming zero losses and then iterating until $(T_w)_{outside}$ from successive iterations agrees to within 0.5°F. The actual heat absorbed within an element is, then

$$Q_{absorbed}=Q_{incident}-Q_{radiative\ loss}-Q_{convective\ loss} \tag{E-9}$$

where

$$Q_{incident}=\text{Insolation} \times \text{Concentration} \times \text{Area} \times \text{Absorptivity} \tag{E-10}$$

$$Q_{radiative\ loss}=\text{Area} \times \sigma\varepsilon[(T_{wall})^4_{outside}-(T_{ambient})^4]$$

$$Q_{convective\ loss}=\text{Area}\ h_{conv}[(T_{wall})_{outside}-(T_{ambient})]$$

and the convective heat transfer coefficient is given by the Hottel correlation [6]

$$h_{conv}[Btu/Ft^2hr^oF]=1+0.3\ (V_{wind}) \tag{E-11}$$

The wind velocity in Eq. (E-11) is in miles per hour. Some of the results shown here are for absorptivity equal to unity and emissivity of 0.85, others are for absorptivity and emissivity equal to 0.9. In all of this work a reflectance for the mirror surface of 0.88 is used.

The fluid mechanical behavior from one end of the receiver to another goes through a series of different regimes in a manner similar to the several heat transfer regime changes experienced. In the two-phase region, although several distinct flow modes have been identified, very little is in the literature concerning flow modes and flow stability for two-phase fluids in helical coils, so for this analysis, the simplistic approach of considering only a flow boiling, low quality two-phase region and a mist flow region is used in estimating the pressure drop. The expressions used to calculate pressure drop in each of the several flow modes are given below.

As long as the liquid remains subcooled and is not in the subcooled film boiling heat transfer regime, we can use the expression

$$(\Delta P/L) = 0.062112 f \rho V^2/D_i \qquad \text{(E-12)}$$

where

$$f = [0.0014 + \frac{0.125}{Re_\ell^{0.32}}](\frac{\mu_\omega}{\mu_\ell})^{0.17} \qquad \text{(E-13)}$$

for the liquid phase pressure drop. When vapor begins to form, we change to a two-phase flow pressure drop prediction recently presented by Wisman [7].

Wisman's method is used as long as the fluid void fraction is less than 0.95. Here the void fraction is defined as

$$\alpha = \frac{A_v}{A_v + A_\ell} \qquad \text{(E-14)}$$

where

$$A_v = X/\rho_v \qquad \text{(E-15)}$$

$$A = (1-X)/\rho_\ell$$

We use the liquid and gas superficial velocities

$$U_v = (GX)/\rho_v$$
$$U_\ell = G(1-X)/\rho_\ell \qquad \text{(E-16)}$$

to calculate a two-phase Reynolds number

$$Re_{tp} = \frac{\rho_\ell U_\ell D_i A\ B}{\mu_\ell} \qquad \text{(E-17)}$$

where

$$A = 1 + \left(\frac{\alpha}{1-\alpha}\right)\left(\frac{\rho_v}{\rho_\ell}\right)\left(\frac{U_v}{U_\ell}\right)^2 \qquad \text{(E-18)}$$

$$B = (1 - \alpha)\ (1 - \alpha^{\frac{1}{2}})$$

The two-phase Reynolds number is used to calculate a friction factor

$$f_{tp} = 0.0056 + \frac{0.5}{Re_{tp}^{\ 0.32}} \qquad \text{(E-19)}$$

and finally a two-phase pressure drop

$$(\Delta P/L)_{tp} = \left(\frac{f}{1-0.5\ f}\right) \left[\frac{0.5(1-\alpha)\rho_\ell U_\ell^{\,2}}{gD_i}\right] \cdot \qquad \text{(E-20)}$$

$$\cdot \left[1 + \frac{\alpha}{1-\alpha}\left(\frac{\rho_v}{\rho_\ell}\right)\left(\frac{U_v}{U_\ell}\right)^2 + \frac{\alpha(\rho_\ell - \rho_v)gD_i}{\rho_\ell U_\ell^{\,2}}\right]$$

This calculation scheme gives results of accuracy comparable to those of the Lockhart-Martinelli-Nelson correlations, with a much less complicated calculational procedure.

Once the void fraction in the fluid reaches 0.95, it is assumed that there is a smooth transition into a mist type of flow. Here we estimate the pressure drop using the turbulent flow friction factor expression, Eq. (E-12), and Eq. (E-13), but with the modification that the fluid is acting like a pseudo single-phase fluid with appropriately modified physical properties. The "pseudo fluid" physical properties are given by

$$\rho_{avg} = \rho_\ell(1-X) + \rho_v X$$

$$\mu_{avg} = \mu_\ell(1-X) + \mu_g X \qquad \text{(E-21)}$$

$$(\mu_{wall})_{avg} = (\mu_\ell)_{wall}(1-X) + (\mu_g)_{wall} X$$

When vaporization is complete, Eqns. (E-15) and (E-16) are used to predict the single phase pressure drops, with the appropriate vapor physical properties.

E-5 PARAMATERS AFFECTING STEAM-GENERATING RECEIVERS

Once the size of a collector dish has been set, the major dimensions of the receiver (length and diameter top and bottom) are also set. In addition, the amount of heat available for absorption is set since

$$\text{HeatAvailable} = \text{Absorptivity (Insolation) (Mirror Area)} - \text{Losses} \quad \text{(E-22)}$$

The steam exit conditions are fixed by the choice of turbines, leaving only the entering water temperature as a variable (the water mass flow rate is set by the heat balance for a given entrance temperature). Fig. E-5 shows how changes in water inlet temperature can affect both the thermal losses and the total mass flowrate for a fixed delivery temperature and pressure and a fixed mirror size.

It is evident from the figure that for entering temperatures above 200°F entry temperature matters take a turn for the worse because the average receiver temperature is now high enough that radiant losses are significant throughout the receiver. In going from an inlet temperature of 200°F to one of 300°F, the total losses increase 17.6 percent while the flow rate per tube only increases 3.7 percent.

The only variables left to the designer are the size of the tube and the number of parallel flow paths. Choice of tube size and the number of tubes to be used is a two-sided

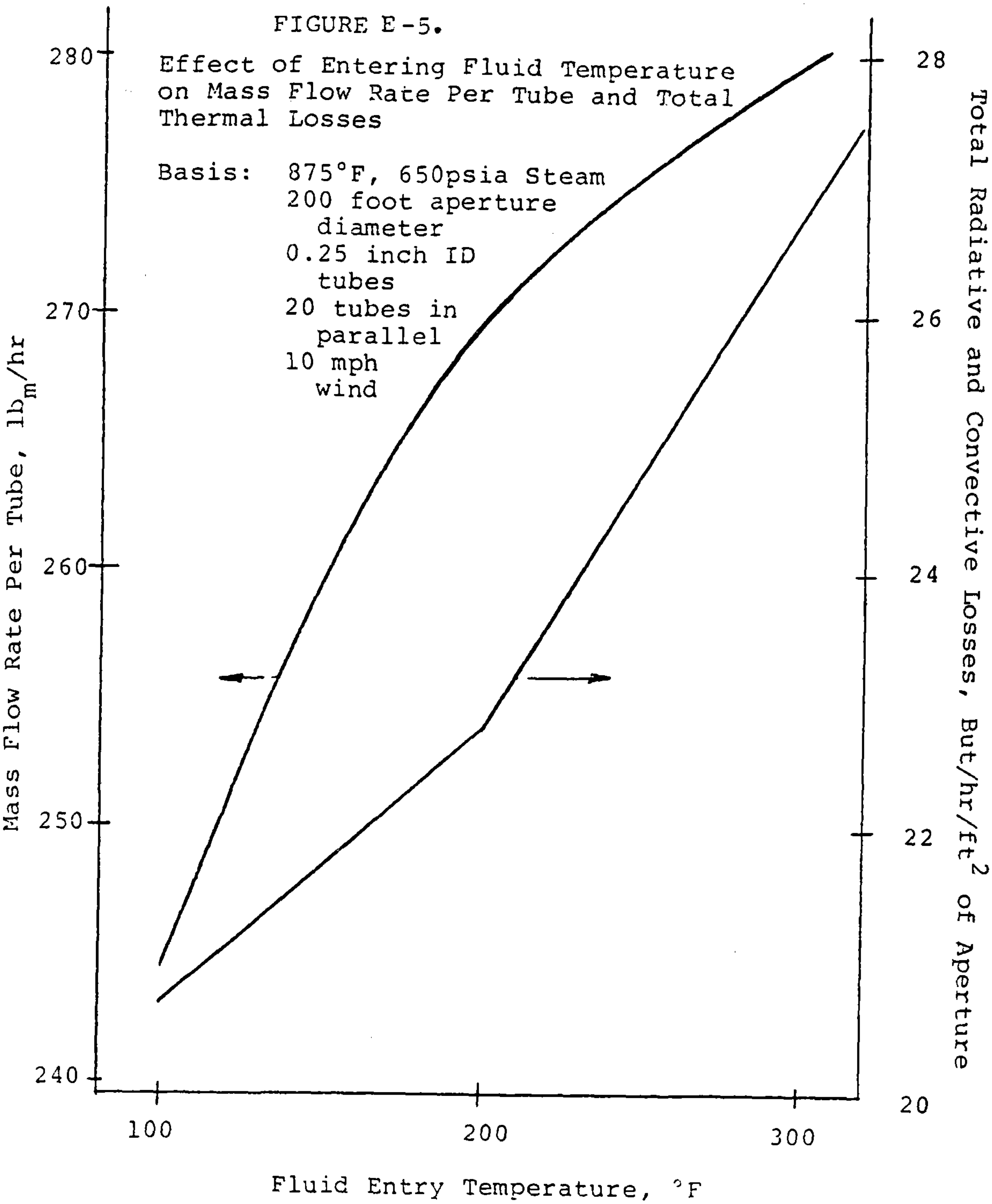
FIGURE E-5.
Effect of Entering Fluid Temperature on Mass Flow Rate Per Tube and Total Thermal Losses
Basis: 875°F, 650psia Steam
200 foot aperture diameter
0.25 inch ID tubes
20 tubes in parallel
10 mph wind
Mass Flow Rate Per Tube, lb_m/hr
240
250
260
270
280
Total Radiative and Convective Losses, But/hr/ft^2 of Aperture
20
22
24
26
28
100
200
300
Fluid Entry Temperature, °F

trade off. On the one hand larger tubes are desirable for their lower pressure drop and improved flow stability. On the other, smaller tubes lead to faster fluid flow rates which results in improved internal heat transfer and lower tube temperatures.

The effect of the number of parallel flow paths is shown in Fig. E-6. Since the pressure drop is proportional to V^2, there is a considerable variation between the cases. In each case the dominant pressure drop contributor is the superheating region.

The contribution of individual flow regions to the pressure drop is seen more clearly in Fig. E-7. No matter which tube size is used, the region from 50 percent vaporized through the superheat region contributes two-thirds of the total pressure drop experienced in the receiver. This is why the receiver is designed so that the superheating region coincides with the region of highest heat flux--to keep it as short as possible in order to minimize the pressure drop.

Unfortunately, one cannot design a system such as this simply to develop minimum pressure drop, because the resulting excessive tube wall temperatures could pose a difficult problem for materials of construction. The effect of changing the number of tubes on the outside tube temperature is seen in Fig. E-8. Note that in all of the curves shown, the wall thickness is constant. The nominal concept is a compromise between pressure drop and average tube wall temperature.

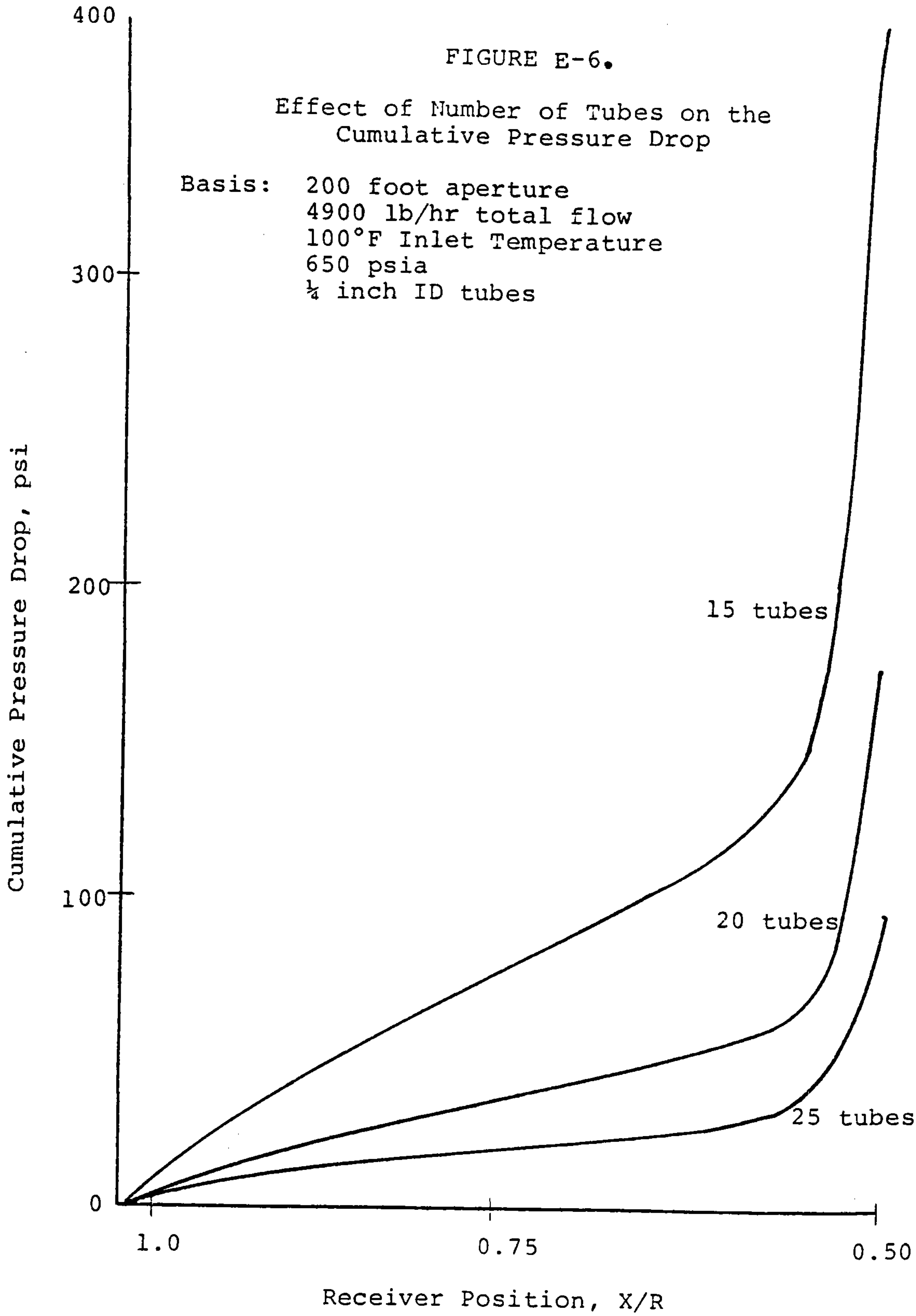

FIGURE E-6.
Effect of Number of Tubes on the Cumulative Pressure Drop
Basis: 200 foot aperture
4900 lb/hr total flow
100°F Inlet Temperature
650 psia
¼ inch ID tubes
400
300
200
100
0
Cumulative Pressure Drop, psi
15 tubes
20 tubes
25 tubes
1.0
0.75
0.50
Receiver Position, X/R

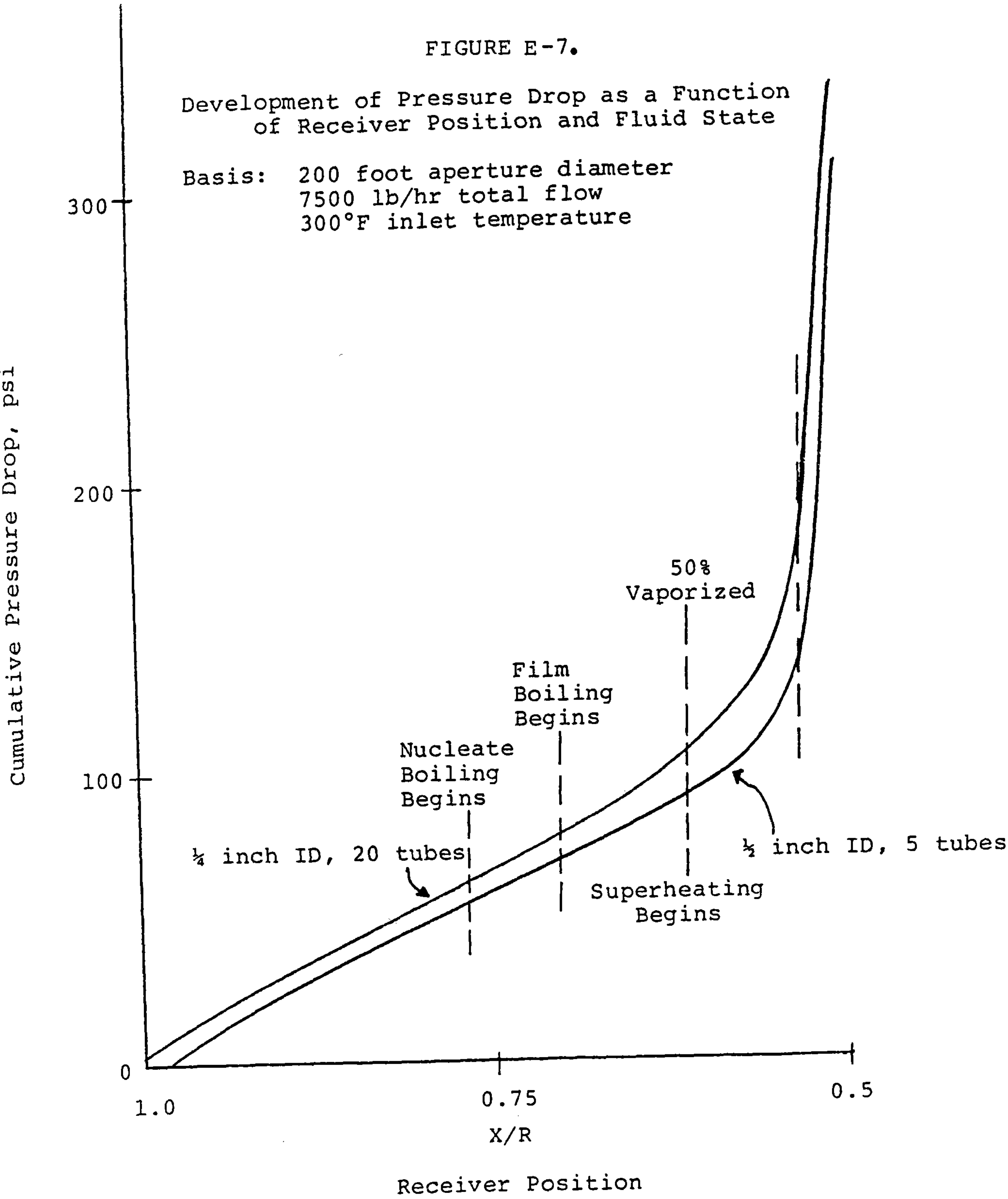
FIGURE E-7.
Development of Pressure Drop as a Function of Receiver Position and Fluid State
Basis: 200 foot aperture diameter
7500 lb/hr total flow
300°F inlet temperature
Cumulative Pressure Drop, psi
300
200
100
0
1.0
0.75
0.5
X/R
Receiver Position
50% Vaporized
Film Boiling Begins
Nucleate Boiling Begins
¼ inch ID, 20 tubes
½ inch ID, 5 tubes
Superheating Begins

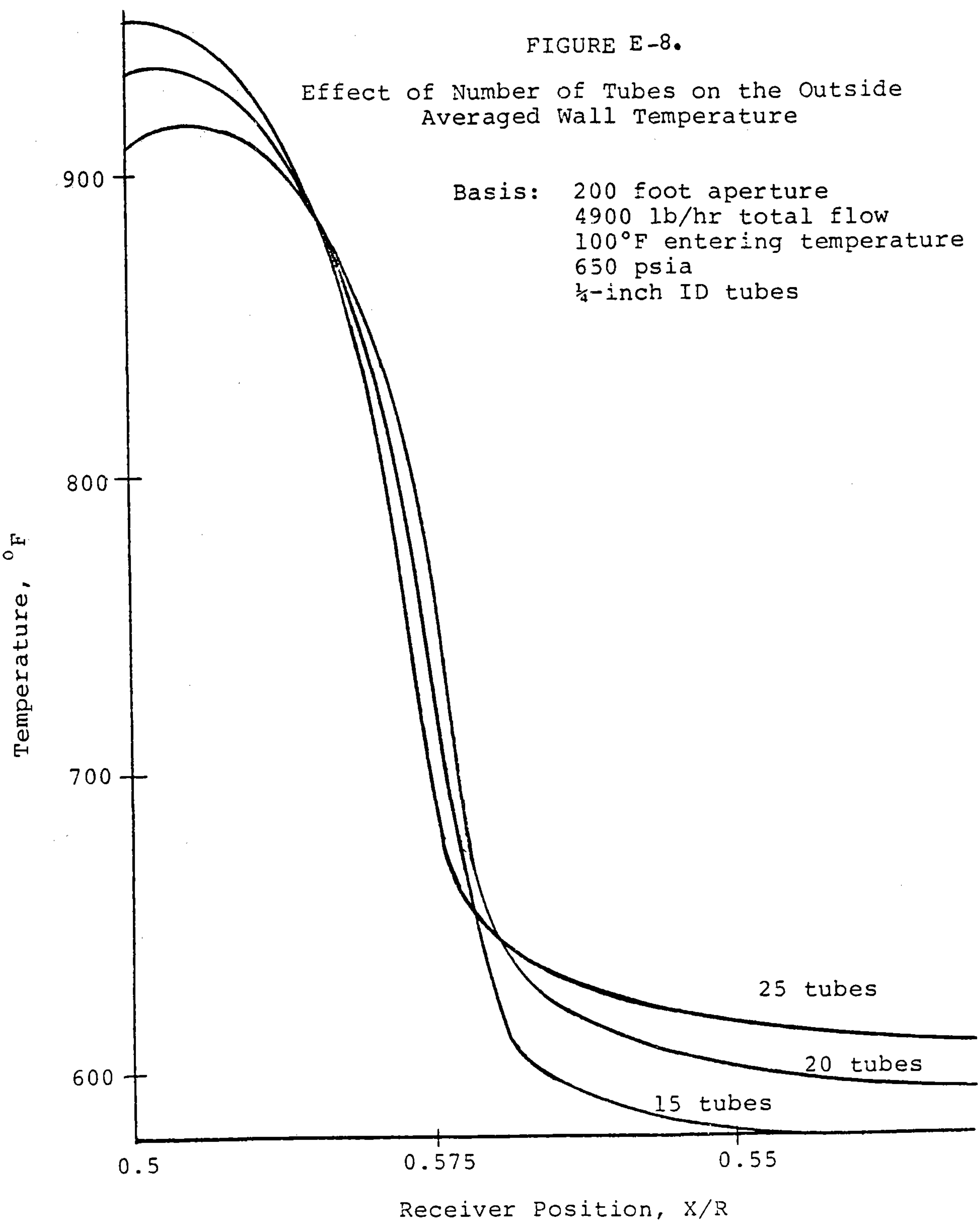
FIGURE E-8.
Effect of Number of Tubes on the Outside
Averaged Wall Temperature
Basis: 200 foot aperture
4900 lb/hr total flow
100°F entering temperature
650 psia
¼-inch ID tubes
900
800
700
600
Temperature, °F
25 tubes
20 tubes
15 tubes
0.5
0.575
0.55
Receiver Position, X/R

Obviously, since we are working at fairly high pressures, the tube wall thickness must be varied to insure long term structural integrity, with heat transfer considerations of secondary importance. The thermal and thermal cycling effects upon materials of construction and their impact upon receiver design are considered in Appendices F and G.

E-6 PARAMETERS AFFECTING HOT OIL RECEIVERS IN DUAL FLUID SYSTEMS

Receivers using a hot oil heat transfer fluid such as Caloria HT-43^R or Dowtherm A^R are subject to the same overall energy balance restrictions that steam generating receivers are. However, when using an organic heat transfer fluid, tube <u>inside</u> wall temperatures assume a critical role. These fluids as a class are subject to thermal degredation at elevated temperatures. As a result, a very strict upper limit must be imposed upon the inside tube wall temperature.

The major variable designer has available in hot oil systems is the fluid inlet temperature. Varying the inlet temperature, for a constant outlet temperature, results in changes in liquid flow rate which, to some extent, control the tube inside wall temperature by controlling the internal heat transfer coefficient. We see from Fig. E-9 that changing the mass flow rate without changing the inlet temperature has really only a small effect on the inside wall temperature.

FIGURE E-9. Effect of Flow Rate on the Inside Tube Wall Temperature Using Caloria HT-43

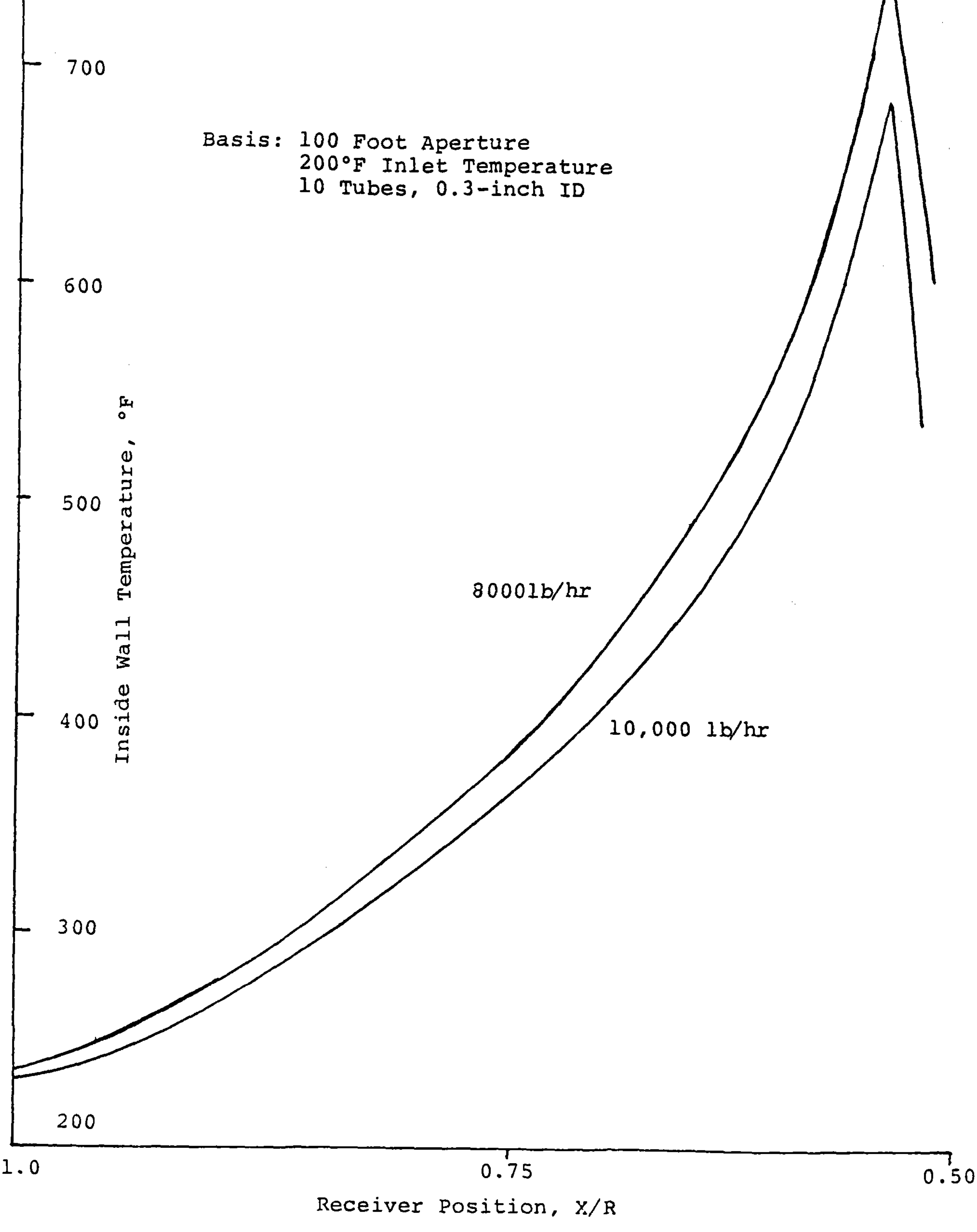

Another option available when using a hot oil system is to reverse the flow direction to take advantage of a cool fluid against a hot wall to improve heat transfer. However, it is evident from Fig. E-10 that this really is counter-productive. In the case represented, the best method for lowering inside wall temperature is to increase flow rate, not reverse flow. The reverse flow scheme has the added disadvantage of a much higher average receiver temperature and, hence, higher thermal losses.

A real benefit of working with a hot oil system is that the pressure drop through the receiver is a much more managable problem because there is no superheat region. The effects of flow rate on pressure drop in a hot oil system are shown in Fig. E-11. It is interesting to note that the higher overall receiver temperature in reversed flow does yield a 20 percent decrease in pressure drop because of lower fluid viscosity.

E-7 EFFECTS OF INCLUDING MULTIPLE REFLECTION COMPONENTS

It is of interest to investigate what the effects of the multiple bounce reflections are on the overall heat transfer problem in the receiver. The simplest case to compare is that of a symmetric concentration profile. The multiple bounce symmetric case is of academic interest only in that it represents an extreme in potential behavior. To examine symmetric multiple bounce contributions, a 90° included angle hemispherical mirror was treated. The outside wall temperatures for two cases

FIGURE E-10. Effect of Flow Direction on Inside Wall Temperature, Caloria Ht-43

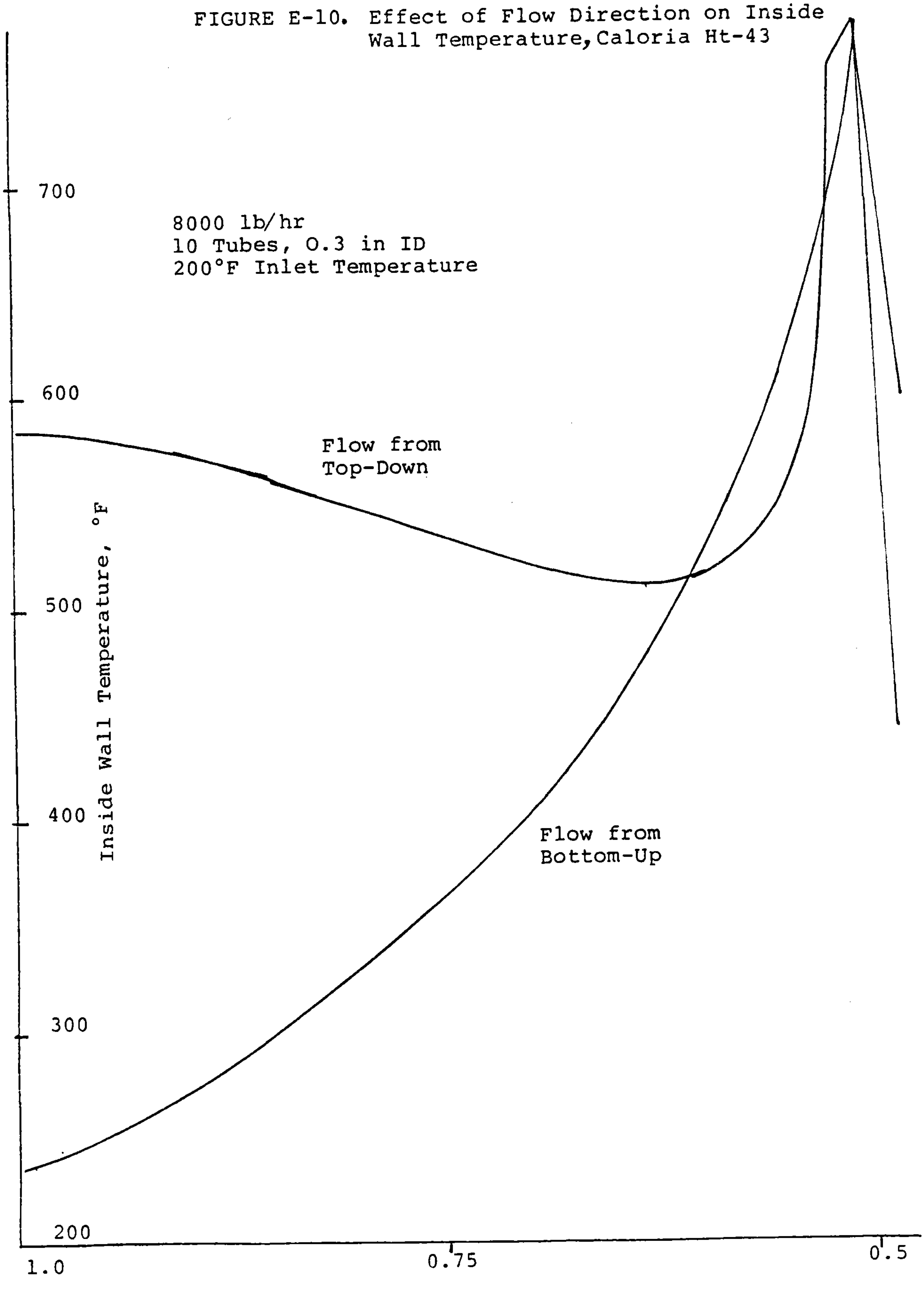

FIGURE E-11. Pressure Drop in a Dual Fluid System,

Caloria HT-43

0.3 in. ID Tubes

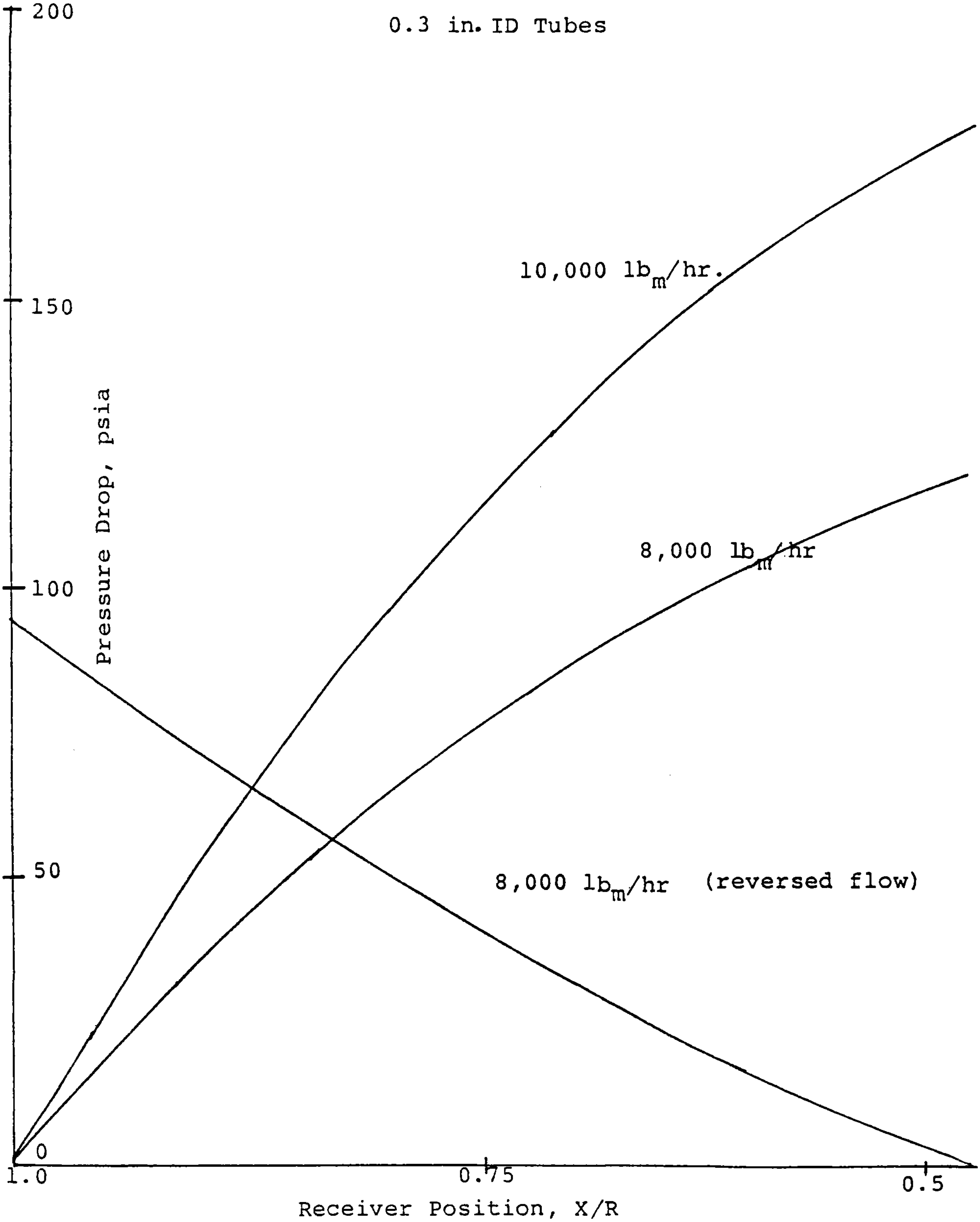

where the mass flow rate was held constant and single bounce reflections or reflections of up to five bounces are included are shown in Fig. E-12. It is apparent that the multiple bounce caustic region has much the same effect as a feed pre-heating section. Also, the fact that the 90° included angle mirror has approximately 25 percent more area, thus allowing a much higher flow rate because more heat is available, is reflected here.

Of much more pratical interest is the situation of low sun angles, where there is a significant, asymmetric concentration of multiple bounce energy present. However, simulation results at sun angles of 30° and 60° show agreement in terms of useful delivered heat within 2 percent between single and multiple bounce cases. The reason is that even though the total delivered power is greatest in the multiple bounce case, the higher average fluid temperature leads to higher losses. This result in some measure justifies continuing to use single bounce data in systems simulation studies.

Of equal interest is a look at what kind of temperature variations around the receiver one might expect. The largest variation in a single element was 218°F at the caustic for a sun elevation of 30°. The variation of temperatures around the receiver at this point is shown in Fig. E-13. While this sort of temperature variation is significant in developing thermal stresses, it is less severe than the temperature gradients within the tube wall itself.

FIGURE E-12. Comparison of Outside Wall Temperatures for Single Bounce and Multiple Bounce Symmetric Input

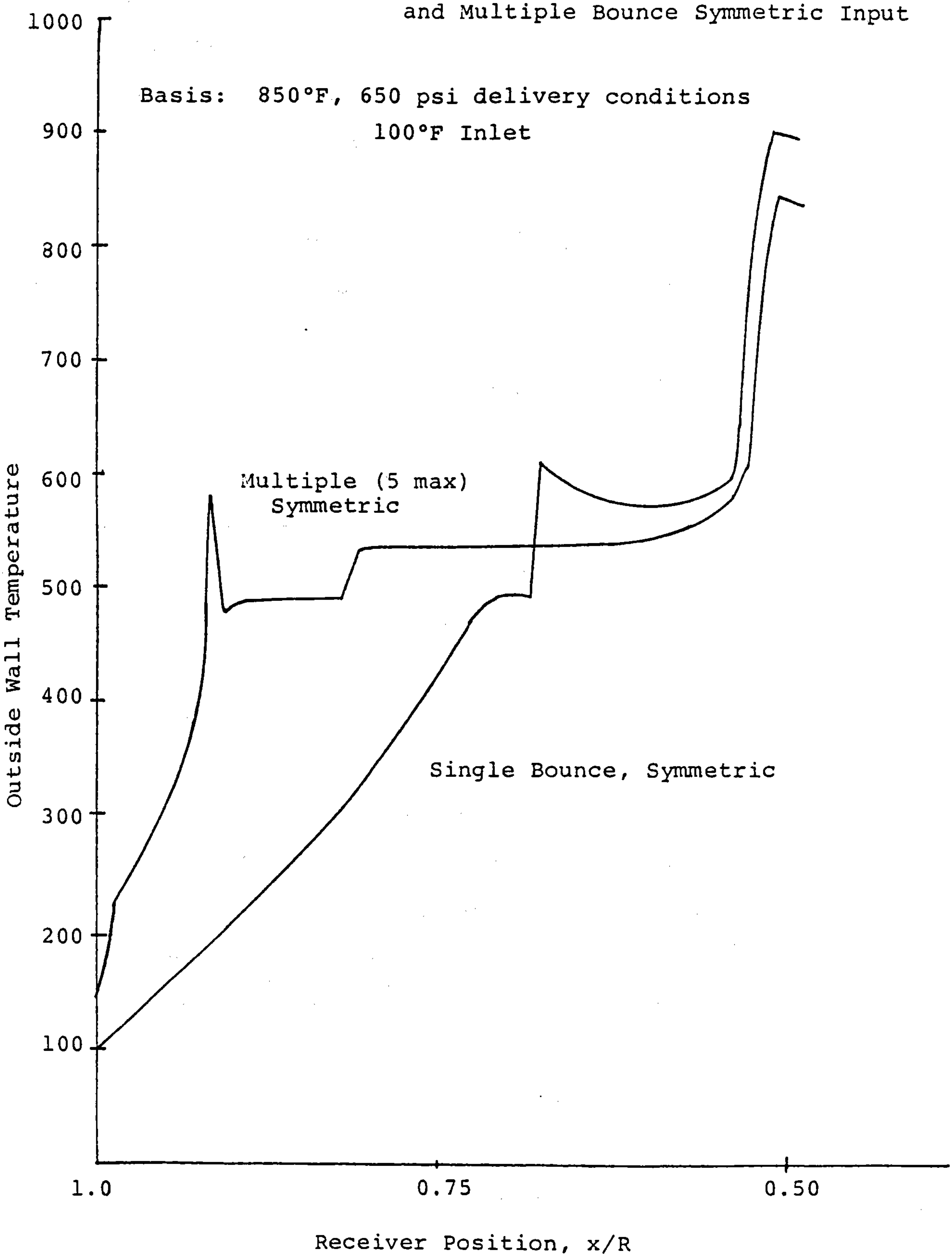

FIGURE E-13. Variation of Outside Wall Temperature Around the Receiver at a 30°Sun Angle (Caustic Region)

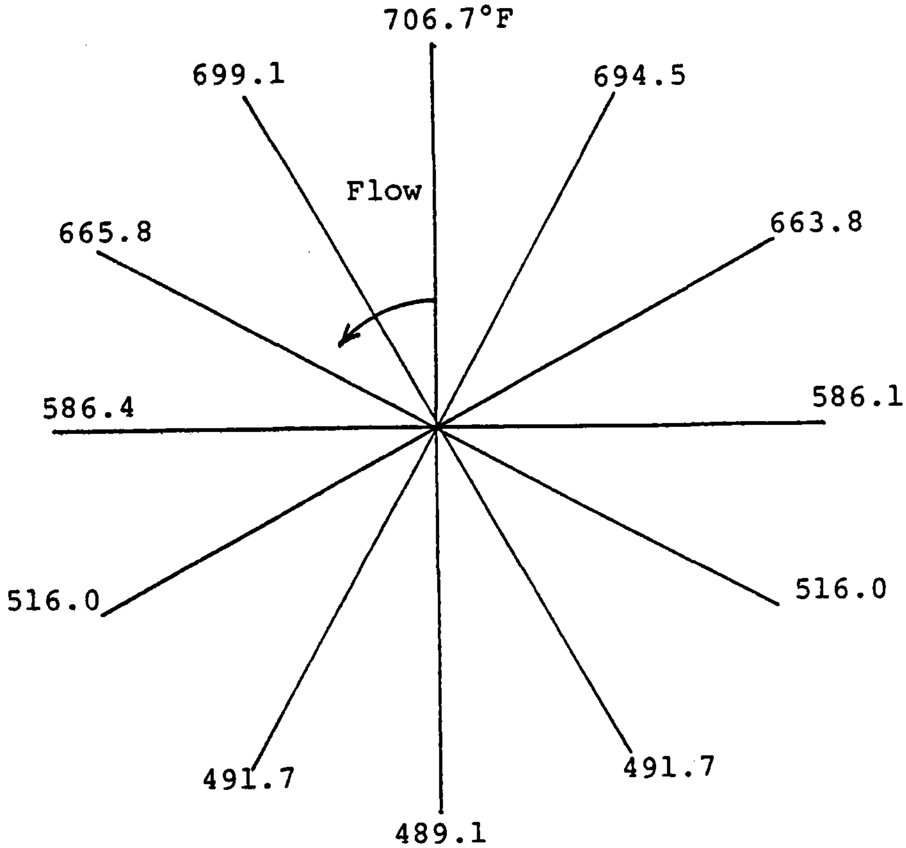

APPENDIX E NOMENCLATURE

c_p - heat capacity, Btu/lb_m°F

$C(x/R_i)$ - sun's concentration as a function of receiver position (x/R).

D_i - inside tube diameter, ft

f - friction factor

G - mass flow rate, lb_m/ft^2hr

h_i - internal heat transfer coefficient, $Btu/ft^2hr°F$

ΔH_{sub} - enthalpy of subcooling Btu/lb_m

I_o - solar insolation, Btu/ft^2hr

k - thermal conductivity, Btu/fthr°F

L_i - length, ft

$\Delta P/L$ - pressure drop, psi/ft

q_{1c} - critical heat flux, Btu/ft^2hr

q/A_i - Heat flux into element i, Btu/ft^2hr

Re - Reynold's Number

r - radius, ft

T - temperature °F

U - superficial velocity, ft/sec

V - wind velocity, miles per hour

X - steam quality

α - absorptivity, void fraction

β - reflectivity

λ - latent heat of vaporization, Btu/lb_m

μ - viscosity, lb_m/fthr

ρ - density, lb_m/ft

APPENDIX E REFERENCES

1. Sieder, E. N. and G. E. Tate, Ind. Eng. Chem., 28, 1429 (1936).

2. Macbeth, R. V., Adv. Chem. Engr., 7,207-293 (1968).

3. Jens, W. H. and P. A. Lottes, "Analysis of Heat Transfer, Burnout, Pressure Drop, and Density Data for High Pressure Water," USAEC Report ANL-4627 (1951).

4. Dengler, C. E. and J. N. Addoms, Chem. Engr. Prog, Symp. Ser., 52 (18), (1956).

5. Rohsenow, W. M., "Boiling," MIT, 1971.

6. Hottel, H. C., ASHRAE Low Temperature Applications of Solar Energy, New York, 1967.

7. Wisman, R., Appl. Sci. Reas., 30, 367-380 (1975).

APPENDIX F. E-SYSTEMS OVERALL RECEIVER THERMAL ANALYSIS

In this appendix, the methodology and results of detailed thermal analyses of the FMDF receiver are presented. These thermal studies are divided into two major categories:

- Overall Receiver Thermal Analysis
- Detailed Internal Heat Transfer and Pressure Drop Studies.

The objectives of these studies were two-fold:

- To define receiver thermal performance under various operating conditions.
- To generate a nominal receiver heat exchanger design, including configuration and materials, which would provide suitable thermal, fluid mechanical, structural and lifetime performance.

F-1 OVERALL RECEIVER THERMAL ANALYSIS

Figure F-1 presents schematically the approach taken for the thermal analysis of the overall receiver. The receiver heat exchanger was assumed to consist of a bundle of parallel flow tubes of total width (w), with this bundle wrapped helically over the outer surface of the conical receiver from the large end to the small end of the truncated cone-shaped receiver support. Once through flow of water/steam (or other heat transfer medium) was assumed to proceed

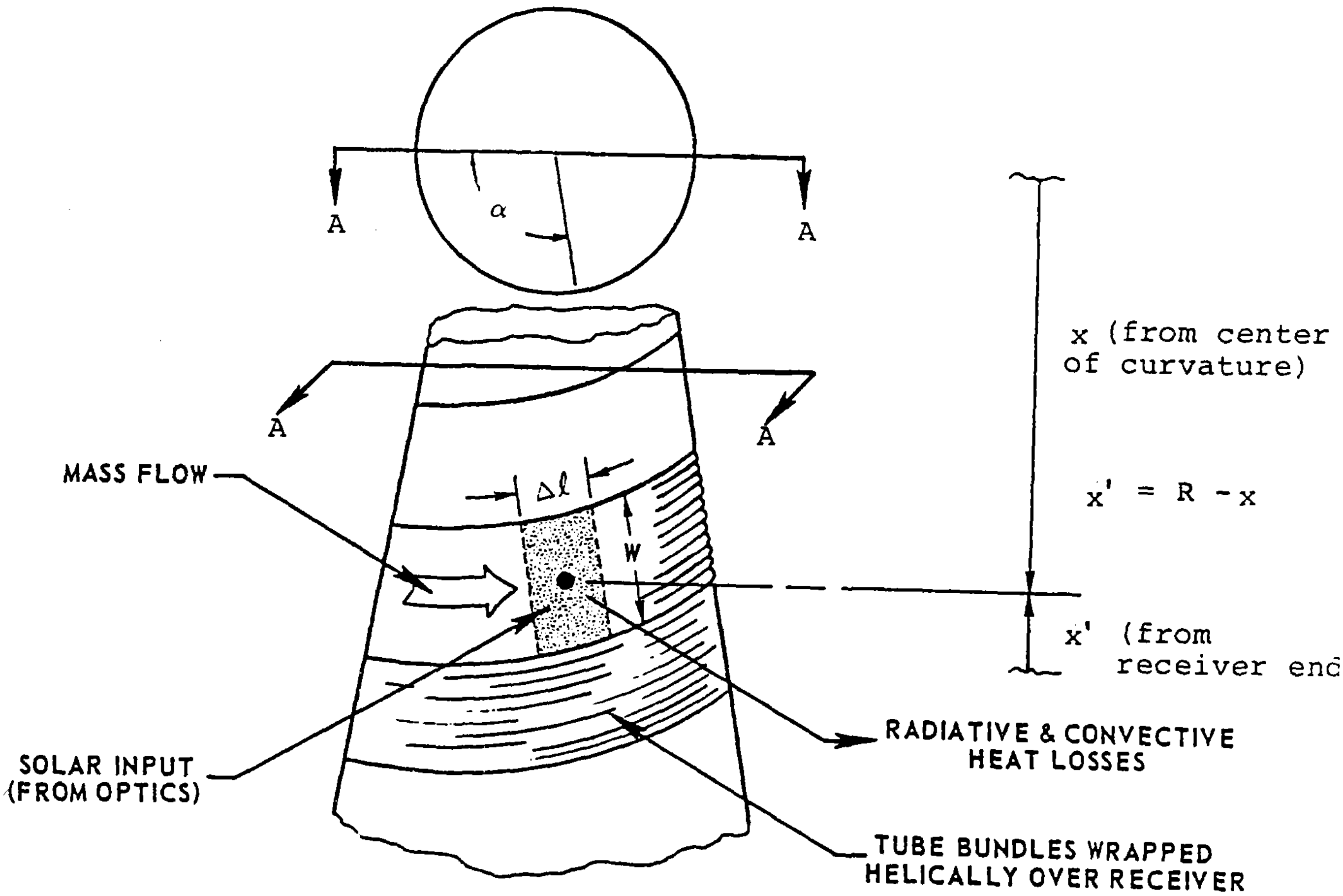

1. ENERGY BALANCE ON RADIAL HEAT FLOW YIELDS OUTSIDE SURFACE TEMPERATURE.
2. ENERGY BALANCE ON FLUID YIELDS ENTHALPY RISE.
3. MOMENTUM BALANCE ON FLUID YIELDS PRESSURE DROP.
4. VARIABLES INCLUDE INTERNAL AND EXTERNAL HEAT TRANSFER, RECEIVER SIZE, TUBE GEOMETRY, OPTICAL PROPERTIES, INLET FLUID CONDITIONS, AND SOLAR/WEATHER PARAMETERS.
5. SOLUTION CONSERVES ENERGY WITHIN 1% AND CORRELATES WITH PREVIOUS AXISYMMETRIC SOLUTION WITHIN 1%.

E-SYSTEMS Energy Technology Center

011877-127

Figure F-1. Receiver Thermal Analysis Methodology from an inlet at the large end of the receiver cone to an outlet at the small end of the receiver. The receiver conical shape is matched to the optics of the FMDF collector, as discussed in Appendix D, where its overall size and shape are discussed in some detail.

The basic analytical methodology utilized was a fluid-following, finite-difference approach, wherein energy and momentum balances were sequentially conducted for each incremental finite area ($W\Delta\ell$ in Figure F-1) to define local surface temperature, fluid enthalpy, and pressure. Local position was specified by the axial coordinate (x') and the circumferential coordinate (α), as shown in Figure F-1. For a continuous helical wrapping of the tube bundle over the receiver cone, α is a simple function of x' from basic geometry:

$$\alpha = \sqrt{\left[\frac{2\pi}{(W/R)}\right]^2 - \mathrm{ctn}^2\frac{\Delta\Psi}{2}} - \sqrt{\left[\frac{2\pi\left(1 - \frac{x'}{R}\right)}{(W/R)}\right]^2 - \mathrm{ctn}^2\frac{\Delta\Psi}{2}}$$

$$- \mathrm{ctn}\,\frac{\Delta\Psi}{2}\tan^{-1}\sqrt{\left[\frac{2\pi\tan\frac{\Delta\Psi}{2}}{(W/R)}\right]^2 - 1}$$

$$+ \mathrm{ctn}\,\frac{\Delta\Psi}{2}\tan^{-1}\sqrt{\left[\frac{2\pi\tan\frac{\Delta\Psi}{2}\left(1 - \frac{x'}{R}\right)}{(W/R)}\right]^2 - 1}, \quad \text{(F-1)}$$

wherein R is mirror radius of curvature and $\Delta\Psi$ is included cone angle. Thus, only one independent position variable (x') must be incremented during the fluid-following numerical integration. The finite area element can likewise be described in terms of x' alone from basic geometry:

$$\Delta A = W\Delta \ell = \pi \tan \frac{\Delta\Psi}{2}\left[x_1'^2 - 2Rx_1' - x_2'^2 + 2Rx_2'\right], \qquad \text{(F-2)}$$

wherein x_1' and x_2' are the position coordinates at the beginning and end respectively of the area element.

In nondimensional form:

$$\frac{\Delta A}{A_{aperture}} = \frac{4}{3}\tan\frac{\Delta\Psi}{2}\left[\left(\frac{x_1'}{R}\right)^2 - \frac{2x_1'}{R} - \left(\frac{x_2'}{R}\right)^2 + \frac{2x_2'}{R}\right], \qquad \text{(F-3)}$$

since $A_{aperture} = \frac{3}{4}\pi R^2$ for the nominal 60° rim angle concentrator.

Detailed individual tube thermal analyses will be discussed in Section F-2, but for modeling simplicity in the overall receiver thermal analysis currently under discussion, the multiple parallel flow paths were analytically treated as a single flow channel, as shown below.

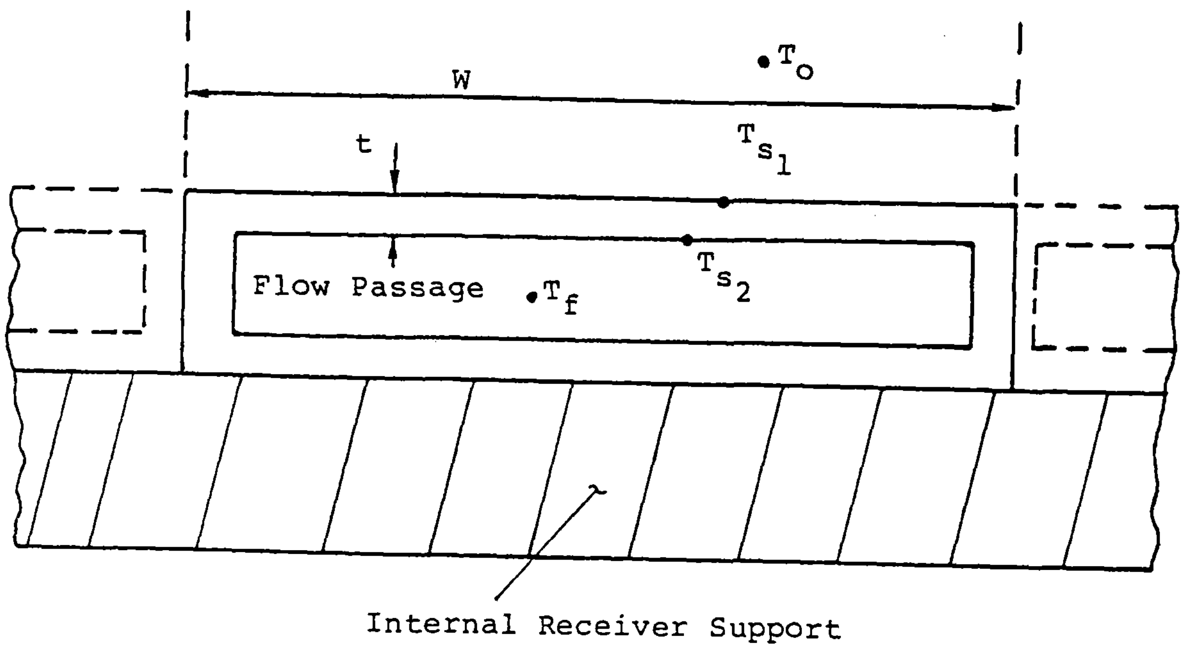

In the previous drawing, T_f is the bulk internal fluid temperature, T_{s_2} is the inside wall surface temperature, T_{s_1} is the outside wall surface temperature, and T_o is the ambient (sink) temperature. The net heat flux absorbed by the fluid is easily calculated:

$$\dot{q}_{net\ in} = C_{x',\alpha} I_{dn}\, \rho \alpha_s - \sigma\epsilon(T_{s_1}^{\ 4} - T_o^{\ 4}) - h_{ext}\,(T_{s_1} - T_o), \qquad \text{(F-4)}$$

wherein $C_{x',\alpha}$ is the local concentration level calculated from the optical solution of Appendix D,

I_{dn} is the direct normal insolation,

ρ is the mirror solar reflectance,

α_s is the receiver surface solar absorptance,

σ is the Stefan - Boltzmann radiation constant (0.1714 x 10^{-8} Btu/hr ft^2 °R^4),

ϵ is the receiver infrared emittance,

h_{ext} is the external convection coefficient.

In the above equation, T_{s_1} must be determined in order to calculate $\dot{q}_{net\ in}$. T_{s_1} is subject to the following radial energy flux equation:

$$\dot{q}_{net\ in} = \left(\frac{1}{\frac{1}{h_i} + \frac{t}{k}}\right)\left(T_{s_1} - T_f\right), \qquad \text{(F-5)}$$

wherein h_i is the internal convection coefficient, and

k is the wall conductivity.

Equating the two relations (F-4) and (F-5) for $\dot{q}_{net\ in}$ given above, and algebraically rearranging terms yields:

$$T_{s_1}^{\ 4} + \left\{ \frac{\left[h_{ext} + \frac{1}{\left(\frac{1}{h_i} + \frac{t}{k} \right)} \right]}{\sigma \epsilon} \right\} T_{s_1}$$

$$- \left\{ \frac{c_{x',\alpha} \; I_{dn} \; \rho\alpha_s}{\sigma \epsilon} + \frac{h_{ext} \; T_o}{\sigma \epsilon} + T_o^{\ 4} + \left[\frac{T_f}{\sigma \epsilon \left(\frac{1}{h_i} + \frac{t}{k} \right)} \right] \right\}$$

$$= 0. \qquad \text{(F-6)}$$

The above simple quartic algebraic equation is easily solved by formula to yield T_{s_1} explicitly. Knowing T_{s_1}, $\dot{q}_{net\ in}$ may be calculated from either equation (F-4) or (F-5) above.

One additional energy balance on the fluid provides the enthalpy change over the finite area element:

$$\dot{q}_{net\ in} \; \Delta A = \dot{m} \; \Delta h_f, \qquad \text{(F-7)}$$

wherein $\dot{m}$ is the mass flow rate through the element (i.e., through the tube bundle), and

Δh_f is the fluid enthalpy change from inlet to outlet of the element.

Equation (F-7) can be more conveniently expressed as follows:

$$\Delta h_f = \dot{q}_{net\ in} \left(\frac{\Delta A / A_{aperture}}{\dot{m} / A_{aperture}} \right). \qquad \text{(F-8)}.$$

One additional set of data is required to complete the thermal solution:

$$T_f = f(h_f, P), \qquad \text{(F-9)}$$

wherein the function f is the equation of state of the fluid, i.e., steam table data for water or property data for oil.

These data were coded and included in the computer program.

Now a momentum balance over the element can be applied to define incremental pressure drop. However, for expediency in this first phase of the study, pressure was assumed constant for the thermal analyses. However, overall pressure drop studies were conducted separately, as discussed in a later section of this appendix.

Using the above equations a computer program was developed which performed the thermal analysis in the manner depicted below:

- Previous T_f known from last increment
- Previous x_1' and x_2' known from last increment
- Increment x' to define new x_1' and x_2'
- Calculate new α from equation (F-1)
- Calculate new ΔA from equation (F-3)
- Calculate new $C_{x',\alpha}$ from optics solution (Appendix D)
- Calculate new surface temperature T_{s_1} from equation (F-6)
- Calculate new $\dot{q}_{net\ in}$ from equation (F-4)
- Calculate new enthalpy change Δh_f from equation (F-8)
- Calculate new fluid temperature T_f from equation (F-9)
- Store or print x_1', x_2', $C_{x',\alpha}$, T_{s_1}, h_f, P, T_f
- Go to next increment.

Typical results of this overall receiver thermal analysis are presented in subsections F-3 through F-5 below. Although the computer program has the capability of varying material properties and heat transfer coefficients as a function of position, temperature, etc., for the major cases run for this first phase of the study, nominal constant values were assumed for simplicity.

F-2 COMPUTER CODE

This section was deleted during final editing, and pages F-10 through F-15 are intentionally left out. The computer code is discussed in the previous section.

F-3 WATER/STEAM RESULTS

The overall receiver thermal analysis computer program has been used to establish the receiver fluid (liquid and/or vapor) temperature, outside surface temperature, fluid enthalpy, net heat losses or net gains, and collection efficiency.

Results of this computer program will be presented for a particular receiver design to demonstrate the power of the program. The receiver cone angle ($\Delta\psi$) is 1 degree. The outside shell or skin is 0.030 inches thick with a thermal conductivity (k) of 11.0 Btu/hr ft°F. The width of the helically coiled fluid channel (W) is 0.5 feet. The convection coefficients are assumed constants with the outside (h_o) of 4.0 Btu/hrft^2°F, or approximately a 10 mile per hour wind over the receiver, and the inside (h_i) of 1000 Btu/hrft^2°F. The fluid is water with a constant pressure of 750 psi and an initial temperature to the receiver of 100°F. The concentrator has a solar reflectance (ρ) of 0.88. The receiver will be coated with a "black" coating with a solar absorptance (α) of 0.9 and an infrared emissivity (ε) of 0.9.

The results are based on a square foot of concentrator aperture area and dimensionless ratios to make the results applicable to any size concentrator with the conditions stated above. For the nominal 200 foot aperture diameter concentrator with a 120° angle of a sphere, the approximate total aperture area is 31,416 ft^2 and the radius of the sphere (R) is 115.47 ft. The receiver length is approximately 50% of the radius (R).

The solar incidence angle (θ_i) and the direct normal insolation (I_{dn}) on the concentrator are variable during the day. At solar noon θ_i is 0° with an I_{dn} of 300 Btu/hrft^2, and at early morning and late afternoon θ_i is 60° with an I_{dn} of 250 Btu/hrft^2.

The fluid flow rate is a variable to compensate for the varying θ_i and I_{dn} to assure the same receiver outlet temperature and enthalpy over the day from early morning to late afternoon. For the 200 foot nominal system, the water flow rate at solar noon is approximately 5,148 pounds per hour and approximately 33% of this flow rate is required at early morning and late afternoon. The desired receiver outlet temperature is 800°F with an outlet enthalpy of 1400 Btu per pound steam at 750 psi pressure.

Figure F-2 shows the receiver fluid and outside surface temperatures for solar noon (θ_i = 0°). Portion A of the fluid temperature curve depicts the water being heated from 100°F to 511°F, while portion B shows the constant 511°F saturated boiling (two phase flow) and the last portion C indicates the liquid has been vaporized and heat is being added to the vapor (superheat region). The outside surface temperature does track the fluid temperature fairly well.

Figure F-3 shows the receiver fluid temperatures for θ_i equal to 0°, 30° and 60°. The assumed flow rates varied

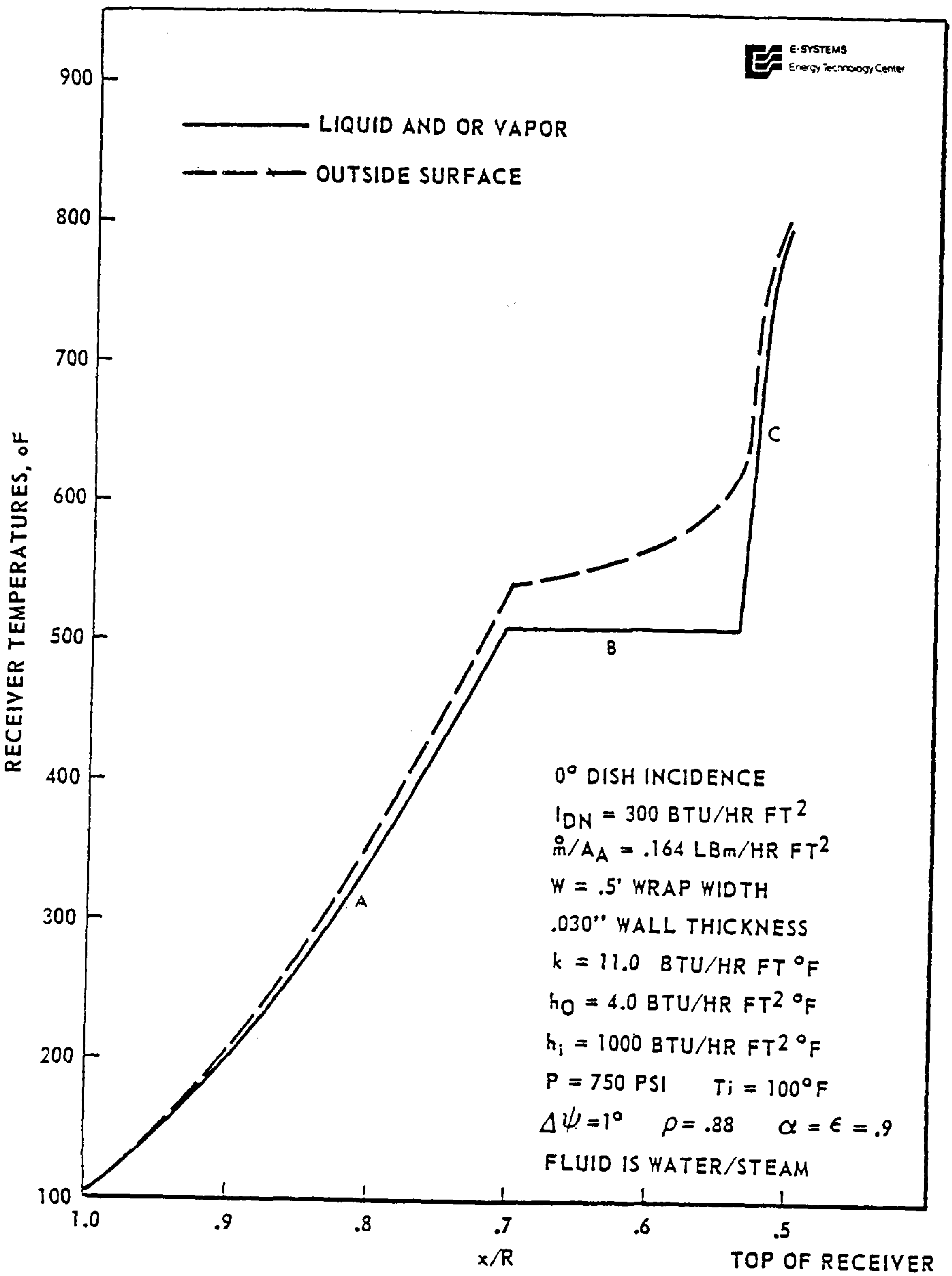

011877-49

Figure F-2. Receiver Fluid and Surface Temperatures for 0° Concentrator Incidence Angle Versus Position on Receiver

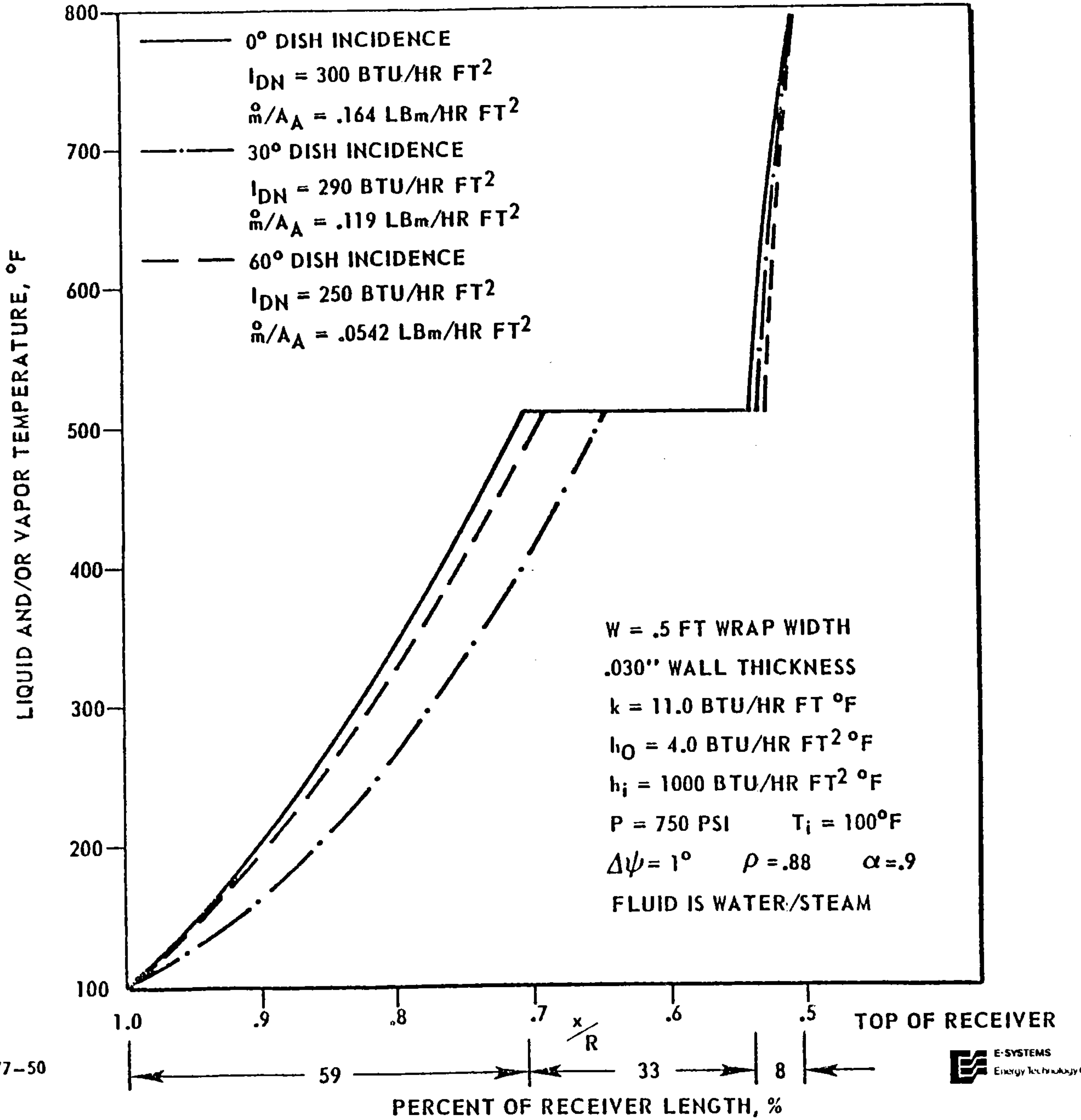

011877-50

E-SYSTEMS
Energy Technology Center

Figure F-3. Receiver Fluid Temperatures for 0°, 30°, and 60° Dish Incidence Versus Position on Receiver from 1,699 to 5,148 pounds per hour (200 foot nominal system) to produce essentially the same outlet conditions.

Figure F-4 shows the receiver enthalpy for θ_i equal to 0°, 30° and 60°. The outlet enthalpy for all three angles were essentially 1400 Btu per pound steam.

Figure F-5 shows the receiver fluid and outside surface temperatures for θ_i equal to 60° in the superheat portion of the receiver. The solar concentration, C_x, varies substantially around the receiver for θ_i equal 60°. C_x is zero on one side and maximum on the other side which affects the helical coil temperatures as shown in this figure. A θ_i of 30° will see a similar effect but not as dramatic since C_x does not vary as as much around the receiver as for θ_i of 60°. A θ_i of 0° has a uniform C_x around the receiver which means the temperatures will be uniform around the receiver as shown in Figure

Figure F-6 shows the net heat loss per unit concentrator aperture area for θ_i equal to 0°, 30°, and 60°. The heat loss presented in this figure for θ_i equal to 0° and h_o equal to 4.0 Btu/hrft^2°F is approximately 17.5 Btu/hrft^2. The heat loss for θ_i equal to 0° but with h_o equal to 1.0 Btu/hrft^2°F is 10.2 Btu/hrft^2 which is considered to be about the minimum possible with this receiver design.

Figure F-7 shows the receiver efficiency, which is defined as $\dot{m}\Delta h_f/I_{dn}A_A$, for θ_i equal to 0°, 30°, and 60°. This efficiency varies over the daytime for a clear day from

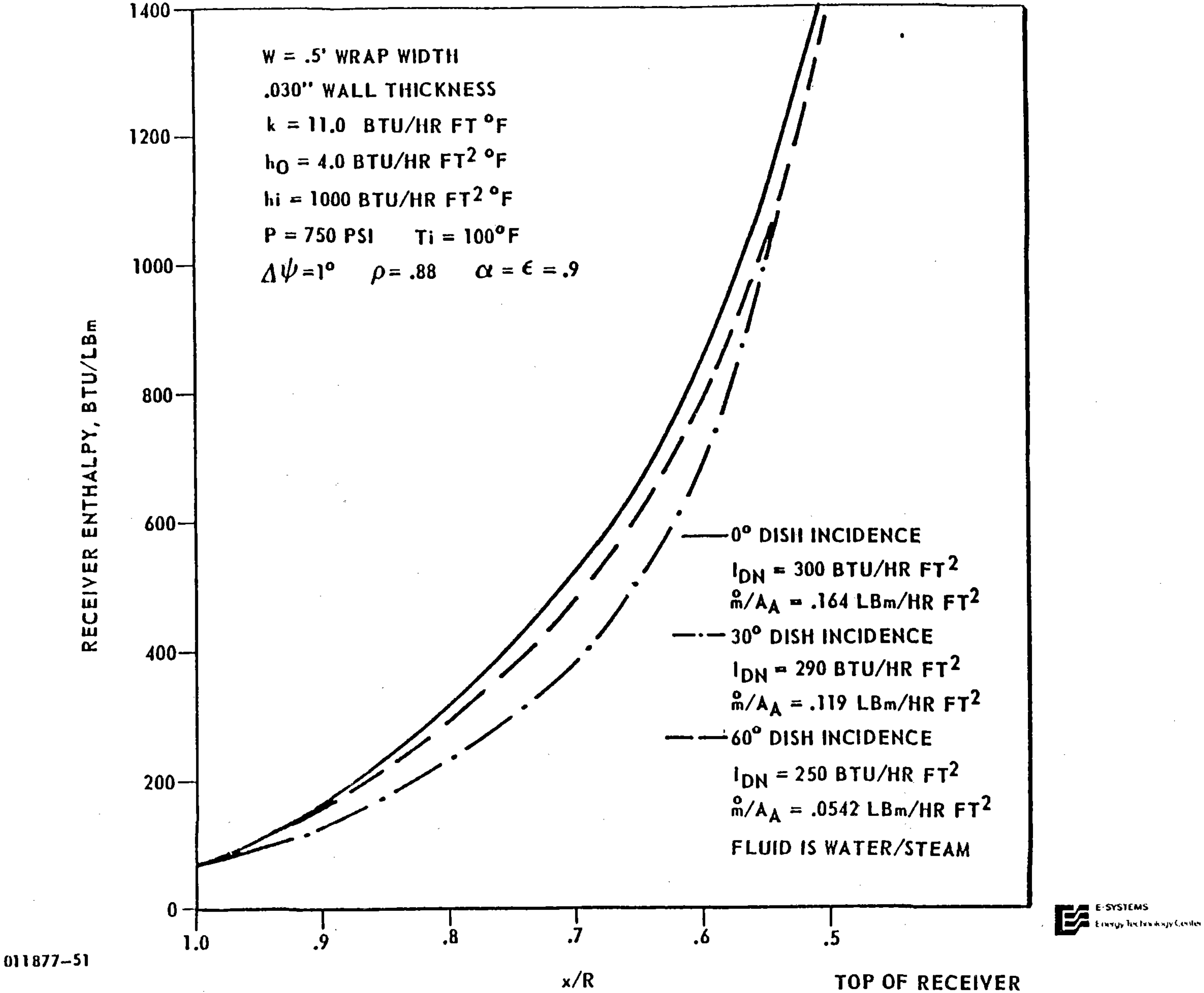

Figure F-4. Receiver Enthalpy for 0°, 30°, and 60° Concentrator Incidence Angle Versus Position on Receiver

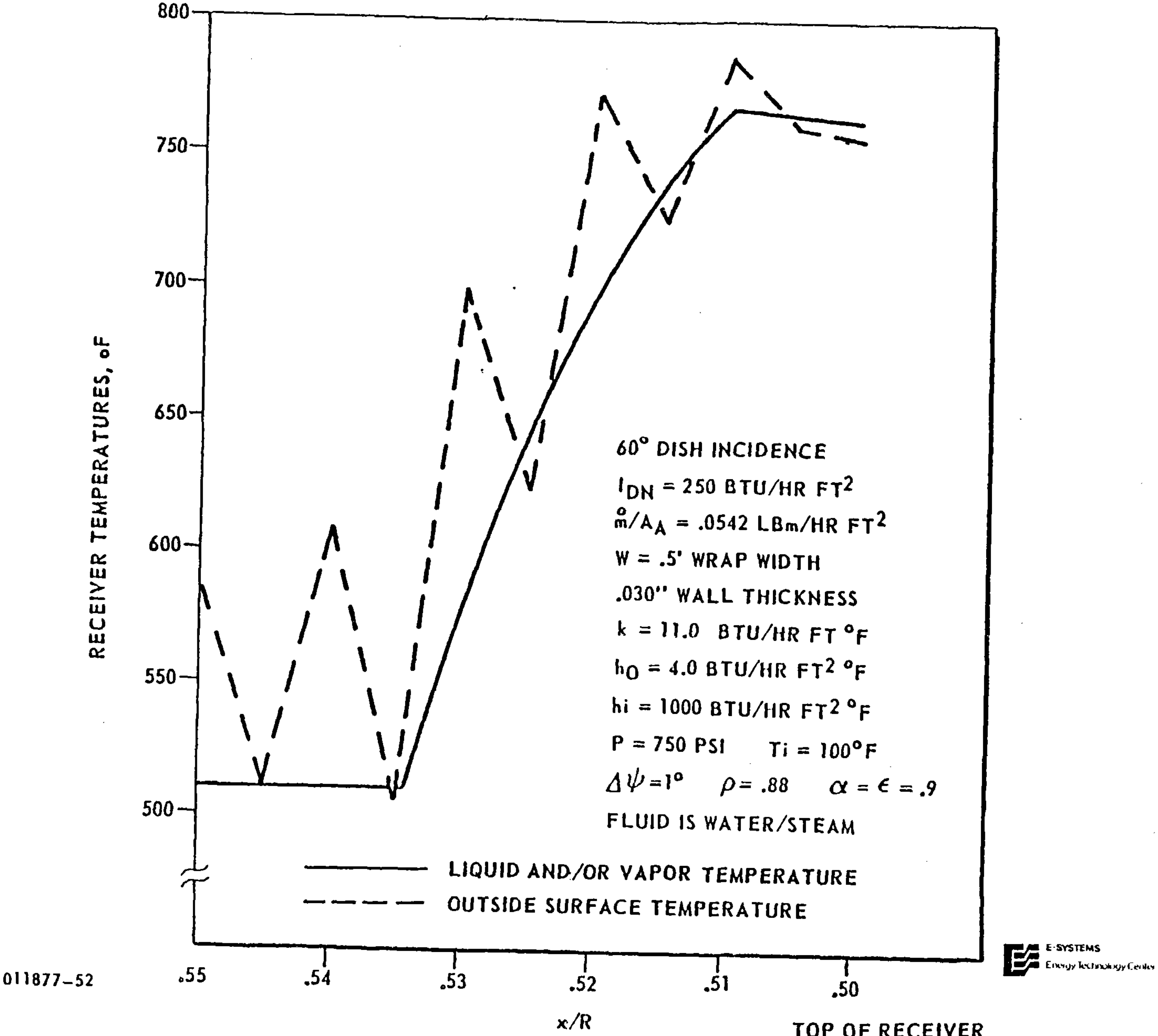

Figure F-5. Receiver Fluid and Surface Temperatures for 60° Concentrator Incidence Angle Versus Position (x/R=.55 to .5) on Receiver

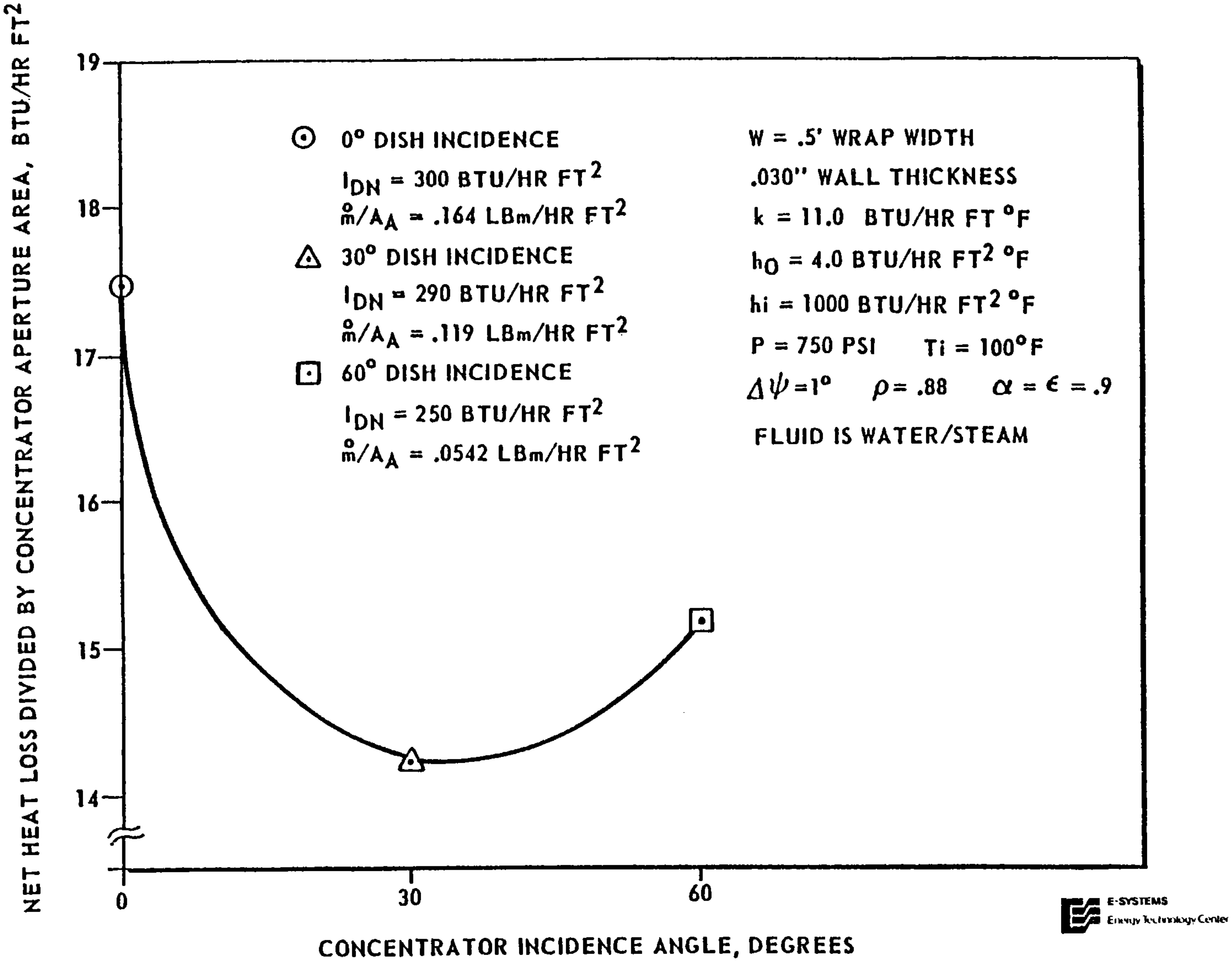

011877-53

Figure F-6. Receiver Net Heat Loss Per Unit Aperture Area Versus Concentrator Incidence Angle

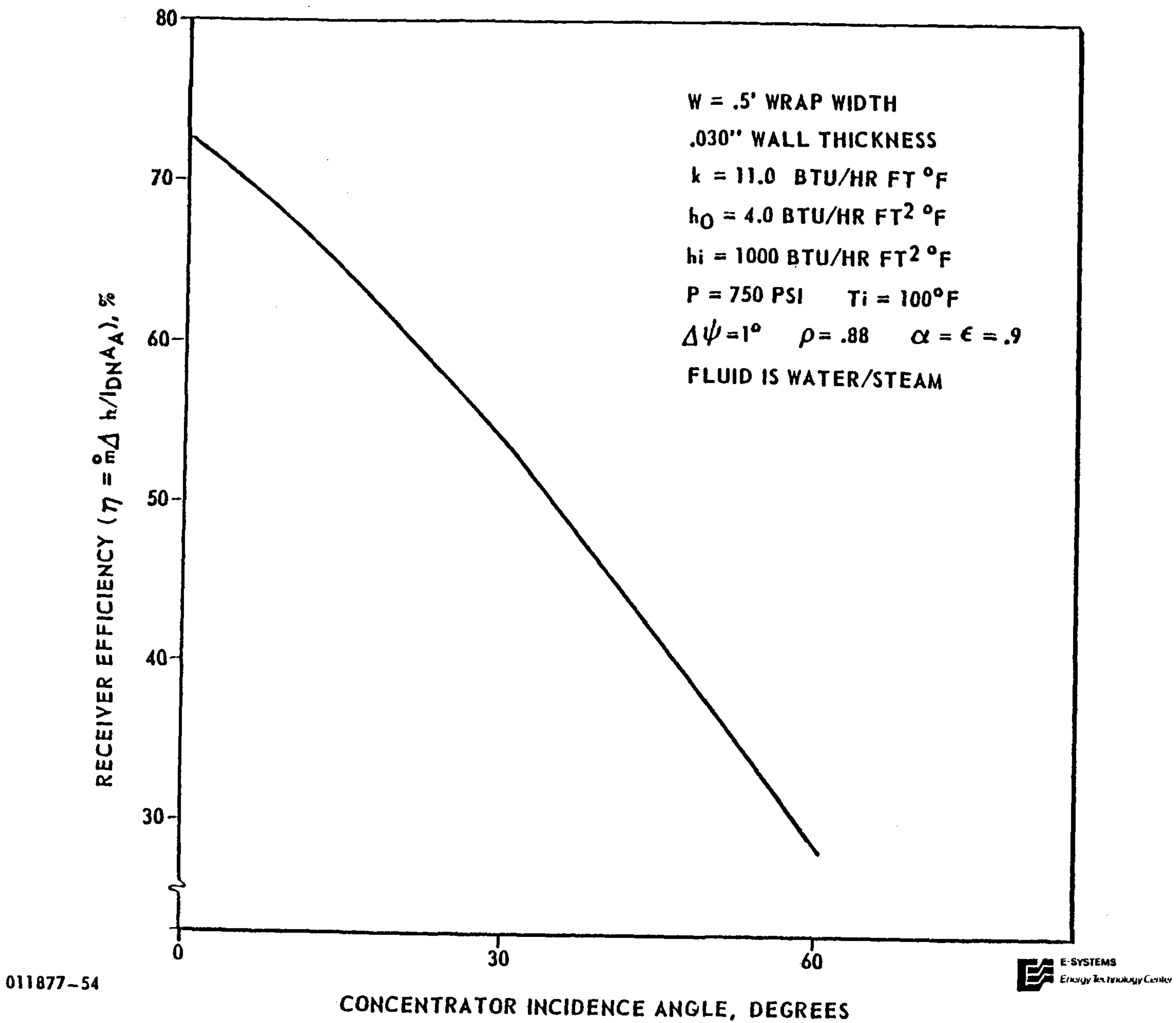

Figure F-7. Receiver Efficiency Versus Concentrator Incidence Angle

28% to 73%. The maximum receiver efficiency calculated for this receiver design is 75%, which is possible with a still air ambient (h_o = 1.0 Btu/hrft^2°F).

The versatility of the overall receiver thermal analysis computer program is shown in the results presented in Figure F-8 Instead of each concentrator/receiver producing steam which is the design presented in Figures F-2 through F-7 , the system would consist of three concentrators (100 foot aperture) in series. The first receiver would be used to heat the water, the second to boil the water, and the third to boil the water and superheat the steam. This system is not currently being considered since it has a slightly lower receiver efficiency than a system with a single concentrator/receiver. These results are presented to show the computer program versatility as well as to indicate the possibility of an alternate piping network layout for Crosbyton system.

F-4 OIL RESULTS

A concentrator/receiver system using an oil (Caloria HT 43) as the working fluid was analyzed and results of the overall receiver thermal analysis computer program will be presented for this system.

The oil system would operate with a high flow rate which results in a small temperature rise through the receiver. The oil temperature then is essentially uniform through the receiver and the receiver outside surface temperature is only slightly higher than the oil temperature.

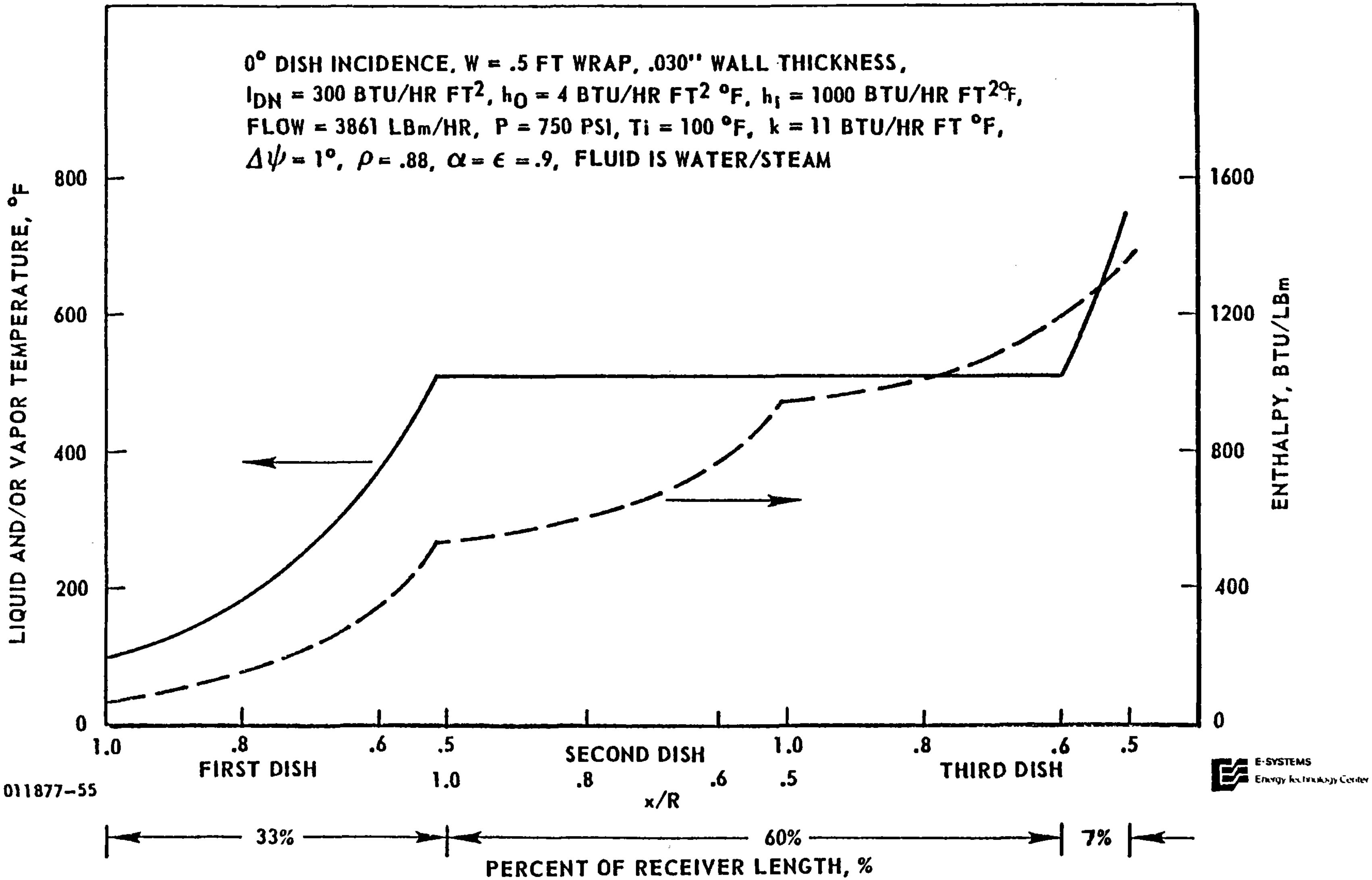

Figure F-8. Receiver Fluid Temperature and Enthalpy Versus Position on Receivers (Three 100 ft. Aperture Concentrators in Series)

The net heat loss per unit concentrator aperture area for θ_i equal to 0° on the oil system is shown in Figure F-9. The desired operating temperature for the oil system is approximately 500° to 600°F, which results in net heat losses of 26 to 36 Btu/hrft^2, respectively. These losses are high compared to the water/steam system net loss of 17.5 Btu/hrft^2 for θ_i equal to 0° as shown in Figure F-6. The end result is that an oil system would operate at a slightly lower overall efficiency compared to a water/steam system.

F-5 900 PSI NOMINAL PROTOTYPE STEAM SYSTEM RESULTS

The 200 foot aperture diameter nominal concentrator using 900 psi steam was analyzed. The current receiver configuration was included in this analysis. Figure F-10 shows the receiver fluid and outside surface temperatures for solar noon or 0° concentrator incidence angle. Figure F-11 shows the receiver enthalpy versus receiver position for 0° incidence angle. The desired outlet conditions were 900 psi and 950°F steam with an enthalpy of 1481.0 Btu/lbm. The net heat loss per unit concentrator aperture area was 20.2 Btu/hrft^2 for a h_i of 4.0 Btu/hrft^2°F.

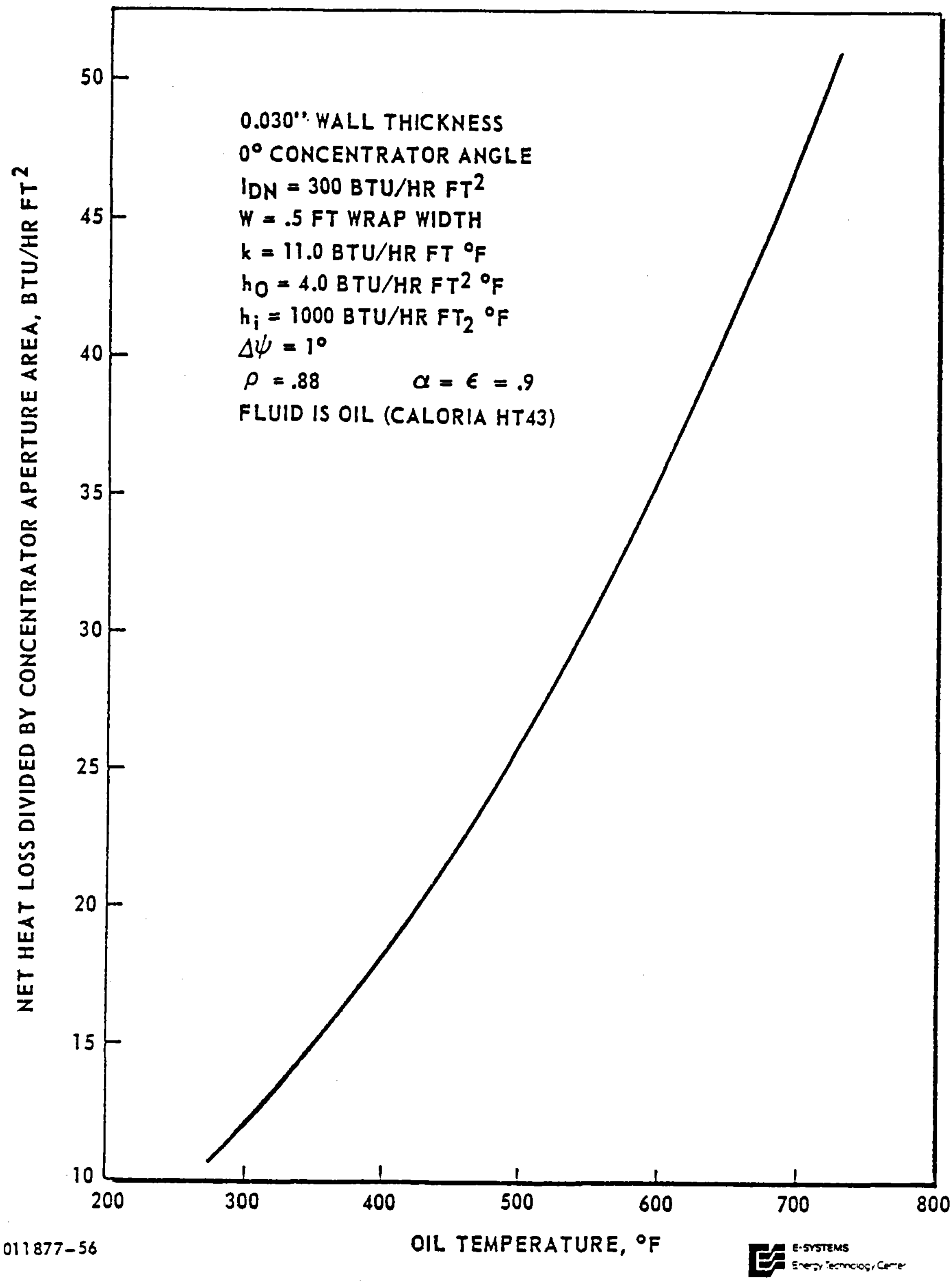

Figure F-9. Receiver Net Heat Loss Per Unit Aperture Area Versus Oil Temperature

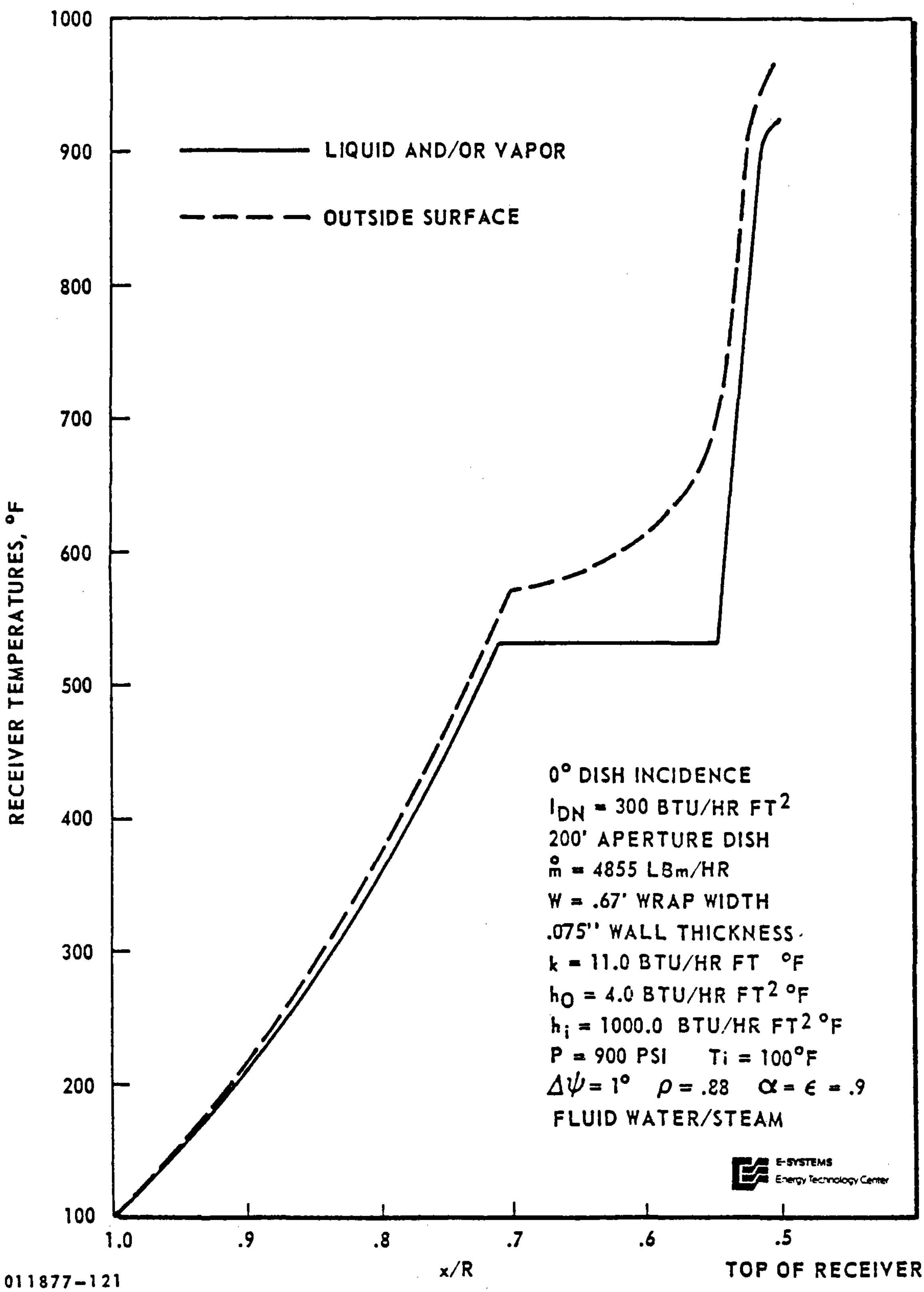

Figure F-10. Receiver Fluid and Surface Temperatures for 0° Concentrator Incidence Angle Versus Position on Receiver for 900 PSI Steam

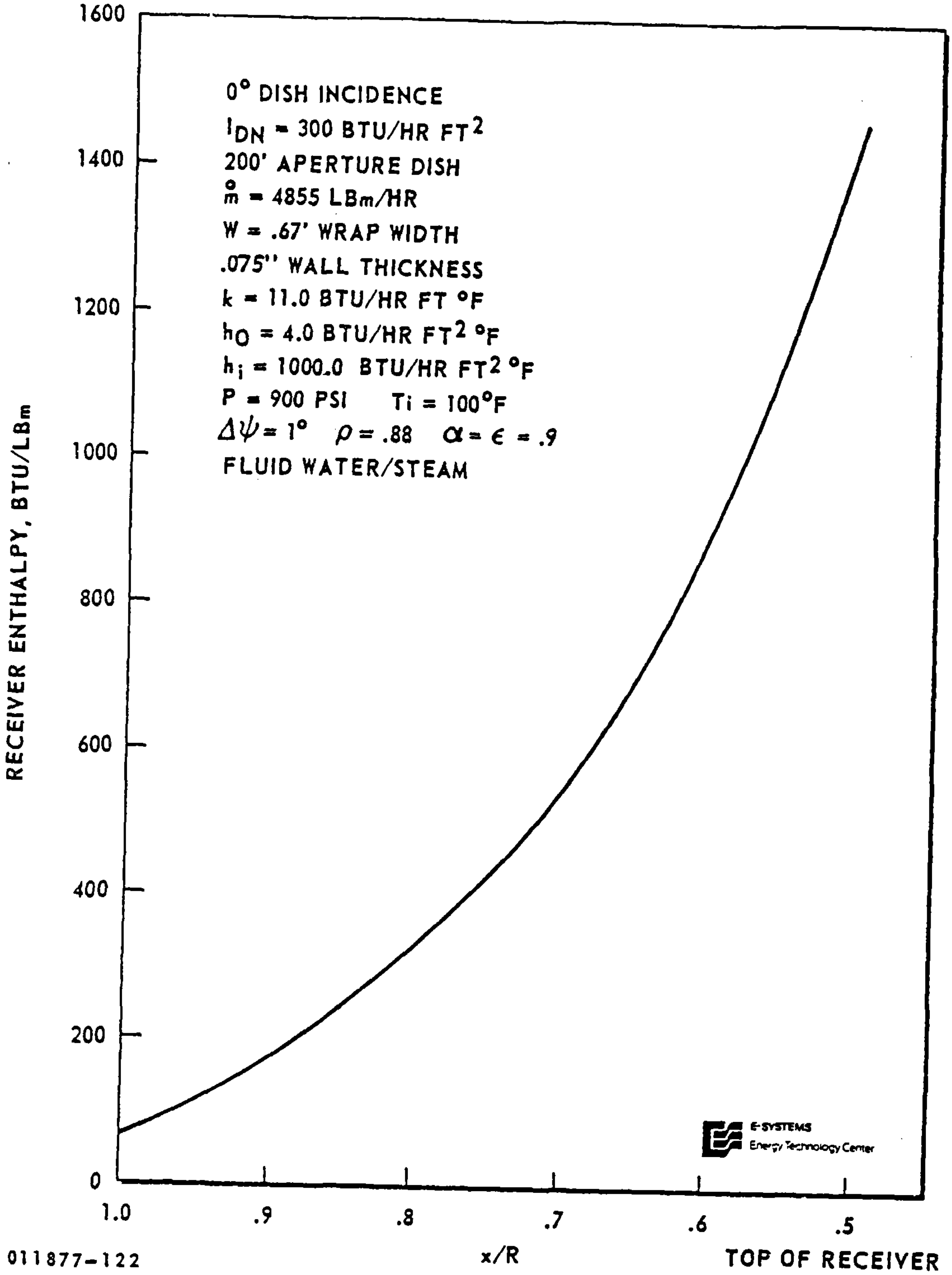

Figure F-11. Receiver Enthalpy for 0° Concentrator Incidence Angle Versus Position on Receiver for 900 PSI Steam

F-6 DETAILED RECEIVER INTERNAL HEAT TRANSFER AND PRESSURE DROP STUDIES

The detailed receiver heat transfer and pressure drop studies consist of establishing tube temperature distribution, pressure drops and internal convection heat transfer coefficients. The receiver working fluid considered at this time are water/steam , and oil (Caloria HT-43^{R}).

The current receiver design consists of a conical support tube with small tubes helically coiled over the whole receiver support tube. The first part of this Appendix presents an overall receiver thermal analysis which assumes the receiver will be covered by a flat surface channel or tube (W being the width of the channel or wrap) helically coiled over the support tube. That analysis also assumes the channel has a material thickness (t) of 0.030 inches between the outside surface and the working fluid in the channel. That analysis could not take into account the fact that the channel is actually made of a number of small tubes in parallel to form the wrap width W. The analysis presented earlier is quite good for an overall look at the receiver but is not adequate to establish the maximum tube temperatures in the current design. This section is devoted to establishing the tube temperatures for a water/steam and an oil system.

Three sizes of tubes were analyzed -- 0.10 inch I.D. (0.16 inch O.D), 0.25 inch I.D., (0.40 inch O.D.), and 0.50 inch I.D. (.70 inch O.D.).

The wall thicknesses were chosen as compromises to minimize the tube temperature differentials (minimum with very thin wall), to maximize the survival time for a tube during a fluid flow failure (maximum with very thick wall), and to assure structural integrity. The structural integrity includes internal pressure, thermal stresses, creep, and fatigue. A structural analysis using the temperature distributions of the tube is presented in Appendix J.

Stainless steels and Inconels are the two materials being considered for the tubes. Fortunately, both materials have similar thermal properties as shown in the following table.

Material Properties	Stainless Steel AISI 301	Inconel 600
Density, lb_m/in^3	0.286	0.307
Specific Heat, $Btu/lb_m°F$		
@ 200°F	0.11	0.11
@ 800°F	0.13	0.125
@1600°F	0.16	0.15
Thermal Conductivity, Btu/hrft°F		
@ 200°F	10.0	8.9
@ 800°F	11.9	11.9
@1600°F	14.5	16.0

The MIL-HDBK-5B is the reference for these material properties. An average thermal property for the two materials is assumed for tube analysis at its respective temperatures.

The inside convection coefficient (h_i) is a variable with the fluid flow rate, the tube size, the number of tubes in parallel, the fluid state and the fluid properties. As discussed earlier, the fluid flow rate varies by approximately a factor of 3 from early morning to solar noon. The fluid state is also important as shown by a water/steam system. For a water/steam system, water is being heated in the first 59% of the receiver, water is boiling (two-phase flow) in the next 33% of the receiver, and steam is being superheated in the last 8% of the receiver. These three distinct regions all have different convection coefficients. An oil system is much simpler since the oil remains in a single phase throughout the receiver. In the steam system tube temperature profiles are determined for h_i ranging from 100 to 1000 Btu/hrft^2°F. The oil system uses h_i in the 500 to 800 Btu/hrft^2°F range for the tube temperature analysis.

Pressure drop calculation results are presented for the tubes for both the water/steam and the oil systems.

A nominal receiver configuration is drawn up from the various analyses on the receiver tubes. The receiver dimensions, and size and number of helically coiled small tubes are presented for a test model and a prototype receiver. The nominal receiver design is a best estimate at the present time and a final design will evolve with the follow on analysis portion of the current contract.

F-7 TUBE TEMPERATURE DISTRIBUTIONS

The receiver tube temperature distributions were established by using a general purpose thermal analyzer computer program.* This analyzer uses a lumped-parameter network (R-C) analogy representation of the physical problem. The numerical techniques in the analyzer solve for temperatures and/or heat fluxes for transient or steady state conditions. The analyzer

*Yakel, D.E., "Thermal Analyzer," Texas Instruments Technical Report TR-72-025 (U) June 1972.

computer program is operational on the E-Systems IBM-370 computer.

The receiver tube thermal model developed for the analyzer computer program is shown in Figure F-12. The model consists of the 107 nodes which are shown in the figure. Nodes 1 through 20 are the exterior surface nodes, nodes 21 through 80 are the interior nodes, nodes 81 through 100 are interior surface nodes, nodes 101 and 102 are the ambient nodes for the convection heat transfer from the tube exterior surface nodes, nodes 103 and 104 are the ambient nodes for the radiation heat transfer from the tube exterior surface nodes, and nodes 105 through 107 are the interior fluid nodes. The model shown in Figure F-12 has two-dimensional conduction with solar heat input to surface nodes 1 through 4. The external surface convection and radiation ambients can be either a heat source or a sink, but for the cases analyzed the ambients acted as sinks. The interior fluid temperature also acts as a heat sink. The model assumes the tube is adiabatic to the adjacent tubes, to the large support cone, and to itself in the third dimension.

Figure F-12 shows the solar heat input having an incidence angle of 70° on the receiver tube. This angle is representative of the caustic region ($x/_R = .53$) of the receiver. The caustic region is where a maximum solar concentration of approximately 650 occurs and it is this region where the tube will have the maximum temperature with the steam at approximately 750°F.

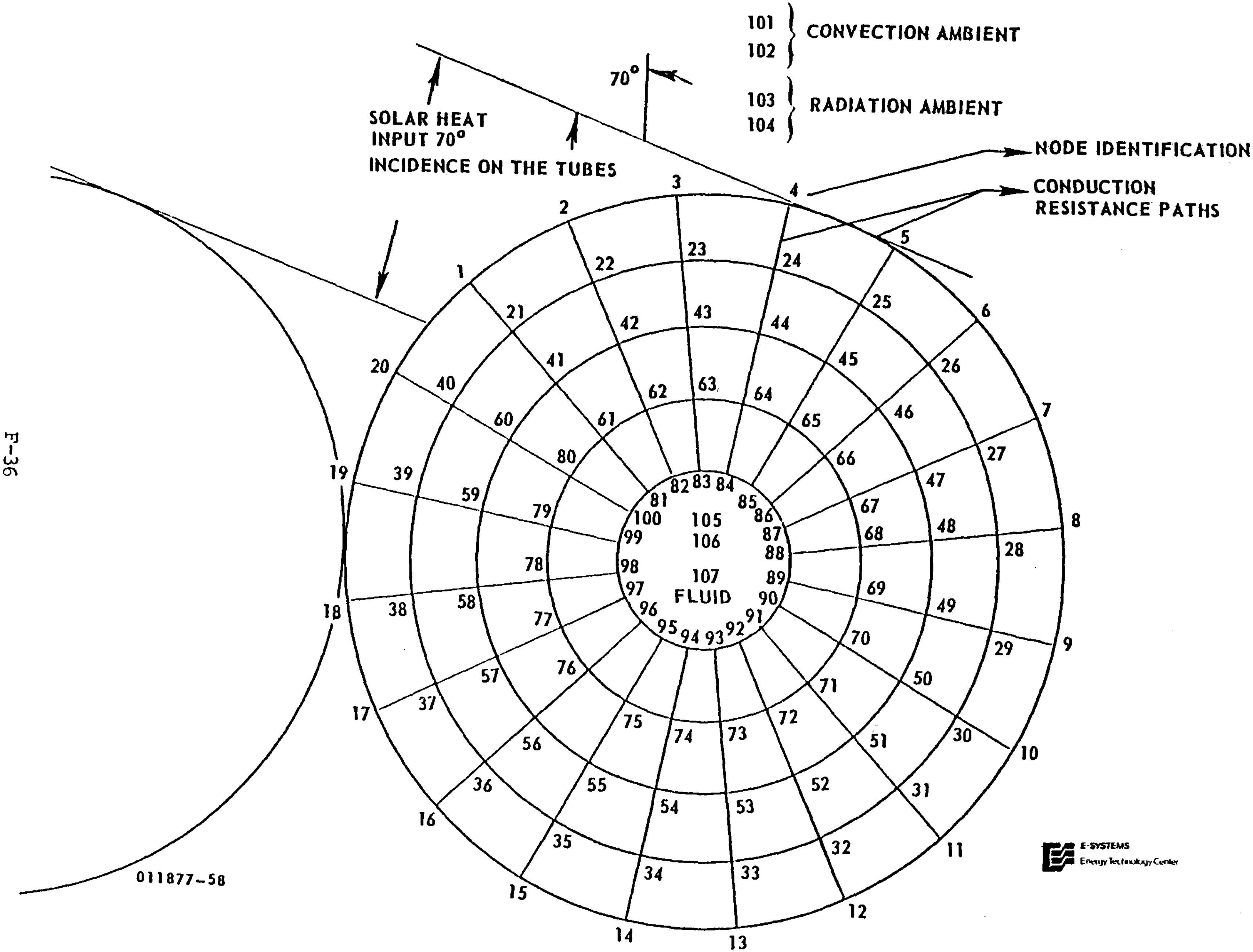

Figure F-12. Thermal Model of the Receiver Tubes

This tube model was developed to establish the highest practical tube temperatures. The tube was not heat sunk to either adjacent tubes or the receiver support tube. The caustic region of the receiver only was considered. The still air ambient (h_o = 1.0 Btu/hrft^2°F) was 100°F and the maximum fluid temperature associated with the caustic region was used. The maximum direct normal insolation (I_{dn}) of 300 Btu/hrft^2 was used with a solar reflectance (ρ) from the concentrator of 0.88. The solar absorptance (α) of the outside tube surface was 0.9 and the infrared emissivity (ε) from the outside tube surface was 0.9. These values for α and ε are possible with "black" coatings. A radiation shape factor of 1.0 was assumed from the outside tube surface to the ambient.

F-8 STEADY STATE TUBE TEMPERATURES FOR A STEAM SYSTEM

The maximum tube temperature distributions will be presented for a steam system with a tube material thermal conductivity which will represent stainless steel or Inconel. Three tube sizes were evaluated: 0.1 inch I.D. (0.16 inch O.D.); 0.25 inch I.D. (0.40 inch O.D.), and 0.5 inch I.D. (0.70 inch O.D.). Four different inside convection coefficients (h_i) will be presented for each tube size - 1000, 500, 250 and 100 Btu/hrft^2°F.

Figures F-13 through F-16 show the temperature distributions for a 0.10 inch I.D. (0.16 inch O.D.) tube with h_i of 1000, 500, 250, and 100 Btu/hrft^2°F, respectively. The

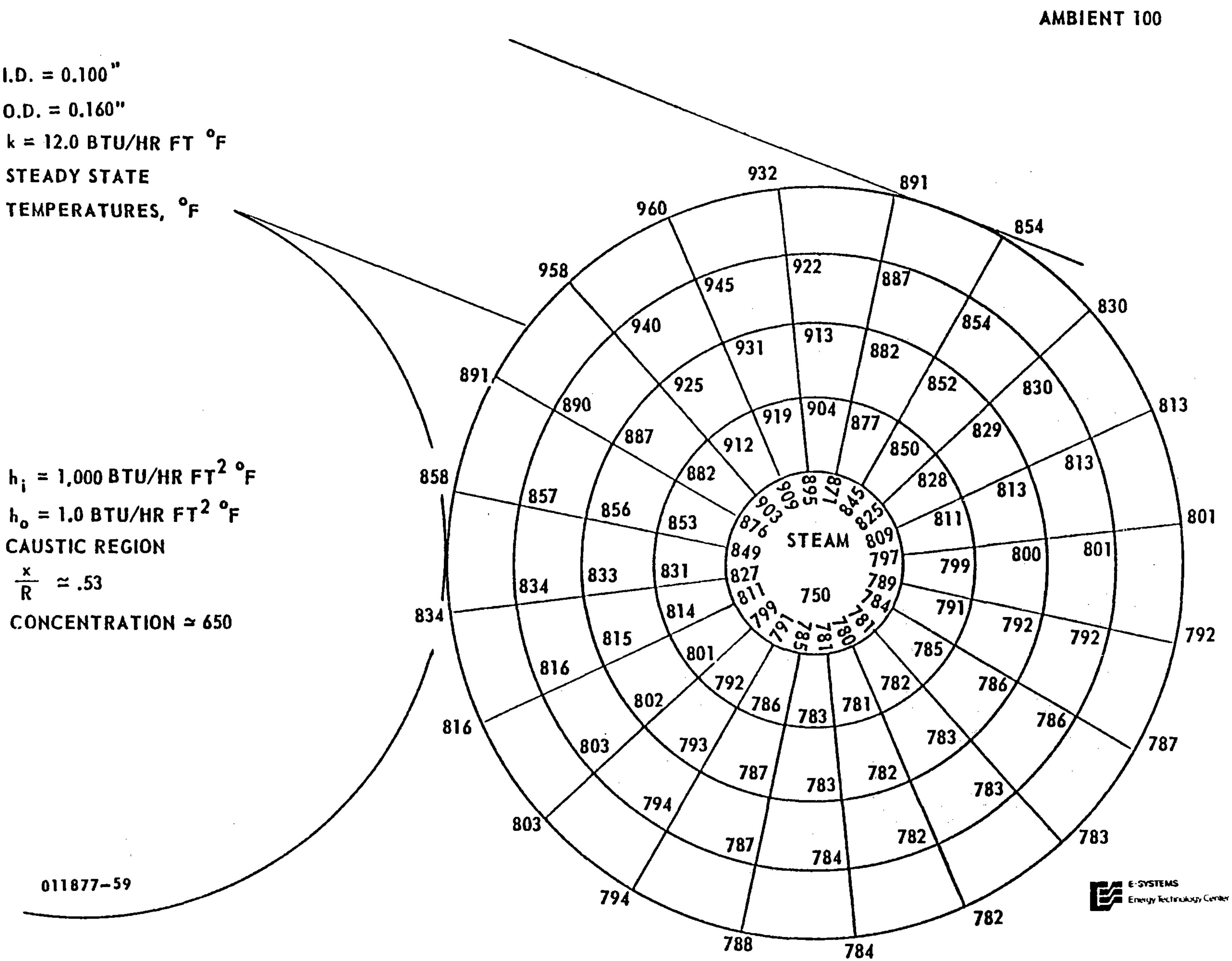

Figure F-13. Steady State Steam Tube Temperatures
(0.10 inch I.D. and h_i = 1000.0 BTU/hr. ft.^{2} °F)

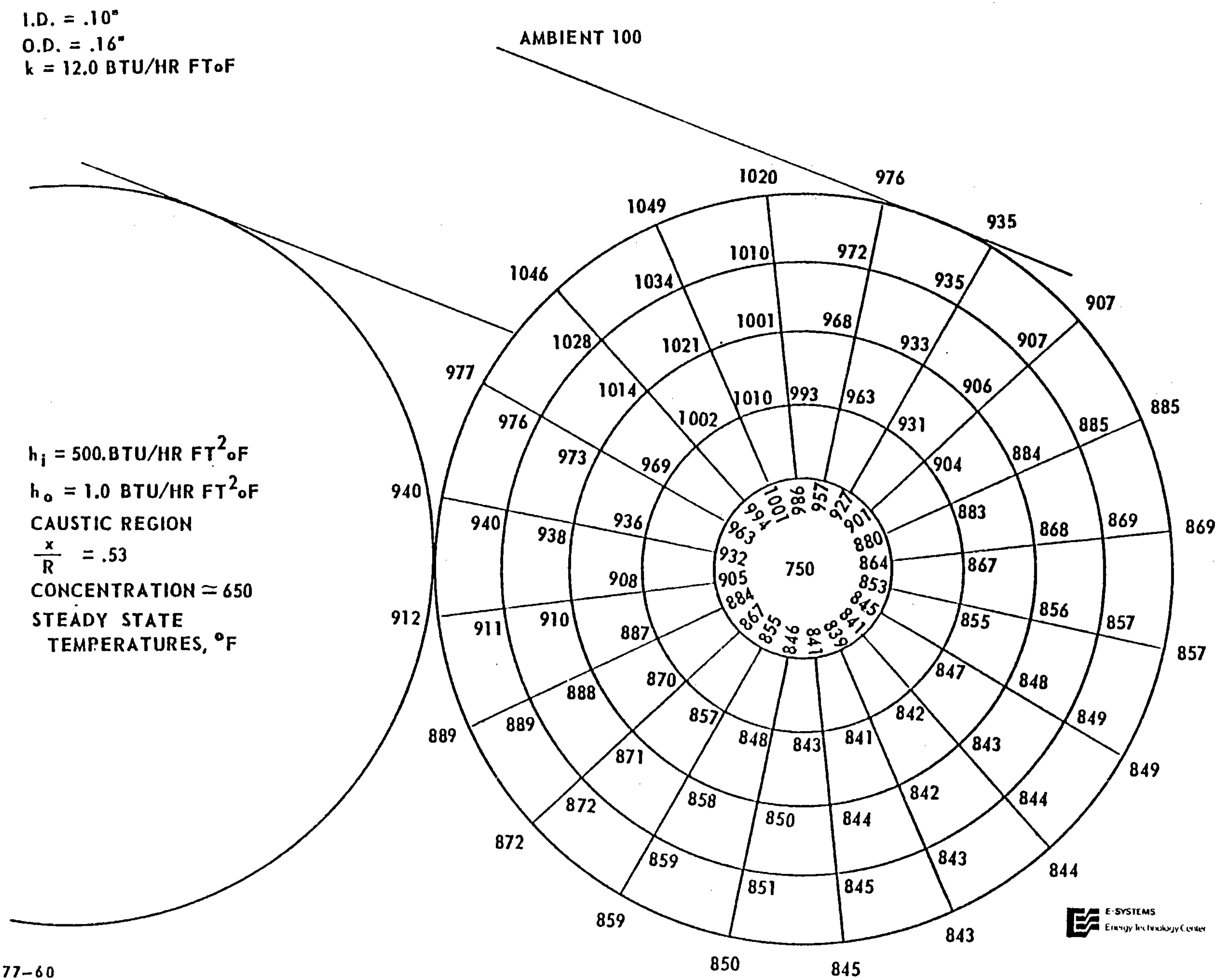

E-SYSTEMS
Energy Technology Center

011877-60

Figure F-14. Steady State Steam Tube Temperatures
(0.10 inch I.D. and h_i = 500.0 BTU/hr. ft.^{2} °F)

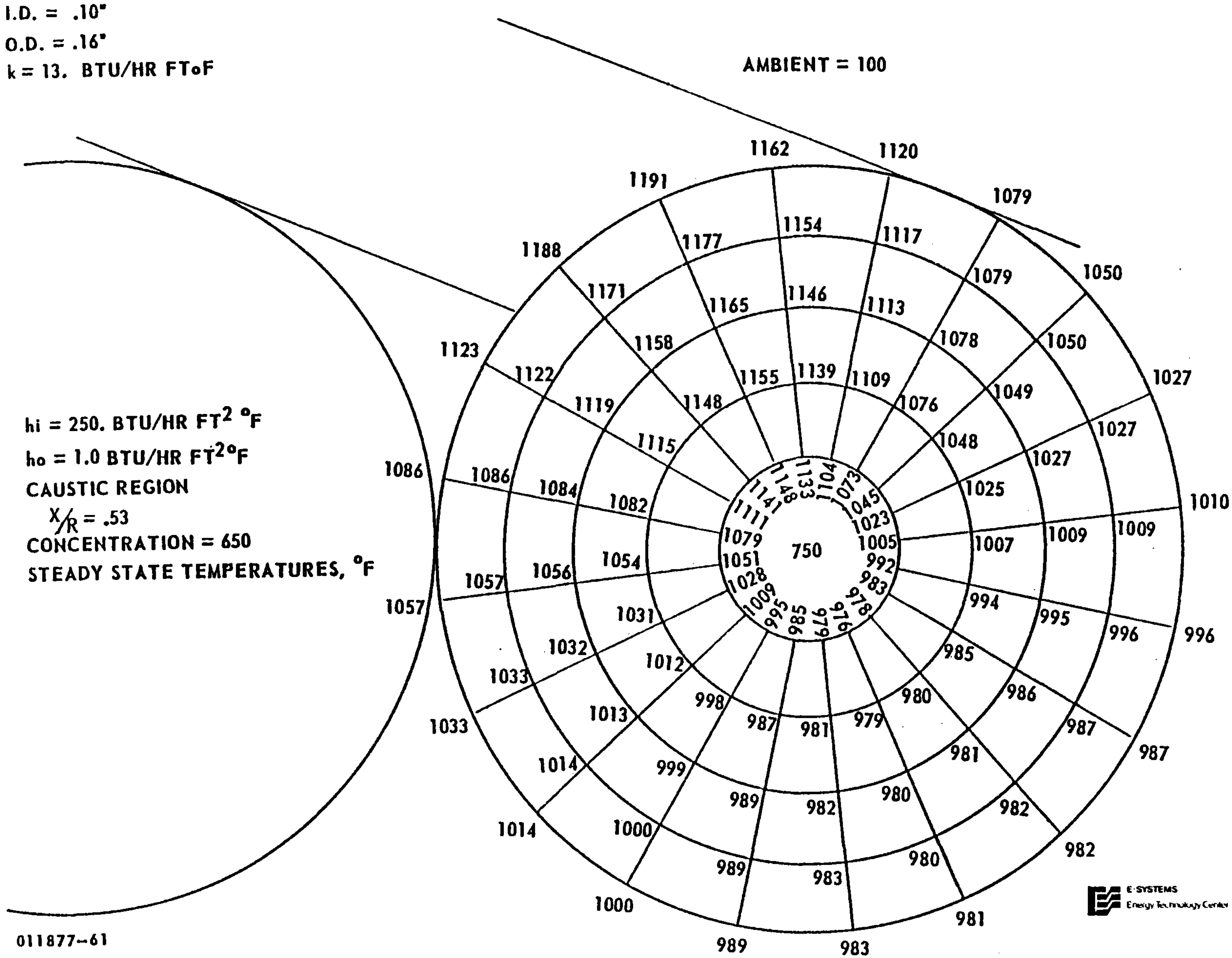

Figure F-15. Steady State Steam Tube Temperatures
(0.10 inch I.D. and h_i = 250.0 BTU/hr. ft.^{2} °F)

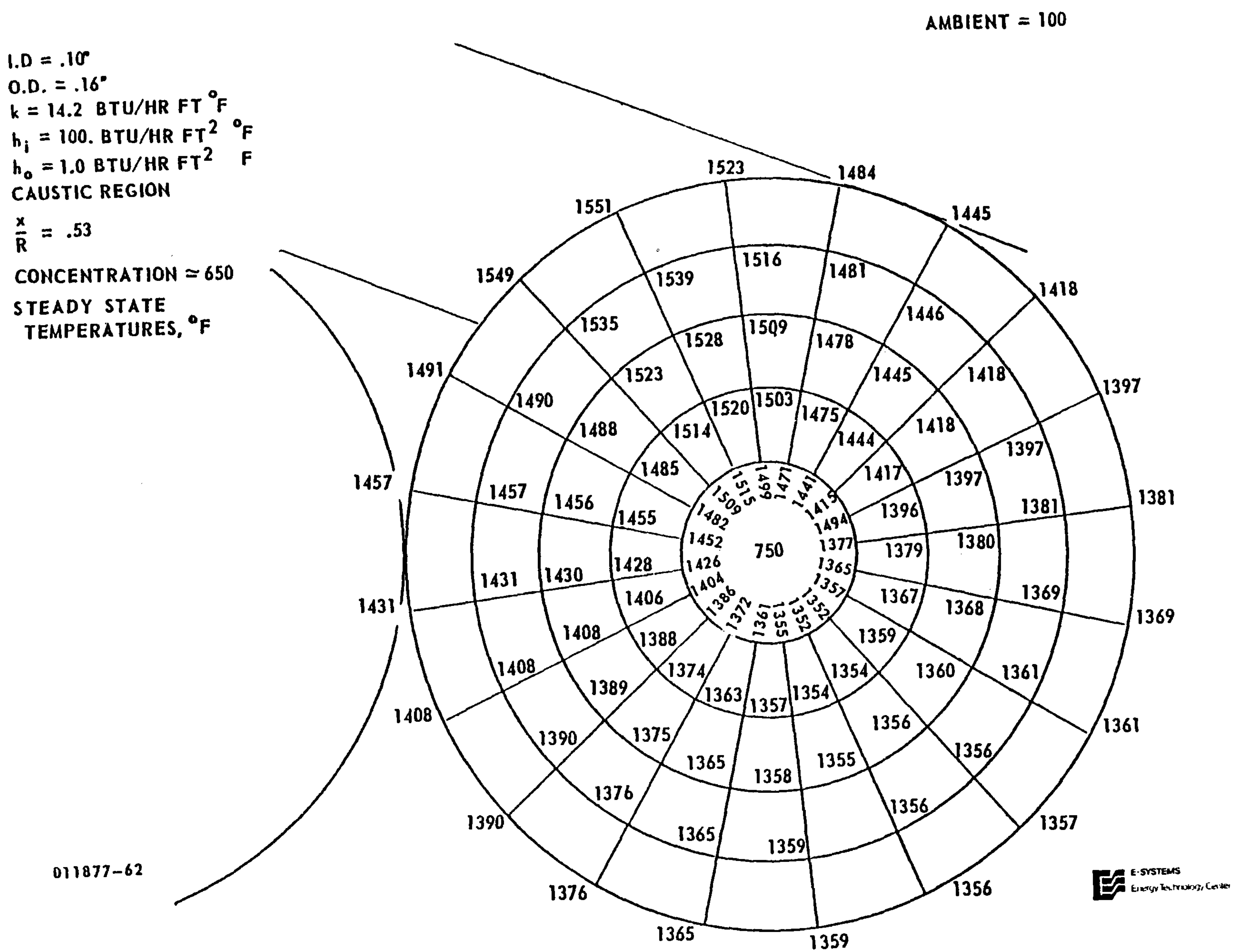

011877-62

Figure F-16. Steady State Steam Tube Temperatures (0.10 inch I.D. and h_i = 100.0 BTU/hr. ft.^{2} °F)

maximum tube temperatures varied from 960°F to 1,550°F for h_i varying from 1000 to 100 Btu/hrft^2°F, respectively.

Figures F-17 through F-20 show the temperature distributions for 0.25 inch I.D. (0.40 inch O.D.) tube with h_i of 1000, 500, 250 and 100 Btu/hrft^2°F, respectively The maximum tube temperatures varied from 1,099°F to 1,735°F for h_i varying from 1,000 to 100 Btu/hrft^2°F, respectively.

Figures F-21 through F-24 show the temperature distributions for 0.50 inch I.D. (0.70 inch O.D.) tube with h_i of 1,000, 500, 250, and 100 Btu/hrft^2°F, respectively. The maximum tube temperatures varied from 1,184°F to 1,919°F for h_i varying from 1,000 to 100 Btu/hrft^2°F respectively.

Figure F-25 is a summary of the maximum and minimum steady state tube temperatures in Figures F-13 through F-24 for the three tube sizes and the four inside convection coefficients assumed for the steam system.

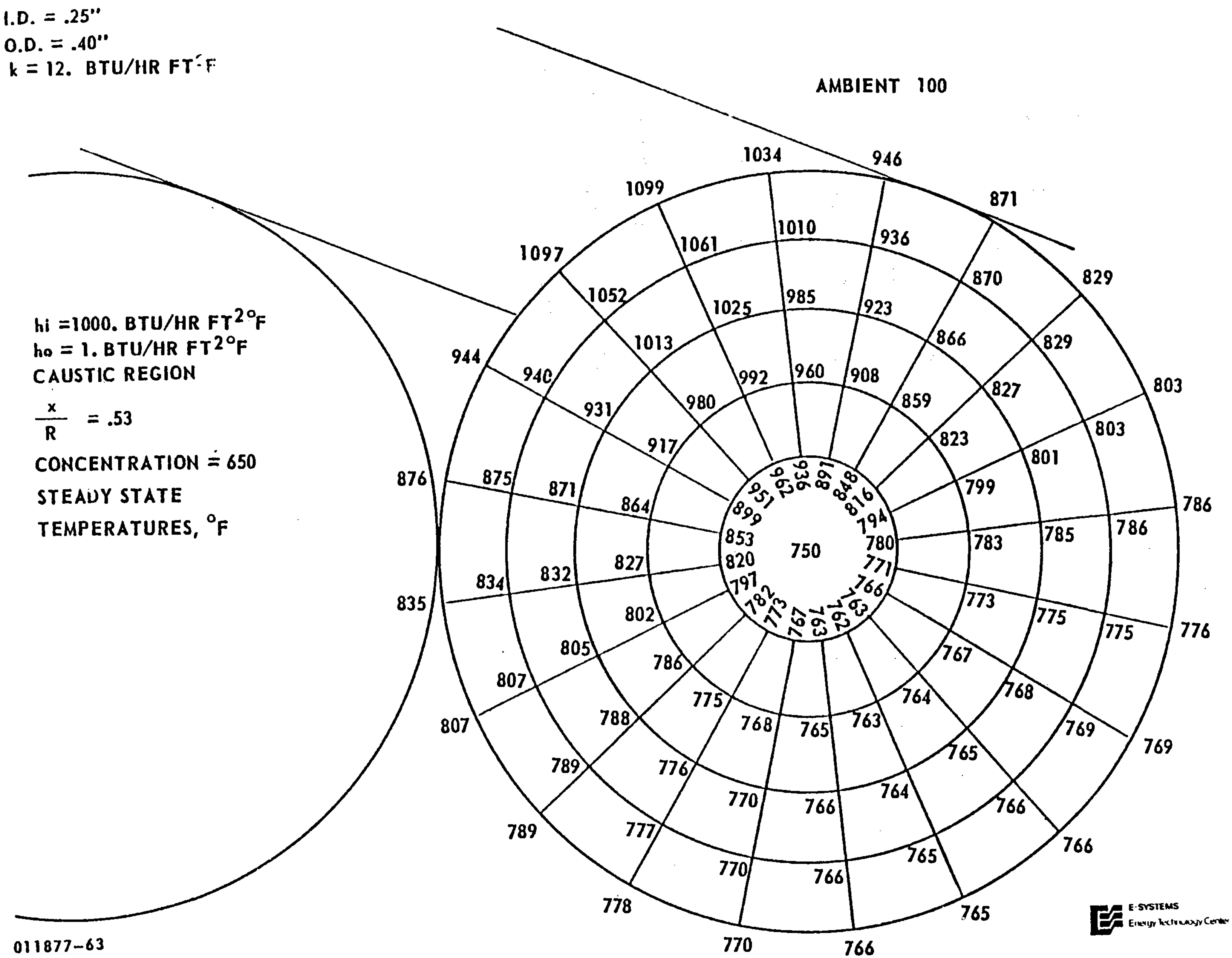

Figure F-17. Steady State Steam Tube Temperatures
(0.25 inch I.D. and h_i = 1000.0 BTU/hr. ft.^{2} °F)

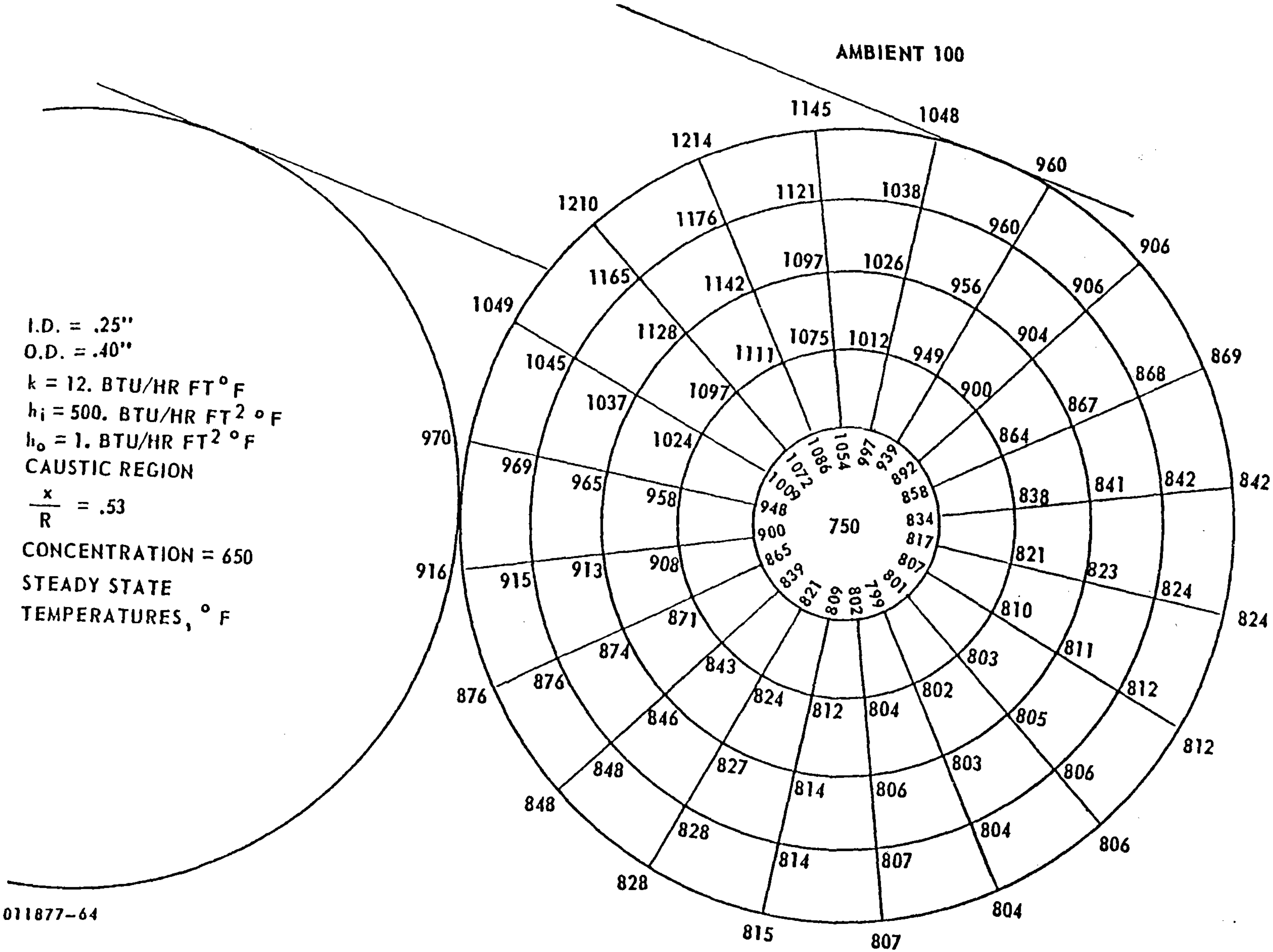

Figure F-18. Steady State Steam Tube Temperatures (0.25 inch I.D. and h_i = 500.0 BTU/hr. ft.^{2} °F)

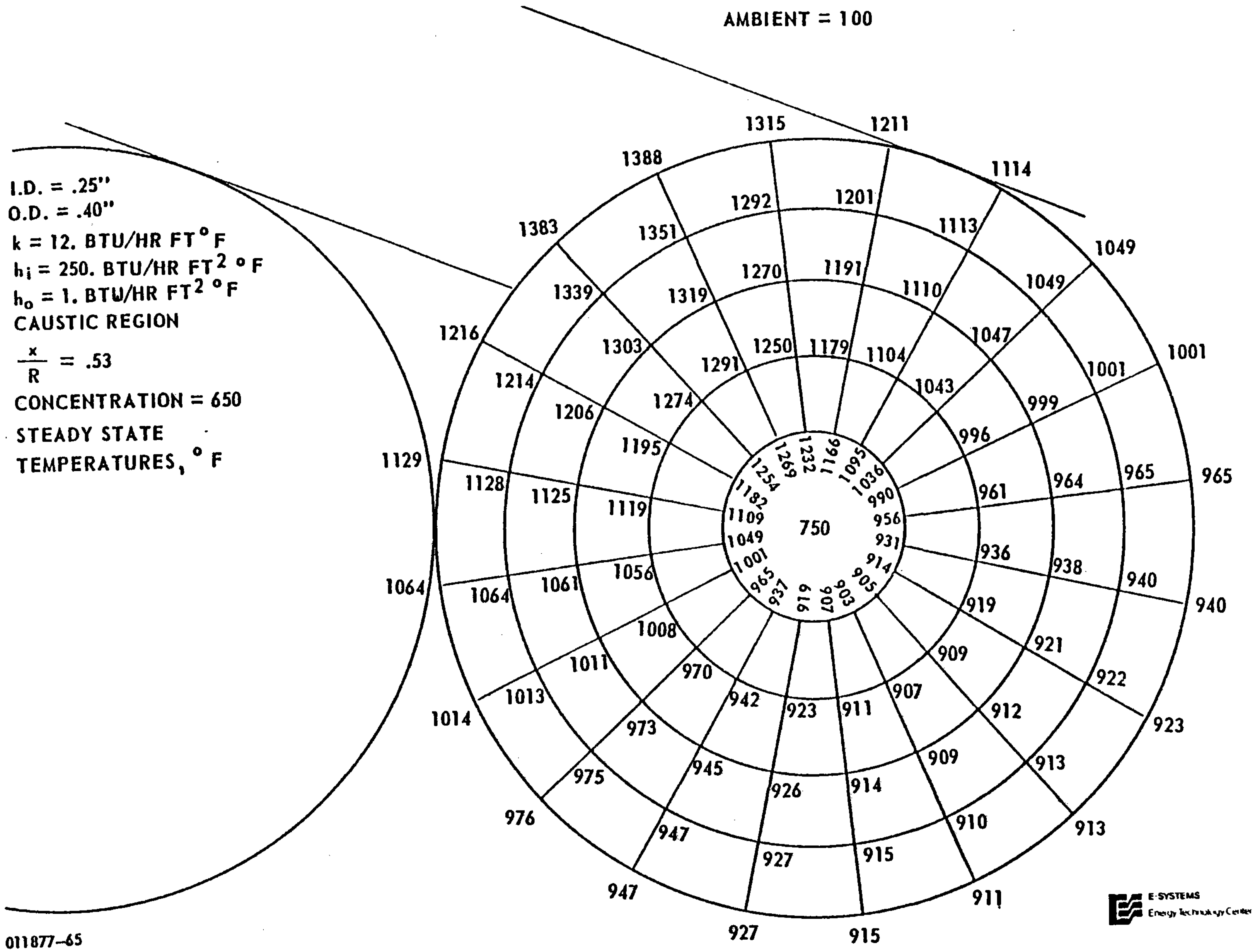

Figure F-19. Steady State Steam Tube Temperatures
(0.25 inch I.D. and h_i = 250.0 BTU/hr. ft.^{2} °F)

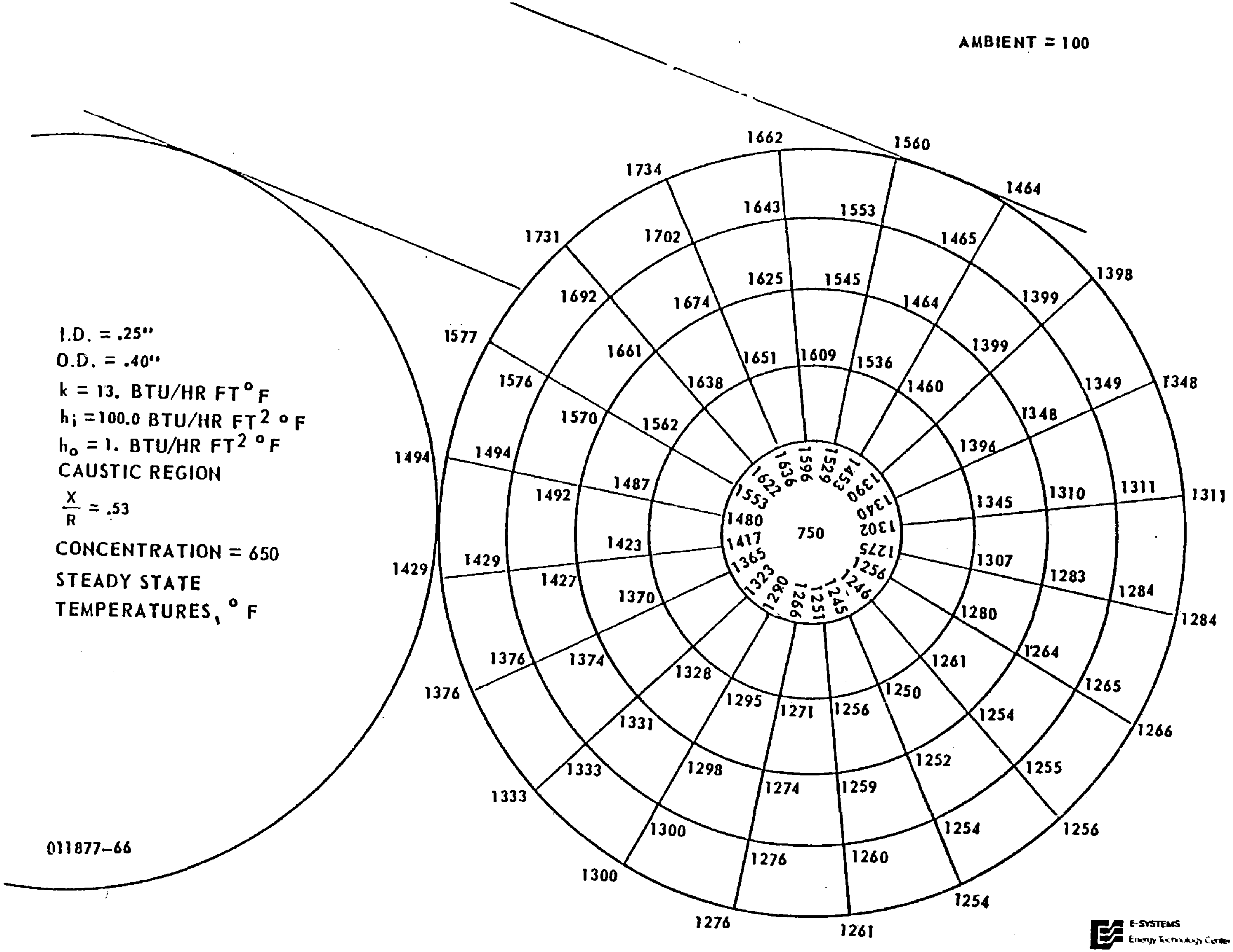

Figure F-20. Steady State Steam Tube Temperatures (0.25 inch I.D. and h_i = 100.0 BTU/hr. ft.^{2} °F)

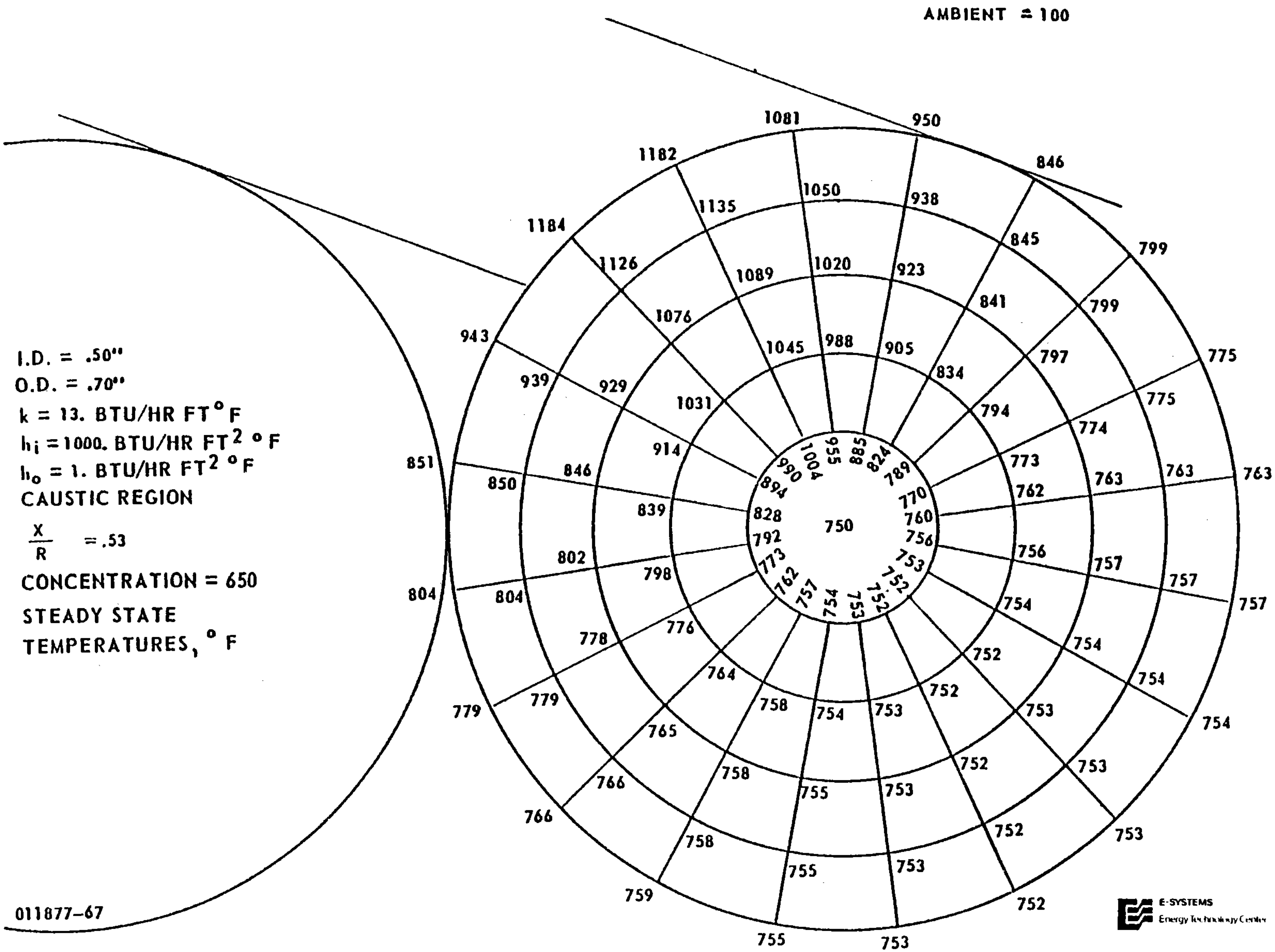

Figure F-21. Steady State Steam Tube Temperatures (0.50 inch I.D. and h_i = 1000.0 BTU/hr. ft.^{2} °F)

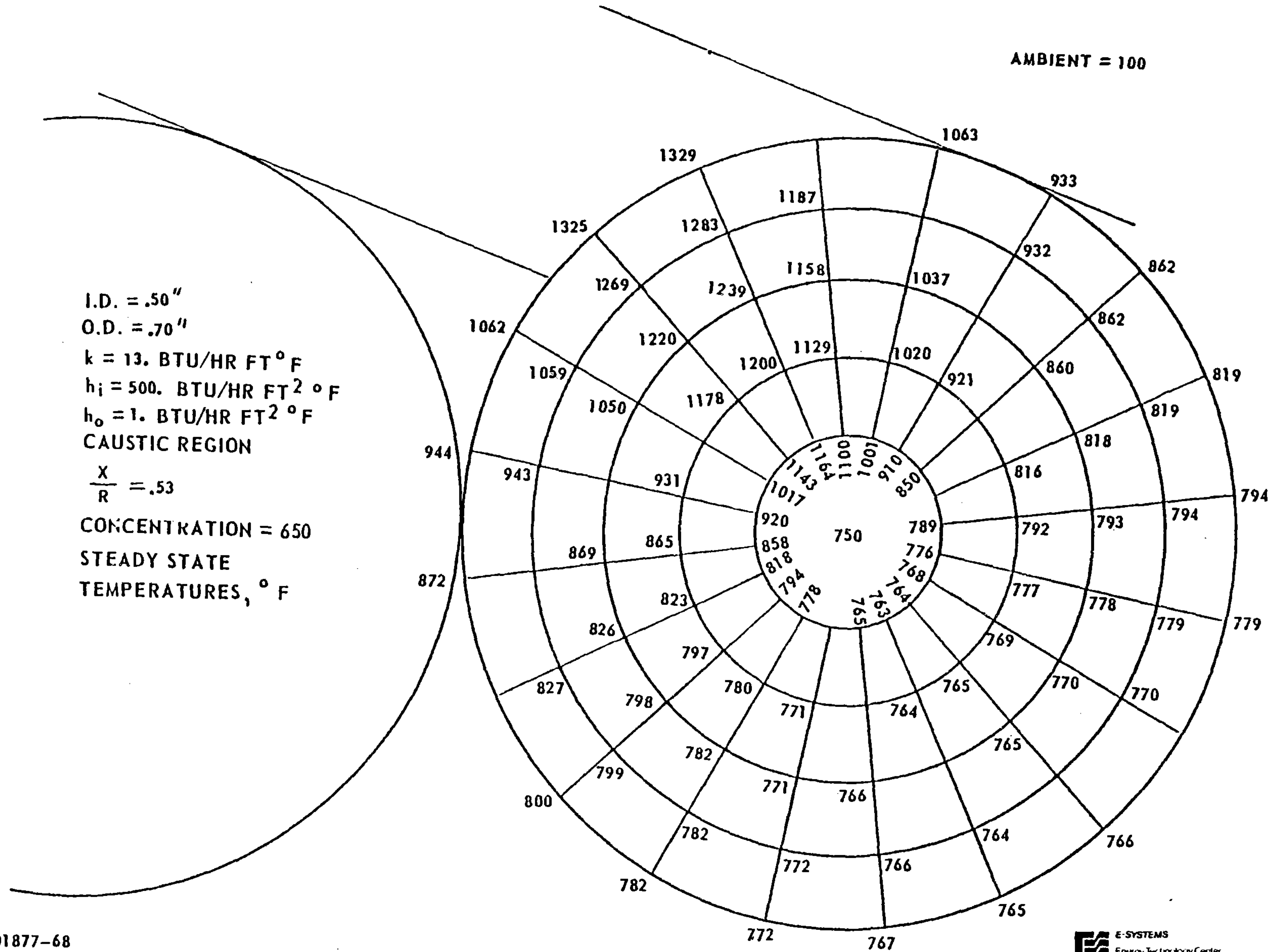

01877-68

E-SYSTEMS Energy Technology Center

Figure F-22. Steady State Steam Tube Temperatures (0.50 inch I.D. and h_i = 500.0 BTU/hr. ft.^{2} °F)

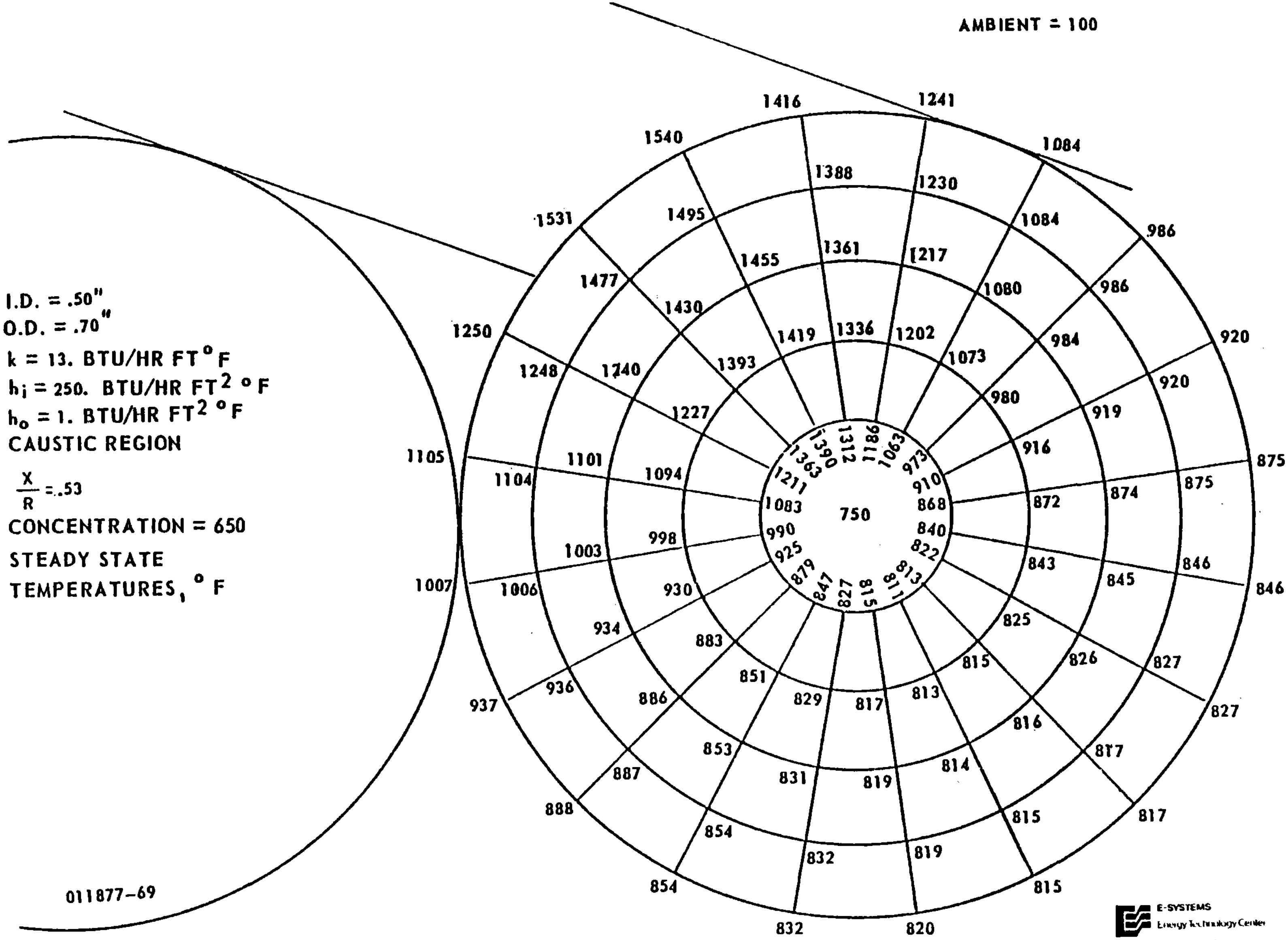

Figure F-23. Steady State Steam Tube Temperatures
(0.50 inch I.D. and h_i = 250.0 BTU/hr. ft.^{2} °F)

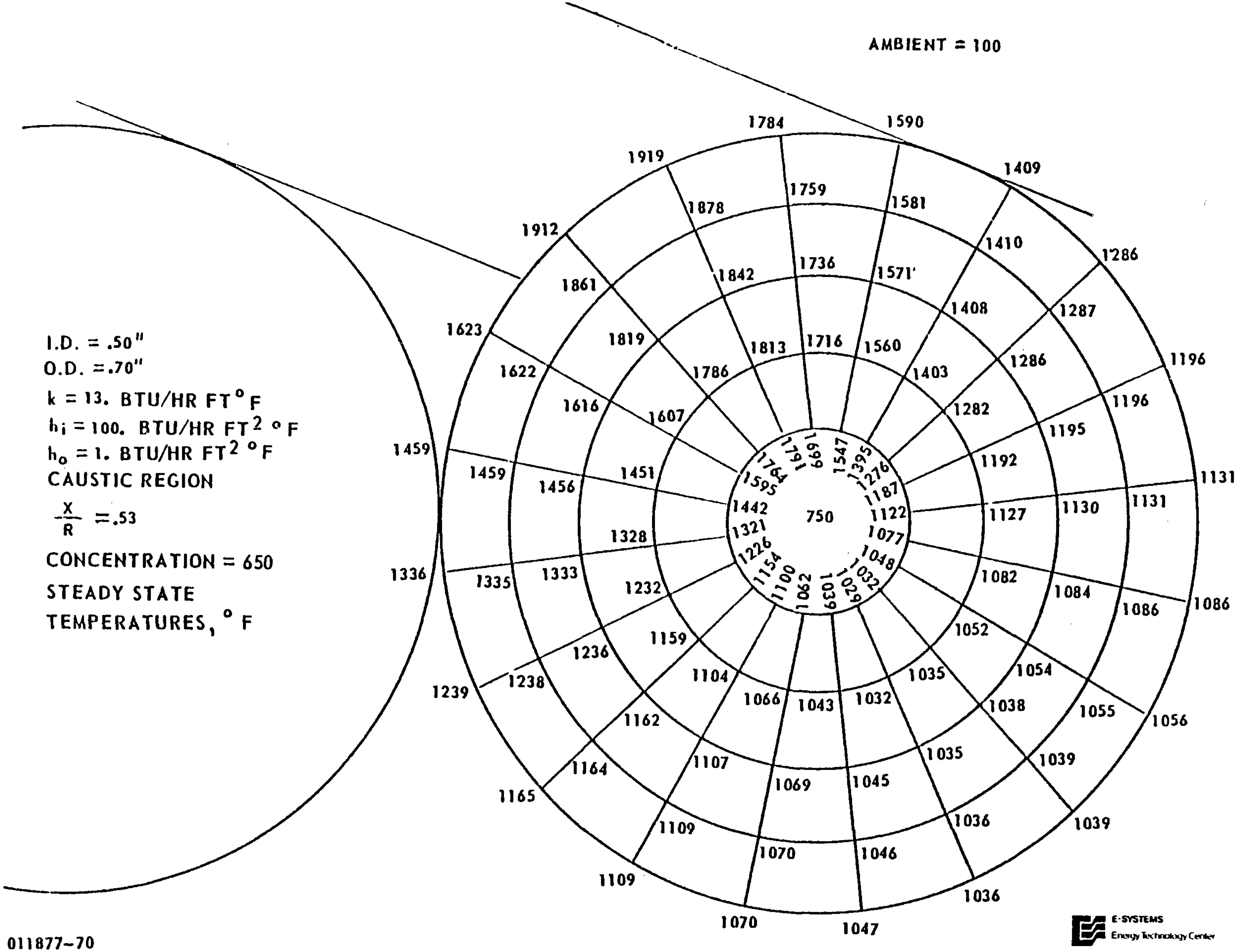

Figure F-24. Steady State Steam Tube Temperatures
(0.50 inch I.D. and h_i = 100.0 BTU/hr. ft.^{2} °F)

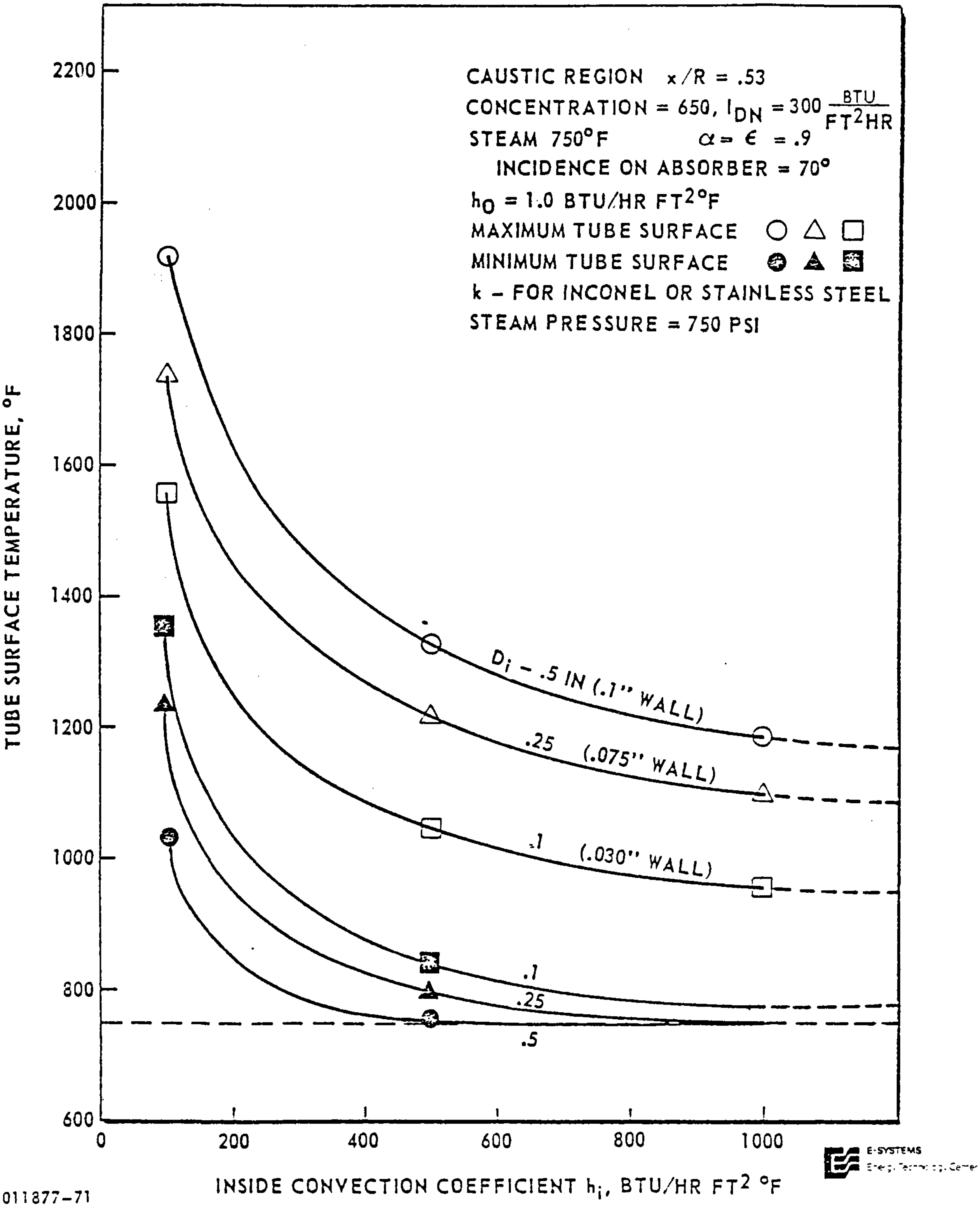

Figure F-25. Summary of Steady State Steam Tube Temperatures

F-9 TRANSIENT TUBE TEMPERATURES FOR A STEAM SYSTEM

The previous subsection presented steady state tube temperatures for a steam system. This subsection will present the tube temperatures under a transient situation occurring due to a shut off of the water flow. The solar load is still on the tube but heat is only being removed from the exterior surface to the surroundings. This results in the tube absorbing the excess heat which in turn drives the tube temperatures up dramatically.

The thermal analyzer tube model was modified to include capacitance for the nodes in the tube and exclude the convection heat sink to the steam. The initial temperatures were assumed to be the steady state temperatures presented above.

A tube with a 0.25 inch I.D. (0.40 inch O.D.) was analyzed with a h_i of 250 and 1,000 Btu/hrft^2°F. The material properties used in this transient model are typical for the stainless steels and Inconels.

Figure F-26 shows the maximum tube temperatures for time varying from 0 to 12 seconds for the 0.25 inch tube. Figures F-27 and F-28 show tube temperature distributions after 12 seconds for the 0.25 tube with h_i equal to 1,000 and 250 Btu/hrft^2°F, respectively. The maximum temperatures the tube attains at the end of 12 seconds are quite high

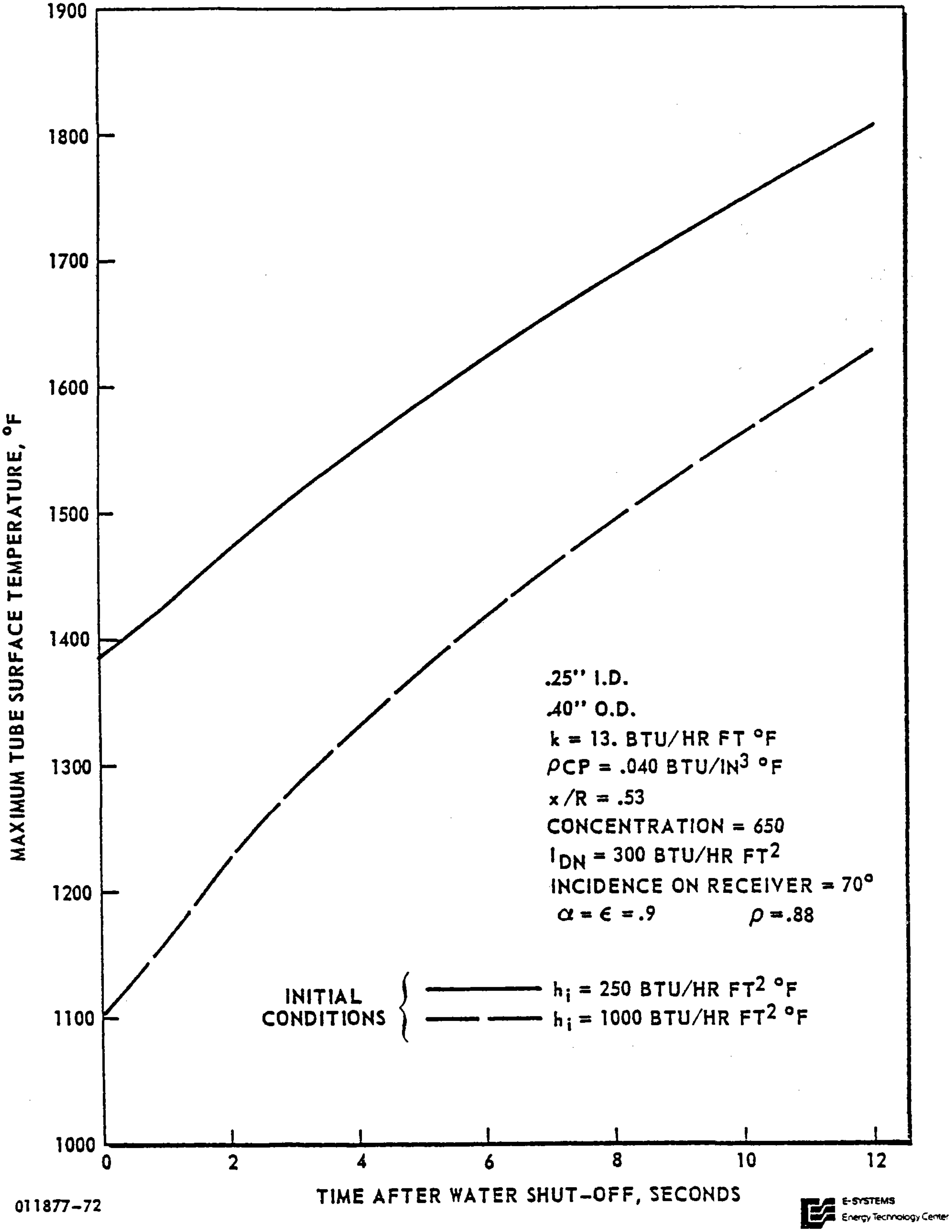

Figure F-26. Maximum Steam Tube Surface Temperatures Under Transient Water Shut-Off Conditions

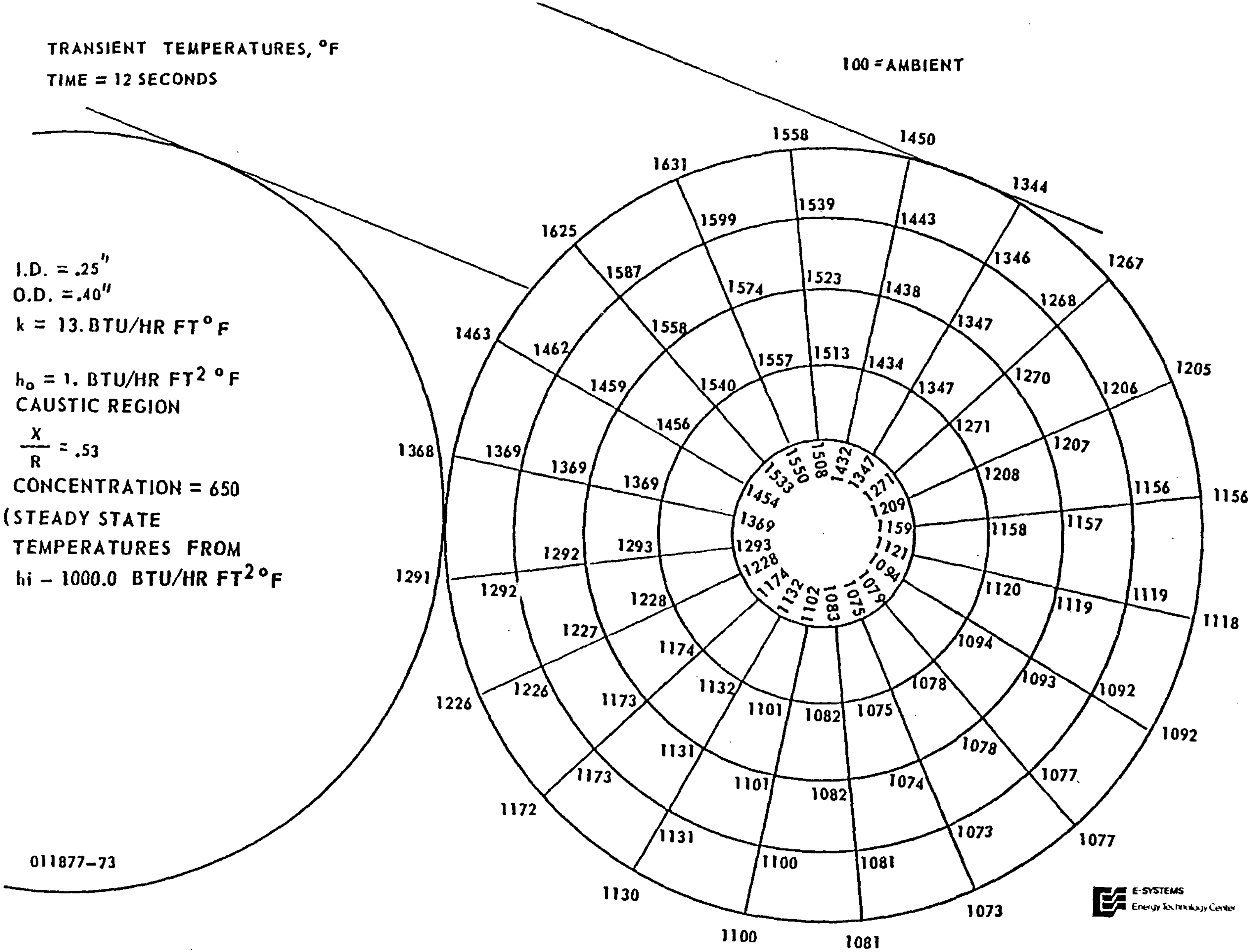

Figure F-27. Transient Steam Tube Temperatures After 12 Seconds
(0.25 inch I.D. and h_i = 1000.0 BTU/hr. ft.^{2} °F)

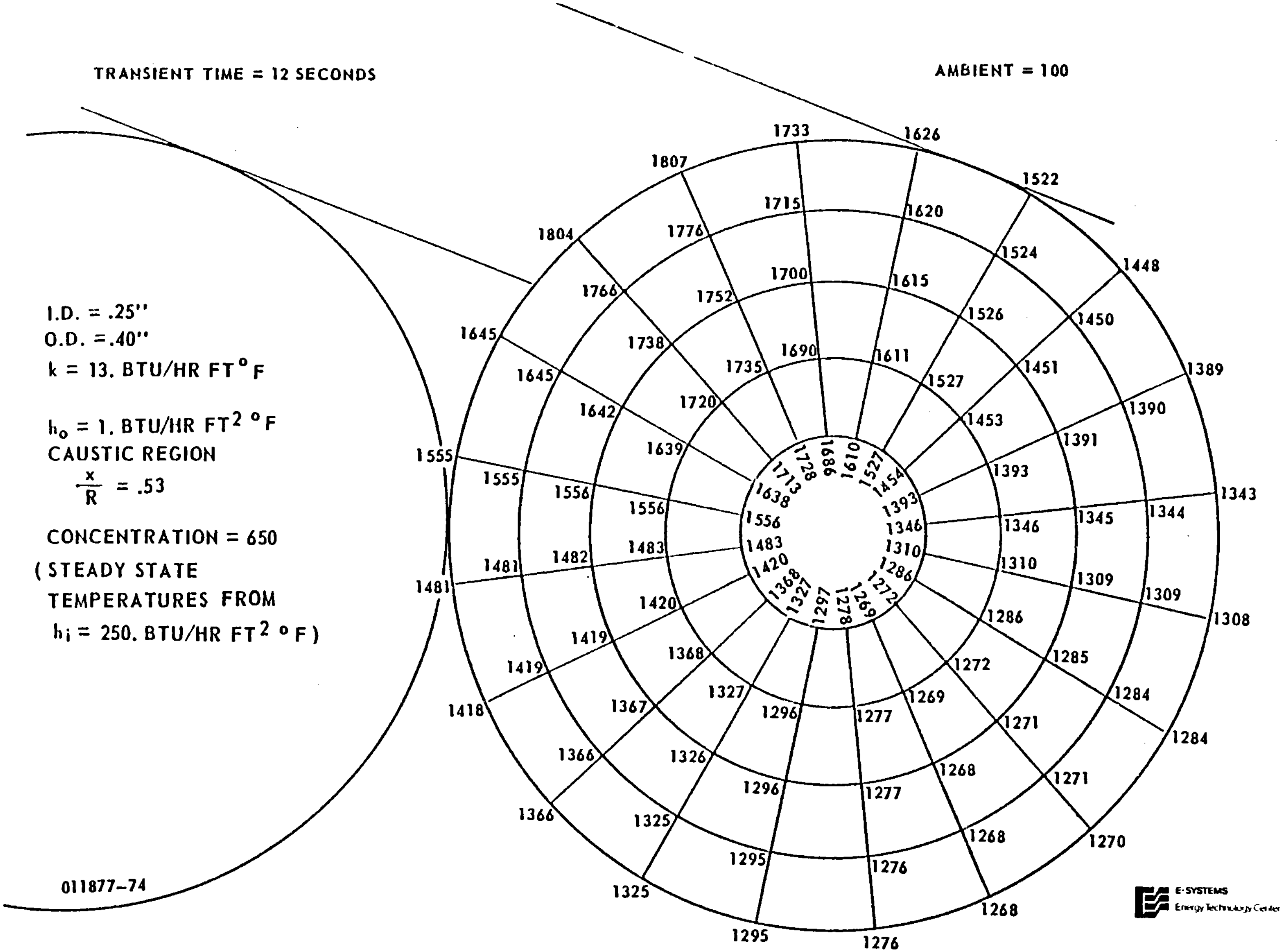

Figure F-28. Transient Steam Tube Temperatures After 12 Seconds
(0.25 inch I.D. and h_i = 250.0 BTU/hr. ft.^{2} °F)

(1,600° to 1,800°F).

F-10 STEADY STATE TUBE TEMPERATURES FOR AN OIL SYSTEM

The maximum steady state tube temperature distributions will be presented for an oil system. The oil system thermal analyzer model uses the same solar heat input, external tube ambient, and tube model as the water/steam system, except the oil temperatures and internal convection coefficients will be different.

Figure F-29 shows the maximum tube temperature distribution for a 0.50 inch I.D. (0.70 inch O.D.) stainless steel tube with 600°F oil and a h_i of 800 Btu/hrft^2°F in the caustic region of the receiver. Figure F-30 shows a tube temperature distribution for the same tube but with 300°F oil and h_i equal to 500 Btu/hrft^2°F. The maximum tube temperature is 1,100°F for the 600°F oil system which is lower than most of the tube temperatures for the steam system.

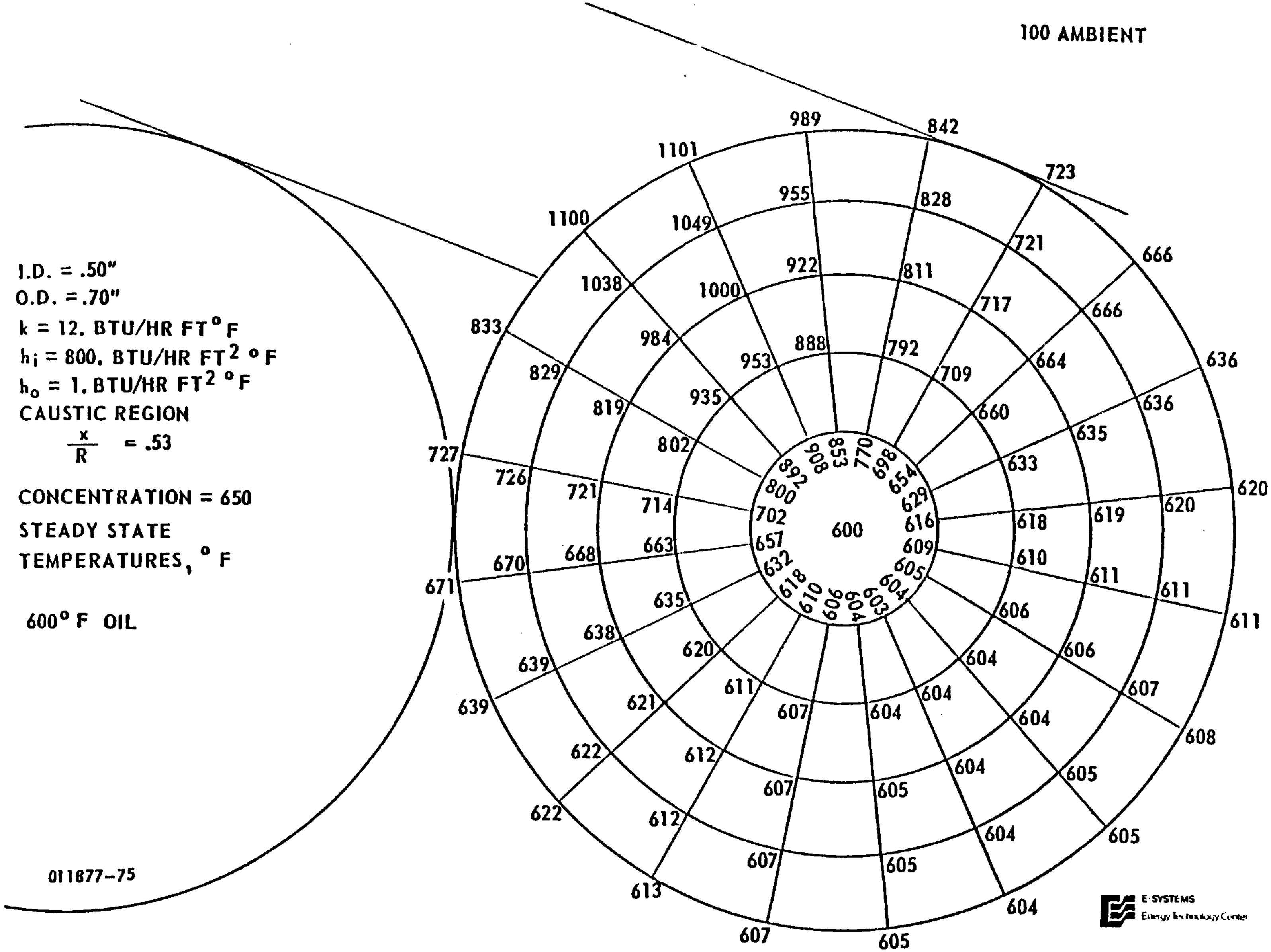

Figure F-29. Steady State Oil Tube Temperatures
(0.50 inch I.D. and h_i = 800.0 BTU/hr. ft.^{2} °F)

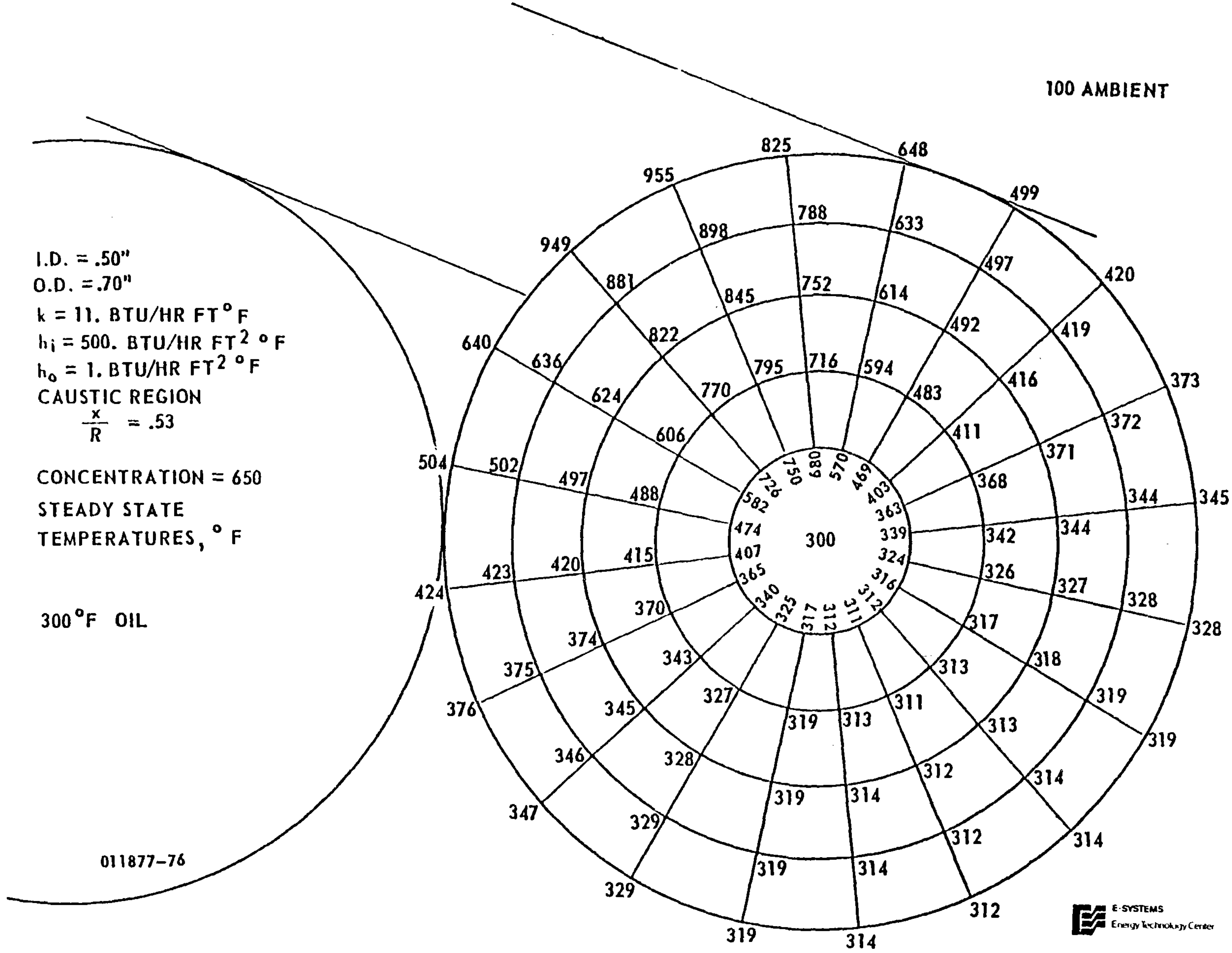

Figure F-30. Steady State Oil Tube Temperatures (0.50 inch I.D. and h_i = 500.0 BTU/hr. ft.^{2} °F)

F-11 INTERNAL CONVECTION AND PRESSURE DROP FOR A WATER/STEAM SYSTEM

The internal convection coefficients and the pressure drops for the receiver tubes are established for a water/steam system. An earlier section discussed the three distinct fluid flow regions for the receiver tubes. The heating of the water occurs in approximately the first 59% of the receiver length, the boiling of the two-phase flow takes up approximately the next 33% of the receiver, and the superheating of the vapor occurs in the remaining 8% of the receiver. Each of these three regions have their respective heat transfer coefficients and pressure drops.

The 200 foot aperture diameter prototype water/steam system was analyzed. The current receiver design uses 20 0.25-inch I.D. (0.40 inch O.D.) tubes in parallel. These tubes are helically coiled over the support cone and have a tube bundle length of approximately 400 feet.

This analysis takes into account how the fluid flow rate varies during the daylight hours from a minimum in early morning and late afternoon to a maximum at solar noon. The maximum flow rate is approximately 5,150 pounds/hour with the minimum being approximately 33% of the maximum.

F-12 HEATING OF THE WATER REGION

The water is heated from 100°F to approximately 511°F in this region of the receiver. The thermal properties used for water under 750 psi pressure are presented below.

Thermal Property	100°F	300°F	511°F
Density, ρ, lb_m/ft^3	62.0	57.3	48.3
Specific Heat, C_p, Btu/lb_m °F	1.0	1.03	1.20
Thermal Conductivity, k, Btu/hrft°F	0.36	0.395	0.345
Prandtl Number, Pr	4.58	1.17	0.87
Dynamic Viscosity, μ, $lb_m/hrft$	1.65	0.45	0.25

The following example calculations presented are for the maximum flow with 100°F water.

$\dot{m}$ = 5,150 lbm/hr

$$V = \frac{\dot{m}}{\rho \text{ area}} = 3.38 \text{ ft/sec}$$

$$Re = \frac{\rho V D}{\mu} = 9{,}516 \text{ (Yes Turbulent)}$$

$$h_i = \frac{0.023\ k}{D} Re^{0.8}\ Pr^{0.4}$$

h_i = 1,116 Btu/hrft^2°F for 100°F Water

$$f = \frac{0.0791}{Re^{.25}} = 0.008$$

$$\frac{\rho V^2}{2g} = 0.076 \text{ psi}$$

$$\Delta P = 4f \frac{L}{D} \frac{\rho V^2}{2g}$$

L is approximately 274 feet for the water heating region, therefore

$\underline{\Delta P = 32 \text{ psi}}$ for 100°F Water

Similar calculations were performed at the minimum and the maximum flow rates with water at 300°F and 511°F. The internal convection coefficients, h_i, are summarized in Figure F-31. The pressure drop varied from 25 to 32 psi for maximum flow and varied from 4.0 to 5.0 psi for minimum flow.

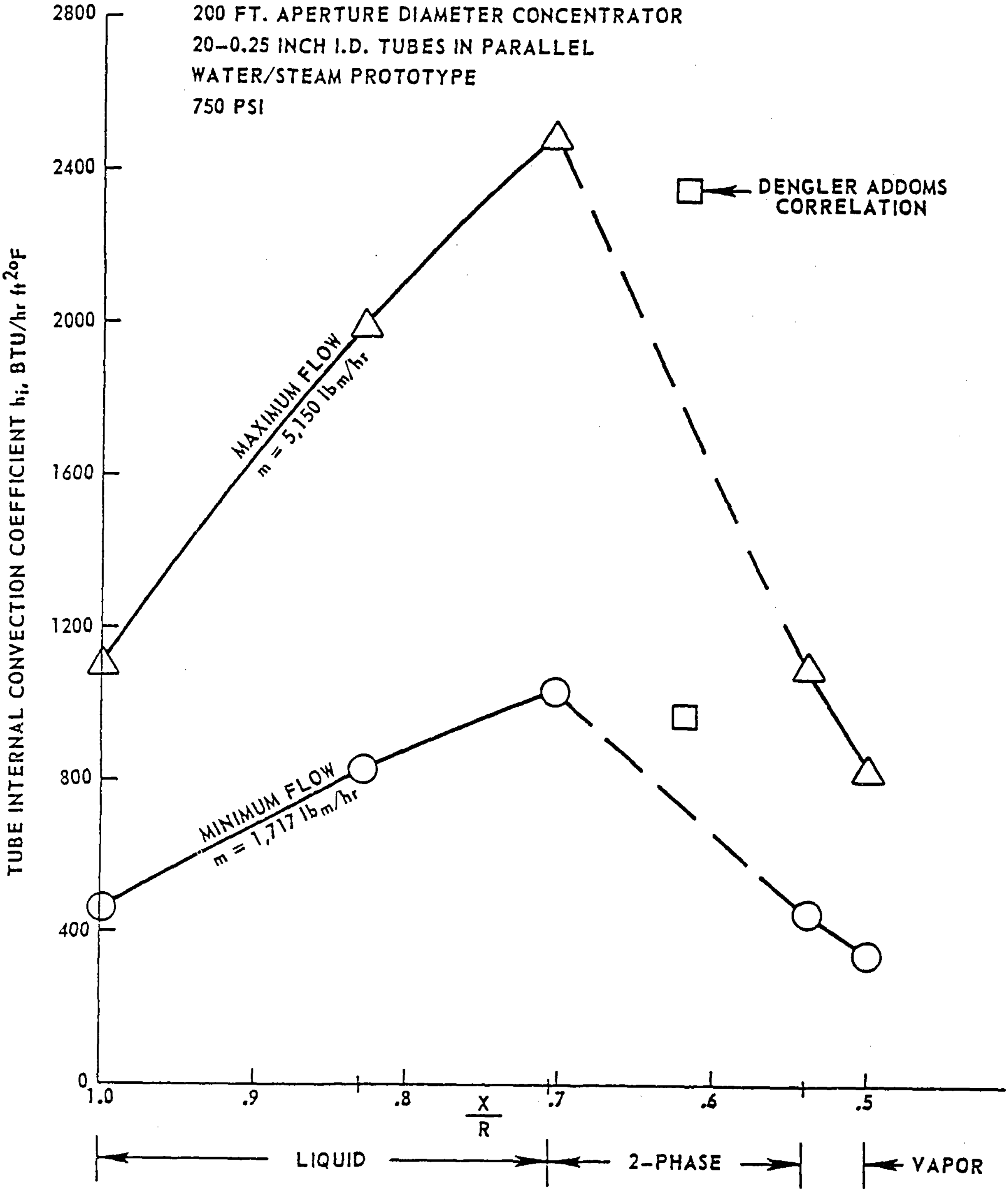

Figure F-31. Tube Internal Convection Coefficient Versus Position on the Prototype Receiver

F-13 HEATING OF THE VAPOR (SUPERHEATING REGION)

The dry steam is heated from 511°F to approximately 800°F in this region of the receiver.

The thermal properties used for superheated steam under 750 psi pressure are presented below:

Thermal Property	511°F	800°F
Density, ρ, lb_m/ft^3	1.641	1.065
Specific Heat, c_p, $Btu/lb_m{}°F$	1.03	.58
Thermal Conductivity, k, Btu/hrft°F	.0295	.0364
Dynamic Viscosity, μ, $lb_m/hrft$	.041	.063
Prandtl Number, Pr	1.42	1.0

The following example calculations presented are for the maximum flow with 511°F steam.

$$\dot{m} = 5{,}150\ lb_m/hr$$

$$V = \frac{\dot{m}}{\rho\ \text{area}} = 127.8\ \text{ft/sec}$$

$$Re = \frac{\rho V D}{\mu} = 382{,}974 \quad \text{(Yes, turbulent)}$$

$$h_i = \frac{.023\ k}{D}\ Re^{.8}\ Pr^{.4}$$

$$h_i = 1{,}099\ \text{Btu/hrft}^2{}°\text{F for 511°F Steam}$$

$$f = \frac{.0791}{Re^{.25}} = .0032$$

$$\frac{\rho V^2}{2g} = 2.89 \text{ psi}$$

$$\Delta P = 4f \frac{L}{D} \frac{\rho V^2}{2g}$$

L is approximately 23 feet for the steam superheating region. Therefore,

$\underline{\Delta P = 40 \text{ psi for } 511°\text{F Steam}}$

Similar calculations were performed for 800°F steam under maximum flow conditions and for 511°F and 800°F steam under minimum flow conditions. The convective heat transfer coefficients, h_i, are summarized in Figure F-31. The pressure drop varied from 40 to 68 psi for maximum flow and varied from 6 to 10 psi for minimum flow.

The superheat region of the receiver is extremely important since the caustic occurs at x/R equal to 0.53. This region extends to x/R approximately equal to 0.54. The minimum h_i calculated for the superheat region is considered acceptable. A minimum acceptable h_i of 250 $Btu/hrft^2 °F$ for the caustic region has been set arbitrarily due to the high tube temperatures associated with low internal convection coefficients.

F-14 BOILING IN THE TWO-PHASE FLOW REGION

The two-phase flow region is very interesting from a heat transfer and pressure drop point of view. Many correlations exist for two-phase flow but none are known for the receiver design being analyzed. Some of the unique features of the receiver design are as follows:

1. System pressure = 750 psi - 1000 psia
2. Receiver tube is helically coiled

   $$\frac{\text{Coil diameter}}{\text{Outside tube diameter}} \approx 30 \text{ to } 60$$

3. Mass flow rate per unit cross-sectional area, G, varies from 252,000 to 755,000 $lb_m/hrft^2$
4. Heat input over a portion of the external tube surface which is adjacent to the internal surfaces wetted by the inertia effects (centrifugal acceleration) as the liquid flows in the coiled tube.
5. Heat input fluxes which vary around the helical coil (except at solar noon the fluxes are uniform and maximum around the coil).
6. Heat input fluxes also vary with axial position in the two-phase flow region.

   Q/A varies from 28,500 to 95,000 $Btu/hrft^2$ for solar noon and zero to 95,000 $Btu/hrft^2$ for other times of the day.

7. Tube internal diameter = o.25 inch and total tube length = 400 feet

$$\frac{\text{Total tube length}}{\text{Tube I.D.}} = 19{,}200$$

$$\frac{\text{Two-Phase flow tube length}}{\text{Tube I.D.}} = 5{,}300$$

8. Water velocities entering the two-phase flow region

$$V_{water} = 1.5 \text{ to } 4.3 \text{ ft/sec}$$

Testing of an actual receiver will be required to assure that the flow is stable, that "burnout" (vapor insulating layer develops around the liquid) will occur only at a steam quality at or near 100%, and that the internal heat transfer coefficients will remain high above the dashed line shown in Figure F-31. The absolute minimum requirements for this two-phase flow region are that the flow be stable and that the internal convection coefficient h_i remain above 250 Btu/hrft^{2}oF for minimum flow.

Typical flow boiling correlations show that the internal coefficients will have values above the dashed line in Figure F-31, unless burnout occurs at low values of quality (less that 50%). However, it is expected that burnout will occur at very near 100% quality due to the unique receiver design. Dengler-Addoms flow boiling correlation is shown for a quality, x, equal to 50%*.

$$\frac{h_{i_{boil}}}{h_{i_\ell}} = 3.5\left(\frac{1}{x_T}\right)^{0.5}$$

$$\text{where } h_{i_\ell} = \frac{0.023k_\ell}{D}\left[Re(1-x)\right]^{0.8}(Pr_\ell)^{0.4}$$

$$x_T = \left(\frac{x}{1-x}\right)^{0.9}\left(\frac{\rho_\ell}{\rho_v}\right)^{0.5}\left(\frac{\mu_v}{\mu_\ell}\right)^{0.1}$$

For x = 0.5, fluid properties evaluated at saturation temperature since the $T_{wall} \approx T_{sat}$, and the minimum flow rate

$$h_{i_\ell} = \frac{.023(.345)}{.0208}\left[20{,}936\cdot(1-.5)\right]^{0.8}(.87)^{0.4}$$

$$h_{i_\ell} = 596 \text{ Btu/hrft}^2{}^\circ\text{F}$$

$$x_T = \left(\frac{0.5}{1-0.5}\right)^{0.9}\left(\frac{48.3}{1.64}\right)^{0.5}\left(\frac{0.041}{0.25}\right)^{0.1}$$

$$x_T = 4.53$$

$$h_{i_{boil}} = 3.5(596)\left(\frac{1}{4.53}\right)^{0.5}$$

$$h_{i_{boil}} = 980 \text{ Btu/hrft}^2{}^\circ\text{F} .$$

The results of the Dengler-Addoms correlation are plotted in Figure F-31 by assuming the quality increases linearly along the two-phase flow portion of the receiver.

* Dengler, C. E. and Addoms, J. N., Chemical Engineering Progress Symposium Series, Vol. 52, No. 18, 1956.

The pressure drop for the two-phase flow region of the receiver has been calculated using revised Martinelli correlations by Thom*. These correlations are valid for water boiling in straight tubes. It is questionable how applicable these correlations are to the coiled tube receiver design. However, these correlations are recognized as the best available at this time. Testing of an actual receiver will be required to establish actual pressure drops throughout the receiver.

A sample calculation using the revised Martinelli correlations for the maximum flow through the two-phase region is presented.

$$\Delta P = 4f \frac{L}{D} \frac{\rho V^2}{2g} \quad \overline{\Phi}_{fo}^{\,2} \quad + G^2 r_2$$

for steam quality of 100% and steam pressure of 750 psi

$$\overline{\Phi}_{fo}^{\,2} \approx 17.0$$

$$r_2 \rho_f \approx 32.0$$

these are the Martinelli factors for steam by Thom; the fluid properties are evaluated at the saturation temperature of 511°F.

$$\dot{m} = 5{,}150 \ lb_m/hr$$

$$V = \frac{\dot{m}}{\rho \ \text{area}} = 4.34 \ ft/sec$$

---

* Wallis, G. B. One-Dimensional Two-Phase Flow, McGraw-Hill Book Company.

$$Re = \frac{\rho VD}{\mu} = 62,786$$

$$f = \frac{0.0791}{Re^{0.25}} = 0.005$$

$$\frac{\rho V^2}{2g} = 0.099 \text{ psi}$$

$$G^2 = \left(\frac{\dot{m}}{A}\right)^2 = \frac{\rho^2 V^2}{g} = 9.48 \ lb_f lb_m/ft^3 in^2$$

$$r_2 = \frac{32.0}{\rho_f} = 0.66 \ ft^3/lb_m$$

$$G^2 r_2 = 6.3 \text{ psi}$$

the length of tube in the two-phase region is approximately 111.0 feet

$$4f \frac{L}{D} \frac{\rho V^2}{2g} \bar{\Phi}_{fo}^{\,2} = 180 \text{ psi}$$

$$\Delta P = 4f \frac{L}{D} \frac{\rho V^2}{2g} \bar{\Phi}_{fo}^{\,2} + G^2 r_2$$

$\underline{\Delta P = 186. \text{ psi}}$ for maximum flow

A similar calculation was performed at the minimum flow rate for this region and the ΔP was approximately 27 psi.

F-15 SUMMARY OF PRESSURE DROPS FOR THE PROTOTYPE RECEIVER

A summary of the pressure drops for the prototype receiver is presented below:

Receiver Location (Length-feet)	ΔP psi for Minimum Flow	ΔP psi for Maximum Flow
Liquid Region (274)	4	26
Two-phase Region (111)	27	186
Vapor Region (23)	8	54
Total Receiver (408)	39	266

F-16 SCALING TECHNIQUES FOR INTERNAL CONVECTION AND PRESSURE DROP FOR WATER/STEAM SYSTEMS

The previous subsections presented an analysis for the 200 foot prototype concentrator/receiver. That analysis is applicable to other sizes of concentrators as shown below.

Assume $\dot{m} \sim$ Area Aperture $\sim R^2$

$$\dot{m}_{Tube} = \frac{\dot{m}}{n_{tubes}}$$

$$Re = \frac{4\ \dot{m}\ tube}{\pi \mu D} = \frac{4\dot{m}}{\pi \mu D n_{tubes}} \sim \frac{\dot{m}}{n_{tubes} D}$$

If $n_{tubes} \sim \dot{m} \sim R^2$ and D is constant, Re and Velocity will be constant for turbulent flow.

$$\frac{h_i D}{k} = \text{Constant}(Re)^{0.8}$$

or

h_i will also be constant

$$f = \frac{\text{Constant}}{(Re)^{0.25}}$$

f is also a Constant

$$\Delta P = 4f\frac{L}{D}\ \frac{\rho V^2}{2g}$$

all of the terms are constant except L (length of the tubes)

$\Delta P \sim L$

however, $L = \dfrac{\pi D_{abs} L_{abs}}{D\ n_{tubes}}$

or L = Constant

and $\underline{\Delta P = \text{Constant}}$.

The following parameters - Re, V, h_i and ΔP - will remain fixed for any size concentrator/receiver, if tube diameter, D, is constant, and the number of tubes, n_{tubes}, and the total mass flow, $\dot{m}$, vary proportionally to the concentrator aperture area or R^2.

The 50 foot test model is scaled down from the 200 foot prototype by the equations presented above. The test model has 1/16 the flow rate and number of tubes as the prototype. Consequently, the two models will have approximately the same internal coefficients and pressure drops.

The previous subsections presented analyses of the prototype system with 20 0.25-inch I.D. tubes. Other sizes and numbers of tubes have been considered for a 100 foot aperture concentrator. Figures F-32 through F-35 show the internal tube size as a variable from 0.10 to 0.50 inch, internal convection coefficients for minimum flow, and pressure drops associated with the superheat region with the maximum flow. These figures are useful for any size concentrator using the scaling laws established above.

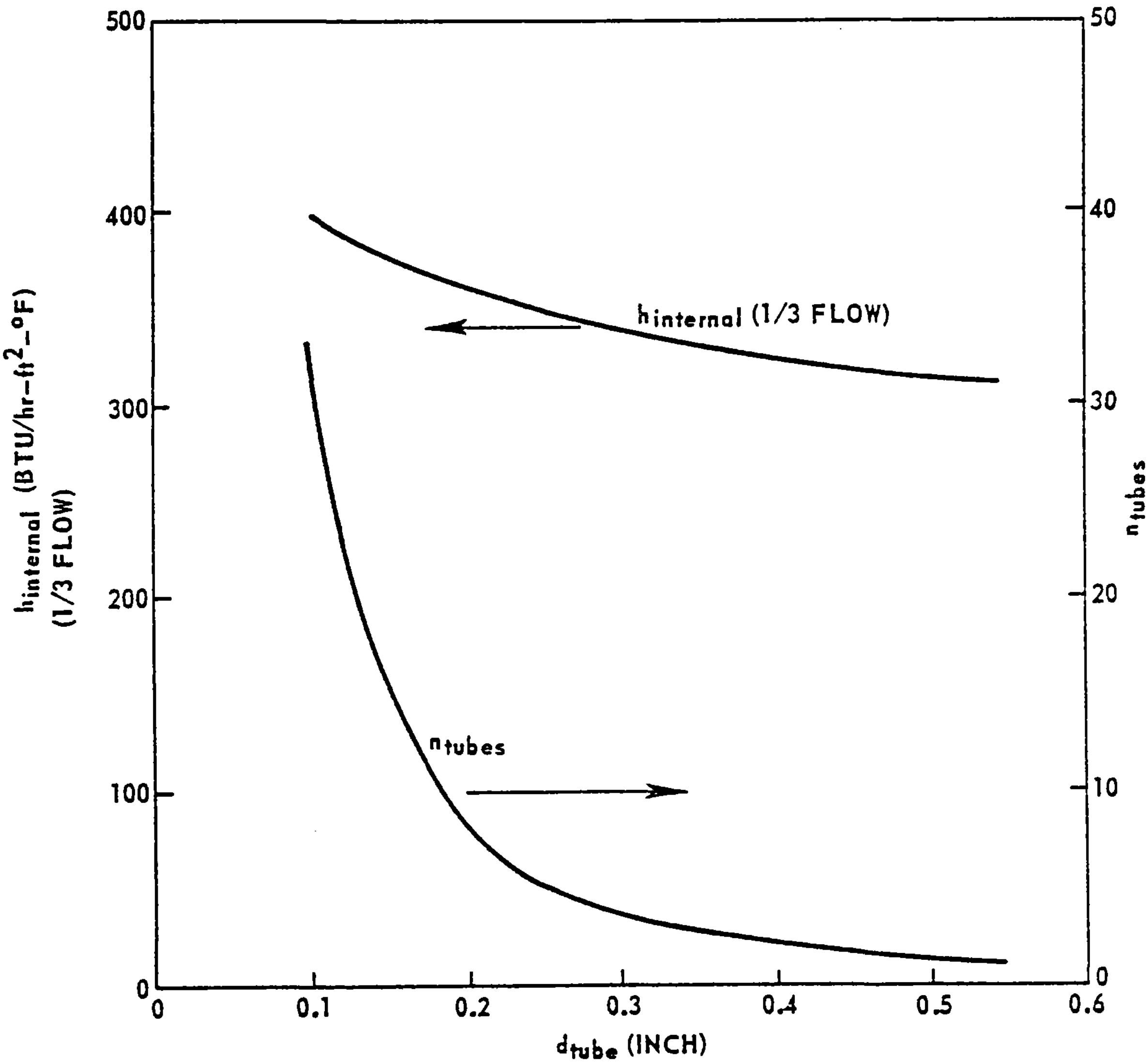

CONSTRAINTS: $\Delta P_{full\ flow}$ = 100 PSI IN THE SUPERHEAT SECTION ALONE, $D_{aperture}$ = 100 ft, TURBULENT FLOW, VAPOR PROPERTIES (750°F, 700 PSIA)

011877–78

E-SYSTEMS Energy Technology Center

Figure F-32. Heat Transfer and Number of Tubes for Various Tube Diameters to Maintain $\Delta P_{\substack{full\ flow \\ superheat}}$ = 100 psi

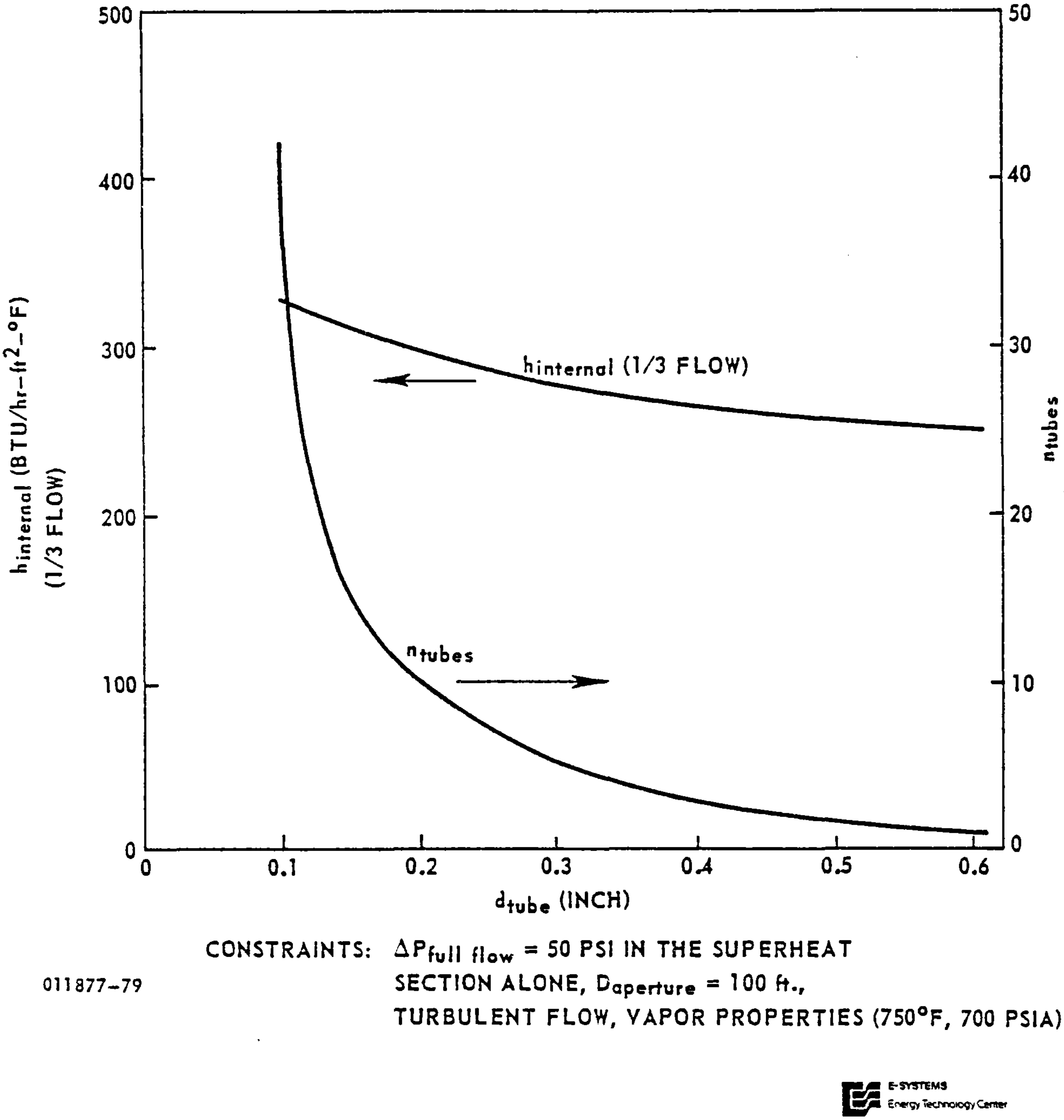

Figure F-33. Heat Transfer and Number of Tubes for Various Tube Diameters to Maintain $\Delta P_{\substack{full\ flow \\ superheat}}$ = 50 psi

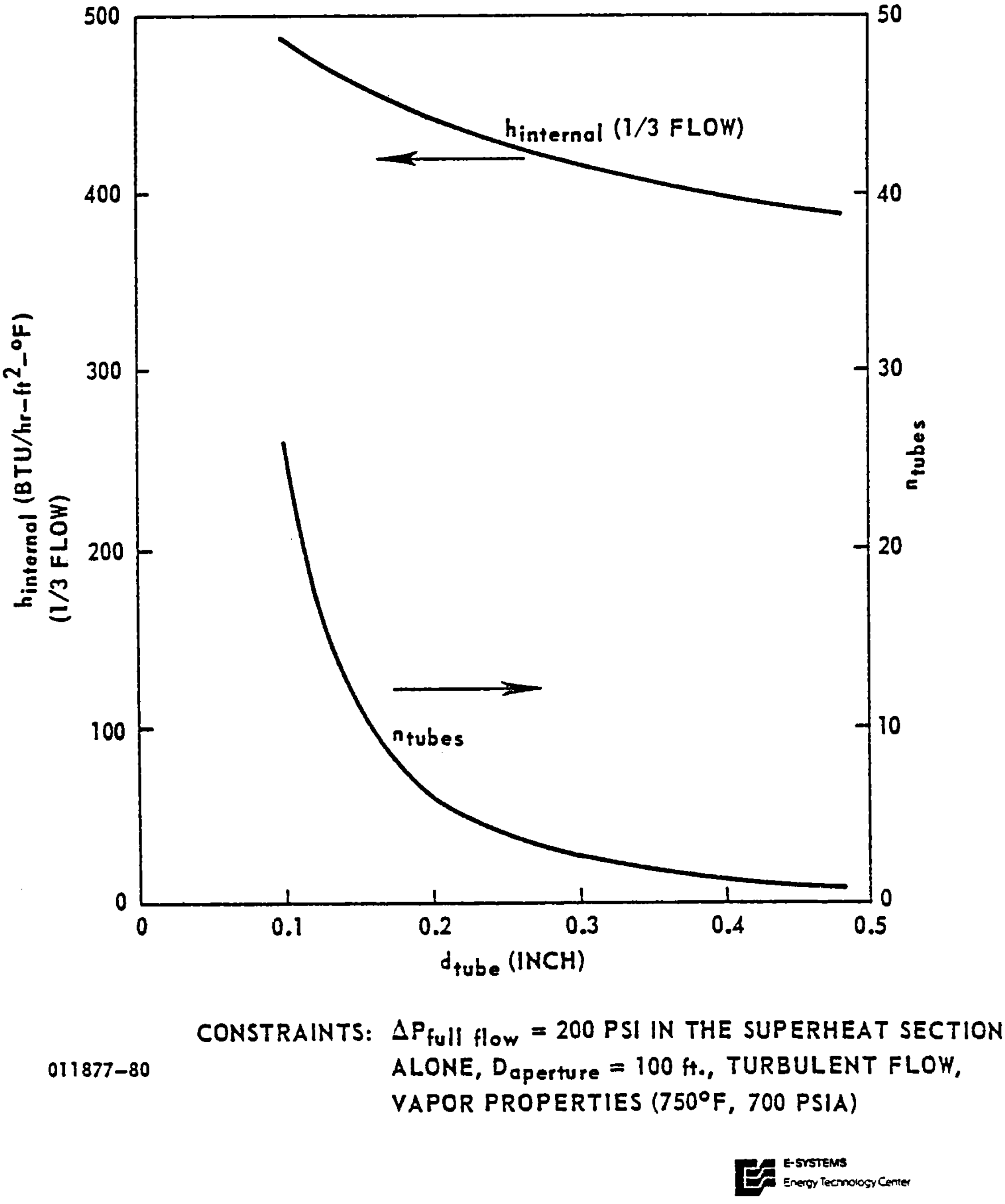

Figure F-34. Heat Transfer and Number of Tubes for Various Tube Diameters to Maintain $\Delta P_{\text{full flow superheat}}$ = 200 psi

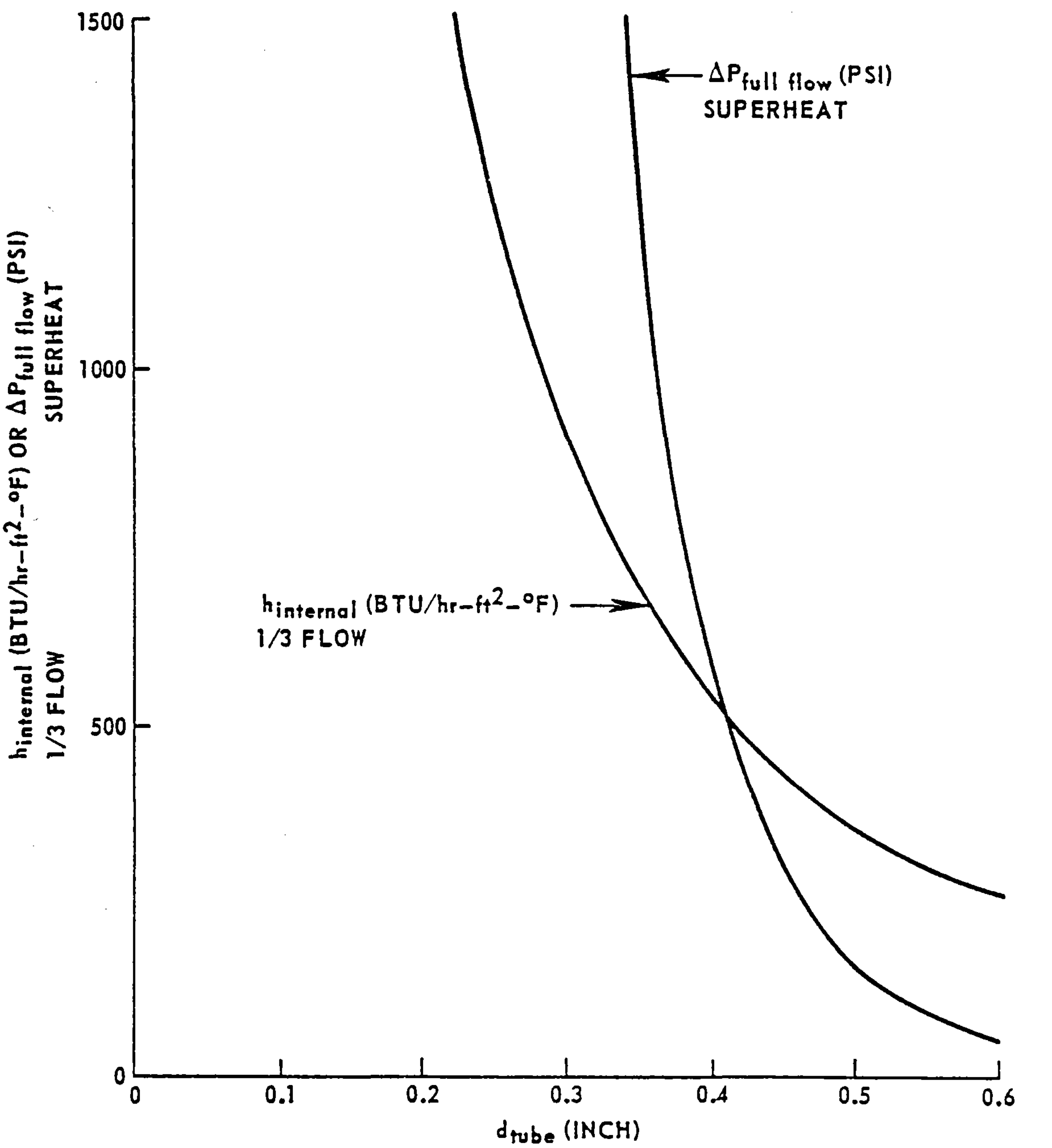

011877–81

CONSTRAINTS: SINGLE TUBE CONTAINING ALL FLOW, ΔP IS FOR SUPERHEAT SECTION ONLY, $D_{aperture}$ = 100 ft., TURBULENT FLOW, VAPOR PROPERTIES (750°F, 700 PSIA)

E-SYSTEMS
Energy Technology Center

Figure F-35. Heat Transfer and Pressure Drop for Various Tube Diameters for Single Tube on Receiver

F-17 INTERNAL CONVECTION AND PRESSURE DROP FOR AN OIL SYSTEM

The internal convection coefficients and the pressure drops for the receiver tubes are established for an oil system using Caloria HT-43. The thermal properties of this oil are shown below:

Density, $\rho, lb_m/ft^3$

@ 300°F - 48.5

@ 600°F - 41.6

Specific Heat, c_p, Btu/lb_m°F

@ 300°F - .60

@ 600°F - .75

Thermal Conductivity, k, Btu/hrft°F

@ 300°F - .0725

@ 600°F - .066

Dynamic Viscosity, μ, lb_m/hrft

@ 100°F - 64.0

@ 300°F - 5.1

@ 600°F - 1.3

The assumed temperature rise of the oil through the receiver tubes in 50°F. This temperature rise and the solar heat input set the required oil flow rates. The solar heat input was established by the overall receiver thermal analysis computer program results presented in earlier.

The 200 foot aperture diameter prototype concentrator/receiver with oil as the working fluid has 64 tubes, 0.50 inch I.D. (0.70 inch O.D.), in parallel and each tube has a length of approximately 71 feet. The following calculations presented are based on this receiver design, the oil has an average temperature of 500°F, and an oil ΔT of 50°F.

$$Q_{Net\ in} = \dot{m}\ c_p \Delta T$$

$$Q_{Net\ in} = 6.64 \times 10^6\ \text{Btu/hr}$$

$$\dot{m} = 189.7.\ lb_m/hr = 536\ gpm$$

$$V_{oil} = 13.7\ ft/sec$$

$$Re_{oil} = \frac{\rho VD}{\mu} = 56{,}603\ \text{(Yes, turbulent)}$$

$$Pr = 16.5\ \text{for } 500°F\ \text{oil}$$

$$\frac{h_i D}{k} = .023\ Re^{0.8}\ Pr^{0.4}\ \text{(Assume Turbulent)}$$

$$h_i = 730.0\ Btu/hrft^2{}°F\ \text{for } 500°F\ \text{oil}$$

$$\Delta P = 4f\frac{L}{D}\ \frac{\rho V^2}{2g}$$

$$f = \frac{0.0791}{(Re)^{0.25}} = 0.0051$$

$$\frac{\rho V^2}{2g} = 0.89\ psi$$

$$\underline{\Delta P = 31\ \text{psi for } 500°F\ \text{Oil}}$$

These values are plotted in Figure F-36 as well as results for other oil temperatures. These results for this prototype oil system are acceptable since h_i is greater than 500 Btu/hrft^2°F for oil temperatures in excess of 300°F. The tube pressure drop, ΔP, is also less than 60 psi for oil temperatures greater than 300°F.

These h_i's and ΔP's are applicable to the 50 foot test model receiver. The receiver would use four 0.50 inch I.D. (0.70 inch O.D.) tubes in parallel.

F-18 NOMINAL RECEIVER CONFIGURATION

The nominal receiver configuration is a 1° cone with the small fluid tubes helically coiled over the receiver support tube. Two sizes of concentrators/receivers are being considered - a 50-foot aperture diameter test model and a 200 foot aperture diameter prototype. The fluid could be either water/steam or oil (Caloria HT-43)^R.

The receiver for the 50-foot test model would have an approximate overall length of 14.2 feet with the 1° cone having a diameter of 3.0 at the top of the receiver inches and 6.0 inches at the bottom. The fluid flow channel for the steam system would consist of a single 0.25 inch I.D. (0.40 inch O.D.) tube helically coiled over the receiver. The oil system would use four 0.50 inch I.D. (0.70 inch O.D.) tubes in parallel. The continuously coiled steam tube would

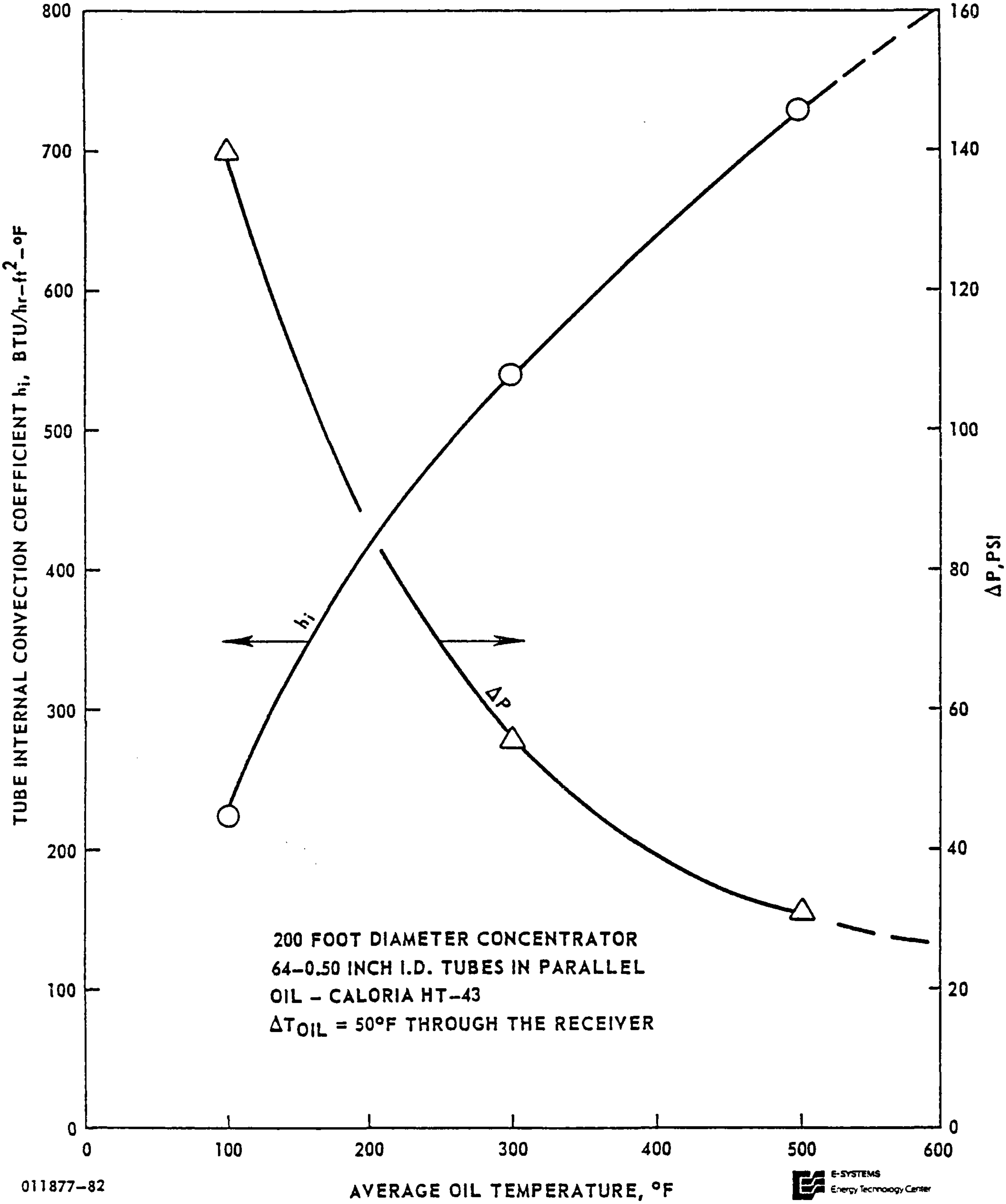

011877-82

E-SYSTEMS Energy Technology Center

Figure F-36. Internal Convection Coefficients and Pressure Drops for the Prototype Oil System have an approximate length of 500 feet while the oil system would have a tube length of approximately 72 feet. The tube material would probably be Inconel for the water/ steam system since it is questionable whether stainless steel will be acceptable at the high temperatures associated with the steam system.

The receiver for the 200 foot prototype would have an approximate overall length of 57.5 feet with the 1° cone having a diameter at the top of the receiver of 12 inches and 24 inches at the bottom as shown in Figure F-37. The fluid flow channel for the steam system would consist of twenty 0.25-inch I.D. (0.40 inch O.D.) tubes in parallel (channel width of wrap W would be 8.0 inches). The oil system would use 64 0.50-inch I.D. (0.70 inch O.D.) tubes in parallel. A manifold at the bottom of the receiver distributes the fluid equally to all tubes. The tubes then are continuous the whole length of the receiver with a manifold at the of the receiver collecting the steam or oil from the tubes. Each of the steam tubes would have an overall length of approximately 400 feet with the oil tubes having an approximate length of 71 feet. Like the 50 foot concentrator, the tube material would probably be Inconel for the water/steam system and possibly stainless steel for the oil system.

The test model and the prototype receiver will

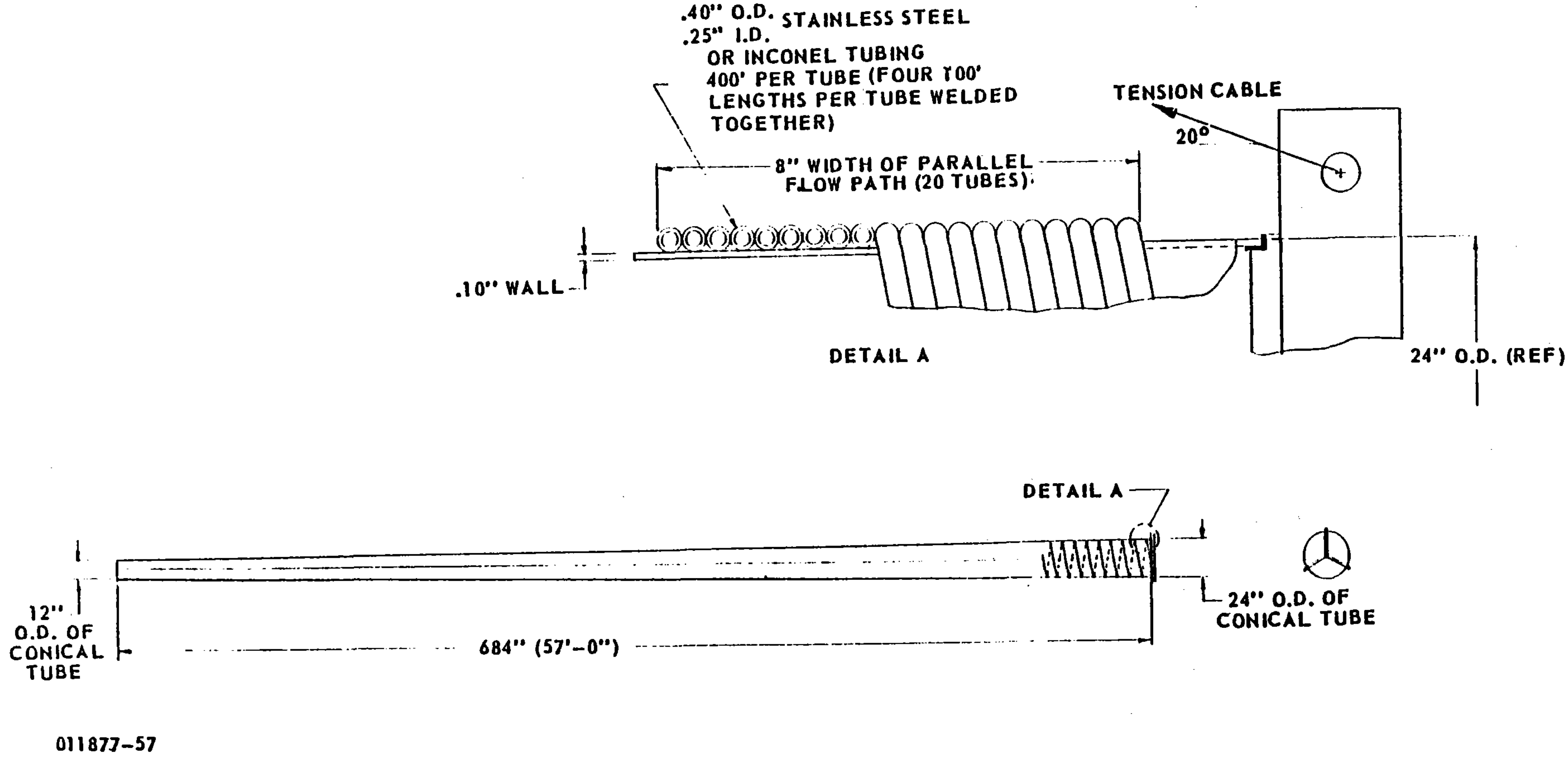

E-SYSTEMS Energy Technology Center

Figure F-37. Nominal Receiver for the 200 Foot Concentrator have maximum steam tube temperatures of approximately 1100°F for fluid flow rates at solar noon (h_i = 1000 Btu/hrft^2°F) and approximately 1400°F for minimum fluid flow rates at early morning (h_i = 250 Btu/hrft^2°F). The water flow rate at solar noon for the prototype steam system would be approximately 5150 pounds/hour and only 25% to 33% of this flow rate would be required at early morning and late afternoon. The oil flow rate for the prototype system would be approximately 540 gallons/minute at solar noon for a 50°F oil temperature rise through the receiver. The test model flow rates scale down by a factor of 16.

The 0.25 inch I.D. Inconel (0.40 inch O.D.) tube has maximum internal stresses of 6,000 to 7,750 psi for the 750 psi steam system. The stresses would be approximately the same for a 100 psi oil system.

The 0.25 inch I.D. tube temperatures under transient water shut off conditions reach 1550° to 1750°F after 10 seconds with the water shut off and the receiver still in the caustic region. The receiver will have to be moved out of the caustic region in 5 to 10 seconds after a flow failure.

APPENDIX G. RECEIVER THERMAL STRESS ANALYSIS AND MATERIAL SELECTION

This appendix describes the stress analysis of the FMDF receiver flow tubing and recomends a suitable material. Due to the criticality of the results separate thermal stress analysis of the receiver tubes were conducted at TTU and E-Systems. The results are described below.

The receiver consists of a band of approximately 20 tubes forming a "ribbon" which is wound helically about the receiver central supporting structure. The tubes are subjected to a concentrated solar energy flux that varies along the length and circumference of the receiver, as described in section IV and Appendix E and F. Because of the geometry of the tubes, only a small circumferential portion of any tube receives incident solar flux, as the major portion of a tube is in the shadow of another tube.

As a result of this non-uniform flux input, thermal gradients are produced in the tubes giving rise to thermal stresses. For this reason a tube stress analysis was conducted to determine magnitudes of stresses resulting from thermal effects as well as from internal pressure.

G-1 TTU ANALYSIS

The stress analysis was conducted by assuming that a two dimensional state of plane strain existed in the tube. This assumption was considered to be appropriate since the thermal gradients (which are the primary cause of the thermal stresses) are much more severe in the tube circumferential direction than along the length of the tube. The analysis was conducted for the thermal distribution in the caustic region ($x/R = .53$) as shown in Figure F-19.

A finite element plane strain analysis was conducted by subdividing the cross section of the circular tube into 160 triangular elements -- 20 in the circumferential direction and 8 in the radial direction. The elements had a quadratic variation of temperature and displacement and are considered to give very accurate results. The analysis was conducted using the thermal properties of the material Inconel 617 at 1300° F. The analysis was conducted for a tube of inside diameter of 0.25", outside diameter of 0.40" and with an internal pressure of 1000 psi. The results of the stress analysis indicate a maximum stress of about 8500 psi in the material.

The material Inconel 617 was selected for the tubing after a number of preliminary stress calculations with various materials indicated that stresses of the level of 8000 to 10000 psi were to be expected.

G-2 E-SYSTEMS ANALYSIS

The incident solar flux is absorbed by one segment of a tube while the balance remains shaded as described in Appendix F. As a result, the flux distribution is non-uniform, leading to circumferential as well as radial gradients in the tube. Although axial gradients exist within the tube, their effects are second order due to the fact that the tube is very long and essentially unrestrained (free to grow in length).

The receiver tube was treated structurally as a planar stress problem. The element of the tube analyzed was taken as a 1/1000 inch thick slice. The slice was defined by a thermal gradient distribution as described in Figure F-19.

A finite element program was used to analyze the effects of thermal gradients within the tube. The section of the tube was divided symmetrically into 320 separate elements, 8 radially and 40 circumferentially as shown in Fig. G-1. This division yielded a structural model with 360 nodes. Note from the geometry that the model is composed of equally spaced elements, every 9^o circumferentially and thickness is divided into 8 divisions, radially. Thus, the geometry of the individual element is set by the parameters of inside radius and outside radius.

The thermal model (Appendix F) was defined by 100 symmetrically spaced nodes, 20 circumferentially and 5 radially. A preprocessor was formulated to relate these node temperatures to element temperatures in the finite element structural mode. Internal pressure was an independent load factor that was applied simultaneously with the thermal load. This load was introduced as a running load on the exposed face of the inner row of elements in the structural model.

Material property variation at elevated temperatures was considered and the appropriate constants entered into the

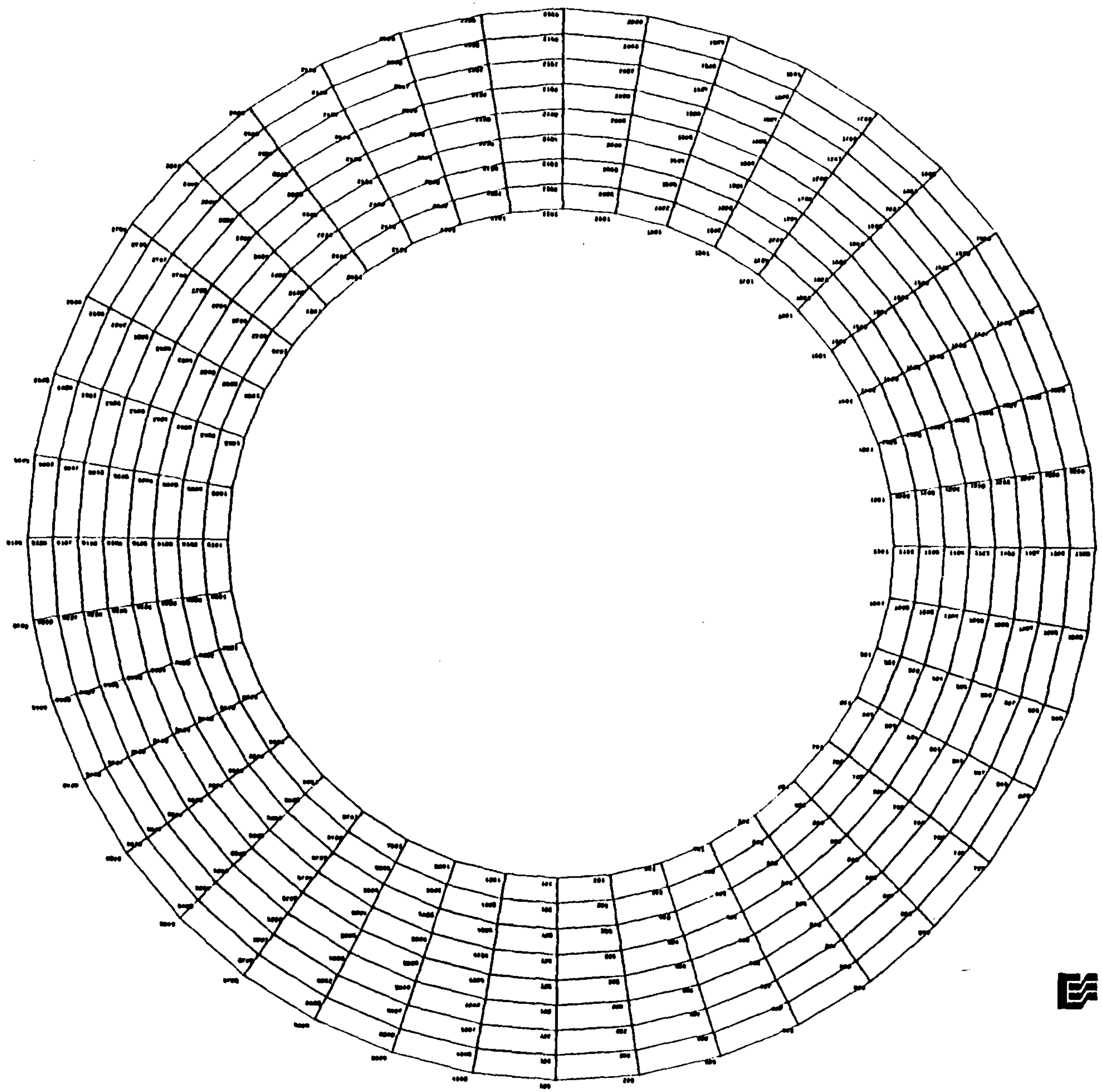

Figure G - 1. Thermal Gradient Tube Model

E-SYSTEMS
Energy Technology Center

program. These properties were modulus of elasticity, Poisson's ratio, and the coefficient of thermal expansion. These material constants were used to define the behavior of the structure at the elevated temperatures described in Appendix F.

The study performed for this report was conducted for a variety of different diameters and thicknesses of tubes. Tubes with internal steam as well as those with oil were considered in the analysis. The tube geometry remained a symmetric model as discussed previously. The results of the study are given in Table G-1 . The critical item of concern was the maximum stress level in the tube. Although stress at all points in the model was calculated, only the maximum value is shown in Table G-1.

Considerations for evaluating the tube from a structural point of view were yield stress and creep allowables for a given temperature. The relative merit of a given tube configuration was based on the margin of safety between the allowables and those values predicted by the computer model. The data in Table G-1 are for Inconel 718 from which the allowable stress at the maximum operating temperature indicated is 20,000 psi. These data indicate no structural problems for any of the tubes with the internal fluid pressure having only a secondary effect.

A brief description of the physical and chemical properties of this material are presented below from Ref. G-1.

Table G-1

E-Systems Thermal Stress Analysis For Receiver Tubes (Inconel 718)

Configuration#	Maximum Stress KSI	Inside Diameter In.	Outside Diameter In.	Internal Heat Transfer Coefficient Btu/hrft^2°F	Internal Fluid	Internal Fluid Temperature Deg F	Internal Fluid Pressure PSI	Conditions
1	11.904	.50	.70	500	Oil	300	750	Steady State
2	7.467	.25	.40	250	Steam	750	750	Transient
3	3.372	.10	.16	1000	Steam	750	750	Steady State
4	7.308	.25	.40	250	Steam	750	750	Steady State
5	8.463	.50	.70	500	Steam	750	750	Steady State
6	5.956	.25	.40	1000	Steam	750	750	Steady State
7	11.783	.50	.70	500	Oil	300	300	Steady State
8	7.748	.25	.40	1000	Steam	750	750	Transient
9	1.613	.25	.40	1000	Steam	750	0	Steady State
10	3.045	.10	.16	1000	Steam	750	0	Steady State

The basic physical composition of Inconel 617 is nickel, 54%; chromium, 22%; cobalt, 12.5%; molybdenum, 9%; others, 1.5%. This alloy has two excellent properties which makes it a suitable choice for the tubing material: corrosion resistance and high creep rupture strength.

Inconel 617 has a high degree of resistance to oxidation and carburization at high temperature. It has very good resistance to corrosion by water and by alkalies. The resistance to corrosion by oxidation results from the formation at elevated temperatures of a thin subsurface zone of oxide particles, primarily of chromium and aluminum. As a secondary benefit, this layer of oxides has good absorptivity characteristics.

Creep rupture strength is important in this application because the material will be subjected to stress levels at elevated temperatures over a time period of 30 years. A conservative estimate of tube creep rupture life would assume a constant stress condition at 9 hours per day for 30 years, or about 98,600 hours. Inconel 617 has a creep rupture strength of 17,000 psi for 100,000 hours at $1300^{\circ}F$.

The fatigue strength of the material at elevated temperatures is also quite good. Estimating 10 thermal cycles per hour over a period of 30 years yields a cycle life of approximately 10^6 cycles. The fatigue strength of Inconel 617 for 10^6 cycles at $1600^{\circ}F$ (which is above the design temperatures of this application) is 21,000 psi.

APPENDIX G REFERENCES

G-1. *Inconel Alloy 617*, Huntington Alloys, Inc., Huntington, W.V., 1972

APPENDIX H. OVERALL COLLECTOR ANALYSIS

H-1 METHODOLOGY

The FMDF collector analysis was based on an evaluation of the equation:

$$\dot{Q}_{coll} = \rho\alpha F_{track} I_{dn} - \dot{Q}_{loss}$$

where $\dot{Q}_{coll}$ = Energy collected per unit aperture area, Btu/hr-ft^2

$\dot{Q}_{loss}$ = Absorber heat loss per unit aperture area, Btu/hr-ft^2

I_{dn} = Direct normal insolation, Btu/hr-ft^2

F_{track} = Instantaneous effective tracking factor

ρ = Mirror surface reflectivity

α = Receiver surface absorptivity

The reflectivity and absorptivity were material properties determined to be 0.88 and 0.90 respectively, as mentioned in the preceding section. The effective tracking factor, F_{track}, was the product of the cosine of the instantaneous incident angle and the effective aperture factor, $(1- .16 \sin(2\theta_i))$. Thus:

$$F_{track} = \cos\theta_i \times (1- .16 \sin(2\theta_i))$$

where the effective aperture factor was for a 60° rim angle collector and negates regions of the dish with multiple reflections (Ref. H-1). When the incident angle, θ_i, was greater than 70°, $F_{track} = 0.9 \times \cos \theta_i$. The effective aperture factor was always less than 1.0 (except for $\theta_i = 0^\circ$), thus providing a conservative optical tracking factor of the FMDF collector since some of the multiple reflections would intercept the receiver.

The receiver heat loss per unit aperture area, $\dot{Q}_{loss}$, was determined by a thermal analysis of the collector receiver as shown earlier. The heat loss of the receiver with steam generation was for constant fluid temperatures of 950°F outlet, 100°F inlet, and approximately 900 psia pressure. The analysis for oil circulation through the receiver, however, was for a large flowrate to minimize temperature increase of the oil and approximate isothermal conditions.

An empirical equation was derived for the receiver heat loss from the thermal analysis data for steam generation in the collector at 950°F. This equation considered ambient temperature, wind velocity and solar incident angle to the collector. Thus:

$$\dot{Q}_{\substack{loss\\steam}} = \dot{Q}_{\substack{loss\\steam}} \cdot Y_{steam}$$

where

$$\dot{Q}_{\substack{loss\\steam}} = 12.2 + .97V + .02V\ (70-T) + .0032V(70-T)$$

$$Y_{steam} = .5258\ [(\theta_i - 33.75°)\pi/180]^2 + .8176$$

V = wind velocity, mph

T = ambient temperature, °F

The heat loss adjustment due to incident angle effects, Y_{steam}, was an equation of the curve in Figure F-6 , where θ_i was in degrees.

The receiver heat loss for the oil circulation study was analytically determined by assuming isothermal receiver conditions. However, comparisons with the receiver thermal analysis results, shown in Figure F-9, indicated losses higher than for a true isothermal condition. This higher heat loss was due to a receiver surface temperature higher than the oil temperature and increasing with increasing concentration. Thus, even though the oil temperature was nearly constant, the receiver surface temperature varied from nearly the inlet oil temperature to several degrees hotter than the oil, being highest at the point of highest concentration. Good agreement between the two methods was obtained by adjustment of the convection heat loss term of the analytical isothermal heat loss equation. Thus:

$$\dot{Q}_{\substack{loss\\oil}} = \dot{Q}'_{\substack{loss\\oil}} \cdot Y_{oil}$$

where

$$\dot{Q}'_{\substack{loss\\oil}} = \frac{1.17h_{ext}}{C_{avg}} (T_{oil} - T) + \frac{\sigma\varepsilon}{C_{avg}} [(T_{oil}+460)^4 - (T+460)^4]$$

Y_{oil} = $-.0007171\ \theta_i + 1.0$

h_{ext} = external receiver surface heat transfer coefficient, Btu/hr-ft^2-°F

= $1 + 0.3V$

C_{avg} = average concentration of the FMDF collector (115 for $\Delta\psi = 1°$)

T_{oil} = bulk oil temperature, °F

σ = Stefan - Boltzmann constant, 0.1714×10^{-8} Btu/hr-ft^2-°R^4

ε = receiver surface emissivity, 0.9

and the other terms were as defined previously. As shown, the convection heat loss term for the isothermal receiver was adjusted by 1.17 to account for the increased heat loss due to the higher receiver surface temperature.

H-2 HOURLY AND DAILY RESULTS

The solar energy collected by the FMDF collector was determined on an hourly basis for a whole day using the equations presented in the previous section. Smaller time increments were not deemed necessary since annual and daily insolation data was only available hourly (although transient studies will be undertaken in the future).

The insolation and weather data used in the FMDF collector analysis was from Reference H-2 (Insolation Climatology Data Base). The insolation data was for Ft. Worth, Texas and the weather (ambient temperature and wind velocity) data was for Midland, Texas. Both data sets were for 1962. It was realized that some errors could be introduced by using separate locations, as discussed in Section II, Site Analysis, but it was felt that the Midland and Fort Worth locations each better represented Crosbyton weather and insolation, respectively. The same year for each data set was selected to minimize the possible performance errors.

The hourly performance of the FMDF solar collector at 15° tilt when generating 950°F steam is represented in Figure H-1 for a typical nearly clear day (April 30, 1962 data). Shown is the direct normal insolation, the energy available after tracking losses (excluding multiple reflections), the energy collected after all optical/thermal losses, and the absorber heat loss for the ambient temperature and wind velocities indicated. The total energy collected for the day was 1367 Btu/ft^2 aperture. The total direct normal insolation received in the day was 3501 Btu/ft^2 (from sunrise to sunset). Thus, the whole day collection efficiency for

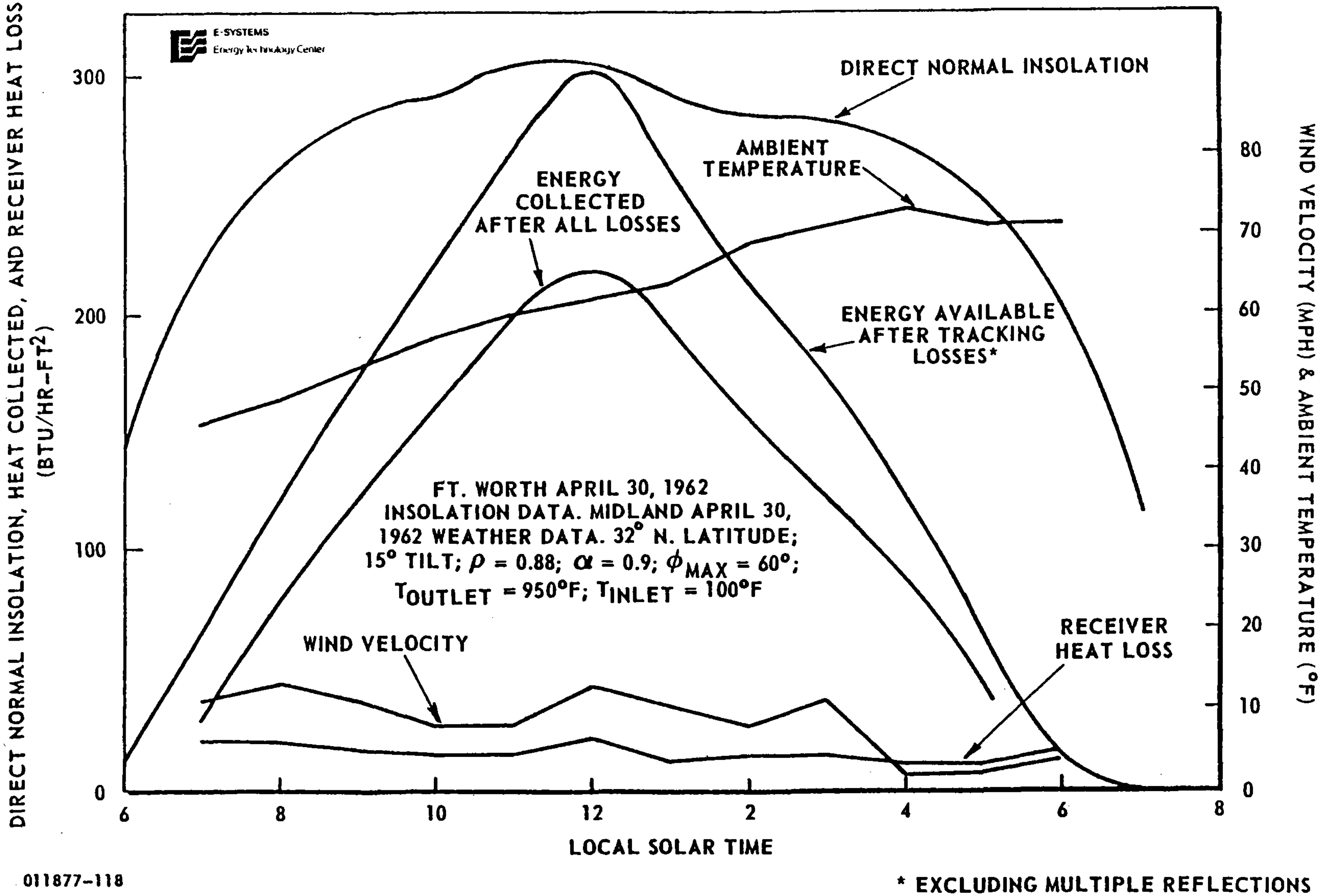

Figure H-1. Hourly Performance of FMDF Solar Collector this day was 39%. At solar noon, however, 220 Btu/ft^2-hr was collected with a solar flux of 307 Btu/ft^2-hr resulting in an hourly efficiency of 71.7%.

The hourly collection efficiency from sunrise to sunset for the equinox and solstice is represented in Figure H-2. As indicated, hourly efficiency values vary from 0 to about 70%, except for the winter solstice period which has a maximum hourly efficiency of about 45%. The peak hourly collection efficiency for the whole year occurred on August 4 for the 1962 data. The maximum hourly collection efficiency occurred with near normal incident flux at solar noon and was 72.7%.

The daily average tracking efficiency, η_{track}, was determined by summing (from sunrise to sunset) the product of the hourly F_{track} and the hourly actual insolation, then dividing by the total daily direct normal insolation (Ref. H-1). This determined the whole-day total insolation which could be effectively concentrated. The daily average tracking efficiency as determined for Figure H-1 was 0.576.

A receiver thermal loss factor, $F_{at\ell}$, (Ref. H-1) was defined as:

$$F_{at\ell} = 1 - \frac{\sum_{sunrise}^{sunset} \dot{Q}_{loss}}{\rho\alpha \sum_{sunrise}^{sunset} F_{track} I_{dn}}$$

For the day represented in Figure H-1, $F_{at\ell}$ = 0.854.

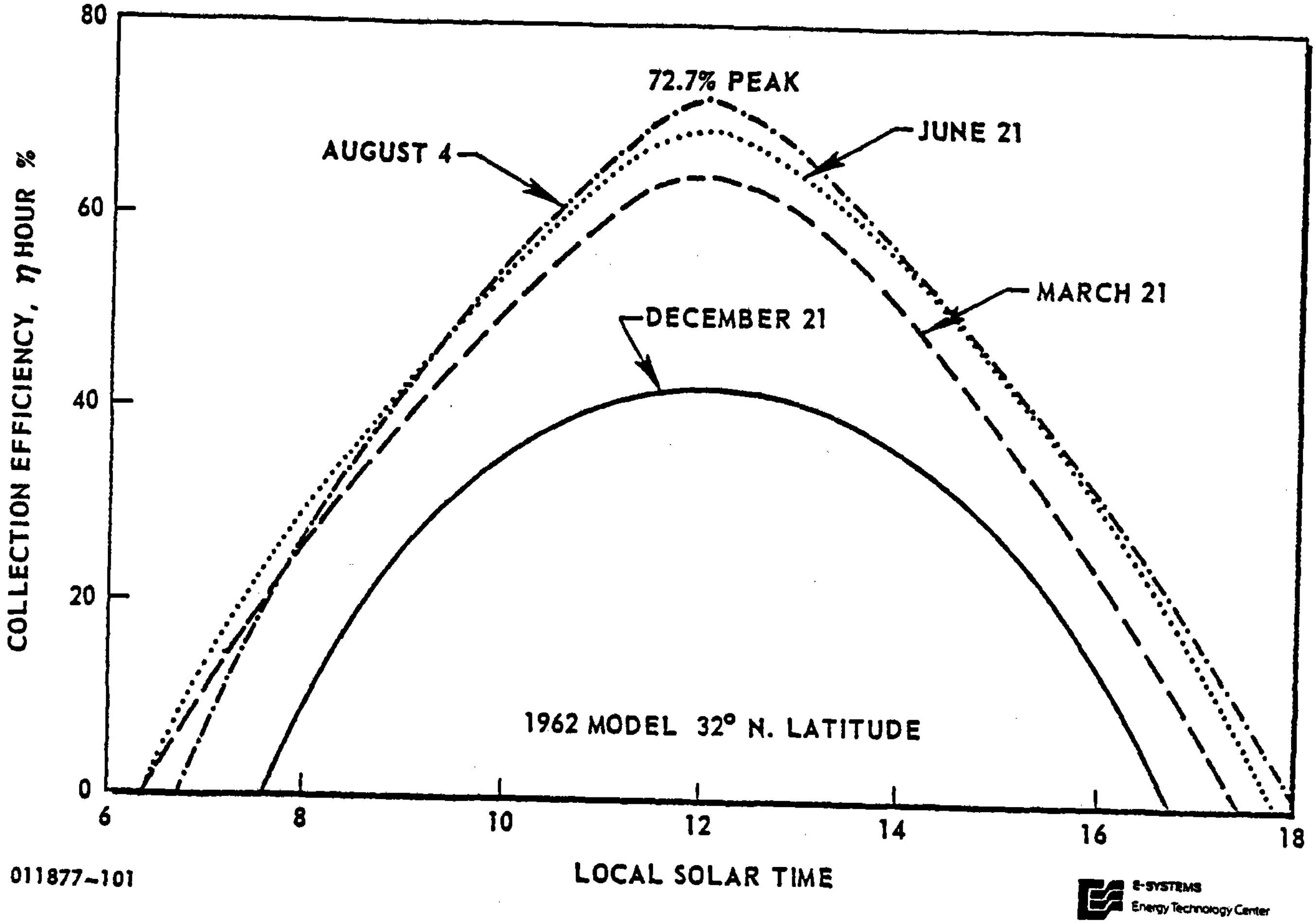

Figure H-2. Hourly Collection Efficiency for FMDF Collector at 15° Tilt & Steam Generation at 950°F

Thus, the whole-day collection efficiency can also be determined as:

$$\eta_{(\text{whole day})} = \rho \alpha \eta_{\text{track}} F_{at\ell}$$

For Figure H-1

$$\eta_{(\text{whole day})} = (0.88)(0.9)(0.576)(0.854)$$

$$= 0.390 = 39.00\%$$

which is the same as determined earlier. The daily average tracking efficiency, absorber thermal loss factor, and whole day collection efficiency is shown in Table H-1 for several days throughout the year. As shown, the whole day efficiency of collection is nearly constant throughout the year with exception of the winter solstice period. The receiver thermal loss factor is high (greater than 80%) also throughout the year with exception of the winter solstice period. The daily tracking efficiency is lowest for the winter solstice, as one would expect. The abnormally high daily tracking efficiency of August 4 is due to the normal incidence radiation received at solar noon on this day. The values as determined in Table H-1 are only for the solar radiation and weather inputs for Ft. Worth and Midland, respectively, for 1962. It is important to note that these values, while considered nominal and conservative, are dependent on the actual radiation and weather conditions.

Table H-1

Daily Average Tracking Efficiency, Absorber Thermal Loss Factor, and Whole Day Collection Efficiency for the FMDF Solar Collector

Day	η_{track}	$F_{at\ell}$	$\eta_{(whole\ day)}$
March 21	0.609	0.858	0.414
June 21	0.601	0.842	0.401
September 21	0.584	0.848	0.392
December 21	0.485	0.732	0.281
April 30	0.576	0.854	0.390
August 4	0.630	0.854	0.426

Note: Fort Worth 1962 Insolation; Midland 1962 weather; 32° N. Latitude; 15° tilt; $\rho = 0.88$; $\alpha = 0.9$; $\phi_{max} = 60°$; $T_{outlet} = 950°F$; $T_{inlet} = 100°F$

H-3 ANNUAL RESULTS

Although hourly and daily performance is important for determining such things as maximum fluid flow rates and operating hours, the annual performance provides an indication of the true effectiveness of a solar collector when used on a year round basis. Also, the annual energy collected is the quantity over which the annual collector cost must be justified. Thus, the annual energy collected is of primary importance for the Crosbyton FMDF solar system.

The annual analysis of the FMDF collector tilted 15° is shown in Figure H-3 where each day has been plotted separately for the whole year. Again, 1962 weather and insolation data was used. The left bar graph covers the period September 22 through March 22 (winter solstice period) while the right bar graph represents the remaining summer period. The daily variation of energy collected is readily noticeable by the large changes from day to day. This effect is due to the daily variation in the data's direct normal insolation (clear, partly cloudy, and overcast). The seasonal variation in energy collected can also be seen in Figure H-3 as the variation of the highest daily values throughout the year. This effect is due to the daily change in declination through the year, thus affecting the daily tracking efficiency.

The annual receiver thermal loss factor for the conditions of Figure H-3 was determined, by the method

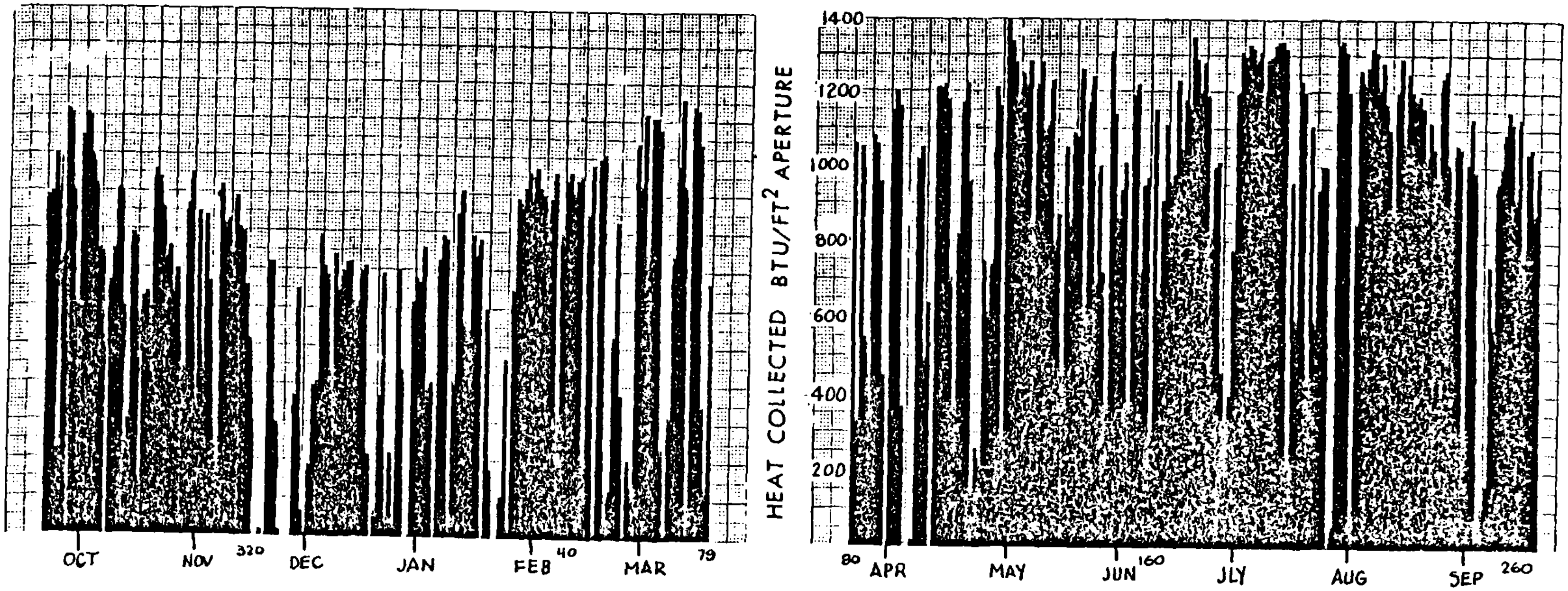

CONDITIONS:
FT. WORTH 1962 INSOLATION DATA; MIDLAND 1962 WEATHER DATA; 32° N. LATITUDE; 15° TILT; NO ACCEPTANCE OF MULTIPLE REFLECTIONS; $\rho = 0.88$; $\alpha = 0.9$; $\phi_{max} = 60°$; $T_{outlet} = 950°F$; $T_{inlet} = 100°F$; $\Delta\psi = 1°$; ABSORBER HEAT LOSS BASED ON AMBIENT TEMPERATURE, WIND VELOCITY, AND SOLAR RADIATION INCIDENCE ANGLE.

Figure H-3. Heat Collection Analysis

discussed in paragraph above to be 0.81. The annual tracking efficiency was found to be 0.569. Thus, the annual FMDF collection efficiency for a 15° tilt is (.81)(.569)(.88)(.9)= .365 or 36.5%. This is also the value obtained when the total annual energy collected is divided by the total annual direct normal insolation received (740,421 BTU/ft^2 for the 1962 data). This annual collection efficiency was based on steam generated in the collector with an outlet temperature of 950°F.

The annual energy collected for tilt angles of zero to 55° has been plotted in Figure H-4 for a 32° North Latitude. This information was used to select the nominal system design of a 15° tilt. As shown by Figure H-4, the maximum annual energy collected occurs at a tilt anle of 30° with about 280,000 Btu/ft^2 collected. This represents a maximum annual collection efficiency of 37.8% (an increase over the 15° tilt value by only 3.4%). The 15° tilt angle was selected for the nominal system design because of the reduced costs, which offset the above efficiency gain. The annual collection efficiency varied from 31.8% at 0° tilt angle to the maximum value of 37.8% at a tilt of 30°.

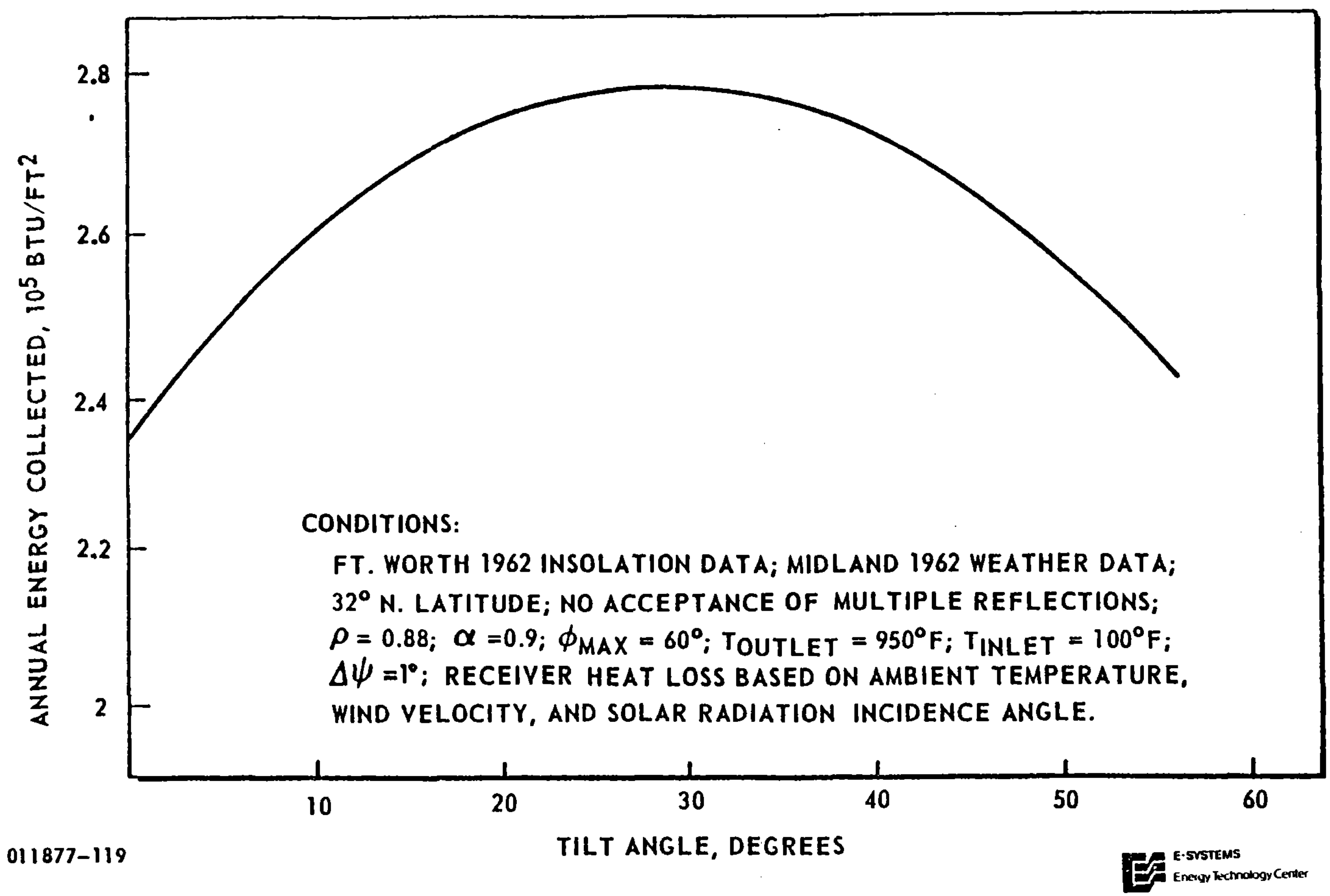

Figure H-4. Annual Energy Collected by FMDF Solar Collector vs. Tilt Angle

APPENDIX H REFERENCES

H-1. O'Neill, Mark J., "Thermo-Optical Performance Analysis of the Fixed Mirror/Distributed Focus Solar Thermal Electrical Power System (FMDF-STEPS)," Report No. 9-1900100/TR76-04 E-Systems, Inc., Dallas, Texas, May, 1976.

H-2. Insolation Climatology Data Base, Report ATR-74 (7417-16)-2 Vol. III, Aerospace Corporation, El Segundo, Calif., 1974.

☆U.S. GOVERNMENT PRINTING OFFICE: 1984-746-081/ 2313REGION NO. 4